Microgels as Protein and Enzyme Carriers: A Pathway to Biocatalytic Glycan Synthesis

Von der Fakultät für Mathematik, Informatik und Naturwissenschaften der RWTH Aachen University zur Erlangung des akademischen Grades einer Doktorin der Naturwissenschaften genehmigte Dissertation

vorgelegt von

Isabel Katja Sommerfeld, M. Sc.

aus

Nürnberg

Berichter:

Univ.-Prof. Dr. rer. nat. Andrij Pich

Univ.-Prof. Dr. rer. nat. Lothar Elling

Tag der mündlichen Prüfung: 28.08.2024

Eidesstattliche Erklärung

Isabel Katja Sommerfeld erklärt hiermit, dass diese Dissertation und die darin dargelegten Inhalte die eigenen sind und selbstständig, als Ergebnis der eigenen originären Forschung, generiert wurden.

Hiermit erkläre ich an Eides statt:

Diese Arbeit wurde vollständig oder größtenteils in der Phase als Doktorand dieser Fakultät und Universität angefertigt;

Sofern irgendein Bestandteil dieser Dissertation zuvor für einen akademischen Abschluss oder eine andere Qualifikation an dieser oder einer anderen Institution verwendet wurde, wurde dies klar angezeigt;

Wenn immer andere eigene – oder Veröffentlichungen Dritter herangezogen wurden, wurden diese klar benannt;

Wenn aus anderen eigenen – oder Veröffentlichungen Dritter zitiert wurde, wurde stets die Quelle hierfür angegeben. Diese Dissertation ist vollständig meine eigene Arbeit, mit der Ausnahme solcher Zitate;

Alle wesentlichen Quellen von Unterstützung wurden benannt;

Wenn immer ein Teil dieser Dissertation auf der Zusammenarbeit mit anderen basiert, wurde von mir klar gekennzeichnet, was von anderen und was von mir selbst erarbeitet wurde;

Teile dieser Arbeit wurden zuvor veröffentlicht und zwar in: **Publications** (Seite VII).

_____ _____

Datum Unterschrift

Preface

The results presented in this thesis were obtained between January 2020 and January 2024 at the DWI - Leibniz Institute for Interactive Materials as part of doctoral studies at the Institute of Technical and Macromolecular Chemistry at RWTH Aachen University under the supervision of Univ.-Prof. Dr. rer. nat. Andrij Pich.

The financial support for this thesis by the Federal Ministry of Education and Research (BMBF) within the framework of the project MiRAGE (Microgel Countercurrent Flow Reactor for Automated Glycan Synthesis - 031B1116B) is gratefully acknowledged. Further financial support was provided by SFB 985 “Functional Microgels and Microgel Systems” and LeibnizTransfer GreenProtect SPP 2451 “Living Materials with Adaptive Functions”. Parts of the analytical investigations were performed at the Center for Chemical Polymer Technology CPT, supported by the European Commission and the federal state of North Rhine-Westphalia (No. 300088302).

Collaborative Work

This thesis has, in part, been derived from collaborative projects:

- Hanna Malyaran performed cytocompatibility experiments with the aid of Annika Rohde under the supervision of Prof. Dr. Sabine Neuss (Biointerface Group, Helmholtz Institute for Biomedical Engineering, RWTH Aachen University).
- Glycosyltransferase production and activity assays were performed by Philip Palm and Dr. Kai P. Hussnaetter with the aid of Rebekka Wagner under the supervision of Prof. Dr. Lothar Elling (Biomaterials, Helmholtz Institute for Biomedical Engineering, RWTH Aachen University).
- The initial conception of the project MiRAGE (Microgel Countercurrent Flow Reactor for Automated Glycan Synthesis) was developed by Prof. Dr. Lothar Elling (Laboratory for Biomaterials, RWTH Aachen University), Prof. Dr. Andrij Pich (DWI – Leibniz Institute for Interactive Materials), Prof. Dr. Matthias Franzreb (Institute of Functional Interfaces of the KIT), and Dr. Erdmann Rapp (glyXera GmbH).

Additionally, measurements conducted by other doctoral students and project leaders in the group of Prof. Dr. Andrij Pich have been utilized for the characterization of the synthesized products:

- Prof. Dr. Dan E. Demco performed proton transverse magnetization relaxation experiments and their partial analysis using OriginPro Software.
- Calorimetry measurements were performed by Nadja A. Wolter with the aid of Hannah Küttner.
- Permeability assays and their plotting using OriginPro Software were conducted by Selin Bulut.

Research assistants conducted a few experiments and characterization techniques:

- Esther Dälken, 2021.
- Tudor Lile, 2023.

Furthermore, this thesis, in part, has been derived from collaborative student research projects:

- Esther Dälken: *Mucus-Inspired Self-Regenerating Microgels*, research internship, 2022.

- Yannick Burleigh: *Supramacromolecular Microgels for Protein Immobilization via Metal Affinity*, Bachelor thesis, 2023.

Other experiments and characterization techniques were conducted by the scientific team, lab technicians, or other staff in the science support team of DWI – Leibniz Institute for Interactive Materials and the Helmholtz Institute for Biomedical Engineering, RWTH Aachen University:

- Dr. Michael Pohl performed Size Exclusion Chromatography.
- Stefan Hauk performed Scanning Electron Microscopy.
- Renate Jansen performed Inductively Coupled Plasma Optical Emission Spectroscopy.
- Rainer Haas performed Size Exclusion Chromatography.
- Truc Pham produced enzymes, prepared buffers, and carried out protein assays.

Publications

Parts of this thesis have been published as journal articles, were submitted to be published, or have been presented at conferences and seminars. Furthermore, other publications were prepared during this Ph.D. project but are not part of this thesis.

Articles

- Isabel K. Sommerfeld, Hannah Malyaran, Sabine Neuss, Dan E. Demco, Andrij Pich, Multiresponsive Core-Shell Microgels Functionalized by Nitrilotriacetic Acid. *Biomacromolecules* **2024**, *25*, 2, 903–923.
- Isabel K. Sommerfeld, Esther Dälken, Lothar Elling, Andrij Pich, Nitrilotriacetic Acid Functionalized Microgels for Efficient Immobilization of Hyaluronan Synthase. *Macromolecular Bioscience* **2024**, 2400075.
- Isabel K. Sommerfeld, Sommerfeld, Isabel K.; Palm, Philip; Hussnaetter, Kai P.; Pieper, Maria I.; Bulut, Selin; Lile, Tudor; Wagner, Rebekka; Walkowiak, Jacek; Elling, Lothar, Pich; Andrij. Microgels with Immobilized Glycosyltransferases for Enzymatic Glycan Synthesis. *Biomacromolecules* **2024**, *25*, 6, 3807–3822.

The following publication was prepared during this Ph.D. project but is not part of this thesis:

- Carina Dey, Isabel K. Sommerfeld, Miluše Vlachová, Nikol Kodra, Pavla Bojarová, Vladimír Křen, Andrij Pich and Lothar Elling, Color-coded galectin fusion proteins as novel tools in biomaterial science*, submitted to Biomaterials Science.*

Poster presentations

- Isabel K. Sommerfeld, Johannes Gottschalk, Lothar Elling, and Andrij Pich: “Mucus-inspired self-regenerating microgel coatings”; Poster presentation at the 11th International Colloids Conference 2022.
- Isabel K. Sommerfeld, Johannes Gottschalk, Lothar Elling, and Andrij Pich: “Mucus-inspired self-regenerating microgel coatings”; Poster presentation at the 36th

European Colloid & Interface Society Conference 2022. Honored with the best poster award.

- Isabel K. Sommerfeld, Esther Dälken, Dan E. Demco, Johannes Gottschalk, Lothar Elling, and Andrij Pich: “Efficient hyaluronic acid production by immobilized hyaluronan synthase in nitrilotriacetate-functionalized microgels”; Poster presentation at the UK Colloids 2023.
- Isabel K. Sommerfeld, Esther Dälken, Dan E. Demco, Johannes Gottschalk, Lothar Elling, and Andrij Pich: “Efficient hyaluronic acid production by immobilized hyaluronan synthase in nitrilotriacetate-functionalized microgels”; Poster presentation at the 37th European Colloid & Interface Society Conference 2023.
- Isabel K. Sommerfeld, Jacek Walkowiak, Kai P. Hussnaetter, Matthias Franzreb, Erdmann Rapp, Lothar Elling, Andrij Pich: “Microgel countercurrent flow reactor for automated glycan synthesis with immobilized enzymes”; Poster presentation at the 37th European Colloid & Interface Society Conference 2023.
- Lothar Elling, Kai P. Hussnaetter, Philip Palm, Andrij Pich, Isabel K. Sommerfeld, Jacek Walkowiak, Matthias Franzreb, Ulrich Thiele, Katharina Bleher, Erdmann Rapp, Robert Burock, Kirill Kolmakov, René Hennig, Max Frick: “Microgel countercurrent flow reactor for automated glycan synthesis with immobilized enzymes”; BMBF status seminar "Future technologies for the industrial bioeconomy" 2023.

Acknowledgments

Having spent years at DWI – Leibniz Institute for Interactive Materials, I extend my heartfelt gratitude to those who supported my doctoral journey. Prof. Dr. Andrij Pich deserves special thanks for his mentorship, guidance, and opportunities to present my research globally. Prof. Dr. Lothar Elling's invaluable support and resources significantly contributed to the success of my research endeavors. Furthermore, I extend my thanks to Prof. Dr. Laura De Laporte for her insights during DWI mentoring.

The collaboration on the MiRAGE project with distinguished researchers like Prof. Dr. Elling, Prof. Dr. Pich, Prof. Dr. Matthias Franzreb, and Dr. Erdmann Rapp has been a privilege, enriching my academic journey. I am especially grateful to my cooperation partners from Prof. Dr. Elling's group, particularly Dr. Kai P. Hussnaetter and Philip Palm, for their significant contributions to our collaborative efforts. Their expertise and dedication have been invaluable in achieving our research goals. I also wish to acknowledge their research assistant, Rebekka Wagner, for her support. I would like to thank Carina Dey for the fruitful collaboration. Additionally, Johannes Gottschalk's assistance with preliminary tests and Hannes Frohnmeyer's help with MP-CE measurements were invaluable. Truc Pham's assistance with enzyme expression is also acknowledged. Generally, I appreciate the help of all members of Prof. Dr. Elling's group, as well as them warmly welcoming me to their office.

Furthermore, I extend my heartfelt thanks to Hanna Malyaran from the group of Prof. Dr. Sabine Neuss for her collaboration on cytocompatibility experiments, assisted by research assistant Annika Rohde.

I extend my thanks to the scientific and science support team of DWI, including Rainer Haas, Dr. Michael Pohl, Dr. Meike Emondts, Dr. Jens Köhler, Dr. Ahmed Mourran, Stefan Hauk, and Renate Jansen, for their assistance with devices, data evaluation, and measurements, which have been crucial to my research. Special thanks go to Prof. Dr. Demco from DWI for performing ^{1}H transverse relaxation measurements and assisting with their interpretation. I am further grateful for the assistance of fellow doctoral students: Inga Litzen for troubleshooting AFM issues, Nadja A. Wolter for dedication to reaction calorimetry experiments, supported by Hannah Küttner, and Selin Bulut for conducting permeability

assays. Special thanks to Maria I. Pieper for her role in the MiRAGE project and to Dr. Jacek Walkowiak for his help with project organization.

I am thankful for the opportunity to supervise several students during their research internships, particularly Esther Dälken for her contributions to generating important data, Yannick Burleigh for conducting pH-dependent DLS measurements, and Tudor Lile for his support during the final stages of my dissertation. I extend my gratitude to all other supervised students, including Gil van Wissen, Markus Ottersbach, Rebecca Sebers, Jens Fußhöller, Ulrika Michels, Nikita Alistratov, and Jinhao Liu. Though their results are not included in my thesis, the experience gained from coordinating their work has been invaluable.

I extend my heartfelt gratitude to my working group and several other colleagues from DWI. Working with you all has been a pleasure, and our shared moments have enriched my experience. Special thanks to Jan for all the coffee breaks, and Inga for our mutual pep talks. I thank Susanne, who embarked on and completed her Ph.D. journey alongside me, and Hannah for the delightful snack supply. I appreciate everyone in our lab, particularly Laura for her dedication to helping newcomers and Inga for not giving up on lab cleanliness. I also want to extend my gratitude to everyone I have had the pleasure of spending time with at various conferences including my conference roommates. Additionally, thanks to all other members of the Pich group.

Outside my work environment, I am deeply grateful to my parents for their support throughout my academic journey. I also want to express my gratitude to my friends Natalia and Janine, as well as my sisters Katharina and Julia, for their support and encouragement. Their friendship has been a source of strength and joy throughout my journey. Additionally, I am thankful to the wonderful people at PoDa Studio, where I found relaxation and joy. Last but certainly not least, I want to offer my sincerest appreciation to Konstantin for his invaluable support.

I am deeply grateful to everyone who has supported me along the way. Your encouragement, guidance, and friendship have been invaluable, and I am truly grateful for each and every one of you.

Table of Contents

Abbreviations

α3GalT	SpyC-MBP-α3GalT
AFM	Atomic Force Microscopy
AMPA	2,2′-Azobis(2-methylpropionamidine)dihydro-chloride
β4GalT	SpyC-pp-catβ4GalT
β3GlcNacT	SpyC-MBP-LgtA
BF	Bright-field
BIS	*N*,*N*′-Methylenebis(acrylamide)
CAPS	*N*-cyclohexyl-3-aminopropanesulfonic acid
cov	Covalent binding of enzymes during encapsulation
CPMG	Carr-Purcell-Meiboom-Gill
CTAB	Cetrimonium bromide
cyt c	Cytochrome c
DLS	Dynamic Light Scattering
DMSO	Dimethyl sulfoxide
E. coli	*Escherichia coli*
EDTA	Ethylenediaminetetraacetic acid
ELS	Electrophoretic Light Scattering
EPT	Electrophoretic phase transition
EPTT	Electrophoretic phase transition temperature
FDA	Fluorescein diacetate
FITC	Fluorescein isothiocyanate
FT	Fourier-Transform
FT-IR	Fourier-Transform Infrared
Gal	Galactose
Galili	Galactose-α-1,3-galactose
GalNAc	*N*-Acetylgalactosamine
GalA	Galacturonic acid
Glc	Glucose
GlcNAc	*N*-Acetylglucosamine

GlcA	Glucuronic acid
GT	Glycosyltransferase
HEPES	*N*-(2-Hydroxyethyl)piperazine-*N'*-(2-ethanesulfonic acid)
HFE	Hydrofluoroether
HMO	Human milk oligosaccharide
HPLC	High-Performance Liquid Chromatography
ICP-OES	Inductively Coupled Plasma Optical Emission Spectroscopy
ILT	Inverse Laplace Transform
IMAC	Immobilized Metal Ion Affinity Chromatography
IPTG	Isopropyl β-D-1-thiogalactopyranoside
IR	Infrared
ISO	International Standardization Organization
L	Large PEG: 20 kDa 8-arm-PEG or 10 kDa 4-arm PEG
LacNAc	*N*-Acetyl-D-Lactosamine
LB	Lysogeny broth
LCST	Lower critical solution temperature
LNnH	Lacto-*N*-neohexaose
LNnP	Lacto-*N*-neopentaose
LNnT	Lacto-*N*-neotetraose
LNT II	Lacto-*N*-triose II
MBP	Maltose binding protein
MES	2-(*N*-Morpholino)ethanesulfonic acid
MP-CE	Multiplexed Capillary Electrophoresis
NDP	Nucleoside diphosphate
NIPAM	*N*-Isopropylacrylamide
NIPMAM	*N*-Isopropylmethacrylamide
NMP	Nucleoside monophosphate
NMR	Nuclear Magnetic Resonance
noncov	Non-covalent binding of enzymes during encapsulation
NTA	Nitrilotriacetic acid
NTAaa	2,2'-((5-Acrylamido-1-carboxypentyl)azanediyl)diacetic acid

NTAMaa	2,2'-((6-Acrylamido-1-methoxy-1-oxohexan-2-yl)azanediyl)diacetate
PABA	*para*-Aminobenzoic acid
PAPA	*para*-Aminophtalic acid
PBS	Phosphate-buffered saline
PDI	Polydispersity index
PDMS	Poly(dimethylsiloxane)
PEG	Poly(ethylene glycol)
PI	Propidium iodide
pNIPAM	Poly(*N*-isopropylacrylamide)
pNTAaa	Poly(2,2'-((5-acrylamido-1-carboxypentyl)azanediyl)diacetic acid)
PR	Peak ratio: ratio of the maximum absorbance between 1750-1700 cm^{-1} divided by the maximum absorbance between 1650-1580 cm^{-1}
pVCL	Poly(*N*-vinylcaprolactam)
p(VCL/NTAaa)	Poly(*N*-vinylcaprolactam-2,2'-((5-acrylamido-1-carboxypentyl)azanediyl)diacetic acid)
R^2	coefficients of determination
RhB-MA	Methacryloxyethyl thiocarbamoyl rhodamine B
S	Small PEG: 10 kDa 8-arm-PEG or 5 kDa 4-arm PEG
SDS	Sodium dodecyl sulfate
SEM	Scanning Electron Microscopy
SE	Secondary Electron
SEC	Size Exclusion Chromatography
SH	Thiol
SNFG	Symbol Nomenclature for Glycans
SpyC	SpyCatcher
SpyT	SpyTag
STEM	Scanning Transmitting Electron Microscopy
TB	Terrific broth
*t*Boc	*t*Boc-linker (*tert*-Butyl (2-thioureidoethyl)carbamate)) comprising a 1-(2-aminoethyl)thiourea linker protected by a *tert*-butyloxycarbonyl group
TCPS	Tissue culture polystyrene

UDP	Uridine diphosphate
UV-Vis	Ultraviolet-Visible
VCL	*N*-Vinylcaprolactam
VP	*N*-Vinylpyrrolidone
VPT	Volume phase transition
VPTT	Volume phase transition temperature
VS	Vinyl sulfone
W/O	Water-in-oil
ζ	Zeta potential

Abstract

The combination of functionalized microgels with biomacromolecules presents versatile opportunities in biomedical and biotechnological fields, offering enhanced biocatalytic applications. This thesis therefore focuses on the synthesis of different microgels for the loading of proteins and enzymes. First, stimuli-responsive microgels containing ionizable functional groups were synthesized utilizing precipitation polymerization. These microgels were characterized using various techniques such as Infrared Spectroscopy, Dynamic and Electrophoretic Light Scattering, NMR relaxometry, and Electron Microscopy. The responsiveness of the microgels to various stimuli was elucidated. Most importantly, these biocompatible microgels demonstrated their utility for ionic binding of positively charged cytochrome c, thereby showcasing their potential for protein immobilization. Moreover, immobilizing His_6-tagged hyaluronan synthase onto these microgels *via* metal affinity binding, particularly using nickel ions, enabled repetitive enzymatic production of hyaluronic acid with unmatched yields, as monitored through capillary electrophoresis. Additionally, other glycosyltransferases were immobilized onto poly(ethylene glycol)-based microgels synthesized using droplet-based microfluidics. Enzyme immobilization through on-chip encapsulation was compared to post-attachment of enzymes to pre-synthesized microgels. For enzyme attachment, non-selective thiol Michael addition and selective SpyTag-SpyCatcher interaction were utilized, complemented by immobilization through mainly non-covalent interactions. Analysis of microgels involved optical microscopy for size determination, infrared spectroscopy for determination of chemical composition, and permeability assays for porosity assessment. Additionally, enzyme immobilization was confirmed using Bradford and fluorescamine assays while High-Performance Liquid Chromatography (HPLC) revealed the enzymatic activities for each glycosyltransferase. Utilizing the most suitable glycosyltransferase-microgels, cascade reactions were demonstrated, showcasing potential pathways toward a larger library of glycan products and a more efficient glycan synthesis. These findings underscore the synergistic potential of combining microgels with biomacromolecules in biomedical and biotechnological applications, particularly in the enzymatic production of complex glycans.

Zusammenfassung

Die Kombination aus funktionalisierten Mikrogelen und Biomakromolekülen eröffnet vielseitige Anwendungen in der Biomedizin und Biotechnologie, insbesondere bei enzymatischen Synthesen. Diese Arbeit befasst sich mit der Synthese verschiedener Mikrogele zur Aufnahme von Proteinen und Enzymen. Zunächst wurden stimuli-responsive, ionisierbare Mikrogele mittels Fällungspolymerisation synthetisiert. Diese Mikrogele wurden mit verschiedenen Techniken wie Infrarotspektroskopie, dynamischer und elektrophoretischer Lichtstreuung, NMR-Relaxometrie und Elektronenmikroskopie charakterisiert, wobei besonders die Stimuli-Responsivität untersucht wurde. Besonders wichtig ist, dass diese biokompatiblen Mikrogele ihre Eignung zur ionischen Bindung des positiv geladenen Cytochrom c zeigten und somit ihr Potenzial für die Proteinimmobilisierung unter Beweis stellten. Anschließend wurde die Immobilisierung einer His_6-Tag Hyaluronan-Synthase in diesen Mikrogelen über Metallchelat-Affinität untersucht, wobei die Verwendung von Ni^{2+} die besten Ergebnisse lieferte. Hyaluronsäure wurde wiederholt in hervorragenden Ausbeuten produziert, was mittels Kapillarelektrophorese überwacht wurde. Zusätzlich wurden weitere Glycosyltransferasen in Polyethylenglykol-basierten Mikrogelen immobilisiert, die mittels tropfenbasierter Mikrofluidik synthetisiert wurden. Die Enzymimmobilisierung durch *On-Chip*-Einkapselung wurde mit der Anbindung von Enzymen an zuvor synthetisierte Mikrogele verglichen. Für die Enzymanbindung wurden Thiol-Michael-Addition, selektive SpyTag-SpyCatcher-Interaktion und nicht-kovalente Wechselwirkungen genutzt. Die Analyse der Mikrogele umfasste optische Mikroskopie, Infrarotspektroskopie und Permeabilitätstests. Darüber hinaus wurde die Enzymimmobilisierung mittels Bradford- und Fluorescamin-Tests bestätigt, während die Hochleistungsflüssigkeitschromatographie zur Überprüfung der enzymatischen Aktivitäten genutzt wurde. Mit den am besten geeigneten Glycosyltransferase-Mikrogelen wurden Kaskadenreaktionen durchgeführt, um eine größere Bibliothek von Glykanprodukten zu erzeugen und Wege zu einer effizienteren Glykansynthese aufzuzeigen. Die verschiedenen Erkenntnisse unterstreichen das synergetische Potenzial der Kombination von Mikrogelen mit Biomakromolekülen in biomedizinischen und biotechnologischen Anwendungen und ebnen den Weg für Fortschritte in diesen Bereichen, insbesondere bei der enzymatischen Synthese komplexer Glykane.

I. Introduction

1. Motivation and Scientific Background

Microgels are three-dimensional, crosslinked polymer networks and are characterized by their ability to swell in compatible solvents.[1] They range in size from 100 nm to 100 µm and are, thus, located in the colloidal regime.[1–3] While they still retain a significant amount of solvent, microgels resemble hard colloids in the collapsed state.[3] Their properties are, however, different from those of common colloids, as they exhibit a soft texture and present a fuzzy surface along with dangling polymer chains when swollen.[3] The reversible switching between the collapsed and the swollen state is often imparted by external stimuli such as pH, ionic strength, or temperature, characterizing them as stimuli-responsive.[4]

Microgels often exhibit excellent biocompatibility owing to their high water content,[5] making them suitable for various bio-applications. Furthermore, their porous structure allows for the uptake and release of various guest molecules, such as proteins, in response to environmental stimuli.[6] Proteins, unlike more stable compounds, are typically highly vulnerable to alterations in their active structure. Changes caused by proteolysis, oxidation, or deamidation, can diminish their functionality.[7] Within a microgel carrier, it is possible to maintain the native conformation of the biomacromolecule and limit its aggregation, thus preserving its biological functionality. The proteins are protected from hydrolysis and other types of chemical and enzymatic degradation.[8]

Thereby, the uptake of biomacromolecules in microgels extends beyond structural proteins. Microgels are particularly intriguing for immobilizing enzymes with specific functions, representing a promising field of research.[9] Enzymes, as natural biocatalysts, are particularly valuable for the synthesis of complex compounds, where chemical synthesis may require selective protection and deprotection along with time-consuming procedures for the removal of side products.[9–11] However, enzymatic synthesis also presents several challenges, including the expensive and time-consuming process of enzyme expression, as well as the separation of products from soluble enzymes.[11] Immobilizing enzymes on a specific carrier could eliminate this issue by allowing for both simplified enzyme reusability and product isolation. The unique combination of deformability and penetrability of microgels, coupled with a stable structure[12]

renders them ideal for the uptake of enzymes and for facilitating enzymatic reactions by allowing substrates and products to penetrate.[13]

Especially for synthesizing glycans, the use of enzymes has proven to be useful,[14] particularly the class of glycosyltransferases (GTs), which catalyze the formation of glycosidic linkages between single saccharide units.[15] Glycans consist of such covalently linked monosaccharides and can exist in the form of oligo- and polysaccharides.[16] Connecting monosaccharides to create glycans results in structures of vast diversity with widely varying properties.[17] This versatility enables glycans to fulfill diverse functions, encompassing lubrication, cell-cell recognition, interactions between cells and other species, as well as roles in protein folding and stability and more.[17–19] The conjugation of glycans to other molecules such as lipids and proteins to form glycoconjugates further extends their properties and functions.[17] Given their significance in numerous biological processes, glycans and glycoconjugates are employed in various industrial sectors. Amongst others, they find applications in the biomedical field, for instance in drug and vaccine development.[20] Additionally, they are utilized in cosmetics[21] and nutrition for the production of human milk oligosaccharides (HMOs)[22] or prebiotics.[23]

Despite the advantages, immobilization offers in enabling multiple cycles of glycan production using the same enzymes,[24,25] only a few GTs have been previously immobilized for their use in glycan synthesis.[26–31] This immobilization strategy, however, has the potential to make glycan synthesis more economical and necessitates further exploration in research.[13,24]

2. Aim and Scope of the Thesis

Within the scope of this thesis, the overarching goal is to combine biomacromolecules and microgels to create materials with exceptional properties leveraging the unique characteristics of both systems. The highly porous and adaptable polymer network of microgels can be used for the uptake of guest molecules which can bring diverse functionalities into the system while microgels preserve their functionality. Their excellent biocompatibility makes microgels suitable for various bio-applications. These characteristics enable microgels to provide an advantageous system for the uptake of biomacromolecules, preserving their native conformation, limiting aggregation, and protecting them from degradation. Additionally, their stimuli-responsive nature facilitates stimuli-dependent uptake and release. Among different biomacromolecules, specific proteins or enzymes can be immobilized. This setup is particularly beneficial for enzymatic synthesis, such as glycan production, by enabling enzyme reuse and simplifying product purification.

The produced glycans play crucial roles in various biological processes, offering diverse functions such as lubrication, cell recognition, and protein stability. Due to their use in numerous industrial sectors, their efficient production is important which can be improved through the use of microgel-immobilized enzymes. GTs thereby catalyze the formation of glycosidic linkages between single saccharide units, enabling the synthesis of various glycans. Next to monoenzymatic reactions, enzymatic cascade reactions in microgels can be used to further expand the library of synthesizable products.

The central focus of this thesis, which revolves around the uptake of biomacromolecules, particularly proteins and enzymes, in microgels, is illustrated in **Figure I.1**. In the first part, a preliminary proof of concept demonstrates the use of microgels for protein uptake. In the second and third parts, complex glycans were synthesized through the enzymatic action of immobilized GTs.

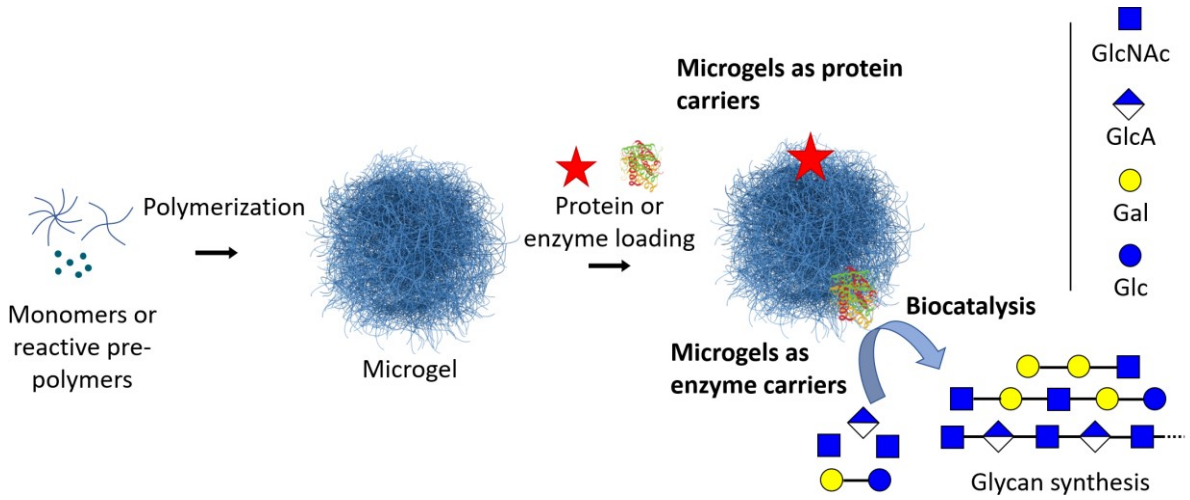

Figure I.1 The scope of this thesis is the uptake of biomacromolecules in microgels that are useful for different applications. Microgels were synthesized starting from their monomers or reactive pre-polymers. A model protein was incorporated to demonstrate the uptake of biomacromolecules. Then, different enzymes were immobilized and used for enzymatic glycan production. Glycans are illustrated using sugar symbols according to the Symbol Nomenclature for Glycans (SNFG). Depicted saccharides are composed of the monosaccharides *N*-acetylglucosamine (GlcNAc), glucuronic acid (GlcA), glucose (Glc), and galactose (Gal), connected through glycosidic linkages. Some of the depicted saccharides are sugar nucleotides, however this is not shown to simplify the process.

The findings are described in three separate chapters, namely

- Multi-Responsive Nitrilotriacetic Acid Functionalized Microgels as Protein Carriers
- Nitrilotriacetic Acid Functionalized Microgels as Carriers for Hyaluronan Synthase: Enzymatic Hyaluronic Acid Synthesis
- PEG-Based Microgels as Carriers for Glycosyltransferase: Enzymatic Cascading for Glycan Synthesis

Initially, a promising system for the uptake of biomacromolecules was synthesized: a synthesis method was developed, using precipitation polymerization to create poly(*N*-vinylcaprolactam) (pVCL)-based core-shell microgels featuring a nitrilotriacetic acid (NTA)-rich shell. The prepared microgels exhibited multi-responsive behavior to stimuli such as temperature, ionic strength, and pH. This characteristic makes them valuable for stimuli-dependent uptake and release of guest molecules. The uptake of guest molecules was demonstrated by the loading of a model protein through electrostatic forces (**Chapter III**).

Subsequently, the immobilization technique for these microgels was further developed from electrostatic immobilization to a method involving specific interactions with the His_6-affinity

tag incorporated in the enzyme hyaluronan synthase. NTA was employed here as a complexing agent for metal affinity binding. The effectiveness of this technique was further evaluated by testing the resulting enzymatic activity (**Chapter IV**).

Finally, poly(ethylene glycol) (PEG)-based microgels containing immobilized GTs were synthesized using droplet microfluidics. GT-microgels fabricated through on-chip enzyme encapsulation were compared to GT-microgels obtained by post-attachment of enzymes to pre-synthesized microgels. The non-selective thiol Michael addition and selective SpyTag-SpyCatcher interaction were employed for enzyme attachment. The microgels were tested for their ability to form glycans, both using the GT-microgels separately and in enzymatic multi-step cascade reactions (**Chapter V**).

3. References

(1) Scheffold, F. Pathways and Challenges towards a Complete Characterization of Microgels. *Nat. Commun.* **2020**, *11*, 4315.

(2) Gold, V., Ed. *The IUPAC Compendium of Chemical Terminology*; International Union of Pure and Applied Chemistry (IUPAC): Research Triangle Park, NC, 2019.

(3) Ponomareva, E.; Tadgell, B.; Hildebrandt, M.; Krüsmann, M.; Prévost, S.; Mulvaney, P.; Karg, M. The Fuzzy Sphere Morphology is Responsible for the Increase in Light Scattering During the Shrinkage of Thermoresponsive Microgels. *Soft Matter* **2022**, *18*, 807–825.

(4) Pasparakis, G.; Vamvakaki, M. Multiresponsive Polymers: Nano-Sized Assemblies, Stimuli-Sensitive Gels and Smart Surfaces. *Polym. Chem.* **2011**, *2*, 1234.

(5) Saunders, B. R.; Laajam, N.; Daly, E.; Teow, S.; Hu, X.; Stepto, R. Microgels: From Responsive Polymer Colloids to Biomaterials. *Adv. Colloid Interface Sci.* **2009**, *147-148*, 251–262.

(6) Sommerfeld, I. K.; Malyaran, H.; Neuss, S.; Demco, D. E.; Pich, A. Multi-Responsive Core-Shell Microgels Functionalized by Nitrilotriacetic Acid. *Biomacromolecules* **2024**, *25*, 903–923.

(7) Smith, M. H.; Lyon, L. A. Tunable Encapsulation of Proteins within Charged Microgels. *Macromolecules* **2011**, *44*, 8154–8160.

(8) Malmsten, M.; Bysell, H.; Hansson, P. Biomacromolecules in Microgels — Opportunities and Challenges for Drug Delivery. *Curr. Opin. Colloid Interface Sci.* **2010**, *15*, 435–444.

(9) Nöth, M.; Gau, E.; Jung, F.; Davari, M. D.; El-Awaad, I.; Pich, A.; Schwaneberg, U. Biocatalytic Microgels (μ-Gelzymes): Synthesis, Concepts, and Emerging Applications. *Green Chem.* **2020**, *22*, 8183–8209.

(10) Choi, J.-M.; Han, S.-S.; Kim, H.-S. Industrial Applications of Enzyme Biocatalysis: Current Status and Future Aspects. *Biotechnol. Adv.* **2015**, *33*, 1443–1454.

(11) Heinzler, R.; Fischöder, T.; Elling, L.; Franzreb, M. Toward Automated Enzymatic Glycan Synthesis in a Compartmented Flow Microreactor System. *Adv. Synth. Catal.* **2019**, *361*, 4506–4516.

(12) Karg, M.; Pich, A.; Hellweg, T.; Hoare, T.; Lyon, L. A.; Crassous, J. J.; Suzuki, D.; Gumerov, R. A.; Schneider, S.; Potemkin, I. I.; Richtering, W. Nanogels and Microgels: From Model Colloids to Applications, Recent Developments, and Future Trends. *Langmuir* **2019**, *35*, 6231–6255.

(13) Sommerfeld, I. K.; Palm, P.; Hussnaetter, K. P.; Pieper, M. I.; Bulut, S.; Lile, T.; Wagner, R.; Walkowiak, J.; Elling, Lothar, Pich; Andrij. Microgels with Immobilized Glycosyltransferases for Enzymatic Glycan Synthesis. *Biomacromolecules* **2024**, *25*, 3807–3822.

(14) Koeller, K. M.; Wong, C. H. Synthesis of Complex Carbohydrates and Glycoconjugates: Enzyme-Based and Programmable One-Pot Strategies. *Chem. Rev.* **2000**, *100*, 4465–4494.

(15) Na, L.; Li, R.; Chen, X. Recent Progress in Synthesis of Carbohydrates with Sugar Nucleotide-Dependent Glycosyltransferases. *Curr. Opin. Chem. Biol.* **2021**, *61*, 81–95.

(16) Anggara, K.; Zhu, Y.; Fittolani, G.; Yu, Y.; Tyrikos-Ergas, T.; Delbianco, M.; Rauschenbach, S.; Abb, S.; Seeberger, P. H.; Kern, K. Identifying the Origin of Local Flexibility in a Carbohydrate Polymer. *PNAS* **2021**, *118*, e2102168118.

(17) Lebrilla, C. B.; Liu, J.; Widmalm, G.; Prestegard, J. H. Oligosaccharides and Polysaccharides. In *Essentials of Glycobiology,* 4th ed.; Varki, A., Cummings, R. D., Esko, J. D., Stanley, P., Hart, G. W., Aebi, M., Mohnen, D., Kinoshita, T., Packer, N. H., Prestegard, J. H., Schnaar, R. L., Seeberger, P. H., Eds.; Cold Spring Harbor Laboratory Press: New York, 2022.

(18) Argüeso, P. Glycobiology of the Ocular Surface: Mucins and Lectins. *Jpn. J. Ophthalmol.* **2013**, *57*, 150–155.

(19) Lu, D.; Yang, C.; Liu, Z. How Hydrophobicity and the Glycosylation Site of Glycans Affect Protein Folding and Stability: A Molecular Dynamics Simulation. *JPC B* **2012**, *116*, 390–400.

(20) Seeberger, P. H.; Freedberg, D. I.; Cummings, R. D. Glycans in Biotechnology and the Pharmaceutical Industry. In *Essentials of Glycobiology,* 4th ed.; Varki, A., Cummings, R. D., Esko, J. D., Stanley, P., Hart, G. W., Aebi, M., Mohnen, D., Kinoshita, T., Packer, N. H., Prestegard, J. H., Schnaar, R. L., Seeberger, P. H., Eds.; Cold Spring Harbor Laboratory Press: New York, 2022.

(21) Salwowska, N. M.; Bebenek, K. A.; Żądło, D. A.; Wcisło-Dziadecka, D. L. Physiochemical Properties and Application of Hyaluronic Acid: A Systematic Review. *J. Cosmet. Dermatol.* **2016**, *15*, 520–526.

(22) Bode, L. Human Milk Oligosaccharides: Every Baby Needs a Sugar Mama. *Glycobiol.* **2012**, *22*, 1147–1162.

(23) Ambrogi, V.; Bottacini, F.; Cao, L.; Kuipers, B.; Schoterman, M.; van Sinderen, D. Galacto-Oligosaccharides as Infant Prebiotics: Production, Application, Bioactive Activities and Future Perspectives. *Crit. Rev. Food Sci. Nutr.* **2023**, *63*, 753–766.

(24) Hussnaetter, K. P.; Palm, P.; Pich, A.; Franzreb, M.; Rapp, E.; Elling, L. Strategies for Automated Enzymatic Glycan Synthesis (AEGS). *Biotechnol. Adv.* **2023**, *67*, 108208.

(25) Sommerfeld, I. K.; Dälken, E.; Elling, L.; Pich, A. Nitrilotriacetic Acid Functionalized Microgels for Efficient Immobilization of Hyaluronan Synthase. *Macromol. Biosci.* **2024**, 2400075.

(26) Ito, T.; Sadamoto, R.; Naruchi, K.; Togame, H.; Takemoto, H.; Kondo, H.; Nishimura, S.-I. Highly Oriented Recombinant Glycosyltransferases: Site-Specific Immobilization of Unstable Membrane Proteins by Using Staphylococcus Aureus Sortase A. *Biochem.* **2010**, *49*, 2604–2614.

(27) Naruchi, K.; Nishimura, S.-I. Membrane-Bound Stable Glycosyltransferases: Highly Oriented Protein Immobilization by a C-Terminal Cationic Amphipathic Peptide. *Angew. Chem. Int. Ed.* **2011**, *50*, 1328–1331.

(28) Makrydaki, E.; Donini, R.; Krueger, A.; Royle, K.; Moya-Ramirez, I.; Kuntz, D. A.; Rose, D. R.; Haslam, S. M.; Polizzi, K.; Kontoravdi, C. Immobilised Enzyme Cascade for Targeted Glycosylation. *Nat. Chem. Biol.* **2024**, 1–10, Online Ahead of Print.

(29) Qiao, M.; Ji, Y.; Linhardt, R. J.; Zhang, X.; Huang, H. Fabricating Bimetal Organic Material Capsules with a Commodious Microenvironment and Synergistic Effect for Glycosyltransferase. *ACS Appl. Mater. Interfaces* **2022**, *14*, 26034–26043.

(30) Liu, H.; Tegl, G.; Nidetzky, B. Glycosyltransferase Co-Immobilization for Natural Product Glycosylation: Cascade Biosynthesis of the C-Glucoside Nothofagin with Efficient Reuse of Enzymes. *Adv. Synth. Catal.* **2021**, *363*, 2157–2169.

(31) Trobo-Maseda, L.; Romero-Fernandez, M.; Guisan, J. M.; Rocha-Martin, J. Glycosylation of Polyphenolic Compounds: Design of a Self-Sufficient Biocatalyst by Co-Immobilization of a Glycosyltransferase, a Sucrose Synthase and the Cofactor UDP. *Int. J. Biol. Macromol.* **2023**, *250*, 126009.

II. Theoretical Background

1. Microgel Properties and Synthesis Strategies

1.1. Exploring Microgels: Beyond Typical Colloids

As previously described, microgels are three-dimensional polymer networks that are known for their ability to swell in compatible solvents.[1] Despite falling within the colloidal regime, they possess distinct properties that set them apart from typical colloids.[2]

According to IUPAC, colloids are defined as molecules or polymolecular particles dispersed in a medium with sizes ranging between 1 nm and 1 µm in at least one dimension.[3] Felix Plamper and Walter Richtering have classified three categories of colloids: rigid particles, flexible macromolecules, and micellar aggregates based on surfactants.[2] Instead of being assigned to one of these categories, microgels combine typical characteristics of all of these (**Figure II.1**).[1,2]

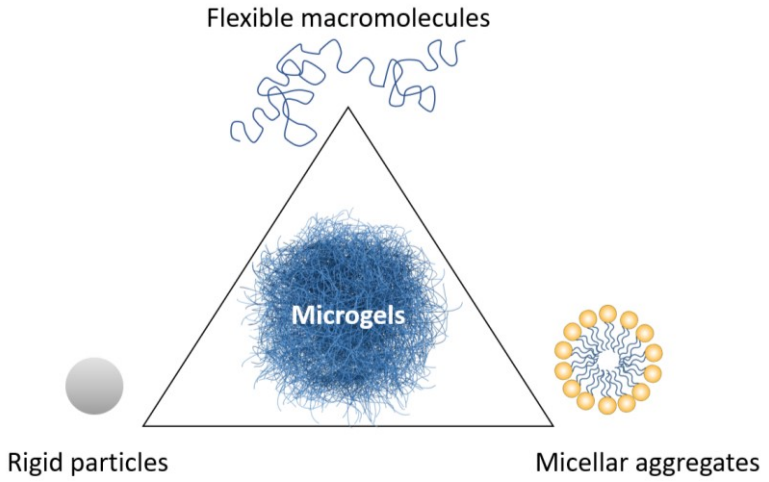

Figure II.1 This illustration was created based on a similar figure of Plamper and Richtering.[2] It illustrates the connection between microgels and typical colloids. Microgels combine properties of rigid particles, flexible macromolecules, and micellar aggregates.

Similar to macromolecules, microgels exhibit softness and respond rapidly to alterations in solvent quality through changes in their local conformation; similar to colloidal particles, they can undergo crystallization at high volume fractions; and similar to surfactants, they can adsorb to interfaces and reduce interfacial tension.[1,4] Therefore, by combining characteristics of very different classes of materials, innovative applications across various fields are enabled,[2] including applications in sensing,[5,6] catalysis,[7,8] and drug delivery.[9,10]

Furthermore, microgel material properties can be finely tuned by selecting distinct architectures and combinations of different monomers, providing the flexibility to introduce chemical functionalities at various positions. Through this approach, microgels facilitate the short-range coexistence of otherwise unstable combinations of chemical reactivity by combining architectural diversity with the compartmentalization of reactive groups.[2]

One example of a material property that can be introduced by specific (co-)monomers is sensitivity to various stimuli. Stimuli-responsive microgels have the ability to change their properties depending on environmental conditions, making them particularly interesting for various applications. Stimuli-responsiveness therefore warrants further discussion.

1.2. Stimuli-Responsiveness of Polymers and Microgels

Microgels can possess stimuli-responsive properties, which can be described as stimuli-induced conformational and chemical changes in the polymeric system.[11,12] These stimuli typically are alterations in the material's environment, including changes in pH or temperature, and the presence or absence of specific chemical and biological compounds. Further stimuli can be the application of electrical, magnetic, or electromagnetic fields.[11]

Especially temperature-responsive properties of microgels, which are connected to the lower critical solution temperature (LCST) of their corresponding linear polymers, have gained much attention.[13,14] The LCST is dependent on various factors, including the degree of polymerization and polydispersity index (PDI).[15] At the LCST, linear polymers experience a coil-to-globule transition. This transition arises from the balance between entropy and enthalpy, mainly involving the movement of solvent molecules versus the hydrogen and van der Waals bonds among solvent molecules and the polymer.[13] At temperatures below the LCST, hydrogen bonding between the polymer and solvent prevents the dissociation of solvent molecules. However, as the temperature increases, hydrophobic interaction between polymer chains increases, while the number of hydrogen bonds decreases due to disruption by the increasing movement of solvent molecules.[15] The release of solvent molecules from the network leads to a collapse of the polymer chains. The associated gain in entropy is explained by the increased translational and rotational motion of solvent molecules when they are no longer packed into a cage surrounding the polymer.[13,15] In microgels, this

temperature-responsivity manifests as a volume change triggered by a significant expulsion of solvent at a specific temperature, known as the volume phase transition temperature (VPTT). This terminology highlights the microgel's volume collapse at this temperature, contrasting with the nearly complete desolvation observed for linear polymers.[13] In **Figure II.2**, the behavior of polymers and microgels upon encountering the LCST (polymers) and the VPTT (microgels) is depicted, showing the similarity between both processes.

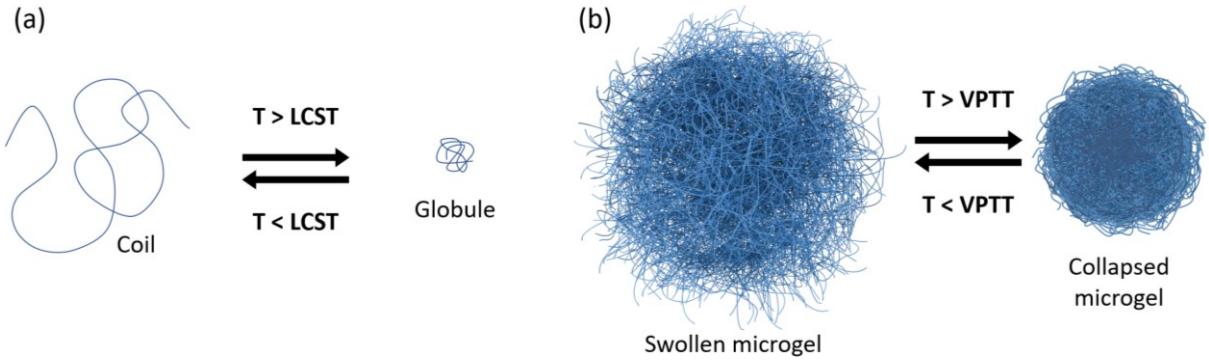

Figure II.2 Schematic depiction of the behavior of (a): linear polymers and (b): microgels upon encountering the LCST and VPTT, respectively. Linear polymers undergo a coil-to-globule transition at the LCST, while microgels display a volume change through a significant expulsion of solvent a the VPTT. Both processes are reversible.

Poly(*N*-isopropylacrylamide) (pNIPAM), with an LCST of 32 °C, is the most extensively studied temperature-sensitive polymer due to the proximity of the LCST to human body temperature and the insensitivity to environmental conditions.[16] A polymer exhibiting a similar LCST is poly(*N*-vinylcaprolactam) (pVCL),[17] which, in contrast, possesses a higher tunability through added salts, surfactants, or cosolvent.[18] Furthermore, its LCST value decreases with increasing polymer chain length and concentration.[17] This tunability can enable specific applications depending on the desired LCST.

Comparing pNIPAM and pVCL with one another, there is no significant difference in short-term biocompatibility, as observed after 12 h by Vihola *et al*.[19] However, Hoare and Pelton[20] have shown that pNIPAM is partially hydrolyzed under acidic conditions. Hydrolysis can lead to the formation of low molecular weight amine compounds which may impart higher cytotoxicity of pNIPAM in long-term studies.[17,21] Contrary, pVCL is rather stable against hydrolysis and, therefore, is expected to be more biocompatible for long-term applications. If hydrolysis of the amide bond occurs under harsh, acidic conditions, a polymeric carboxylic acid

forms.[22] Without the formation of low molecular weight compounds, higher biocompatibility is expected making pVCL more suitable for biomedical applications.[21,23]

Next to NIPAM and VCL, other known monomers suitable for the synthesis of temperature-responsive polymers or microgels are for example *N*-vinylpyrrolidone (VP) (LCST 30 °C)[24] and *N*-isopropylmethacrylamid (NIPMAM) (LCST 42 °C)[25]. The monomers are shown in **Figure II.3** along with their LCST.

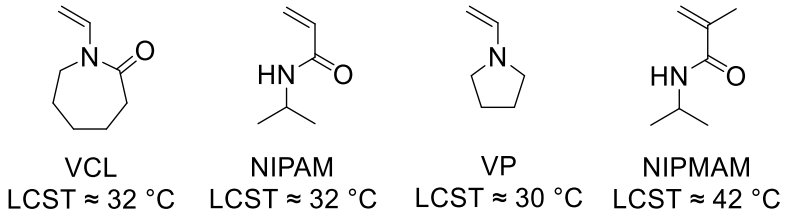

Figure II.3 Chemical structures of different monomers that exhibit temperature-responsive behavior when polymerized, along with typical LCST values[16,18,24,25] of their polymers.

The LCST of linear polymers can be further altered depending on specific needs: incorporating hydrophilic and ionic comonomers leads to an increase of the LCST,[26–28] while incorporating hydrophobic comonomers leads to a decrease.[27,28] Analogous to this, the VPTT of microgels can be affected.[29,30] The incorporation of hydrophilic groups reduces the hydrophobic attraction between polymer chains, while the incorporation of ionic groups imparts electrostatic repulsion between polymer chains, both leading to an increase in the VPTT. Contrary, the incorporation of hydrophobic groups leads to higher hydrophobic attraction and therefore a decrease in the VPTT.[31,32]

Microgels can exhibit a core-shell structure characterized by variations in crosslinking density or functionalization, leading to distinctive volume phase transition (VPT) behavior. This phenomenon occurs because the swelling and deswelling of microgels may not happen simultaneously in all compartments. Instead, a stepwise VPT can occur, where different parts of the microgel undergo a phase transition at different temperatures. A stepwise VPT is typically attributed to an inhomogeneous distribution of functional groups within the microgel core and shell. At lower temperatures, the initial deswelling can be explained by the collapse of uncharged, more hydrophobic polymer chains, while deswelling at higher temperatures is usually attributed to the collapse of more hydrophilic or charged polymer chains.[33–35] Such a stepwise collapse is schematically illustrated in **Figure II.4**, depicting a core-shell microgel with

negative charges in the microgel shell. The stepwise collapse is not only more pronounced for a higher number of charged comonomers, but also for lower amounts of crosslinker being used, primarily due to the presence of long dangling chains.[33] The number of steps in this deswelling process depends on the level of heterogeneity, which, in turn, is influenced by the distribution of comonomers within the microgel.[33,35]

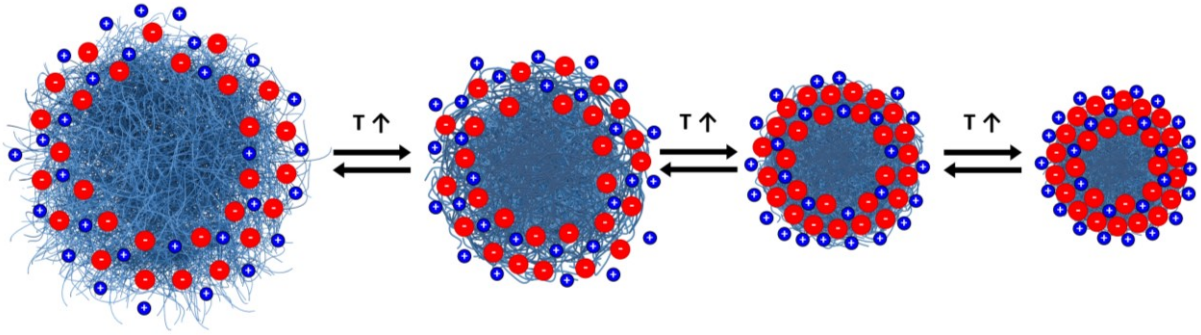

Figure II.4 Schematic depiction of core-shell microgels across the VPT, transitioning from the swollen to the collapsed state (from left to right). The microgels feature a neutral core and a negatively charged shell (with the negatively charged groups depicted in red and counterions depicted in blue). This stepwise VPT arises from the inhomogeneous distribution of charged groups within the microgel core and shell, resulting in stronger repulsion among polymer chains within the microgel shell compared to the core. Deswelling at lower temperatures is attributed to the collapse of uncharged, more hydrophobic polymer chains while deswelling at higher temperatures is attributed to the collapse of more hydrophilic or charged polymer chains. The VPT is reversible.

The responsiveness of microgels to stimuli other than temperature often stems from similar underlying mechanisms, involving the interplay of hydrophobic interactions among polymer chains and interactions between the polymer chains and the solvent.[36,37] However, among different stimuli, temperature-responsiveness has been investigated the most, primarily due to its utilization in a very well-known synthesis pathway: precipitation polymerization.

1.3. Precipitation Polymerization

One of the most commonly used methods to synthesize microgels is precipitation polymerization, which was first established by Pelton *et al*. in 1986.[14,38] The method is used for the synthesis of temperature-sensitive microgels and is performed well above the LCST of the formed polymers.[32]

All components, monomers, crosslinkers, and initiators, are dissolved in water, which is heated to the polymerization temperature. Here, the employed water-soluble initiators decompose, generating free radicals.[32] Microgel particle formation occurs through a homogeneous nucleation mechanism and uses the low solubility of the polymers above the LCST. Once the polymers reach a certain critical length, they precipitate out of solution, which accounts for the term "precipitation polymerization".[12,32] Collapsed polymer chains form colloidally unstable precursor particles which can grow further through various mechanisms until reaching colloidal stability. They grow through the aggregation of several precursor particles, deposition on the surface of larger polymer particles, or further reaction with monomers or macroradicals.[14,32] Reaching a critical size, microgels become stabilized through charges originating from the initiator fragments incorporated into the polymer chains during nucleation and growth.[32] These charges are normally located on the outer part of the microgel and lead to electrostatic repulsion of microgel particles from one another.[33] After completion of the polymerization reaction, the solution is cooled down, causing the synthesized microgels to swell below the VPTT. Here, microgels are stabilized by steric repulsion of dangling chains, an enthalpic effect, and due to the formation of hydrogen bonds between polymer segments and water molecules, an entropic effect.[32] The simplified mechanism for precipitation polymerization according to Pich and Richtering[32] is depicted in **Figure II.5**.

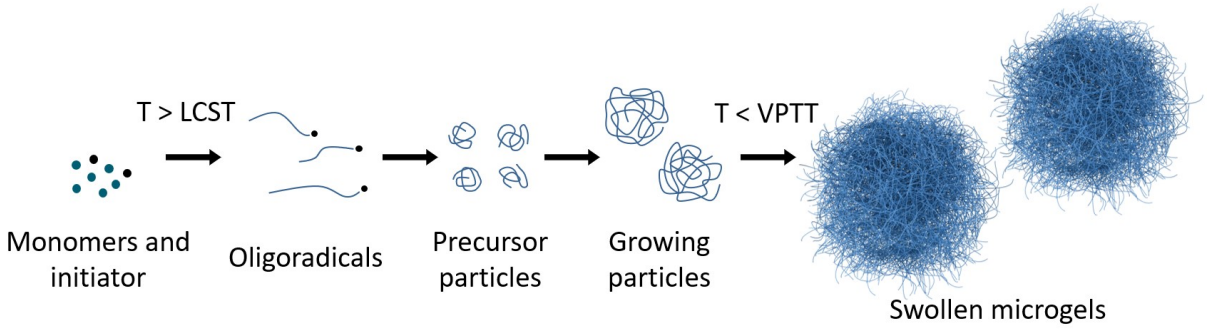

Figure II.5 The simplified mechanism for precipitation polymerization according to Pich and Richtering.[32] Monomers, including crosslinker, are dissolved in water along with the initiators. The solution is heated to the polymerization temperature, which is located above the LCST. Oligoradicals grow until reaching a critical length, upon which they precipitate to form precursor particles. The particles further through various mechanisms until reaching colloidal stability. After completing synthesis, the microgels are cooled down and swell below the VPTT.

Employing precipitation polymerization for microgel synthesis offers several advantages. Various operational modes, including batch, semi-batch, or continuous polymerization, enable the optimization of reaction conditions and the customization of microgel properties to meet specific requirements. Additionally, microgel size can be finetuned by introducing comonomers or surfactants, resulting in microgels ranging from as small as 100 nm to 3 µm with a highly narrow size distribution. Furthermore, the integration of various comonomers enhances the versatility of microgel functionality.[32]

However, precipitation polymerization also comes with a few limitations. The high polymerization temperature poses challenges, as it allows for the use of only thermostable materials, making it difficult to incorporate biomacromolecules during the polymerization process.[32] Additionally, generating larger microgels above 3 µm or nanogels[3] with sizes below 100 nm can be difficult.[32] Finally, the formation of a sol fraction, comprising linear or slightly branched polymer chains, during the polymerization process might impact the overall yield and purity of the microgels. This fraction can be removed by an additional purification step but along with a certain loss of yield. Effective cleaning procedures may involve dialysis or centrifugation followed by redispergation in water.[14,32]

1.4. Droplet-Based Microfluidics

Targeting some major drawbacks of precipitation polymerization, the additional use of droplet-based microfluidics for specific applications proves advantageous. This approach allows for the generation of larger microgel particles, typically ranging from 10 µm to several hundreds of micrometers.[39,40] The microgels generated during this process surpass the colloidal regime[3] with their sizes reaching macroscopic levels. While IUPAC clearly defines microgels as particles with diameters up to 100 µm, the definition in literature is often extended to hundreds of micrometers.[41–43] Therefore, throughout this thesis, the term “microgels” will also be used to refer to gel particles with larger sizes. It is important to note that they may possess different properties compared to colloidal microgels, and can therefore be used in other areas.[44,45]

Using droplet-based microfluidics, microgels are prepared *via* emulsion templating: In this process, at least two immiscible fluids are dispersed to form droplets, which are subsequently

subjected to gelation.[40] The key to controlling the morphology of microgels lies in controlling the size and shape of the templating pre-microgel droplets and retaining their shape by a crosslinking process.[40,46]

Two methods for droplet-based microfluidics have been developed: the assembly of different glass microcapillaries to form a microfluidic device or the imprinting of microfluidic channels on a poly(dimethylsiloxane) (PDMS) device *via* soft lithography.[46] Furthermore glass capillary-PDMS hybrid devices have previously been fabricated.[47] While glass capillaries are highly resistant to chemicals, they are more susceptible to mechanical failure or damage compared to PDMS devices. Additionally, fabricating glass capillary devices requires advanced skill and precision and may be more time-consuming. Conversely, creating PDMS devices is notably simpler. Finally, the fabrication technique for PDMS devices offers exceptional precision and design flexibility, allowing for the fabrication of microfluidic channels with customized geometries.[46] Given the inherent advantages of PDMS devices, this thesis will primarily focus on their utilization for droplet-based microfluidics.

Photolithography is used to pattern a negative photoresist on a silicon wafer, employing a true-to-scale printed photomask as a template.[46,48] The patterned silicon wafer obtained, referred to as the master, serves as the basis for generating replicas. Non-crosslinked PDMS is poured onto the master and cured to produce replicas. Once the cured PDMS replica is removed from the master, it is typically bonded to a glass cover and connected to tubing, which can be inserted through the PDMS using tubing punch holes. This bonding process is facilitated by an earlier treatment of both the cover slide and the PDMS replica with oxygen plasma, promoting covalent bonding between the PDMS replica and the cover slide.[48] This process results in the fabrication of a PDMS device with micrometer-sized channels.

Different geometries can then be used for droplet formation. In all geometries, two immiscible phases are used, where the stream of the dispersed phase is interrupted by the continuous phase, leading to the formation of droplets.[49] In the T-junction geometry, as the droplet phase enters the junction, the continuous phase establishes a thin film layer between the dispersed phase and the device walls. This leads to a rise in pressure, effectively compressing the dispersed phase and inducing droplet formation.[49,50] Co-flowing geometry involves the two phases flowing in the same direction within two concentric channels, with the dispersed phase

being fed into the inner channel and the continuous phase being fed into the outer channel. When the continuous phase stream exerts sufficient shear stress, it can break up the aqueous phase into droplets, driven by the surface tension and the interaction between immiscible fluids.[39,49] In flow-focusing geometry, the two immiscible liquids are introduced through one central and two side channels from opposite directions. The aqueous phase in the central channel is constrained in the narrow orifice by the shear force exerted by the stream of the continuous phase. The highly regular breakup of the thread of the dispersed phase results in droplets with a narrow size distribution.[49]

Fabricating and operating co-flow and flow-focusing devices is more demanding compared to T-junction devices because they require more complex channel geometries and additional channel inlets.[48] However, especially the flow-focusing geometry offers significant advantages as it enables a more stable formation of droplets due to the symmetric shearing effect.[51,52] Furthermore, flow-focusing typically offers improved monodispersity, a superior frequency of droplet generation, and high flexibility in the size of the generated droplets.[48] Therefore, flow focusing is one of the most frequently used techniques, if not the most frequently used technique, to generate droplets in microfluidic devices.[48,52]

With the focus laid on flow-focusing microfluidic devices, the next step after droplet formation is crosslinking or polymerization of the pre-microgels. Typically, a water-in-oil (W/O) emulsion containing monomers or chemically reactive polymers in the aqueous phase is created. Subsequently, polymerization and crosslinking reactions can be conducted within the droplets.[49,53] The crosslinked microgels can then be purified by several washing steps, removing the continuous oil phase and surfactants used for droplet stabilization.[53]

The crosslinking or polymerization reactions in the droplets can be initiated by thermal or photoinitiators, which are widely used in droplet-based microfluidics.[49,53,54] However, temperature and UV irradiation can be harmful to biological substances.[55,56] Additionally, the presence of free radicals, whether UV-irradiation or thermally generated, may harm biomolecules.[55,57] Therefore, as a viable alternative to initiation by temperature or UV light, this thesis focuses on pH initiation.[57,58] Here, the use of click chemistry can be especially useful.

Click chemistry is a set of chemical reactions with specific properties, defined by Sharpless *et al.* in 2001.[59] The reactions should mimic natural processes by linking small building blocks *via*

heteroatom links. The reactions should take place under physiological conditions, employing simple processes that can tolerate the presence of oxygen and water. The reaction should exhibit a high thermodynamic driving force, facilitating rapid completion to yield a single product with minimal formation of byproducts. The reaction product should then be readily isolable in high yields.[59]

Hydrothiolation additions can be facilitated by radicals or by catalytic processes involving nucleophiles, acids, or bases and meet the criteria outlined for click reactions. Consequently, Hoyle *et al.*[60] have termed these reactions as "thiol click reactions". Specifically, the reaction of interest is referred to as thiol Michael addition, which proceeds through an anionic chain mechanism.[60] The pH-initiated thiol Michael addition has often been employed in microfluidics for crosslinking processes within pre-microgel droplets.[58,61–64] Thereby biological substances such as cells[58,61] or proteins[64] have been incorporated. Possible thiol Michael acceptors are, amongst others, vinyl sulfones or acrylates.[65] It has been shown that the Michael addition products of thiols with acrylates are prone to degradation due to partial hydrolysis of the ester linkages in the polymer chains.[66,67] Therefore, the reaction of thiols with vinyl sulfones can be chosen as a more suitable technique, the products of which, connected *via* thioether sulfone bonds, are more stable.[61,65]

Using thiol Michael addition, the polymerization reaction is directly initiated when counter-reactive groups meet at a suitable pH. Therefore, either a pH change or the injection of different aqueous phases is needed. A possible geometry of a microfluidic device is shown in **Figure II.6**, featuring the use of separate aqueous phases.

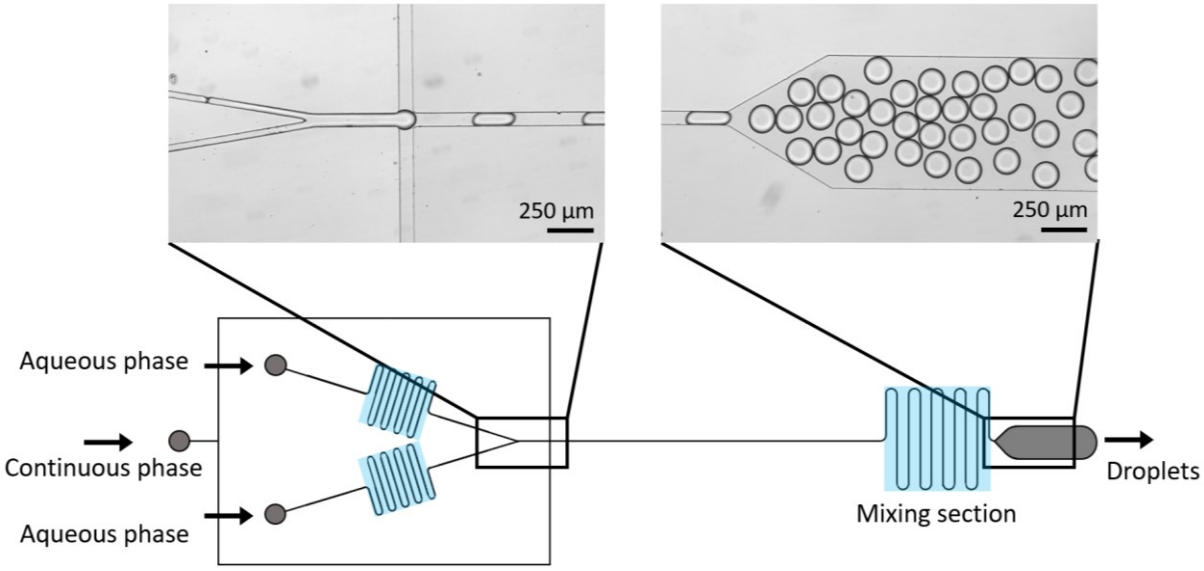

Figure II.6 Schematic drawing of the microfluidic device geometry, featuring optical microscopy brightfield images of the fabricated PDMS device. The device is designed with a flow-focusing geometry for droplet formation. Two separate aqueous phases are introduced through distinct inlets, mixing shortly before being pinched off by the continuous phase, which is supplied through another inlet. The mixing sections supporting turbulent flow are highlighted in blue.

In summary, compared to precipitation polymerization, droplet-based microfluidics offers the advantages of fabricating larger microgels and enabling synthesis at room temperature. While microgels produced *via* precipitation polymerization can be utilized for biomolecule attachment post-synthesis, droplet-based microfluidics emerges as the preferred method for biomolecule uptake during microgel synthesis. Consequently, the subsequent chapter discusses these distinct immobilization methods for biomolecules with the focus being laid on proteins and enzymes.

2. Protein and Enzyme Immobilization on Microgels

As previously described, microgels are ideal for the uptake and release of guest molecules[68] because of their high porosity, high hydrophilicity, and biocompatibility.[35,69] Aiming towards different applications, peptides, proteins, and enzymes have been immobilized in microgels.[68,70] The reasons for immobilization are of different nature. While many biomacromolecule-microgel compounds aim toward drug delivery,[70] immobilized enzymes are mainly used for biocatalytic applications.[68] The use of immobilized enzymes enables their multiple reuse, as well as simple recovery of products.[71,72]

R. A. Sheldon[73] has defined three primary categories for enzyme immobilization, which can be transferred to the immobilization of proteins and other structurally similar biomacromolecules. These are summarized as crosslinking of enzymes to each other, or binding to support, subdivided into entrapment, and carrier binding,[73] which will be explained in more detail below. Instead of using the term “carrier binding”, the term “post-attachment” is used in this thesis for a more illustrative description.

Crosslinking enzymes or proteins to one another does not require the use of an additional carrier. However, due to low mechanical stability and low reproducibility,[74] crosslinking is ruled out as an option in this thesis. Additionally, this immobilization technique is not suitable for applications where an uptake-release behavior is desired, such as drug delivery. The use of a carrier further enables the incorporation of a large variety of functional groups, extending possible applications such as surface attachment or selective interaction with desired molecules.[73,75]

The carrier-based immobilization methods are entrapment in polymer matrices during polymerization or crosslinking, and binding to pre-fabricated support (post-attachment). They are schematically depicted in **Figure II.7**. For both methods, the location of the protein can vary from the external surface of the microgel to the microgel core.[73] The synthesis of the support in the presence of the protein (entrapment or *in situ* immobilization) restricts the selection of possible materials and synthesis types, as proteins, enzymes, and other biomolecules are often not temperature-stable.[55,56,68] As previously discussed, microgel synthesis through precipitation polymerization requires high temperatures,[32] whereas droplet-based microfluidics does not.[57,58] Therefore, droplet-based microfluidics would be the

more suitable way to immobilize enzymes or proteins through entrapment. In contrast, immobilization on a pre-fabricated microgel carrier (post-attachment) ensures that the enzyme or protein is not exposed to harsh conditions.[75] This method is therefore suitable for microgels synthesized through both precipitation polymerization and droplet-based microfluidics. Microgels synthesized through precipitation polymerization have a higher surface-to-volume ratio due to their smaller size,[32] which may enable higher surface functionalization. Conversely, microgels synthesized through droplet-based microfluidics can accommodate a higher amount of biomolecules in their core due to their lower surface-to-volume ratio. The ideal location for immobilized biomolecules depends on the specific requirements of each application, considering factors such as accessibility and microenvironment. Post-attachment can be facilitated through various methods, including covalent attachment, ionic binding, complexation, or weak interactions as shown in **Figure II.7**.[73] Using entrapment, the same interaction types can be employed for immobilization.[76] However, according to its denotation, *in situ* immobilization further utilizes the entrapment in a pore of suitable size, confining the enzyme or protein through steric effects.[77,78]

Weak interactions, such as van der Waals forces or hydrophobic interactions, may fully retain enzymatic activity but are often too weak to maintain enzyme attachment to the carrier.[68,73] Ionic binding offers stronger attachment, however, it can be pH-dependent,[35,79] which may not be advantageous for each application. Furthermore, regarding enzyme immobilization, the presence of ions can affect the kinetics of the enzymatic reaction, as well as the diffusion of enzyme substrates and products.[69] Covalent bond formation provides stable enzyme attachment to the carrier,[73] but it is often non-specific and can lead to alterations in the protein or enzyme structure, either through chemical or conformational changes.[68,71,80] Complexation, which can be of electrostatic or covalent nature[81] can be considered as an additional option for binding. It involves the mutual binding of carrier and protein to a metal ion.[76] Possibly combining different advantages of the binding types, a very interesting type of binding can be referred to as affinity binding. It describes a carrier interacting with a specific group in the enzyme or protein[75,82,83] and therefore has the advantage of not binding to unwanted regions. It can entail different types of binding, from weak interactions, and ionic or covalent binding to complexation, and can also be a combination of different binding types.[82] Various challenges may arise during immobilization, depending on the specific protein

selected and binding type. Generally, immobilization can induce an unfavorable protein conformation due to interactions with the polymer network.[76] Additionally, diffusional limitations can pose significant challenges, particularly for enzyme immobilization, where substrates need to diffuse to and away from the enzyme.[76] Therefore, each immobilization requires careful observation of the resulting protein immobilization efficiency or the retained enzymatic activity.

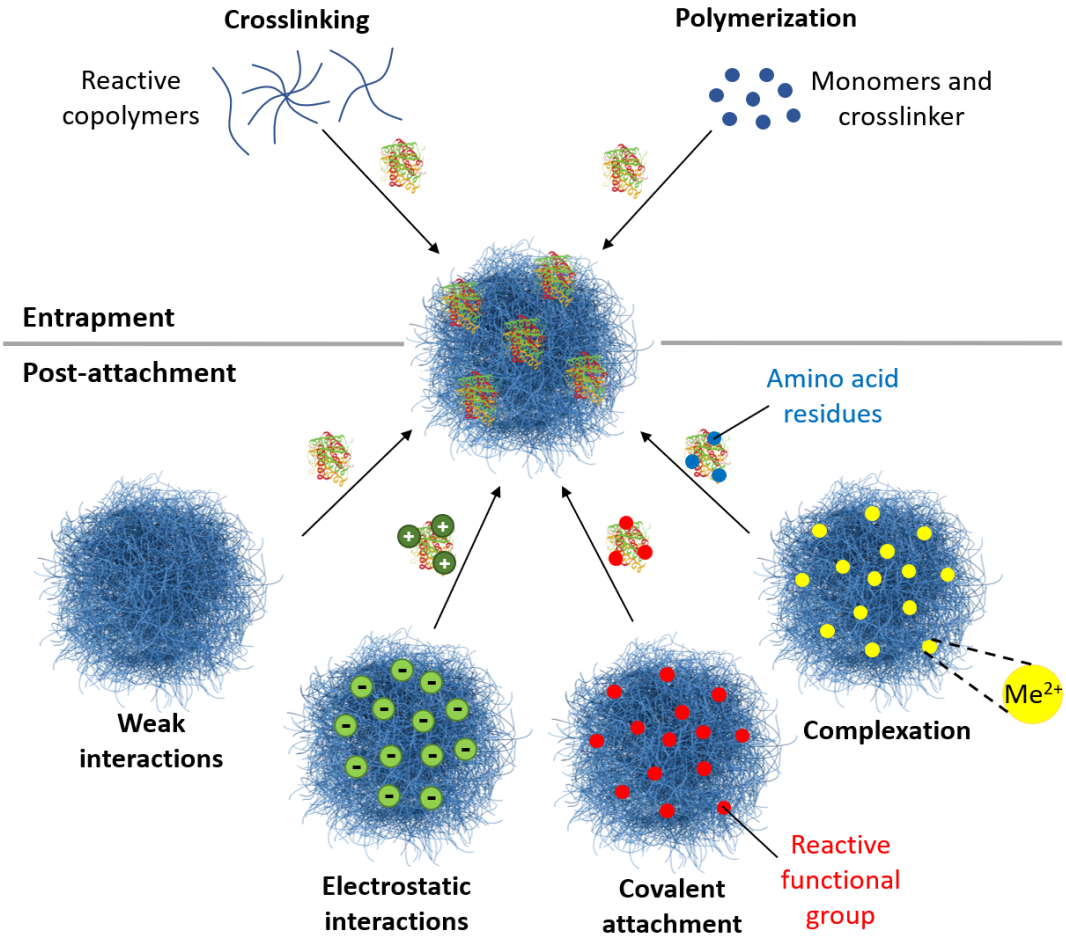

Figure II.7 Different carrier-based methods of enzyme and protein immobilization according to Sheldon,[73,76] here with microgel-carriers. For entrapment (top), the synthesis of the polymer network is performed in the presence of the protein, either through crosslinking of reactive copolymers or by polymerization of monomers and crosslinkers. For post-attachment (bottom), proteins are bound to pre-synthesized microgels. Various types of interactions or binding types are utilized to attach the protein to the microgel, including weak interactions such as van der Waals and hydrophobic interactions, electrostatic interactions, formation of covalent bonds, or mutual complexation of metal ions (Me^{2+}) by the protein and microgel. In addition to the depicted interactions, combinations of these are also possible. While these are not schematically shown for entrapment, the same interaction types can be employed for immobilization, accompanied by confinement through steric effects.

Having established various techniques for protein and enzyme immobilization, it is crucial to revisit the selection of the species intended for immobilization. In the first segment of this thesis, the primary goal is to establish a proof of concept regarding the utilization of microgels as protein immobilization platforms. This is achieved by incorporating a model protein, without specifying a particular type of protein for later applications. However, in the subsequent sections, the focus shifts towards enzyme immobilization, specifically targeting the immobilization of glycosyltransferases (GTs). These enzymes catalyze the formation of glycosidic linkages between individual saccharide units, thereby facilitating glycan synthesis.

3. Glycosyltransferases and Glycan Production

Glycans, which are oligo- or polysaccharides, are biopolymers of various chain lengths consisting of repeating units of monosaccharides.[84] Glycoconjugates encompass a wide range of compounds, including glycoproteins, glycolipids, carbohydrate-based polymers, and glycosides of natural products.[85] The involvement of glycans and glycoconjugates in numerous biological processes, including cell-cell interactions, protein folding, and protein stability, underscores their significant relevance in various biological contexts.[86,87] The versatile uses of glycans and their conjugates give rise to numerous industrial applications, spanning biomedical applications, nutrition, and cosmetics, among others.[80] Glycans and glycoconjugates exhibit remarkable structural diversity, making their chemical synthesis labor-intensive due to numerous steps of selective protection and deprotection.[88,89] Consequently, enzymatic synthesis emerges as a highly attractive alternative.[89]

GTs are an especially interesting class of enzymes, as they serve as a valuable tool for synthesizing glycans, glycoconjugates, and their analogs.[90] GTs thereby catalyze the formation of glycosidic linkages, which are covalent O-, S-, N-, or C-bonds connecting saccharides, typically monosaccharides, to other residues.[91,92] This is realized through the transfer of a saccharide from a donor to an acceptor substrate. While sugar phosphates, sugar lipids, and simple saccharides can serve as donors, the majority of donor substrates are nucleotide sugars.[92] Using sugar nucleotides as donor substrates, Leloir-type GTs are the most widely used enzymes for the formation of glycosidic bonds in nature. Thereby, either a nucleoside diphosphate (NDP) or a nucleoside monophosphate (NMP) monosaccharide can be used.[90] A few of the most common nucleotide sugars for glycan synthesis are depicted in **Figure II.8** using sugar symbols according to the SNFG as well as their respective structural formula.[93]

Having defined sugar nucleotides as donor substrates for Leloir GTs, a versatile choice of acceptor substrates can be made, including saccharides, proteins, lipids, nucleic acids, and other natural and artificial compounds. Therefore, GTs demonstrate exceptional chemical diversity in terms of both acceptor substrates and products.[92] GT-catalyzed reactions typically exhibit stereospecificity and regiospecificity. Thereby, the stereochemistry of the anomeric carbon of the donor monosaccharide is either retained or inverted.[90,92] **Figure II.9** schematically illustrates Leloir GT catalyzed reactions for the formation of glycosidic linkages

using either NDP or NMP sugars. It also indicates glycosidic linkage formation for non-Leloir GTs, which catalyze reactions similarly.[90,91]

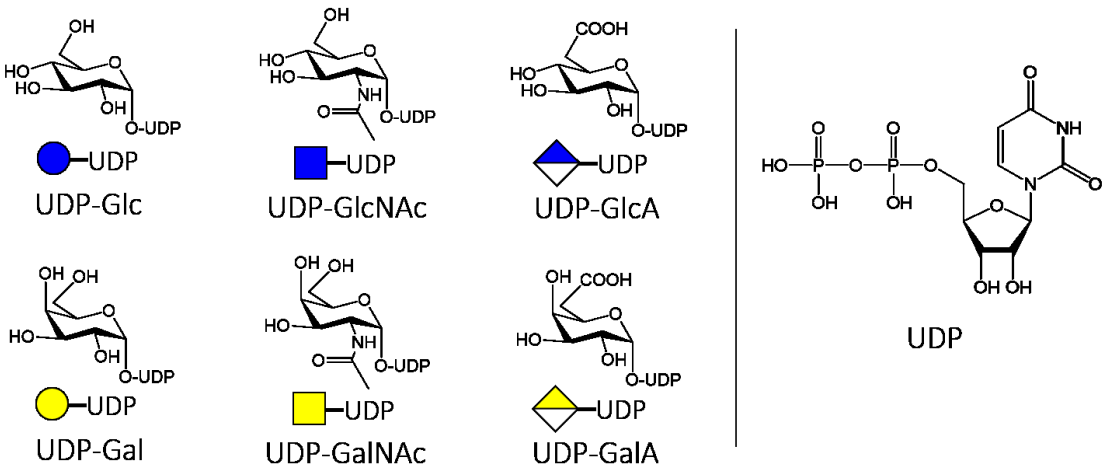

Figure II.8 According to Hussnaetter et al.[93] some of the most common nucleotide sugars for glycan synthesis include uridine diphosphate (UDP) connected to various monosaccharides such as glucose (Glc), *N*-acetylglucosamine (GlcNAc), glucuronic acid (GlcA), galactose (Gal), *N*-acetylgalactosamine (GalNAc), and galacturonic acid (GalA), resulting in different nucleotide sugars. Each nucleotide sugar is represented using its structural formula and SNFG symbol. These UDP sugars act as donor substrates for Leloir GTs, facilitating the transfer of the respective monosaccharides to an acceptor substrate.

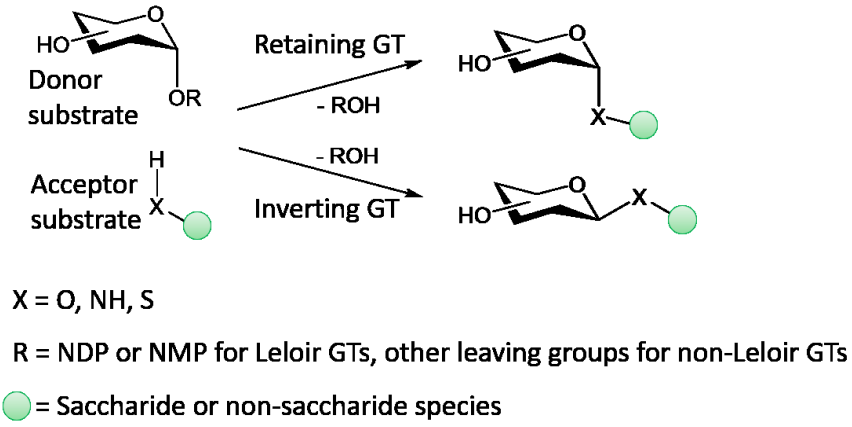

Figure II.9 During a GT-catalyzed reaction, a donor substrate is transferred to an acceptor substrate, forming a glycosidic linkage between them *via* a heteroatom (O, NH, or S). This process results in the retention or inversion of the stereochemistry of the anomeric carbon of the donor monosaccharide, depending on whether the GT is retaining or inverting. The acceptor substrate can be a saccharide or a non-saccharide species, while the donor substrate is a saccharide equipped with a leaving group (R). While sugar phosphates, sugar lipids, and simple saccharides can serve as donors for non-Leloir GTs, the majority of donor substrates are nucleotide sugars (NDP or NMP saccharides), which are substrates for Leloir GTs.[90,91]

The popularity of enzymatic glycan synthesis is rapidly increasing, due to a continuously expanding toolbox of both native and engineered GTs. With a better understanding of their substrate specificities and reaction mechanisms, researchers are increasingly turning to enzymatic methods for synthesizing complex glycans.[93] Additionally, various cost-efficient processes have been developed for synthesizing defined glycan structures in high yields.[85,93] These processes are continuously expanded due to the improved availability of GTs. Next to monoenzymatic reactions, one-pot-multienzyme reactions can be used to further expand the library of synthesizable products without the need to isolate intermediate products.[93] Therefore, not only monoenzymatic reactions but also cascade reactions of different GTs will be investigated within this thesis.

4. References

(1) Karg, M.; Pich, A.; Hellweg, T.; Hoare, T.; Lyon, L. A.; Crassous, J. J.; Suzuki, D.; Gumerov, R. A.; Schneider, S.; Potemkin, I. I.; Richtering, W. Nanogels and Microgels: From Model Colloids to Applications, Recent Developments, and Future Trends. *Langmuir* **2019**, *35*, 6231–6255.

(2) Plamper, F. A.; Richtering, W. Functional Microgels and Microgel Systems. *Acc. Chem. Res.* **2017**, *50*, 131–140.

(3) Gold, V., Ed. *The IUPAC Compendium of Chemical Terminology*; International Union of Pure and Applied Chemistry (IUPAC): Research Triangle Park, NC, 2019.

(4) Lyon, L. A.; Fernandez-Nieves, A. The Polymer/Colloid Duality of Microgel Suspensions. *Annu. Rev. Phys. Chem.* **2012**, *63*, 25–43.

(5) Sigolaeva, L. V.; Gladyr, S. Y.; Gelissen, A. P. H.; Mergel, O.; Pergushov, D. V.; Kurochkin, I. N.; Plamper, F. A.; Richtering, W. Dual-Stimuli-Sensitive Microgels as a Tool for Stimulated Spongelike Adsorption of Biomaterials for Biosensor Applications. *Biomacromolecules* **2014**, *15*, 3735–3745.

(6) Wang, H.; Yi, J.; Velado, D.; Yu, Y.; Zhou, S. Immobilization of Carbon Dots in Molecularly Imprinted Microgels for Optical Sensing of Glucose at Physiological pH. *ACS Appl. Mater. Interfaces* **2015**, *7*, 15735–15745.

(7) Tan, K. H.; Xu, W.; Stefka, S.; Demco, D. E.; Kharandiuk, T.; Ivasiv, V.; Nebesnyi, R.; Petrovskii, V. S.; Potemkin, I. I.; Pich, A. Selenium-Modified Microgels as Bio-Inspired Oxidation Catalysts. *Angew. Chem. Int. Ed.* **2019**, *58*, 9791–9796.

(8) Kleinschmidt, D.; Fernandes, M. S.; Mork, M.; Meyer, A. A.; Krischel, J.; Anakhov, M. V.; Gumerov, R. A.; Potemkin, I. I.; Rueping, M.; Pich, A. Enhanced Catalyst Performance Through Compartmentalization Exemplified by Colloidal L-Proline Modified Microgel Catalysts. *JCIS* **2020**, *559*, 76–87.

(9) Guerzoni, L. P. B.; Bohl, J.; Jans, A.; Rose, J. C.; Koehler, J.; Kuehne, A. J. C.; Laporte, L. de. Microfluidic Fabrication of Polyethylene Glycol Microgel Capsules with Tailored Properties for the Delivery of Biomolecules. *Biomater. Sci.* **2017**, *5*, 1549–1557.

(10) Agrawal, G.; Agrawal, R.; Pich, A. Dual Responsive Poly(N-vinylcaprolactam) Based Degradable Microgels for Drug Delivery. *Part. Part. Syst. Charact.* **2017**, *34*, 1700132.

(11) Klinger, D.; Landfester, K. Stimuli-Responsive Microgels for the Loading and Release of Functional Compounds: Fundamental Concepts and Applications. *Polymer* **2012**, *53*, 5209–5231.

(12) Saunders, B. R.; Laajam, N.; Daly, E.; Teow, S.; Hu, X.; Stepto, R. Microgels: From Responsive Polymer Colloids to Biomaterials. *Adv. Colloid Interface Sci.* **2009**, *147-148*, 251–262.

(13) Lyon, L. A.; Meng, Z.; Singh, N.; Sorrell, C. D.; St John, A. Thermoresponsive Microgel-Based Materials. *Chem. Soc. Rev.* **2009**, *38*, 865–874.

(14) Pelton, R. Temperature-Sensitive Aqueous Microgels. *Adv. Colloid Interface Sci.* **2000**, *85*, 1–33.

(15) Zhao, C.; Ma, Z.; Zhu, X. X. Rational Design of Thermoresponsive Polymers in Aqueous Solutions: A Thermodynamics Map. *Prog. Polym. Sci.* **2019**, *90*, 269–291.

(16) Lutz, J.-F.; Akdemir, O.; Hoth, A. Point by Point Comparison of Two Thermosensitive Polymers Exhibiting a Similar LCST: Is the Age of Poly(NIPAM) Over? *JACS* **2006**, *128*, 13046–13047.

(17) Ramos, J.; Imaz, A.; Forcada, J. Temperature-Sensitive Nanogels: Poly(N-vinylcaprolactam) versus Poly(N-isopropylacrylamide). *Polym. Chem.* **2012**, *3*, 852–856.

(18) Laukkanen, A.; Valtola, L.; Winnik, F. M.; Tenhu, H. Formation of Colloidally Stable Phase Separated Poly(N-vinylcaprolactam) in Water: A Study by Dynamic Light Scattering, Microcalorimetry, and Pressure Perturbation Calorimetry. *Macromol.* **2004**, *37*, 2268–2274.

(19) Vihola, H.; Laukkanen, A.; Valtola, L.; Tenhu, H.; Hirvonen, J. Cytotoxicity of Thermosensitive Polymers Poly(N-isopropylacrylamide), Poly(N-vinylcaprolactam) and Amphiphilically Modified Poly(N-vinylcaprolactam). *Biomaterials* **2005**, *26*, 3055–3064.

(20) Hoare, T.; Pelton, R. Functional Group Distributions in Carboxylic Acid Containing Poly(N-isopropylacrylamide) Microgels. *Langmuir* **2004**, *20*, 2123–2133.

(21) Hou, L.; Wu, P. LCST Transition of PNIPAM-b-PVCL in Water: Cooperative Aggregation of Two Distinct Thermally Responsive Segments. *Soft Matter* **2014**, *10*, 3578–3586.

(22) Vihola, H.; Laukkanen, A.; Hirvonen, J.; Tenhu, H. Binding and Release of Drugs into and from Thermosensitive Poly(N-vinylcaprolactam) Nanoparticles. *Eur. J. Pharm. Sci.* **2002**, *16*, 69–74.

(23) Lau, A. C. W.; Wu, C. Thermally Sensitive and Biocompatible Poly(N-vinylcaprolactam): Synthesis and Characterization of High Molar Mass Linear Chains. *Macromol.* **1999**, *32*, 581–584.

(24) Maeda, Y.; Nakamura, T.; Ikeda, I. Hydration and Phase Behavior of Poly(*N*-vinylcaprolactam) and Poly(*N*-vinylpyrrolidone) in Water. *Macromol.* **2001**, *35*, 217–222.

(25) Kokufuta, M. K.; Sato, S.; Kokufuta, E. LCST Behavior of Copolymers of N-Isopropylacrylamide and N-Isopropylmethacrylamide in Water. *Colloid Polym. Sci.* **2012**, *290*, 1671–1681.

(26) Muttaqien, S. E.; Nomoto, T.; Takemoto, H.; Matsui, M.; Tomoda, K.; Nishiyama, N. Poly(N-isopropylacrylamide)-Based Polymer-Inducing Isothermal Hydrophilic-to-Hydrophobic Phase Transition via Detachment of Hydrophilic Acid-Labile Moiety. *Biomacromolecules* **2019**, *20*, 1493–1504.

(27) Zhang, H.; Marmin, T.; Cuierrier, É.; Soldera, A.; Dory, Y.; Zhao, Y. A New Comonomer Design for Enhancing the pH-Triggered LCST Shift of Thermosensitive Polymers. *Polym. Chem.* **2015**, *6*, 6644–6650.

(28) Feil, H.; Bae, Y. H.; Feijen, J.; Kim, S. W. Effect of Comonomer Hydrophilicity and Ionization on the Lower Critical Solution Temperature of N-Isopropylacrylamide Copolymers. *Macromolecules* **1993**, *26*, 2496–2500.

(29) Hertle, Y.; Zeiser, M.; Hasenöhrl, C.; Busch, P.; Hellweg, T. Responsive P(NIPAM-co-NtBAM) Microgels: Flory–Rehner Description of the Swelling Behaviour. *Colloid Polym. Sci.* **2010**, *288*, 1047–1059.

(30) Belthle, T.; Lantzius-Beninga, M.; Pich, A. Pre- and Post-Functionalization of Thermoresponsive Cationic Microgels with Ionic Liquid Moieties Carrying Different Counterions. *Polym. Chem.* **2023**, *14*, 848–861.

(31) Bhaladhare, S.; Bhattacharjee, S. Chemical, Physical, and Biological Stimuli-Responsive Nanogels for Biomedical Applications (Mechanisms, Concepts, and Advancements): A Review. *Int. J. Biol. Macromol.* **2023**, *226*, 535–553.

(32) Pich, A.; Richtering, W. *Chemical Design of Responsive Microgels*; Advances in Polymer Science 234; Springer Berlin Heidelberg: Berlin, Heidelberg, 2010.

(33) Del Monte, G.; Truzzolillo, D.; Camerin, F.; Ninarello, A.; Chauveau, E.; Tavagnacco, L.; Gnan, N.; Rovigatti, L.; Sennato, S.; Zaccarelli, E. Two-Step Deswelling in the Volume Phase Transition of Thermoresponsive Microgels. *PNAS* **2021**, *118*, e2109560118.

(34) Richtering, W.; Pich, A. The Special Behaviours of Responsive Core–Shell Nanogels. *Soft Matter* **2012**, *8*, 11423.

(35) Sommerfeld, I. K.; Malyaran, H.; Neuss, S.; Demco, D. E.; Pich, A. Multi-Responsive Core-Shell Microgels Functionalized by Nitrilotriacetic Acid. *Biomacromolecules* **2024**, *25*, 903–923.

(36) Garcia, A.; Marquez, M.; Cai, T.; Rosario, R.; Hu, Z.; Gust, D.; Hayes, M.; Vail, S. A.; Park, C.-D. Photo-, Thermally, and pH-Responsive Microgels. *Langmuir* **2007**, *23*, 224–229.

(37) Hoare, T.; Pelton, R. Highly pH and Temperature Responsive Microgels Functionalized with Vinylacetic Acid. *Macromolecules* **2004**, *37*, 2544–2550.

(38) Pelton, R. H.; Chibante, P. Preparation of Aqueous Latices with N-Isopropylacrylamide. *Colloids Surf.* **1986**, *20*, 247–256.

(39) Wang, J.-T.; Wang, J.; Han, J.-J. Fabrication of Advanced Particles and Particle-Based Materials Assisted by Droplet-Based Microfluidics. *Small* **2011**, *7*, 1728–1754.

(40) Di Lorenzo, F.; Seiffert, S. Effect of Droplet Size in Acrylamide-Based Microgel Formation by Microfluidics. *Macromol. React. Eng.* **2016**, *10*, 201–205.

(41) Jiang, W.; Li, M.; Chen, Z.; Leong, K. W. Cell-Laden Microfluidic Microgels for Tissue Regeneration. *Lab Chip* **2016**, *16*, 4482–4506.

(42) Gregoritza, M.; Abstiens, K.; Graf, M.; Goepferich, A. M. Fabrication of Antibody-Loaded Microgels using Microfluidics and Thiol-ene Photoclick Chemistry. *Eur. J. Pharm. Biopharm.* **2018**, *127*, 194–203.

(43) Kim, J.-W.; Utada, A. S.; Fernández-Nieves, A.; Hu, Z.; Weitz, D. A. Fabrication of Monodisperse Gel Shells and Functional Microgels in Microfluidic Devices. *Angew. Chem. Int. Ed.* **2007**, *46*, 1819–1822.

(44) Seiffert, S. Non-Spherical Soft Supraparticles from Microgel Building Blocks. *Macromol. Rapid Commun.* **2012**, *33*, 1286–1293.

(45) Lehmann, S.; Seiffert, S.; Richtering, W. Diffusion of Guest Molecules within Sensitive Core-Shell Microgel Carriers. *JCIS* **2014**, *431*, 204–208.

(46) Seiffert, S. Functional Microgels Tailored by Droplet-Based Microfluidics. *Macromol. Rapid Commun.* **2011**, *32*, 1600–1609.

(47) Jeong, W. J.; Kim, J. Y.; Choo, J.; Lee, E. K.; Han, C. S.; Beebe, D. J.; Seong, G. H.; Lee, S. H. Continuous Fabrication of Biocatalyst Immobilized Microparticles Using Photopolymerization and Immiscible Liquids in Microfluidic Systems. *Langmuir* **2005**, *21*, 3738–3741.

(48) Seemann, R.; Brinkmann, M.; Pfohl, T.; Herminghaus, S. Droplet Based Microfluidics. *Rep. Prog. Phys.* **2012**, *75*, 16601.

(49) Tumarkin, E.; Kumacheva, E. Microfluidic Generation of Microgels from Synthetic and Natural Polymers. *Chem. Soc. Rev.* **2009**, *38*, 2161–2168.

(50) Garstecki, P.; Fuerstman, M. J.; Stone, H. A.; Whitesides, G. M. Formation of Droplets and Bubbles in a Microfluidic T-Junction-Scaling and Mechanism of Break-up. *Lab Chip* **2006**, *6*, 437–446.

(51) Nan, L.; Zhang, H.; Weitz, D. A.; Shum, H. C. Development and Future of Droplet Microfluidics. *Lab Chip* **2024**, *24*, 1135–1153.

(52) Feng, H.; Zheng, T.; Li, M.; Wu, J.; Ji, H.; Zhang, J.; Zhao, W.; Guo, J. Droplet-Based Microfluidics Systems in Biomedical Applications. *ELECTROPHORESIS* **2019**, *40*, 1580–1590.

(53) Heida, T.; Neubauer, J. W.; Seuss, M.; Hauck, N.; Thiele, J.; Fery, A. Mechanically Defined Microgels by Droplet Microfluidics. *Macromol. Chem. Phys.* **2017**, *218*, 1600418.

(54) Duncanson, W. J.; Lin, T.; Abate, A. R.; Seiffert, S.; Shah, R. K.; Weitz, D. A. Microfluidic Synthesis of Advanced Microparticles for Encapsulation and Controlled Release. *Lab Chip* **2012**, *12*, 2135–2145.

(55) Rossow, T.; Heyman, J. A.; Ehrlicher, A. J.; Langhoff, A.; Weitz, D. A.; Haag, R.; Seiffert, S. Controlled Synthesis of Cell-Laden Microgels by Radical-Free Gelation in Droplet Microfluidics. *JACS* **2012**, *134*, 4983–4989.

(56) Li, W.; Zhang, L.; Ge, X.; Xu, B.; Zhang, W.; Qu, L.; Choi, C.-H.; Xu, J.; Zhang, A.; Lee, H.; Weitz, D. A. Microfluidic Fabrication of Microparticles for Biomedical Applications. *Chem. Soc. Rev.* **2018**, *47*, 5646–5683.

(57) Zhao, Q.; Zhang, S.; Wu, F.; Li, D.; Zhang, X.; Chen, W.; Xing, B. Rational Design of Nanogels for Overcoming the Biological Barriers in Various Administration Routes. *Angew. Chem. Int. Ed.* **2021**, *60*, 14760–14778.

(58) Rutte, J. M. de; Koh, J.; Di Carlo, D. Scalable High-Throughput Production of Modular Microgels for In Situ Assembly of Microporous Tissue Scaffolds. *Adv. Funct. Mater.* **2019**, *29*, 1900071.

(59) Kolb, H. C.; Finn, M. G.; Sharpless, K. B. Click Chemistry: Diverse Chemical Function from a Few Good Reactions. *Angew. Chem. Int. Ed.* **2001**, *40*, 2004–2021.

(60) Hoyle, C. E.; Bowman, C. N. Thiol-ene Click Chemistry. *Angew. Chem. Int. Ed.* **2010**, *49*, 1540–1573.

(61) Guerzoni, L. P. B.; Rose, J. C.; Gehlen, D. B.; Jans, A.; Haraszti, T.; Wessling, M.; Kuehne, A. J. C.; Laporte, L. de. Cell Encapsulation in Soft, Anisometric Poly(ethylene) Glycol Microgels Using a Novel Radical-Free Microfluidic System. *Small* **2019**, *15*, e1900692.

(62) Neubauer, J. W.; Hauck, N.; Männel, M. J.; Seuss, M.; Fery, A.; Thiele, J. Mechanoresponsive Hydrogel Particles as a Platform for Three-Dimensional Force Sensing. *ACS Appl. Mater. Interfaces* **2019**, *11*, 26307–26313.

(63) Hauck, N.; Neuendorf, T. A.; Männel, M. J.; Vogel, L.; Liu, P.; Stündel, E.; Zhang, Y.; Thiele, J. Processing of Fast-Gelling Hydrogel Precursors in Microfluidics by Electrocoalescence of Reactive Species. *Soft Matter* **2021**, *17*, 10312–10321.

(64) LeValley, P. J.; Parsons, A. L.; Sutherland, B. P.; Kiick, K. L.; Oakey, J. S.; Kloxin, A. M. Microgels Formed by Spontaneous Click Chemistries Utilizing Microfluidic Flow Focusing for Cargo Release in Response to Endogenous or Exogenous Stimuli. *Pharmaceutics* **2022**, *14*.

(65) Nair, D. P.; Podgórski, M.; Chatani, S.; Gong, T.; Xi, W.; Fenoli, C. R.; Bowman, C. N. The Thiol-Michael Addition Click Reaction: A Powerful and Widely Used Tool in Materials Chemistry. *Chem. Mater.* **2014**, *26*, 724–744.

(66) Vandenbergh, J.; Ranieri, K.; Junkers, T. Synthesis of (Bio)-Degradable Poly(β-thioester)s via Amine Catalyzed Thiol−Ene Click Polymerization. *Macromol. Chem. Phys.* **2012**, *213*, 2611–2617.

(67) Elbert, D. L.; Hubbell, J. A. Conjugate Addition Reactions Combined with Free-Radical Cross-Linking for the Design of Materials for Tissue Engineering. *Biomacromolecules* **2001**, *2*, 430–441.

(68) Nöth, M.; Gau, E.; Jung, F.; Davari, M. D.; El-Awaad, I.; Pich, A.; Schwaneberg, U. Biocatalytic Microgels (μ-Gelzymes): Synthesis, Concepts, and Emerging Applications. *Green Chem.* **2020**, *22*, 8183–8209.

(69) Guisan, J. M., Ed. *Immobilization of Enzymes*; Immobilization of Enzymes and Cells. Methods in Biotechnology 22; Humana Press, 2006.

(70) Bysell, H.; Månsson, R.; Hansson, P.; Malmsten, M. Microgels and Microcapsules in Peptide and Protein Drug Delivery. *Adv. Drug Delivery Rev.* **2011**, *63*, 1172–1185.

(71) Homaei, A. A.; Sariri, R.; Vianello, F.; Stevanato, R. Enzyme Immobilization: An Update. *J. Chem. Biol.* **2013**, *6*, 185–205.

(72) Torres-Salas, P.; Del Monte-Martinez, A.; Cutiño-Avila, B.; Rodriguez-Colinas, B.; Alcalde, M.; Ballesteros, A. O.; Plou, F. J. Immobilized Biocatalysts: Novel Approaches and Tools for Binding Enzymes to Supports. *Adv. Mater.* **2011**, *23*, 5275–5282.

(73) Sheldon, R. A. Enzyme Immobilization: The Quest for Optimum Performance. *Adv. Synth. Catal.* **2007**, *349*, 1289–1307.

(74) Sheldon, R. A.; Schoevaart, R.; van Langen, L. M. Cross-Linked Enzyme Aggregates (CLEAs): A Novel and Versatile Method for Enzyme Immobilization (A Review). *Biocatal. Biotransform.* **2005**, *23*, 141–147.

(75) Sommerfeld, I. K.; Dälken, E.; Elling, L.; Pich, A. Nitrilotriacetic Acid Functionalized Microgels for Efficient Immobilization of Hyaluronan Synthase. *Macromol. Biosci.* **2024**, 2400075.

(76) Sheldon, R. A.; Basso, A.; Brady, D. New Frontiers in Enzyme Immobilisation: Robust Biocatalysts for a Circular Bio-Based Economy. *Chem. Soc. Rev.* **2021**, *50*, 5850–5862.

(77) Li, Y.; Gao, F.; Wei, W.; Qu, J.-B.; Ma, G.-H.; Zhou, W.-Q. Pore Size of Macroporous Polystyrene Microspheres Affects Lipase Immobilization. *J. Mol. Catal. B: Enzym.* **2010**, *66*, 182–189.

(78) Sirisha, V. L.; Jain, A.; Jain, A. Enzyme Immobilization. *Marine Enzymes Biotechnology: Production and Industrial Applications, Part II - Marine Organisms Producing Enzymes*; Advances in Food and Nutrition Research; Elsevier, 2016; pp 179–211.

(79) Egan, T.; O'Riordan, D.; O'Sullivan, M.; Jacquier, J.-C. Cold-Set Whey Protein Microgels as pH Modulated Immobilisation Matrices for Charged Bioactives. *Food Chem.* **2014**, *156*, 197–203.

(80) Sommerfeld, I. K.; Palm, P.; Hussnaetter, K. P.; Pieper, M. I.; Bulut, S.; Lile, T.; Wagner, R.; Walkowiak, J.; Elling, Lothar, Pich; Andrij. Microgels with Immobilized Glycosyltransferases for Enzymatic Glycan Synthesis. *Biomacromolecules* **2024**, *25*, 3807–3822.

(81) Begum, Z. A.; Rahman, I. M. M.; Tate, Y.; Egawa, Y.; Maki, T.; Hasegawa, H. Formation and Stability of Binary Complexes of Divalent Ecotoxic Ions (Ni, Cu, Zn, Cd, Pb) with

Biodegradable Aminopolycarboxylate Chelants (DL-2-(2-Carboxymethyl)Nitrilotriacetic Acid, GLDA, and 3-Hydroxy-2,2'-Iminodisuccinic Acid, HIDS) in Aqueous Solutions. *J. Solution Chem.* **2012**, *41*, 1713–1728.

(82) Weber, P. C.; Ohlendorf, D. H.; Wendoloski, J. J.; Salemme, F. R. Structural Origins of High-Affinity Biotin Binding to Streptavidin. *Science* **1989**, *243*, 85–88.

(83) Gau, E.; Mate, D. M.; Zou, Z.; Oppermann, A.; Töpel, A.; Jakob, F.; Wöll, D.; Schwaneberg, U.; Pich, A. Sortase-Mediated Surface Functionalization of Stimuli-Responsive Microgels. *Biomacromolecules* **2017**, *18*, 2789–2798.

(84) Anggara, K.; Zhu, Y.; Fittolani, G.; Yu, Y.; Tyrikos-Ergas, T.; Delbianco, M.; Rauschenbach, S.; Abb, S.; Seeberger, P. H.; Kern, K. Identifying the Origin of Local Flexibility in a Carbohydrate Polymer. *PNAS* **2021**, *118*, e2102168118.

(85) Rexer, T.; Laaf, D.; Gottschalk, J.; Frohnmeyer, H.; Rapp, E.; Elling, L. Enzymatic Synthesis of Glycans and Glycoconjugates. In *Advances in Glycobiotechnology*; Rapp, E., Reichl, U., Eds. 175; Springer International Publishing: Cham, 2021; pp 231–280.

(86) Valverde, P.; Ardá, A.; Reichardt, N.-C.; Jiménez-Barbero, J.; Gimeno, A. Glycans in Drug Discovery. *MedChemComm* **2019**, *10*, 1678–1691.

(87) Varki, A. Biological Roles of Glycans. *Glycobiology* **2017**, *27*, 3–49.

(88) Wang, C.-C.; Lee, J.-C.; Luo, S.-Y.; Kulkarni, S. S.; Huang, Y.-W.; Lee, C.-C.; Chang, K.-L.; Hung, S.-C. Regioselective One-Pot Protection of Carbohydrates. *Nature* **2007**, *446*, 896–899.

(89) Weijers, C. A. G. M.; Franssen, M. C. R.; Visser, G. M. Glycosyltransferase-Catalyzed Synthesis of Bioactive Oligosaccharides. *Biotechnol. Adv.* **2008**, *26*, 436–456.

(90) Na, L.; Li, R.; Chen, X. Recent Progress in Synthesis of Carbohydrates with Sugar Nucleotide-Dependent Glycosyltransferases. *Curr. Opin. Chem. Biol.* **2021**, *61*, 81–95.

(91) Mestrom, L.; Przypis, M.; Kowalczykiewicz, D.; Pollender, A.; Kumpf, A.; Marsden, S. R.; Bento, I.; Jarzębski, A. B.; Szymańska, K.; Chruściel, A.; Tischler, D.; Schoevaart, R.; Hanefeld, U.; Hagedoorn, P.-L. Leloir Glycosyltransferases in Applied Biocatalysis: A Multidisciplinary Approach. *Int. J. Mol. Sci.* **2019**, *20*.

(92) Palcic, M. M. Glycosyltransferases as Biocatalysts. *Curr. Opin. Chem. Biol.* **2011**, *15*, 226–233.

(93) Hussnaetter, K. P.; Palm, P.; Pich, A.; Franzreb, M.; Rapp, E.; Elling, L. Strategies for Automated Enzymatic Glycan Synthesis (AEGS). *Biotechnol. Adv.* **2023**, *67*, 108208.

III. Multi-Responsive Nitrilotriacetic Acid Functionalized Microgels as Protein Carriers

Large parts of this chapter are reprinted with permission from Sommerfeld, I. K., Malyaran, H., Neuss, S., Demco, D. E., & Pich, A. Multiresponsive Core-Shell Microgels Functionalized by Nitrilotriacetic Acid. *Biomacromolecules* **2024**, 25, 2, 903–923.[1] *Copyright 2024 American Chemical Society (ACS). Specifically, most Figures are adapted from this publication, with minor modifications.*

Contributions to this Chapter

The synthesis of the reported compounds was conducted either by myself or by Esther Dälken under my supervision during her employment as a research assistant and during her research internship at DWI – Leibniz-Institute for Interactive Materials in 2022. Yannick Burleigh partially conducted pH-dependent DLS measurements within his Bachelor thesis at DWI – Leibniz-Institute for Interactive Materials in 2023. Samples for those measurements were provided by me. Dan E. Demco performed ^{1}H transverse relaxation measurements. Stefan Hauk recorded electron microscopy images. Nadja A. Wolter and Hannah Küttner conducted the calorimetry measurements. Tudor Lile assisted with the incorporation of cytochrome c into microgels under my precise instruction, within his employment as a research assistant. Hanna Malyaran performed and evaluated cytotoxicity tests under the supervision of Prof. Dr. Sabine Neuss, with the assistance of research assistant Annika Rohde, who carried out the microscopic imaging. Aside from cytotoxicity data, all other data were processed and evaluated by me.

1. Introduction

Stimuli-responsive microgels are an interesting class of materials, useful for the stimuli-dependent uptake and release of guest molecules such as proteins.[1–3] Microgels may exhibit responsiveness to various stimuli, including changes in pH or temperature, the presence of signaling molecules, or the application of electrical, magnetic, or electromagnetic fields.[4]

For example, the incorporation of ionizable functional groups into a microgel can provide it with pH-responsivity.[5,6] This stimuli-responsiveness is typically observed at pH values around the pK_a of the microgel.[5] With properties akin to those of linear polyelectrolytes, microgels containing ionizable functional groups can be denoted as polyelectrolyte microgels.[7] Characterized by a high electrostatic repulsion between polymer chains,[8] charges govern the swelling degree and stabilization of those microgels. Previously, both positively charged[9,10] and negatively charged[11–13] microgels have been synthesized, with the charge determining their ability to take up guest molecules. For instance, anionic microgels are capable of accommodating cationic drugs,[7,13] dyes,[14] proteins,[15] or other cationic molecules.[12] Thus, the uptake of guest molecules plays a crucial role in drug delivery, among other applications.[13]

One functional group suitable for incorporating carboxylic acid groups is nitrilotriacetic acid (NTA). Even at low comonomer contents, the aminopolycarboxylic acid NTA facilitates the incorporation of a large number of carboxylic groups, enabling strong electrostatic interactions with positively charged guest molecules. Earlier studies have employed water-in-oil (W/O) emulsion polymerization[16–18] or precipitation polymerization[19] techniques to equip microgels with NTA groups. Specifically, Mizrahi *et al.* developed acrylamide-based microgels,[16] Heida, Köhler, *et al.* used poly(ethylene glycol) and hyaluronic acid-based microgels,[17,18] while Li *et al.* prepared *N*-isopropyl acrylamide (NIPAAm) based microgels,[19] all while incorporating NTA groups.

While a few researchers have synthesized microgels containing NTA, previous studies have not explored the incorporation of NTA into poly(*N*-vinylcaprolactam) (pVCL)-based microgels. Additionally, existing studies on NTA microgels have not extensively investigated the responsiveness of these microgels to stimuli such as temperature, pH, and ionic strength. However, understanding stimuli-responsiveness is crucial as it influences the uptake and release of guest molecules that rely on the microgel swelling ratio.[4,13,20,21] Moreover, previous studies have not specifically addressed the localization of NTA within the microgels. These research gaps highlight the need for comprehensive studies to elucidate the behavior and characteristics of NTA-containing microgels, especially in the context of their potential applications.

Therefore, the primary objective of this chapter is the synthesis of NTA-functionalized microgels with enhanced accessibility for larger biomolecules, particularly proteins. Due to its high charge density, NTA strongly binds to positively charged molecules through ionic interactions, thereby facilitating the stable binding of positively charged proteins. To achieve better accessibility, the shell of the microgel, instead of the whole structure, was functionalized with NTA. A semi-batch precipitation polymerization method was used, which resulted in the delayed incorporation of an NTA-containing comonomer. Additionally, the NTA content was varied to investigate its influence on the microgel properties. The synthesized microgels underwent comprehensive analysis, including assessments of NTA content, microgel size, polydispersity, and electrophoretic mobility. Stimuli-responsiveness was thoroughly examined through variations in temperature, ionic strength, and pH. Further characterization of the microgel structure was conducted using techniques such as Nuclear Magnetic Resonance (NMR) relaxometry, Atomic Force Microscopy (AFM), Scanning Electron Microscopy (SEM), and reaction calorimetry. Exploring their potential use in biotechnological applications, cytotoxicity, and cell proliferation tests were performed to ensure biocompatibility. Additionally, the uptake of positively charged biomolecules *via* electrostatic interactions was demonstrated using the model protein cytochrome c (cyt c).

The scope of this chapter is summarized in **Figure III.1**. The schematic depiction illustrates the distinct stepwise swelling and deswelling pattern of p(VCL/NTAaa) microgels, resulting from the non-uniform distribution of NTA within the microgel. The collapse of uncharged polymer chains occurs more readily than that of the charged NTA moieties, which are stabilized by electrostatic repulsion. Highlighting their potential for the uptake of biomacromolecules, the anionic NTA groups were utilized to immobilize the positively charged model protein cyt c.

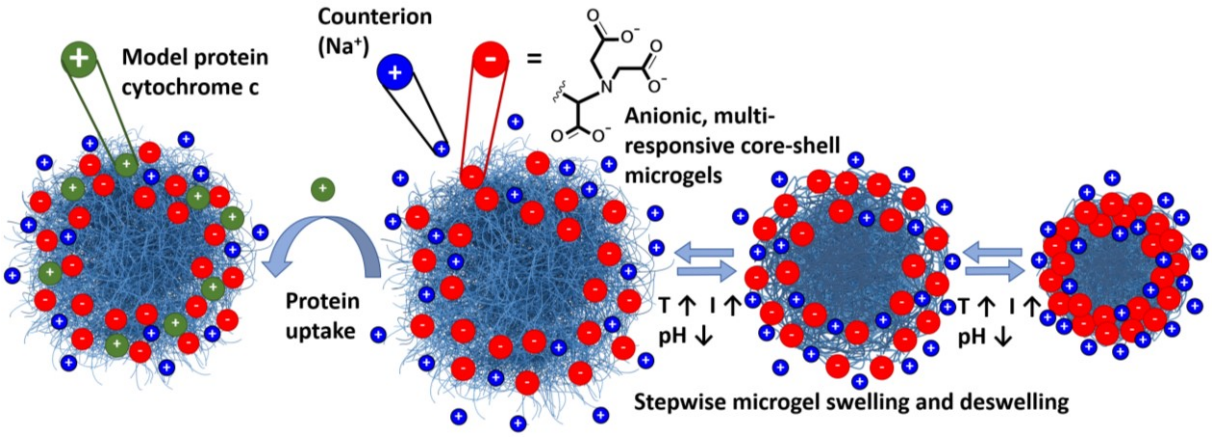

Figure III.1 Schematic depiction of the scope of the current chapter: Multi-responsive core-shell microgels with an NTA-functionalized microgel shell exhibit a stepwise swelling and deswelling behavior attributed to the heterogeneous distribution of NTA within the microgel. The responsiveness of the microgels to stimuli such as temperature (T), ionic strength (I) and pH is investigated. The uncharged polymer chains collapse more readily than the charged NTA moieties, which are stabilized by electrostatic repulsion. NTA groups were utilized for the immobilization of the positively charged model protein cyt c. *Reprinted with permission from the American Chemical Society*[1] *with minor modifications.*

2. Materials and Methods

2.1. Materials

Organic solvents were obtained in analytical grade and utilized as provided by Omnisolv while ultra-pure water (Merck, HPLC grade) was used for all aqueous reactions.

For monomer synthesis, DOWEX® 50WX8, hydrogen form, 100-200 mesh, (Sigma Aldrich) Roti®-Quant (Carl Roth), *N,N'*-bis(carboxymethyl)-L-lysine, acryloyl chloride (Sigma-Aldrich, 97 %) and sulphuric acid (H_2SO_4, Sigma Aldrich, 95 %) were employed. Additionally, the following chemicals were used for microgel synthesis: *N*-Vinylcaprolactam (VCL, Sigma-Aldrich, 98 %), *N*,*N*'-methylenebis(acrylamide) (BIS, Sigma-Aldrich, 99 %), cetrimonium bromide (CTAB, Carl Roth, 99 %), and 2,2'-azobis(2-methylpropionamidine)dihydro chloride (AMPA, Sigma-Aldrich, 97 %). Among these, VCL underwent distillation and recrystallization from *n*-hexane while BIS, AMPA, and CTAB were employed without further purification.

Buffer preparations involved the use of maleic acid (Sigma Aldrich, 99 %), formic acid (Alfa Aesar, 97 %), 2-(*N*-morpholino)ethanesulfonic acid (MES, Sigma Aldrich, 99 %), *N*-(2-hydroxyethyl)piperazine-*N'*-(2-ethanesulfonic acid) (HEPES, Sigma-Aldrich, 99 %), *N*-cyclohexyl-3-aminopropanesulfonic acid (CAPS, Sigma Aldrich, 99 %), hydrochloric acid (HCl, Sigma Aldrich, 37 %), and sodium hydroxide (NaOH, Merck, 99.5 %).

Cytotoxicity assays necessitated the use of phosphate buffered saline (PBS), Roswell Park Memorial Institute 1640 medium, newborn calf serum, penicillin, streptomycin, and L-glutamine, all purchased from Gibco (Darmstadt, Germany), along with an L929 mouse fibroblast cell line from ATCC (Wesel, Germany). Additionally, Ringer solution (B. Braun, Melsungen, Germany), fluorescein diacetate (FDA, Sigma-Aldrich, Steinheim, Germany), propidium iodide (PI, Sigma-Aldrich, Steinheim, Germany) and TritonX-100 (Sigma-Aldrich, Steinheim, Germany) were employed.

2.2. Synthesis of 2,2'-((5-Acrylamido-1-carboxypentyl)azanediyl)diacetic Acid

The monomer dimethyl 2,2'-((5-acrylamido-1-carboxypentyl)azanediyl)diacetic acid (NTAaa) was synthesized following the method described by Mizrahi *et al.*[16] Initially, a solution

containing acryloyl chloride (530 µL, 6.52 mmol) in toluene (25 mL) was added slowly to an ice-cooled solution of *N,N'*-bis(carboxymethyl)-L-lysine (1.6 g, 6.10 mmol) in 0.4 M NaOH (50 mL). After overnight stirring, toluene was evaporated under reduced pressure, followed by the removal of sodium ions. This was realized by washing DOWEX® 50WX8 with water until the filtrate became colorless. Subsequently, the ion exchange resin was combined with the reaction mixture, followed by incubation for several hours to ensure complete ion exchange. DOWEX® 50WX8 was then filtered off and washed with water until a neutral pH was reached. Subsequently, the filtrate was lyophilized. The resulting product was obtained as a white powder, which was characterized using NMR spectroscopy (**Figure SIII.1**).

^{1}H-NMR (400 MHz, DMSO-d_6, δ = 2.50): δ = 8.16 (t, 1H, NH), 6.21 (dd, 1H, CH), 6.03 (dd, 1H, CH), 5.53 (dd, 1H, CH), 3.46 (q, 4H, CH_2), 3.32 (t, 1H, CH), 3.07 (q, 2H, CH_2), 1.56 (m, 2H, CH_2), 1.40 (m, 2H, CH_2), 1.28 (m, 2H, CH_2) ppm.

2.3. Synthesis of Dimethyl 2,2'-((6-acrylamido-1-methoxy-1-oxohexan-2-yl)azanediyl)diacetate

To a solution of NTAaa (1.299 g, 4.1 mmol) in MeOH (26 mL), concentrated sulfuric acid (221 µL) was added. After heating to 65 °C, the solution was refluxed for 3h. The solution was concentrated *via* rotary evaporation, and dichloromethane (DCM) was added. It was then extracted using saturated aqueous solutions of $NaHCO_3$ (2 x 50 mL) and NaCl (1 x 50 mL). After the majority of solvent was removed *via* rotary evaporation, DCM was added. Subsequently, the mixture underwent extraction using saturated, aqueous solutions of $NaHCO_3$ (2 x 50 mL) and NaCl (1 x 50 mL). Residual water was removed by drying with anhydrous Na_2SO_4. The product was obtained as a yellow, highly viscous liquid (889.8 mg, 2.5 mmol, 60 %) after the removal of all solvents. The product 2,2'-((6-acrylamido-1-methoxy-1-oxohexan-2-yl)azanediyl)diacetate (NTAMaa) was characterized through NMR spectroscopy (**Figure SIII.2**). For subsequent use, NTAMaa was dissolved in dimethyl sulfoxide (DMSO) at 17.9 mg mL^{-1}.

^{1}H-NMR (400 MHz, DMSO-d_6, δ = 2.50): δ = 8.04 (t, 1H, NH), 6.19 (dd, 1H, CH), 6.04 (dd, 1H, CH_2), 5.54 (dd, 1H, CH_2), 3.58 (m, 13H, CH_2, CH_3), 3.39 (t, 1H, CH), 3.08 (m, 2H, CH_2), 1.57 (m, 2H, CH_2), 1.40 (m, 2H, CH_2), 1.22 (m, 2H, CH_2) ppm.

2.4. Microgel Synthesis

A semi-batch precipitation polymerization of poly(*N*-vinylcaprolactam-2,2'-((5-acrylamido-1-carboxypentyl)azanediyl)diacetic acid) (p(VCL/NTAaa)) microgels was conducted. VCL (275.6 mg, 1.98 mmol, 99 mol%) and BIS (8.0 mg, 0.05 mmol, 2.6 mol%), along with the stabilizer CTAB (1.2 mg, 0.003 mmol, 0.165 mol%) were dissolved in H_2O (13.5 mL) and degassed with nitrogen. The polymerization was then initiated at 70 °C by fast addition of AMPA (6.6 mg, 0.02 mmol, 1.2 mol%, in 0.5 mL H_2O). Over 8 minutes, NTAMaa (7.2 mg, 0.02 mmol, 1 mol%) dissolved in DMSO (6 mL) was added, starting approximately 25 to 45 seconds after initiation. High precision in the addition process was realized by utilizing a syringe pump. After stirring the solution at 70 °C for 5h, it was allowed to cool to room temperature with continuous stirring. Then, 1.5 mL of 0.1 M NaOH was added to the obtained p(VCL/NTAMaa) microgels, followed by another 24 hours of stirring at room temperature to yield deprotected p(VCL/NTAaa). The product was purified by dialysis against water using a regenerated cellulose membrane (MWCO = 12 – 14 kDa) for 5 days and obtained as a white powder following lyophilization. The NTA content in the microgels was determined using Fourier Transform Infrared (FT-IR) spectroscopy. To implement the synthesis of microgels with different comonomer compositions, the ratio of VCL to NTAMaa was adjusted while maintaining the total molar quantity of the comonomers at 2 mmol (100 mol%).

The synthesis of pVCL microgels was performed by batch polymerization. VCL (2.0879 g, 15 mmol, 100 mol%) was dissolved in H_2O (149 mL) along with BIS (60.1 mg, 0.39 mmol, 2.6 mol%). The mixture was degassed and heated to 70 °C, initiating the reaction by the addition of AMPA (48.8 mg, 0.18 mmol, 1.2 mol%) in H_2O (1 mL). After letting the reaction proceed for 3 h, the microgels were purified and freeze-dried as described above.

2.5. Synthesis of Linear pVCL and pNTAaa Homopolymers for FT-IR Calibration

Linear pVCL and pNTAaa were synthesized for FT-IR calibration. VCL (696.0 mg, 5 mmol, 100 mol%) was dissolved in H_2O (49 mL) and the solution was degassed using nitrogen. After heating to 70 °C, AMPA (16.3 mg, 0.06 mmol, 1.2 mol%) was added, and dissolved in 1 mL H_2O. The polymerization reaction was left to react for 3 h, yielding pVCL.

For pNTAaa synthesis, NTAaa (158.2 mg, 0.5 mmol, 100 mol%) was dissolved in 4.5 mL H_2O. The synthesis proceeded similarly to the reaction described above: a degassed solution was heated to 70 °C, and the reaction was initiated by adding AMPA (1.6 mg, 0.6 µmol, 1.2 mol%, in 0.5 mL H_2O). The reaction mixture was allowed to react for 5 hours.

Finally, the polymer solutions were dialyzed against water using a regenerated cellulose membrane (MWCO = 3.5 kDa), followed by lyophilization. Both polymers were obtained as white powders. After blending them in different molar ratios (χ_{NTA} = 0, 2.5, 5, 10, 15, 100 mol%), the resulting mixtures were used for recording FT-IR spectra.

2.6. Cytotoxicity and Cell Proliferation Assay

2.6.1. Cell Culture

All cell culture procedures were conducted following approval by the local ethics committee from RWTH Aachen University (EK 300/13) and adhered to sterile conditions within a laminar flow workbench. Before use, all surfaces and materials underwent disinfection with 70 % ethanol, with the workbench additionally subjected to UV light treatment. Cell culture medium and PBS were preheated in a water bath at approximately 37 °C before usage. Cellular incubation occurred in a humidified atmosphere comprising 20 % O_2 and 5 % CO_2 at 37 °C. Before the experiments, all cells were screened to confirm the absence of mycoplasma contamination.

2.6.2. Cytotoxicity/Viability Test According to ISO 10993–5

For evaluation of the cytotoxicity or cytocompatibility of p(VCL/NTAaa) microgels (χ_{NTA} = 0, 0.5, 2.0, 2.2, and 11.8 mol%), an L929 mouse fibroblast cell line cultured in Roswell Park Memorial Institute 1640 medium was utilized, supplemented with 5 % newborn calf serum, 1 % penicillin (80 U mL^{-1}), 1 % streptomycin (80 µg mL^{-1}), and 1 % L-glutamine. Following the protocols 10993–5 of the International Standardization Organization (ISO) an indirect cytotoxicity test was conducted. Incubation of microgels (1 mg mL^{-1}) with cell culture medium was performed for 1, 3, and 7 days. L929 mouse fibroblasts with an initial cell seeding density

of 5.0×10^4 cells cm^{-2} were exposed to microgel-supernatant for one day before conducting live/dead stainings. 10 µL FDA (5 mg mL^{-1} in acetone) and 10 µL PI (0.5 mg mL^{-1} in PBS) were combined in 600 µL of Ringer solution. Cell staining was performed with 20 µL of this stock solution, followed by analysis through fluorescence microscopy (DMI6000B, Leica, Wetzlar, Germany),[22–24] where differentiation of viable (green fluorescent) and dead (read fluorescent) cells can be made. A dead cell control was prepared by the addition of 20 µL TritonX-100 (0.1 % dissolved in PBS), prompting cell lysis. Images were quantified using ImageJ software.

2.6.3. Cell Proliferation Assay

P(VCL/NTAaa) microgels (χ_{NTA} = 0, 0.5, 2.0, 2.2, and 11.8 mol%) at 1 mg mL^{-1} were covered with L929 cell culture medium, discarding the medium after 7 days of incubation. Using a seeding density of 5.0×10^4 cells cm^{-2} L929 mouse fibroblasts, cells were cultured in the microgel supernatant in a 24-well plate, and placed in the CELLCYTE X™ (CYTENA, USA). Images were taken every six hours and for seven days.

2.7. Incorporation of Cytochrome c in Microgels

Cyt c (1 mg mL^{-1}) was immobilized on microgels (2 mg mL^{-1}), by mixing both in 10 mM MES pH 6.5 with an ionic strength of 10 mM. PVCL and p(VCL/NTAaa) (χ_{NTA} = 2.2 mol%) microgels were utilized. After initial assessment through UV-Vis spectroscopy, samples were dialyzed (regenerated cellulose membrane, MWCO = 25 kDa) against the above-mentioned buffer for 5 days, with samples taken for UV-Vis assessment after 2 days, 4 days, and 5 days.

2.8. Analytical Methods

2.8.1. Nuclear Magnetic Resonance Spectroscopy

A 400 MHz Bruker DPX-400 FT-NMR spectrometer was used to conduct NMR spectroscopy measurements, for which samples were dissolved in D_2O or DMSO-d_6.

2.8.2. Fourier-Transform Infrared Spectroscopy

Samples were placed on a diamond crystal plate of an FT-IR Spectrum 3 by PerkinElmer utilizing a GladiATR Single reflection by PIKE Technologies. FT-IR spectroscopy was then conducted in the spectral range of 4000 and 400 cm^{-1} with 4 scans per measurement and a resolution of 4 cm^{-1}. Spectrum v10.7.2. software facilitated the recording of measurements, preceded by a background measurement before sample measurement. Subsequently, all spectra were subjected to baseline correction and normalization.

2.8.3. Electrophoretic Light Scattering

Electrophoretic Light Scattering (ELS) was performed on a Malvern Instruments Zetasizer Ultra Pro. Aqueous samples were transferred to disposable folded capillary cells (DTS1070) at 0.5 mg mL^{-1}. Measurements were performed at 5 °C using a scattering angle of θ = 12.8° with an applied voltage of 150 V and up to 100 runs. All samples were measured threefold. Data were analyzed using the software ZS Xplorer.

2.8.4. Dynamic Light Scattering

The Zetasizer Ultra Pro from Malvern Instruments was further used to conduct Dynamic Light Scattering (DLS) with data analysis using ZS Xplorer software. Aqueous samples were transferred to 12 mm squared polystyrene cuvettes (DTS0012) at 0.5 mg mL^{-1}. Samples were measured threefold at a scattering angle θ = 90° with 5 runs. The temperature was adjusted from 5 °C to 65 °C in 2.5 °C steps.

Furthermore, a measurement at 25 °C was conducted, with the microgels (0.5 mg mL^{-1}) dispersed in different buffers, all at an ionic strength of 10 mM. Buffer recipes were obtained using the Buffer Calculator of Robert Beynon:[25] maleate buffer (pH 1.5 and 2.5); formate buffer (pH 3.0, 4.0, and 4.5); MES buffer (pH 5.5 and 6.5); HEPES buffer (pH 8.0); and CAPS buffer (pH 9.7 and 11). The acid or base of the buffer component was dissolved in water along with NaCl for adjustment of the ionic strength. The pH was adjusted with NaOH or HCl.

2.8.5. NMR Relaxometry

The Carr-Purcell-Meiboom-Gill (CPMG) spin-echo train was employed to assess proton transverse magnetization relaxation (T_2 relaxation).[26] The CPMG pulse sequence is represented as $90°_x-(\tau-180°_y-\tau)_n$. Here, 2τ and n denote the spin-echo time and the number of loops of the Hahn spin-echo sequence, respectively. The rotation of the net magnetization during the application of the radio-frequency (rf) is presented using their flip angles, which can be in the x or y direction. For the implementation of the CPMG, a 20 MHz low-field, time-domain Bruker minispec mq20 NMR spectrometer was employed. Excitation (90°) and refocusing (180°) rf pulses were activated for 10.5 µs each, using different rf power attenuation P with $P_{90°}/P_{180°} = 6.02$. Imperfections of the irradiation pulses were lowered by implementing a cycle of refocusing rf pulses in eight phases (y; -y; x; -x; -y; y; -x; x). A total of 4000 spin echo loops (n) and a recycle delay of 5 s were employed, resulting in a spin-echo time set at 2τ = 0.1 ms.

All microgels (5 mg mL^{-1}) were measured in D_2O at 24 °C. A three-component exponential function was utilized to evaluate the normalized decay of the spin-echo train $I(\tau)/I(0)$:[27–29]

$$\frac{I(\tau)}{I(0)} = A_0 + A_{core}\exp\left\{-\frac{2\tau}{T_{2,short}}\right\} + A_{shell}\exp\left\{-\frac{2\tau}{T_{2,long}}\right\} + A_x\exp\left\{-\frac{2\tau}{T_{2,x}}\right\}$$

Here, the baseline A_0 and the amplitudes A_{core}, A_{shell}, and A_x are represented. These amplitudes are proportional to the number of protons in the core, shell, and a third region x of the microgels. The third region corresponds to an outer shell and dangling chains, or HDO due to T_2 relaxation occurring in D_2O. The T_2 relaxation times $T_{2,short}$, $T_{2,long}$, and $T_{2,x}$ also correspond to the microgel architecture. In the core of the microgel, a shorter $T_{2,short}$ is caused by stronger dipolar magnetic interactions due to a higher concentration of protons while T_2 increases with the distance to the microgel core. Next to analysis with the three-component exponential function, the normalized decay was processed by Inverse Laplace Transform (CONTIN).[30]

2.8.6. Atomic Force Microscopy

AFM imaging was conducted using a NanoScope V system from Veeco Instruments in tapping mode. The setup included a Nanoworld NCH-50 POINTPROBE®-Silicon SPM-Sensor cantilever

with a resonance frequency of 320 kHz and a force constant of 42 nm^{-1}. For their analysis, microgel samples were deposited onto plasma-activated silicon wafers using spin coating. The acquired AFM images were analyzed using Gwyddion software.

2.8.7. Scanning Electron Microscopy

SEM measurements were conducted on a Hitachi SU9000 with secondary electron (SE) and Scanning Transmitting Electron Microscopy (STEM) detectors. Here, the SE detector provides surface images, while the STEM detector provides images in which all planes of the sample are displayed overlapped due to the transmission of the sample by electrons. Samples were coated with roughly 3 nm carbon on the Leica ACE EM 600 prior to the measurement. Measurements were performed with an acceleration voltage of 30 kV and currents between 10.1 and 10.5 µA.

2.8.8. Reaction Calorimetry

Real-time calorimetric measurements were recorded by performing microgel synthesis in a triple-walled 500 mL AP01-0.5-RTCal glass reactor attached to a Mettler Toledo RC1e reaction calorimeter. For this, the reactor was supplied with a baffle, a Hastelloy® stirrer, and a Solvias Turbido™ turbidity probe. During measurements, the isothermal mode was utilized, maintaining the reaction temperature T_r at a constant value through self-regulation of the jacket temperature T_j. Data were analyzed with iControl RC1e™ 5.0 software.

The compounds VCL (1.6285 g, 11.7 mmol, 97.5 mol%), NTAMaa (107.5 mg, 0.3 mmol, 2.5 mol%), (7.2 mg, 0.0198 mmol, 0.165 mol%) and BIS (48.1 mg, 0.312 mmol, 2.6 mol%) were dissolved in a mixture of H_2O (84 mL) and DMSO (36 mL). The temperature was then elevated to 70 °C, stirring at 400 rpm. Upon reaching 70 °C, the solution was degassed for 30 min using N_2. After equilibration of the heat flow for 60 min, generating a stable baseline, the polymerization was initiated by the addition of AMPA (39.1 mg, 0.144 mmol, 1.2 mol%). The reaction was observed for 120 min. In two more reactions, the amount of employed NTAMaa (0, 2.5, and 5 mol%) was adjusted, keeping the total molar amount of both comonomers VCL and NTAMaa at 12 mmol (100 mol%).

2.8.9. UV-Vis Spectroscopy

A Jasco V-780 spectrophotometer was used to conduct UV-Vis spectroscopy, scanning between 300-800 nm at a speed of 400 nm min^{-1} with a data interval of 1 nm. The instrument was outfitted with deuterium (D2) and tungsten iodine (WI) lamps, with light sourcing switched at 340 nm. Measurements were conducted at room temperature, and background measurements were taken and automatically subtracted from subsequent scans.

3. Results and Discussion

3.1. Monomer Synthesis and Characterization

NTAaa was synthesized using the method outlined by Mizrahi *et al*.[16] Its composition was confirmed *via* NMR spectroscopy, as shown in **Figure SIII.1** , validating the successful synthesis of the target product. In contrast to the previous findings,[16] the NMR analysis in this thesis reveals a higher purity level, evidenced by the transition from an oily texture to a white powdery appearance, suggesting the absence of residual organic solvents or other contaminants. To avoid electrostatic repulsion during polymerization, protective groups were introduced to the carboxyl groups *via* acidic esterification with MeOH. The resulting NMR spectrum (**Figure SIII.2**) illustrates complete conversion to the product dimethyl NTAMaa.

3.2. Fundamental Characterization of the Microgels

3.2.1. Investigation of the Microgel Composition via FT-IR Spectroscopy

Microgels composed of crosslinked p(VCL/NTAaa) were effectively synthesized utilizing a semi-batch approach as per **Scheme III.1**.

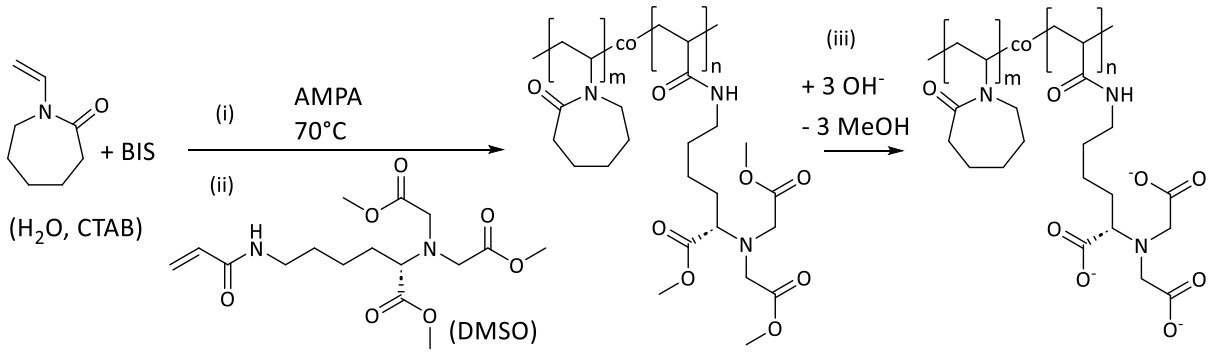

Scheme III.1 The synthesis of p(VCL/NTAaa) microgels with varying NTAaa content involved a three-step process: (i) The polymerization of VCL in H_2O was initiated by AMPA (1.2 mol%), in the presence of the crosslinker BIS (2.6 mol%) and the surfactant CTAB (0.165 mM), (ii) followed by the delayed addition of NTAMaa in DMSO. After NTAMaa addition the polymerization was left to proceed at 70 °C for 5 h. (ii) The methyl ester groups of NTA were subsequently hydrolyzed upon the addition of NaOH. Microgels were purified *via* dialysis.

The microgels were subsequently subjected to characterization using IR spectroscopy. **Figure III.2a** displays the corresponding spectra of both pVCL and p(VCL/NTAaa) microgels (theoretical molar amount $\chi_{NTA,theor}$ = 2.5 mol%).

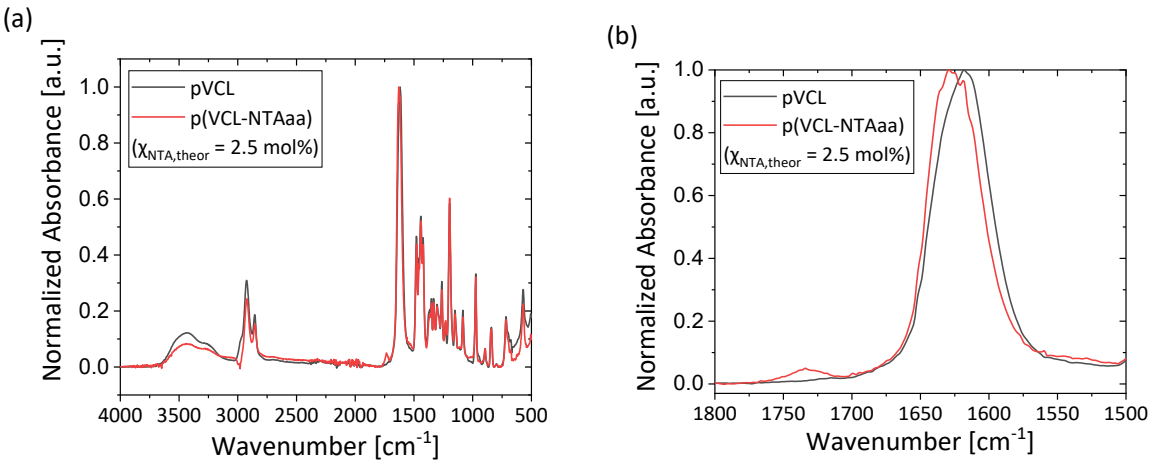

Figure III.2 (a) FT-IR spectra of p(VCL/NTAaa)) ($\chi_{NTA,theor}$ = 2.5 mol%) and pVCL microgels, along with (b) enlarged FT-IR spectra (1800 to 1500 cm^{-1}) of the microgels. *Reprinted with permission from the American Chemical Society*[1] *with minor modifications.*

The obtained pVCL and p(VCL/NTAaa) microgels exhibit largely overlapping FT-IR peaks, as anticipated due to the low NTA content in p(VCL/NTAaa). A broad band appears at 3500-3000 cm^{-1}, primarily attributed to the O-H vibration of water. Additionally, the O-H vibration of the NTA carboxylic groups is located at these wavenumbers. Sharp bands at 1927 cm^{-1} and 1854 cm^{-1} arise from asymmetric and symmetric vibrations of methylene groups. Different carbonyl bands are evident at 1750-1500 cm^{-1}. The prominent peak at 1650-1580 cm^{-1} is caused by the C=O vibration of the VCL-amide. While the band caused by the C=O vibration of the NTAaa-amide in cis-conformation is also expected here, it cannot be distinguished from the VCL band. Furthermore, the C=O band corresponding to the trans-conformation of the NTAaa amide is expected at 1550-1500 cm^{-1}, but the peak is not clearly observable due to the low comonomer content in p(VCL/NTAaa). The vibration of NTAaa carboxylic acid C=O bonds is reflected in a small but pronounced peak at 1750-1700 cm^{-1}, highlighting the difference between pVCL and p(VCL/NTAaa) microgels. Therefore, a magnified section of the FT-IR spectra between 1800 and 1500 cm^{-1} is depicted in **Figure III.2b**. C-N stretching causes a band at 1480 cm^{-1} while the bending of methylene groups results in a peak at 1460 cm^{-1}. These peaks are accompanied by several other specific and unspecific peaks in the fingerprint region of the FT-IR spectrum.

In the synthesis of p(VCL/NTAaa), the amount of comonomer $\chi_{NTA,theor.}$ was altered. To quantify the resulting NTA content, an IR calibration was conducted, a method that has been employed to determine the content of several other comonomers in microgels.[31,32] For this purpose, linear pVCL, and pNTAaa homopolymers were synthesized and subsequently combined in fixed molar ratios (χ_{NTA} = 0, 2.5, 5, 10, 15, 100 mol%). The FT-IR spectra of the mixtures are depicted in **Figure III.3a** with magnified spectra in **Figure III.3b**.

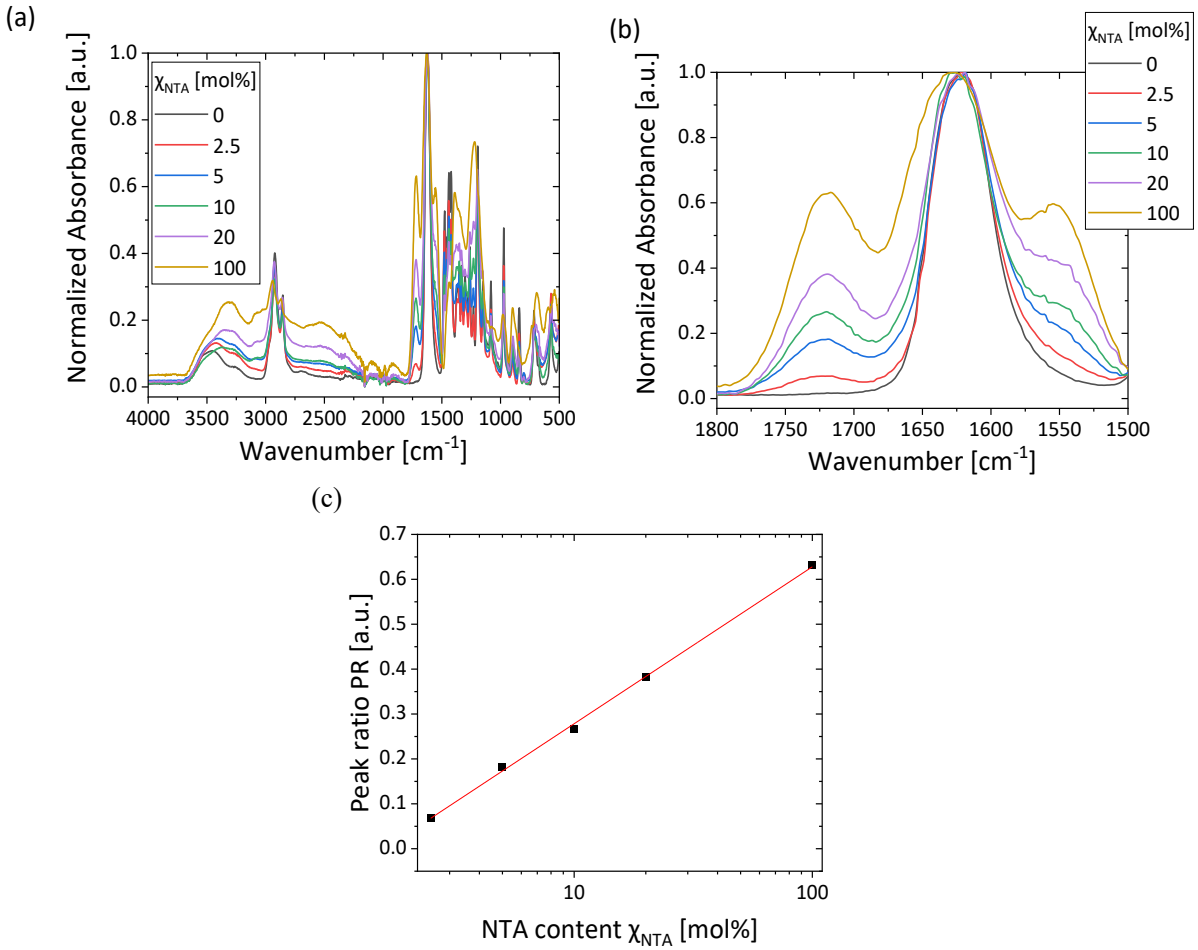

Figure III.3 (a) FT-IR spectra (1800 to 1500 cm^{-1}) of linear pVCL and pNTAaa homopolymers mixed in fixed molar ratios resulting in χ_{NTA} = 0 mol% to 100 mol%, along with (b) enlarged FT-IR spectra (1800 to 1500 cm^{-1}) of the polymer mixtures. (c) FT-IR spectra obtained from these mixtures were utilized to establish a calibration curve. The ratio of maximum absorbance between 1750-1700 cm^{-1} to the maximum absorbance between 1650-1580 cm^{-1}, referred to as the peak ratio (PR), was plotted against χ_{NTA} using a logarithmic scale, followed by a linear fit of the points. Unknown χ_{NTA} can now be calculated from the obtained **Equation III.1**. *Reprinted with permission from the American Chemical Society*[1] *with minor modifications.*

The peak ratio (PR), defined as the maximum absorbance between 1750-1700 cm^{-1} ($A_{1750\text{-}1700}$) divided by the maximum absorbance between 1650-1580 cm^{-1} ($A_{1650\text{-}1580}$), was plotted against

the NTAaa amount (χ_{NTA} = 2.5, 5, 10, 15, 100 mol%). This approach leads to asymptotic behavior due to the dependence of both peaks on NTAaa. While $A_{1750\text{-}1700}$ is solely dependent on NTAaa, $A_{1650\text{-}1580}$ depends on both NTAaa and VCL. To address this, a logarithmic depiction of the x-axis was utilized, revealing linear behavior within the specified range, as illustrated in **Figure III.3c**. The obtained linear fit is represented by **Equation III.1**.

$$PR = -0.07118 + 0.34956 \cdot \log_{10}(\chi_{NTA})$$

Equation III.1 Linear fit obtained from the plot of the peak ratio (PR) against the NTAaa amount (χ_{NTA} = 2.5, 5, 10, 15, 100 mol%), utilizing a logarithmic depiction of the x-axis. PR is thereby defined as the maximum absorbance between 1750-1700 cm^{-1} ($A_{1750\text{-}1700}$) divided by the maximum absorbance between 1650-1580 cm^{-1} ($A_{1650\text{-}1580}$).

The NTA content within p(VCL/NTAaa) microgels was assessed by rearranging the equation:

$$\chi_{\mathrm{NTA}} = 10^{(\mathrm{PR}+0.07118)\cdot 0.034956^{-1}}$$

Equation III.2 Calculation of χ_{NTA} from the obtained PR.

The theoretical and actual comonomer content in different p(VCL/NTAaa) microgels are presented in **Table III.1**, with corresponding spectra shown in **Figure III.4**.

Table III.1 Theoretical ($\chi_{NTA,theor}$) and actual ($\chi_{NTA,actual}$) amount of NTA as determined *via* FT-IR spectroscopy. The listed yields of the microgel synthesis were determined gravimetrically.

$\chi_{NTA,theor.}$ [mol%]	$\chi_{NTA,actual}$ [mol%]	Yield [%]
0	0	83.1
0.5	-	68.4
1.5	2.0	14.1
2.5	2.2	85.4
10	11.8	63.9

As previously discussed, the C=O vibration peak of the NTA carboxylic groups can be clearly distinguished from other peaks, but the peak possesses low intensity. Therefore, only NTA contents exceeding approximately 1 mol% could be accurately determined. As a result, when referencing the p(VCL/NTAaa) microgels by their NTA content χ_{NTA}, their theoretical NTA content is used for concentrations up to 1 mol%, while their observed NTA content is used for concentrations surpassing 1 mol%. It is important to note that the signal-to-noise ratio of the FT-IR spectra may be relatively large at NTA contents below 2.5 mol%, potentially resulting in deviations from accurate values. Nevertheless, these data, when combined with techniques such as ELS, allow for qualitative assessments of the microgels' chemical composition.

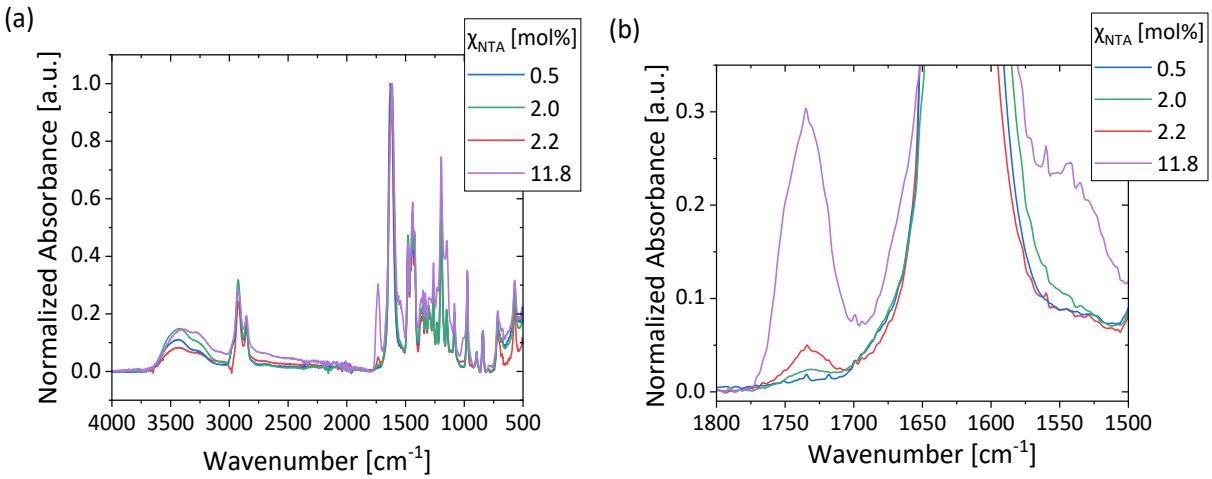

Figure III.4 (a) FT-IR spectra of p(VCL/NTAaa) microgels (χ_{NTA} = 0.5 mol%, 2.0 mol%, 2.2 mol% and 11.8 mol%), along with (b) enlarged FT-IR spectra (1800 to 1500 cm^{-1}) of the microgels. Significant NTAaa peaks are observed for comonomer contents above 1 mol%. *Reprinted with permission from the American Chemical Society*[1] *with minor modifications.*

3.2.2. Microgel Characterization via Dynamic and Electrophoretic Light Scattering

To gather additional insights, the p(VCL/NTAaa) microgels underwent analysis using DLS and ELS utilizing dilute aqueous microgel dispersions (0.5 mg mL^{-1}). The measurements were performed at 25 °C, below the volume phase transition temperature (VPTT) of the microgels. To reveal possible correlations, their pH value at room temperature was additionally determined. At lower χ_{NTA}, the pH remained approximately equal to the pH of the H_2O used (pH 6). However, at higher χ_{NTA}, the pH decreased to values as low as pH 4. The results of ELS and DLS measurements are shown in **Table III.2**, along with the measured pH.

A substantial increase in the magnitude of the electrophoretic mobility (μ_E) was observed as the comonomer content increased, ranging from low concentrations (χ_{NTA} = 0.5 mol%) to higher ones (χ_{NTA} = 2.0 mol% to 11.8 mol%). This phenomenon can be attributed to the semi-batch method employed, wherein NTA is added after the initial microgel core formation. Consequently, the majority of negatively charged carboxylic groups are situated in the microgel shell, resulting in a negative surface potential. Upon closer observation of the μ_E, a steep decrease is shown from the lowest comonomer concentration up to 2.2 mol%, while no further decline is observed at NTAaa concentrations exceeding 2.2 mol%, a phenomenon attributed to two main effects: the saturation of surface carboxylic groups and variations in

pH. Within p(VCL/NTAaa) microgels, carboxylic acid groups are predominantly located in the outer part. However, they may not be situated directly on the surface but also within a deeper part of the microgel shell: If the surface is fully saturated with charges from carboxylic groups, more NTAaa may be located further away from the surface due to an increased thickness of the NTAaa-rich microgel shell. Therefore, as the NTAaa content increases, the surface potential decreases only until reaching a saturation of surface charge. On the other hand, as the comonomer content increases, a greater number of dissociated protons, caused by the higher number of built-in carboxylic groups, lead to a reduction in pH. The generated hydrogen ions can shield the negative surface potential of the microgels, resulting in reduced absolute μ_E. This shielding effect is evident for high NTA contents (χ_{NTA} = 11.8 mol%) where the pH value was measured to be significantly below neutral pH at pH 4, as indicated in **Table III.2**.

Table III.2 Electrophoretic mobility (μ_E), hydrodynamic diameter (D_h), and PDI of p(VCL/NTAaa) microgels synthesized with different amounts of NTA ($\chi_{NTA,theor}$). The actual NTA content ($\chi_{NTA,actual}$) was determined using FT-IR spectroscopy while μ_E, D_h, and PDI were determined using ELS (μ_E) and DLS (Dh, PDI) measurements at T = 25 °C with scattering angles of θ = 90° (DLS) and θ = 12.8° (ELS) in H_2O.

χ_{NTA} [mol%]	μ_E [µm cm V^{-1} s^{-1}][a)]	D_h [nm][a)]	PDI [a.u.][a)]
0	0.23 ± 0.01[b)]	576 ± 15[b)]	0.086 ± 0.051[b)]
0.5	-1.30 ± 0.30[b)]	584 ± 20[b)]	0.132 ± 0.035[b)]
2.0	-1.32 ± 0.05[c)]	431 ± 4[c)]	0.049 ± 0.008[c)]
2.2	-2.98 ± 0.10[c)]	640 ± 11[c)]	0.147 ± 0.018[c)]
11.8	-2.98 ± 0.20[d)]	770 ± 22[d)]	0.068 ± 0.056[d)]

[a)] The employed aqueous 0.5 mg mL^{-1} p(VCL/NTAaa) dispersion possessed a neutral pH at lower NTA contents ($\chi_{NTA,actual}$ = 0.1 to 0.5 mol%) and a moderately acidic pH of 5 or 4 at higher NTA contents ($\chi_{NTA,actual}$ = 2.0 to 11.8 mol%); [b)] pH 6, this pH is equal to the pH of the HPLC water employed; [c)] pH 5; [d)] pH 4.

A notable difference in μ_E was observed when comparing results for χ_{NTA} = 2.0 mol% and 2.2 mol%. As previously discussed, there may be larger deviations of the determined χ_{NTA} from inherent values at lower comonomer contents, caused by a lower signal-to-noise ratio in FT-IR. Consequently, it may be anticipated that the sample with the determined concentration of χ_{NTA} = 2.0 mol% is more closely located towards the amount of comonomer utilized in the reaction ($\chi_{NTA,theor}$ = 1.5 mol%). This would account for the relatively large difference in μ_E between both samples (χ_{NTA} = 2.0 and 2.2 mol%).

The polydispersity indices (PDIs) of microgels were determined to be below 0.15 at 25 °C, indicating the formation of relatively uniform microgels. The hydrodynamic diameters (D_h) of the microgels span from 431 to 770 nm. However, it remains uncertain whether the visible

size variations between samples correlate with the employed comonomer quantity or yield. A trend could not be conclusively established due to the analysis of a limited sample amount. Following, further analyses on microgel size across a temperature range of 5 °C to 65 °C were performed, employing 2.5 °C increments to ascertain the location of the VPTT.

3.3. Temperature-Responsiveness of the Microgels

3.3.1. Microgel Size

The temperature-dependent DLS measurement results for pVCL and p(VCL/NTAaa) (χ_{NTA} = 0.5 mol% to 11.8 mol%) are displayed in **Figure III.5**. Heating and cooling cycles were performed to demonstrate the reversible deswelling and swelling of the microgels. A sigmoidal Boltzmann fit was employed for the determination of the VPTT from the obtained heating curves, with the VPTT being positioned at the inflection point. To provide a clearer visualization of the volume phase transition (VPT) for the microgels containing χ_{NTA} = 2.0 mol% and 2.2 mol%, all fitting lines are omitted from **Figure III.5** and instead shown in **Figure SIII.3**.

The lower critical solution temperature (LCST) of linear pVCL polymers in water typically falls between 30 °C and 32 °C.[33] This LCST is influenced by various polymer features including the degree of polymerization, [33] and plays a significant role in determining the VPTT of pVCL-based microgels. Unlike linear pVCL polymers that undergo a coil-to-globule transition in water above the LCST, pVCL microgels experience a transition from a swollen to a collapsed state at comparable temperatures. Much like the LCST, the VPTT of temperature-responsive microgels can be adjusted through the introduction of different comonomers: Hydrophobic comonomers cause the VPTT to transition towards lower temperature[31,34] while hydrophilic and ionic comonomers cause a shift towards higher temperatures.[9,35,36] Introducing hydrophilic components diminishes the hydrophobic attraction among polymer chains, resulting in an elevated VPTT. Conversely, the presence of ionic groups elevates the VPTT due to electrostatic repulsion among polymer chains and the osmotic pressure arising from counterion dissociation.[36,37]

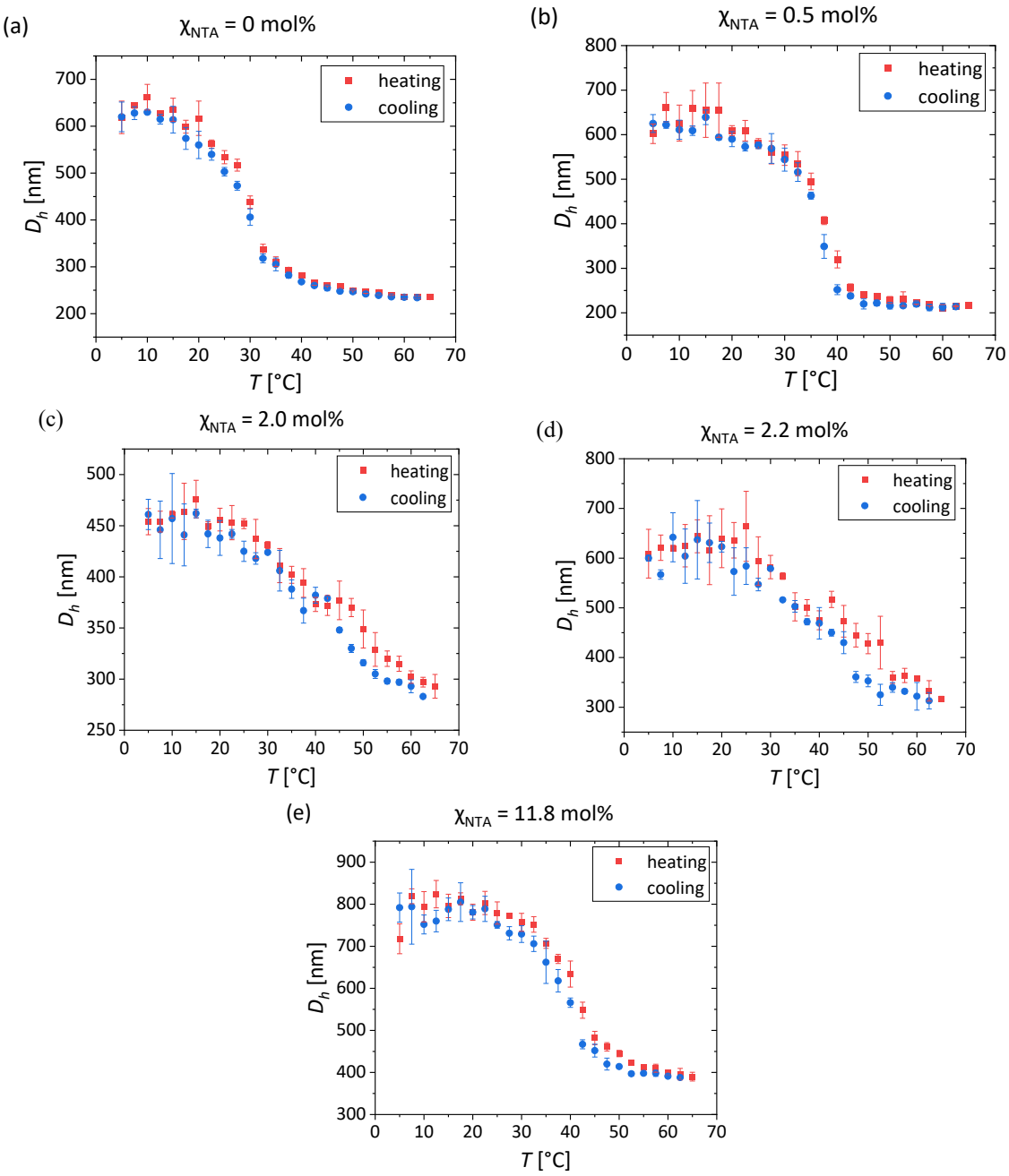

Figure III.5 The D_h of microgels was examined regarding its temperature-dependence, through DLS measurements conducted with a scattering angle of $\theta = 90°$ in H_2O. Results for p(VCL/NTAaa) microgels with varying comonomer content are presented: χ_{NTA} = (a) 0 mol%, (b) 0.5 mol%, (c) 2.0 mol%, (d) 2.2 mol%, (e) 11.8 mol%. The sigmoidal fits, used to determine the VPTT of microgels are displayed in **Figure SIII.3** with the results listed in **Table SIII.1**. *Reprinted with permission from the American Chemical Society*[1] *with minor modifications.*

A characteristic temperature-responsive behavior was observed for pVCL microgels with a VPTT at 28.2 °C (**Figure SIII.3a**). Notably, microgels containing NTAaa exhibited significantly higher VPTT owing to the comonomer's heightened hydrophilicity. Even at a low NTA content of 0.5 mol%, the VPTT was elevated by 9 °C to 37.2 °C (**Figure III.5b**). A further increase of the

VPTT up to 50.8 °C was shown for microgels with increased NTA amounts (χ_{NTA} = 2.0 mol%, 2.2 mol%), showcased in **Figure SIII.3c-d**. It is noteworthy that there is a significant difference in VPTT when comparing samples with χ_{NTA} = 2.0 mol% versus 2.2 mol%. This observation lends support to the hypothesis that the difference in χ_{NTA} between both samples is larger than established by FT-IR. We propose that the NTA concentration in the microgel with χ_{NTA} = 2.0 mol% is slightly lower than determined. The VPTTs are listed in **Table SIII.1**.

These observations provided an initial assessment, but the sigmoidal Boltzmann function, while applied to fit the data, did not precisely match the observed data points. In contrast, a stepwise reduction in microgel size was observed for samples containing 2.0 and 2.2 mol% NTA (**Figure III.5c-d**). In the following section, the cause of the stepwise size reduction is discussed. Additionally, a subsequent section will address why this behavior was not observed in samples containing χ_{NTA} = 11.8 mol%.

The observed stepwise VPT (χ_{NTA} = 2.0 and 2.2 mol%) likely stems from the microgel's core-shell structure, as postulated by renowned researchers in previous works.[36,38–40] It has previously been suggested that each polymer chain in the microgel has its own VPTT.[41,42] The individual polymer chains can therefore collapse at different temperatures depending on their degree of polymerization and their overall chemical composition, introducing varying hydrophilicity and charge density.[41,43] Thus, a stepwise VPT can occur when the swelling and deswelling of individual polymer chains in the microgel do not happen simultaneously. For example, in microgels with charged functional groups, initial deswelling is explained by the collapse of uncharged, more hydrophobic polymer chains, while deswelling at higher temperatures is attributed to the collapse of more hydrophilic or charged polymer chains.[38]

For the p(VCL/NTAaa) microgels, initial deswelling occurs due to the augmented hydrophobic interaction between uncharged pVCL chains causing the collapse of the VCL-rich core.[36,38–40] This phenomenon occurs at temperatures slightly higher than the determined VPTT of pVCL, with two reasons explaining the increase in VPTT in the VCL-rich microgel core: either a small fraction of hydrophilic comonomer has been incorporated into the core, or the charged microgel shell disturbs the collapse of the core. Given the low reactivity of NTAaa (3.5.4 Reaction Calorimetry), the second reason is much more likely. When the core and shell are interconnected, the collapse of the microgel core induces a partial contraction in the shell as

well.[44] Because of electrostatic forces resulting in repulsion among the polymer chains, the microgel shell resists collapsing, also hindering the collapse of the core. For additional clarity, the initial deswelling was fitted for both microgels (**Figure SIII.4a** and **Figure SIII.4c**), each yielding a VPTT of 33.1 °C, slightly heightened compared to the VPTT of pVCL.

After the first collapse, a relatively stable size is observed over a narrow temperature range, succeeded by further size reduction (**Figure III.5c-d**). This behavior is proposed to arise from the collapse of charged polymer chains which are mostly located in the microgel shell. Therefore, differing VPTT values in distinct areas of the microgel cause a stepwise collapse.[45,46] Del Monte *et al.*[38] demonstrated, through a combination of experimental and simulation data, that the collapse of partially charged microgels is not continuous but occurs in a stepwise manner. Their research revealed that core-shell microgels with peripheral charges undergo a multi-step deswelling process, where the VPT of the microgel core precedes the VPT of the microgel shell. The number of deswelling steps depends on the level of heterogeneity within the microgel,[38] including the distribution of comonomers. In this thesis, a semi-batch polymerization was used for microgel fabrication. Therein, the comonomer NTAaa is added over 8 minutes, after an initial period for microgel core formation, spanning 25-45 s. This approach results in the formation of microgels with a pVCL core and a p(VCL/NTAaa) shell characterized by an increasing NTAaa concentration from the microgel core to the microgel shell. This radial distribution explains the observed multi-step VPT phenomenon in p(VCL/NTAaa) microgels containing 2.0 mol% or 2.2 mol% of NTA (**Figure III.5c-d**).

While the first VPTT was readily determined, pinpointing the specific temperature associated with the subsequent size reduction was only achievable for the microgel with χ_{NTA} = 2.0 mol% (53.1 °C; **Figure SIII.4b**, **Table SIII.1**): Instead of being fixed to one specific temperature, the observed deswelling in the microgel with χ_{NTA} = 2.2 mol% (**Figure SIII.4d**) appears to unfold in multiple steps, suggesting structural heterogeneity characterized by the radially decreasing NTAaa content. Hence, the higher comonomer content leads to increased structural heterogeneity, manifesting in a greater number of distinct areas within the microgel.

Despite the significantly higher NTA content in the microgel containing χ_{NTA} = 11.8 mol%, its VPTT was determined to be 40.6 °C (**Figure SIII.3e**), which is lower compared to previous samples (χ_{NTA} = 2.0 mol%, 2.2 mol%). This discrepancy can be attributed to the observed lower

pH due to the increased presence of carboxylic groups in the microgel. Previous studies have indicated that a decrease in pH results in a lower VPTT for microgels with acidic comonomers.[47,48] At lower pH levels, an abundance of hydrogen ions in the solution causes a shielding effect around the negatively charged NTA. Consequently, the chain-chain electrostatic repulsion between polymer chains diminishes, causing a reduced average interchain distance and an earlier collapse along with a lower VPT.[48] Next to the changes in VPTT, the shielding effect contributes to a less pronounced stepwise deswelling.

3.3.2. Electrophoretic Mobility

For a comprehensive understanding of other effects caused by the phase transition, changes in μ_E were observed across a temperature range of 20 °C to 65 °C. A notable increase in μ_E was observed for pVCL microgels, whereas p(VCL/NTAaa) exhibited decreasing μ_E with increasing temperature (**Figure III.6**). These phenomena are attributed to the VPT: The collapse of the microgels results in an augmented charge density on their surface.

Initially, pVCL microgels carry a minor positive charge owing to the integrated positively charged fragments from the initiator AMPA. As the temperature rises, the microgel contracts, resulting in a substantial increase in surface charge density[38,49] (**Figure III.6a**). Conversely, the surface charge of p(VCL/NTAaa) microgels is predominantly affected by carboxylic groups: While AMPA is also present in these microgels, it does not play a significant role due to the presence of a much higher number of negative charges. Consequently, the heightened surface charge density upon heating translates into more negative μ_E (**Figure III.6b**). This observation suggests the occurrence of an electrophoretic phase transition (EPT) in addition to the VPT.

To determine the temperature at which the EPT occurs (EPTT), a sigmoidal Boltzmann fit was applied to the μ_E curves (**Figure III.6**), identifying the inflection point of the curve as the EPTT. According to the literature, the EPTT typically occurs at higher temperatures compared to the respective VPTT.[49,50] This deviation is primarily attributed to the heterogeneous structure of the microgels. It is anticipated that the densely crosslinked, neutral core undergoes collapse at lower temperatures, already largely contributing to the VPT of the microgel, but not as much to the EPT. Subsequently, the collapse of the charged microgel shell occurs, potentially accompanied by a further reduction in the core size.[38,49,51] This collapse causes a pronounced

increase in charge density, therefore contributing to both, a further decrease in volume and the EPT. To summarize, the EPTT being higher than the VPTT can be attributed to the charged polymer chains consistently being the last to collapse. This is reflected in all EPTT results.

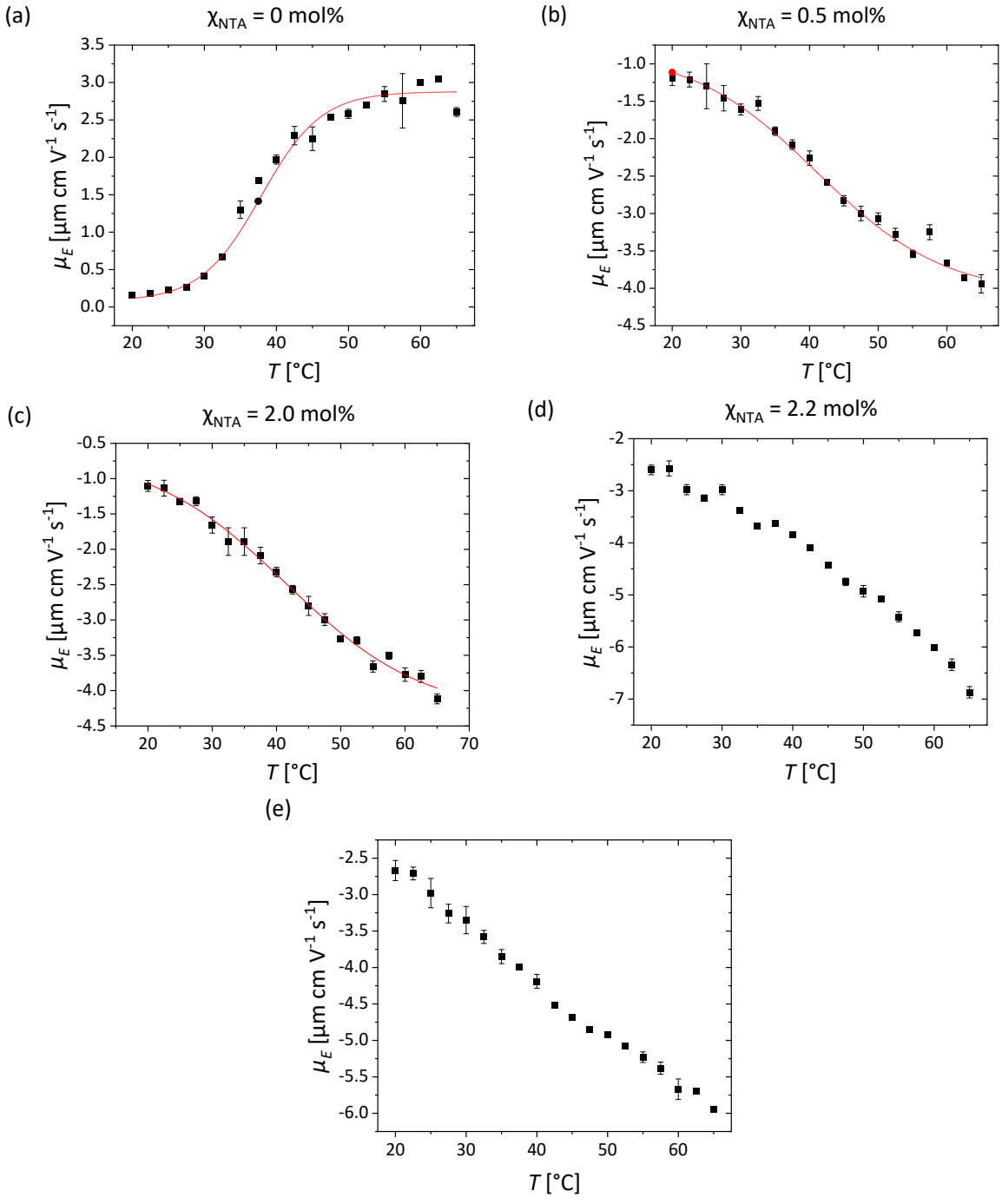

Figure III.6 The electrophoretic mobility (μ_E) was examined regarding its temperature dependence through ELS measurements conducted with a scattering angle of θ = 12.8° in H_2O. Results for p(VCL/NTAaa) microgels with varying comonomer content are presented: χ_{NTA} = (a) 0 mol%, (b) 0.5 mol%, (c) 2.0 mol%, (d) 2.2 mol%, (e) 11.8 mol%. The electrophoretic mobilities in (a)-(c) exhibit characteristics of a sigmoidal curve, while μ_E of microgels containing higher χ_{NTA} displays a more linear behavior. The data were fitted with sigmoidal

Boltzmann functions to determine the EPTT, omitting the curves with more linear behavior: (a) 37.9 ± 0.6 °C, (b) 41.1 ± 1.0 °C, and (c) 41.5 ± 1.4 °C with corresponding degrees of determination of (a) R^2 = 0.994, (b) R^2 = 0.992, and (c) R^2 = 0.992. *Reprinted with permission from the American Chemical Society*[1] *with minor modifications.*

The electrophoretic mobilities of p(VCL/NTAaa) microgels with lower χ_{NTA} (**Figure III.6a-c**) exhibit sigmoidal characteristics, whereas μ_E of microgels with higher χ_{NTA} (**Figure III.6d-e**) shows a rather linear behavior. This is caused once more by the uneven distribution of comonomer throughout the microgel, contributing to the microgel's structural heterogeneity, and leading to multiple steps of collapse. Additionally, the EPTT of the microgels with higher χ_{NTA} may be expected at higher temperatures caused by the presence of highly charged polymer chains, which elevate both the VPTT[36,37] and EPTT. Overall, the accuracy of the sigmoidal fits for determining the EPTT is rather low, as evidenced by the low coefficients of determination (R^2).

Figure SIII.5 further illustrates the temperature-dependent variation of the zeta potential (ζ). Expectedly, the curves exhibit strong similarities to those derived from electrophoretic mobility (μ_E); however, the inflection points are marginally shifted to lower temperatures. This discrepancy can be elucidated by the intricate interplay between ζ and μ_E, as described by the Henry equation (**Equation III.3**).[9,52] Since the behavior of ζ is similar to μ_E, the obtained curves do not require further discussion.

$$\zeta = \frac{3}{2}\left(\frac{\mu_E \eta}{\epsilon_0 \epsilon_r f(\kappa a)}\right)$$

Equation III.3 In the displayed Henry equation, ε_o and ε_r denote the electrical permittivity of vacuum and the relative electrical permittivity of water, respectively, while η represents the temperature-dependent viscosity. Moreover, the Henry function f(κa) significantly influences the equation, with κa corresponding to the ratio of particle radius (a) to the Debye screening length (κ^{-1}).[52,53] The Debye screening length is thereby a measure of the thickness of the electrical double layer.[9]

In summary, the findings demonstrate that the VPTT of p(VCL/NTAaa) microgels is elevated compared to pVCL microgels, attributable to the presence of the hydrophilic, charged comonomer. The VPT of microgels closely correlates with their EPT, due to the higher charge density resulting from the collapse of the microgels. Notably, the stepwise collapse of

uncharged, followed by charged polymer segments places the EPTT at higher temperatures than the VPTT.

Given the significant number of carboxylic groups within the system, it is anticipated that the microgels not only demonstrate temperature-responsiveness but also exhibit sensitivity to other stimuli. Consequently, further investigations explored how the size of the microgels varies with changes in ionic strength and pH.

3.4. Ionic Strength- and pH-Responsiveness of the Microgels

The size of polyelectrolyte microgels can be influenced not only by temperature but also by ionic strength, which may have a significant impact.[39,54,55] Therefore, DLS measurements were conducted to assess the dependency of microgel size on the solution's ionic strength, which was adjusted by the addition of NaCl (**Figure III.7a**). Moreover, the presence of ionizable groups results in pH-responsiveness of microgels.[13,56] Hence, further examination was carried out on the pH-dependence of microgel size (**Figure III.7b**).

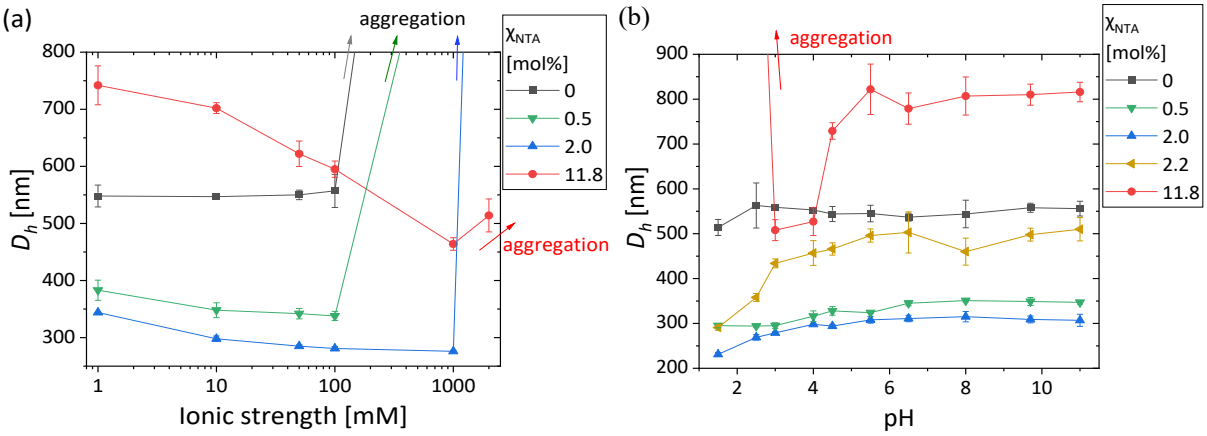

Figure III.7 The D_h of microgels was examined regarding its (a) ionic strength- and (b) pH dependence, through DLS measurements conducted with a scattering angle of θ = 90° in H_2O. Results for p(VCL/NTAaa) microgels with varying comonomer content are presented: (a) χ_{NTA} = 0, 0.5, 2.0 and 11.8 mol%, (b) pH χ_{NTA} = 0, 0.5, 2.0, 2.2 and 11.8 mol%. The ionic strength was adjusted by the addition of NaCl while the pH was adjusted through the use of different buffers with their concentration and ionic strength fixed at 10 mM. *Reprinted with permission from the American Chemical Society*[1] *with minor modifications.*

The pVCL microgels exhibit minimal variation in size with changes in ionic strength but tend to aggregate at ionic strength levels of 100 mM and above (**Figure III.7a**). In HPLC water, pVCL microgels display low ionization, reflected in their μ_E of 0.23 µm cm V^{-1} s^{-1} (**Table III.2**). The low

ionization stems from the non-ionic nature of VCL and BIS, with minor positive charges attributed to fragments from the initiator AMPA. The p(VCL/NTAaa) microgels, however, demonstrate more negative μ_E (**Table III.2**), explained by the incorporation of the acidic comonomer NTAaa. The presence of these ionic groups induces a stronger dependence on the ionic strength: An increase in ionic strength results in a shielding effect, diminishing microgel size by reducing repulsion among carboxylic acid groups (**Figure III.7a**), an effect intensifying with increasing NTA content. P(VCL/NTAaa) microgels exhibit enhanced electrostatic stabilization, a phenomenon that further intensifies with increasing χ_{NTA}. The microgels experience aggregation only at higher ionic strength levels.

The incorporation of carboxylic groups in each NTAaa unit in p(VCL/NTAaa) microgels suggests responsiveness not only to ionic strength but also to changes in pH. Conversely, pVCL microgels, lacking ionizable groups, are not expected to be pH-responsive. This lack of pH-dependent size variations for pVCL was confirmed, while p(VCL/NTAaa) microgels displayed a notable pH-dependence (**Figure III.7b**). The carboxylic groups incorporated into the microgels are protonated at low pH values and deprotonated at high pH values, resulting in a charged state. This leads to an increase in microgel size due to electrostatic repulsion. Particular attention should be paid to the microgel response around the dissociation constant pK_a of NTA. When the pH equals the pK_a, the concentration of the acid (-COOH) is expected to be equal to that of its corresponding base ($-COO^-$). Consequently, an enlargement in size is anticipated around the pK_a due to the increased presence of the charged species.

Instead of just one, NTA has three incorporated carboxylic acid groups, and therefore three pK_a values. Irving et al.[57] determined these at 0 (pK_{a1}), 2.5 (pK_{a2}), and 9.7 (pK_{a3}), assuming NTA concentrations up to 1 mM at 20 °C. For larger NTA concentrations, pK_{a1} shifts to 1.7, whereas the other pK_a values remain unchanged beyond the second decimal place. With rising temperature, both pH and pK_a decrease, leading to an anticipated slightly lower pK_a at the herein-employed 25 °C. Moreover, the incorporation of NTA into microgels is likely to impact the pK_a. Nonetheless, these pK_a values were employed as a preliminary estimate.

Within the obtained data, a noticeable size increase of p(VCL/NTAaa) microgels is observed within the pH range of 1.5 to 6.5 (**Figure III.7b**). NTA in microgels with higher χ_{NTA} thereby possesses a higher pK_a, indicated by the size increase occurring at higher pH values. This can

be attributed to the polyacidic nature of the microgel. As opposed to monomeric acids, additional electrostatic work is required for the dissociation against existing electrostatic forces, caused by the charges in the microgel.[58–60] The greater the number of incorporated acidic groups, the higher the amount of electrostatic work needed for deprotonation, consequently leading to an elevated pK_a.[59]

Notably, the sample containing χ_{NTA} = 11.8 mol% aggregates at pH 2.5 and lower (**Figure III.7b**), attributed to insufficient electrostatic stabilization of the microgels at these pH values. It is proposed that this is caused by attractive interactions among NTA-rich polymer chains after they have been protonated.

Once again, larger differences are observed between the samples with χ_{NTA} = 2.0 mol% and 2.2 mol%. As previously described, the comonomer content of the microgel sample with determined χ_{NTA} = 2.0 mol% may be closer to 1.5 mol%, thereby explaining these differences.

In summary, the findings demonstrate that p(VCL/NTAaa) microgels exhibit responsiveness to temperature, as well as to ionic strength and pH. Compared to monomeric NTA, the dissociation of the carboxylic groups in microgels is shifted to larger pK_a. The more NTA is incorporated into the microgels, the higher the pK_a. Following these comprehensive studies of the stimuli-responsiveness of p(VCL/NTAaa) microgels, attention is now shifted toward methods for further structural elucidation. The results from DLS and ELS indicate a heterogeneous core-shell structure, with NTAaa predominantly located in the microgel shell. This aspect will be further clarified.

3.5. Microgel Morphology and Formation Mechanism

3.5.1. ^{1}H Transverse Relaxation Measurements for Analysis of the Microgel Morphology

For deeper insights into microgel morphology, ^{1}H transverse relaxation (T_2) NMR measurements were conducted. The dynamics of side chains and backbone within the polymer network reflect the microgel's structure, influenced by crosslink density and structural defects. T_2 relaxation analysis, as referenced by previous studies,[27,30,61,62] provides details on internal motions in polymer systems, considering spatial restriction and time scale

of motion. Utilizing the model-free approach by Lipari and Szabo for macromolecules in solution,[63] T_2 relaxation in microgels can be quantitatively described, incorporating parameters for both internal and overall motion. The relaxation decays display a multicomponent nature, with intensities sensitive to the amount of protons in different regions of the microgel.[9,28] Elevated proton concentrations thereby amplify dipolar magnetic interactions. The amount of protons varies throughout the microgel due to differences in crosslinking, with a decreasing proton concentration from the highly crosslinked microgel core to the microgel shell and dangling chains. The overall softness of the microgel depends on its crosslink density, which in turn influences T_2 parameters: A higher degree of crosslinking diminishes side-chain mobility, resulting in further acceleration of the T_2 relaxation. Analysis of relaxation times from spin-echo decay processes therefore provides insights into microgel heterogeneity, predominantly influenced by polymerization kinetics, which leads to a denser core due to faster consumption of crosslinker.[64] In the employed semi-batch polymerization, the core-shell structure of the microgel is further accentuated by the delayed addition of NTAaa, promoting the accumulation of comonomer in the microgel shell.

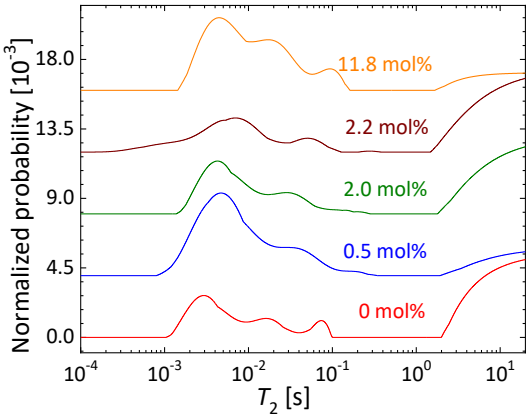

Figure III.8 T_2 spectra of p(VCL/NTAaa) (χ_{NTA} = 0 mol%, 0.5 mol%, 2.0 mol%, 2.2 mol% and 11.8 mol%), obtained from the application of ILT to the proton T_2 spin-echo decays of the microgels. The peaks correspond to the core-shell morphology (T_2 < 1 s) and HDO (T_2 > 1 s).

All NMR measurements were conducted in D_2O, therefore, a contribution of HDO to the spin-echo decay can be anticipated. However, owing to the high purity of D_2O (99.8 %), any resultant effect is expected to be minimal. Proton T_2 spin-echo decays of p(VCL/NTAaa) microgels are depicted in **Figure SIII.6**. Data analysis involved applying the Inverse Laplace Transform (ILT) of the spin-echo decays.[30] Obtained ILT spectra (**Figure III.8**) exhibit several peaks, with those on the left side (T_2 < 1 s) associated with the microgel's core and shell, while

the peak on the right side (T_2 > 1 s) corresponds to HDO. It is noteworthy that the lower signal-to-noise ratio at higher spin-echo times in the T_2 spin-echo decays (**Figure SIII.6**) may result in variations in peak positions and intensities in the ILT spectra (**Figure III.8**), as noted in previous studies.[30] This warrants careful consideration for the HDO peak.

The presence of multiple peaks indicates the microgel's heterogeneous nature, with distinct regions exhibiting varying relaxation times. The shortest relaxation time is associated with the microgel core, whereas longer relaxation times correspond to its shell. Interestingly, rather than two peaks for the microgel core and shell, there appear to be three peaks, suggesting a microgel structure with an inner and outer shell. Peaks at longer relaxation times display varying intensities across different samples without a recognizable trend. This variability can be attributed to the aforementioned lower signal-to-noise ratio at higher T_2 values.[30]

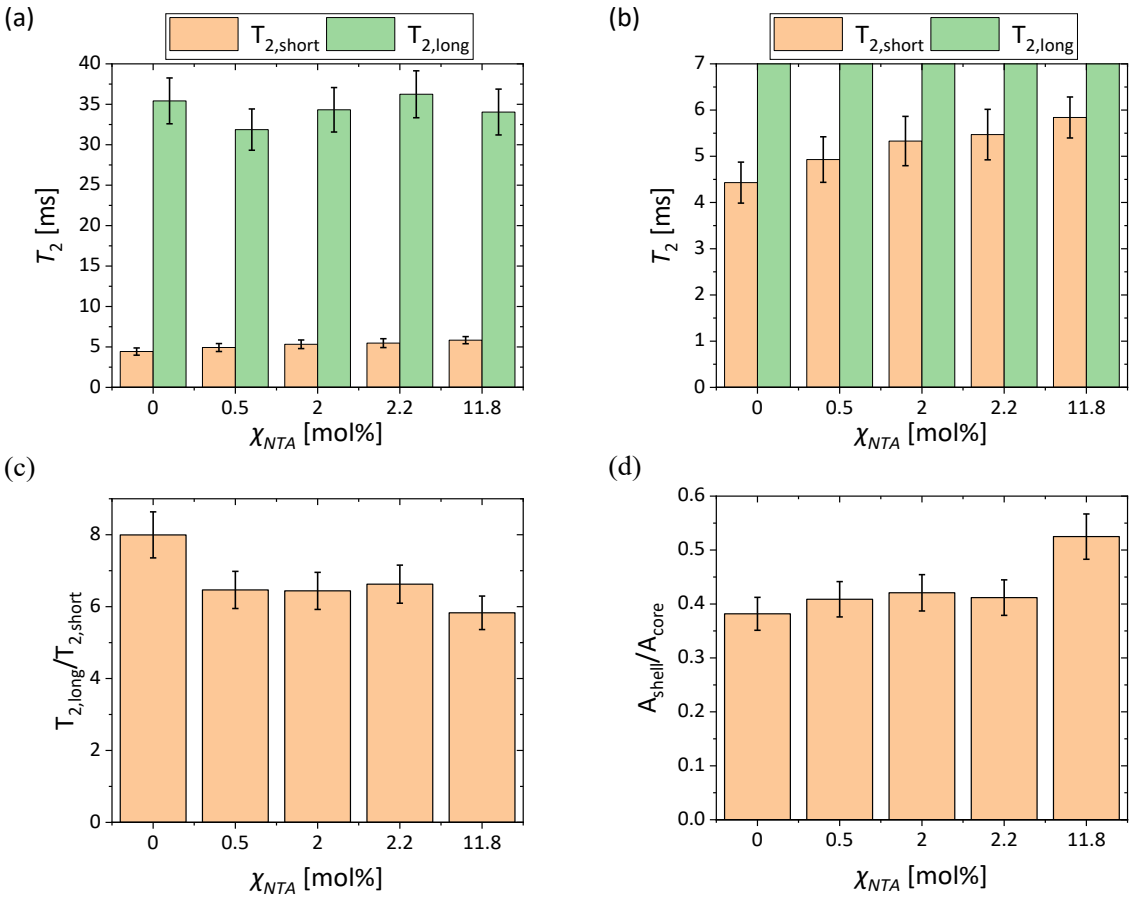

Figure III.9 Data obtained from the proton T_2 spin-echo decays for p(VCL/NTAaa) microgels containing comonomer contents of χ_{NTA} = 0 mol%, 0.5 mol%, 2.0 mol%, 2.2 mol% and 11.8 mol%. (a) Proton short and long T_2 - transverse relaxations, along with (b) an enlarged section. (c) Dynamic contrast $T_{2,long}/T_{2,short}$, and (d) proton concentration contrast A_{shell}/A_{core} obtained from exponential fitting. Samples were measured at 24 °C at a microgel

concentration of 5 mg mL^{-1}. *Reprinted with permission from the American Chemical Society*[1] *with minor modifications.*

In prior studies, only two peaks were found in the T_2 spectra, corresponding to the core and corona of pVCL microgels.[65] However, by measuring the CPMG decay at significantly higher spin-echo times, it was possible to analyze higher values of T_2, thus unveiling three distinct relaxation times. A microgel characterized by a core-inner shell-outer shell morphology is therefore anticipated. Similar structures have been documented in prior literature.[38] The obtained pVCL microgels without incorporated comonomer feature a BIS-rich core, a VCL-rich inner shell, and a VCL-rich outer shell which contains AMPA fragments: The positively charged initiator fragments arrange themselves at a maximum distance from each other due to electrostatic repulsion. In p(VCL/NTAaa) microgels, the three distinct microgel layers are expected to be a BIS-rich core, a VCL-rich inner shell, and an NTAaa-rich outer shell.

Additionally, the microgel's proton T_2 spin-echo decays (**Figure SIII.6**) were effectively fitted with a three-phase exponential decay, yielding high coefficients of determination (R^2 = 0.995 to 0.998). This is described in detail in **Materials and Methods**. The comparison of short and long T_2 ($T_{2,short}$ and $T_{2,long}$) obtained from fitting CPMG decays is presented in **Figure III.9a**, providing further evidence for a core-shell microgel morphology. These T_2 values obtained from fitting are comparable to each other. However, a direct comparison to T_2 values from ILT is not feasible because both methods may generate slightly different values. Furthermore, the exponential fitting approach allowed for comparison solely between the T_2 values of the core and shell, owing to the lower signal-to-noise ratio observed at higher spin-echo times.

An increase of $T_{2,short}$ can be observed with increasing χ_{NTA}, which was highlighted in an expanded section of $T_{2,short}$ depicted in **Figure III.9b**. Such an increase may stem from either a reduced quantity of crosslinks in the microgel core or the integration of hydrophilic NTAaa groups, both contributing to decreased chain stiffness. Conversely, the acquired $T_{2,long}$ results exhibit a more intricate trend, revealing a declining relaxation time when contrasting pVCL microgels with those of p(VCL/NTAaa) featuring low χ_{NTA}. This may be explained by the presence of NTAaa during polymerization: It is presumed that the integration of NTAaa hampers the crosslinking of the microgel core, resulting in a less densely crosslinked core, while the crosslinker is partially incorporated into the microgel shell. When comparing p(VCL/NTAaa) microgels among each other, an increase in $T_{2,long}$ is evident up to χ_{NTA} values of

2.2 mol%, caused by the presence of hydrophilic NTAaa groups resulting in a decreased chain stiffness. However, contrasting these $T_{2,long}$ values with those obtained for χ_{NTA} = 11.8 mol%, $T_{2,long}$ decreases instead of further increasing. As previously elucidated, the integration of NTAaa into the microgels induces a pH decrease, resulting in the protonation of NTA. Consequently, the diminished chain mobility can be explained by the presence of fewer protonated, hydrophilic NTA groups.

The dynamic contrast equals the ratio $T_{2,long}/T_{2,short}$ (**Figure III.9c**). This ratio of relaxation times reflects functional group mobility in the shell and core, and thus elucidates differences in crosslinking density and hydrophilicity, indicating variations in the softness of the shell and core. From this dynamic contrast analysis, a more densely crosslinked microgel core for pVCL compared to p(VCL/NTAaa) microgels is anticipated. Among p(VCL/NTAaa) microgels minimal changes in dynamic contrast are observed with varying comonomer content, suggesting similar crosslinking densities across these microgels. An exception here is the sample with χ_{NTA} = 11.8 mol%, which exhibits a lower dynamic contrast, attributed to pH variation. Protonation of NTA leads to significantly shorter $T_{2,long}$, impacting the dynamic contrast. The employed semi-batch polymerization method maintains consistent kinetics of microgel core polymerization in the first 30 seconds of the reaction. Although a substantial portion of BIS is converted before NTAMaa addition due to its rapid polymerization,[66] NTAMaa may negatively influence crosslinking after its addition, which starts after the initial 30 seconds. This may cause further changes in dynamic contrast.

The contrast in proton concentration, represented by A_{shell}/A_{core} is shown in **Figure III.9d** and exhibits a notable rise with increasing comonomer content. This indicates the presence of more protons within the microgel shell, associated with a thicker, NTA-rich shell due to the increased amount of comonomer in the microgels.

The obtained results indicate that the incorporation of higher concentrations of NTAMaa could potentially influence polymerization rates and the mechanism of microgel formation. Consequently, AFM and reaction calorimetry were employed to gain further insights into the microgel structure and its formation mechanism.

3.5.2. Atomic Force Microscopy of the Microgels

Utilizing AFM, microgels were visualized in their dried state, allowing for the observation of microgel morphology. For this, the samples were spin-coated onto plasma-activated Si wafers. A comparison between p(VCL/NTAaa) microgel samples with varying comonomer content revealed significant morphological changes. **Figure III.10** illustrates p(VCL/NTAaa) microgels with comonomer contents of 0.5 mol% and 11.8 mol%, showcasing variations in morphology and stiffness. Additionally, AFM images of microgel samples with χ_{NTA} = 0 mol%, 2.0 mol%, and 2.2 mol% are depicted in **Figure SIII.7**. Across different comonomer contents, strong variations in the microgel morphology were observed (**Figure III.10ab**). These can be attributed to an increased χ_{NTA}. Prior research has extensively shown that the introduction of comonomers plays a pivotal role in shaping microgel morphology. For instance, Grabowski *et al*.[67] have demonstrated that altering the comonomer content alone can yield entirely distinct microgel shapes, a phenomenon observed across different synthesis methods, including batch and semi-batch. In this system, it is hypothesized that a core consisting of pVCL and BIS forms initially, before the addition of NTAMaa. The selective integration of NTAMaa into the microgel shell, facilitated by its delayed introduction and lower reactivity, likely accounts for the evident core-shell structure. Utilizing AFM, a subtle asymmetry was observed in p(VCL/NTAaa) microgels with χ_{NTA} = 2.2 mol% and higher (**Figure III.10**, **Figure SIII.7**). These microgels showcase a core-shell morphology with an off-centered core, possibly arising from strong hydrophobic interactions between NTAMaa moieties during polymerization, leading to their self-assembly and the resultant asymmetrical structure. It needs to be noted, that a few p(VCL/NTAaa) microgels exhibit multiple cores, presumably due to shell formation around two core microgels and, therefore, caused by the employed semi-batch method.

Overall, the core-shell morphologies observed in microgels with χ_{NTA} = 2.2 mol% and higher, resemble “fried-egg” structures found in previous studies.[68–70] Respective microgels typically feature a denser, more crosslinked core and a softer microgel shell.[68] This “fried-egg” structure is featured in the height profiles of those microgels and in phase images (**Figure III.10**, **Figure SIII.7**). Here, the microgel core exhibits a higher phase shift compared to the underlying Si wafer, indicating a stronger interaction of the cantilever with the polymeric material. This suggests that the polymer material is relatively softer than the metal surface.

The microgel shell on the other hand displays a phase shift comparable to that of the Si wafer. This phenomenon suggests a lower polymer density toward the periphery of the adsorbed microgel, resulting in reduced interaction with the cantilever and a correspondingly lower phase shift. Previous research has indicated that in tapping mode AFM, the cantilever may interact not only with the sample but also with the harder underlying surface.[71]

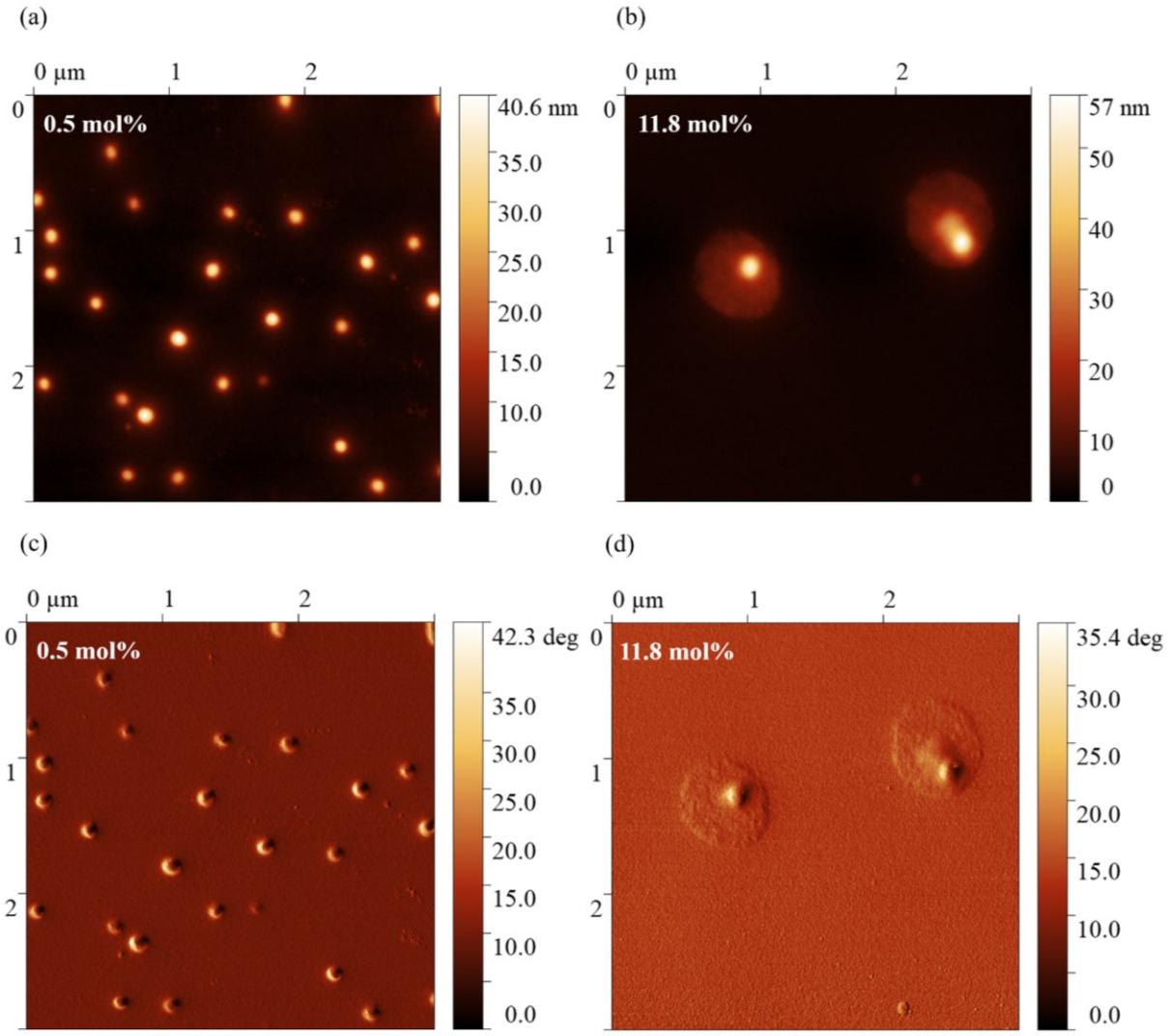

Figure III.10 AFM images of p(VCL/NTAaa) microgels with their (a, b) height profiles, and (c,d) phase images. Microgels possess χ_{NTA} = (a, c) 0.5 mol% and (b, d) 11.8 mol%. The samples were spin-coated onto plasma-activated Si wafers. *Reprinted with permission from the American Chemical Society.*[1]

The comparison between the sizes obtained from AFM measurements and DLS results revealed interesting insights. At lower χ_{NTA} levels, the microgels in their dried state appeared relatively small, constituting only about 30 % of their swollen size. Contrary, with increased

χ_{NTA}, the hydrophilic polymer chains exhibited more extensive spreading on the Si wafer, resulting in larger observed microgel diameters *via* AFM. In these instances, AFM measurements indicated sizes reaching up to 85% of those obtained from DLS. This trend corresponds well with previous observations due to the formation of a soft shell around the microgel core at higher χ_{NTA}. The summarized results are listed in **Table III.3**.

Table III.3 Comparison of the D_h of p(VCL/NTAaa) microgels obtained from DLS and the diameters from AFM (D_{AFM}). AFM samples were dried on a Si wafer and subsequently measured. Here, microgels with varying χ_{NTA} are compared. DLS was performed at T = 25 °C at a scattering angle of θ = 90°.

χ_{NTA} [mol%]	D_h [nm][a)]	D_{AFM} [nm]	D_{AFM} / D_h [%]
0	576 ± 15[b)]	280 ± 35	48.6
0.5	584 ± 20[b)]	187 ± 33	32.0
2.0	431 ± 4[c)]	128 ± 20	29.7
2.2	640 ± 11[c)]	379 ± 77	59.2
11.8	770 ± 22[d)]	666 ± 54	84.5

[a)] The used 0.5 mg mL^{-1} p(VCL/NTAaa) dispersion resulted in a neutral pH at low NTA contents ($\chi_{NTA,actual}$ = 0.1 to 0.5 mol%) and in a slightly acidic pH of 5 or 4 at higher NTA contents ($\chi_{NTA,actual}$ = 2.0 to 11.8 mol%); [b)] pH 6, the pH corresponds to the pH of the used HPLC water; [c)] pH 5; [d)] pH 4.

3.5.3. Scanning Electron Microscopy of the Microgels

Following the comprehensive examination of the microgels using AFM, electron microscopy was employed to gather additional insights into the microgel structure. Scanning electron microscopy (SEM) coupled with a bright-field scanning transmission electron microscopy (BFSTEM) detector was utilized to visualize the microgels, focusing on revealing their internal microstructure rather than surface features. The resulting images (**Figure SIII.8**) exhibit similarities to the AFM images discussed previously. However, distinct from AFM, BFSTEM allows for the visualization of a microgel shell for all χ_{NTA}, with the thickness of the shell increasing with χ_{NTA}. The microgel cores display a higher density attributed to the elevated crosslinker content. Nevertheless, the overall contrast in BFSTEM images remains low due to the low density of the polymeric microgel samples. Further SEM images were acquired using a secondary electron detector (**Figure SIII.9**), albeit with a much lower resolution. SEM images are found in the **Supplementary Data**.

3.5.4. Reaction Calorimetry

To delve deeper into the distribution of comonomers within the microgel, calorimetric studies were conducted. A precipitation polymerization of VCL and NTAMaa crosslinked with 2.6 mol% BIS and initiated with 1.2 mol% AMPA, was performed to conduct real-time turbidity and calorimetric measurements (**Figure III.11**). Instead of using a semi-batch method, batch polymerization was performed to minimize inaccuracies in measuring the heat generation rate: The heat generation rate is affected when comonomers are added after initiation, which could potentially distort the obtained data. Aside from earlier NTAMaa addition, the selected batch polymerization method is, however, analogous to the previous semi-batch approach. The observed turbidity (**Figure III.11a**) during the reaction shows an increase with increasing particle size, reaching a plateau when the microgels reach their final size, as previously reported in the literature.[72] It is noteworthy that the turbidity of microgels is generally influenced by the refractive index, making it highly dependent on the water content of the microgels.[73,74] Additionally, the turbidity can vary based on the precise polymer composition *via* changes in the dielectric constant.[75,76] Consequently, turbidity is only primarily dictated by size under conditions of constant polymer composition and water content. However, a plateau is expected to occur as the microgels reach their final size, attributed to the consistent composition of the microgels at the end of the polymerization process.

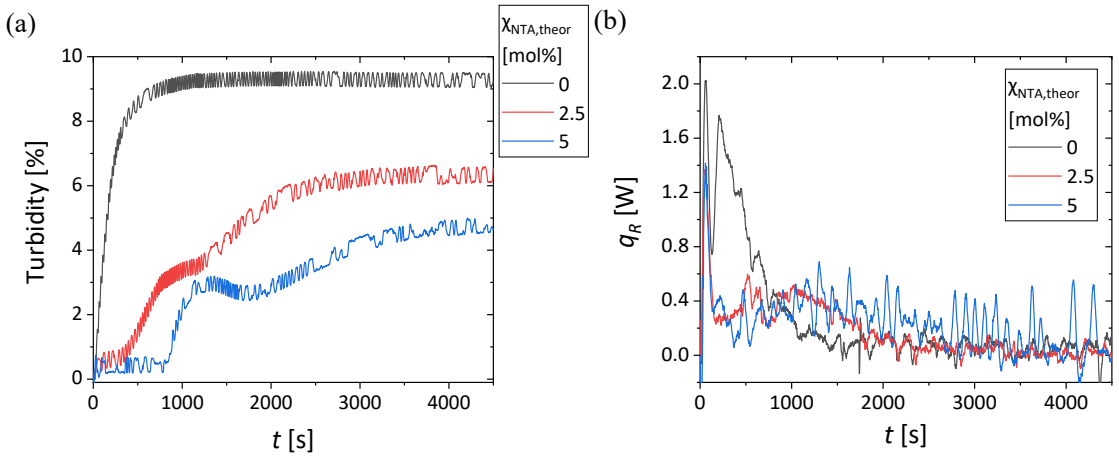

Figure III.11 Real-time measurements of (a) turbidity, and (b) heat generation rate (q_R), recorded during batch polymerization of p(VCL/NTAaa) microgels with 2.6 mol% BIS. *Reprinted with permission from the American Chemical Society*[1] *with minor modifications.*

Figure III.11b (with a magnified section in **Figure SIII.10**) provides the visualization of the heat generation rate throughout the polymerization reaction. This rate is intimately linked to the

polymerization rate, given the exothermic nature of polymerization reactions,[77] making it an ideal parameter for monitoring the reaction progress.

The polymerization reaction of VCL in DMSO/water exhibits slower kinetics compared to polymerization reactions reported in literature conducted solely in water.[77] The heat generation rate for VCL polymerization in DMSO/water plateaus around 1200-1600 s, coinciding with the stabilization of turbidity. This suggests completion of the reaction within this timeframe, whereas literature-reported VCL polymerization reactions typically span 300-500 s.[72,77] Despite using similar amounts of initiator AMPA and crosslinker BIS, the variance in reaction duration can be attributed to the solvent composition; the presented reactions were conducted in a DMSO/water mixture rather than solely in water. The enhanced solubility of formed pVCL/BIS polymer chains in DMSO necessitates longer polymer chains for precursor particle precipitation. Previous studies have indicated that polymerization rates of VCL and BIS are heightened in the precipitated gel state compared to the solution.[77,78] Hence, a lower polymerization rate is anticipated in DMSO/water mixtures, aligning with these findings.

The initial peak in the heat generation rate curves of pVCL polymerization corresponds to the crosslinker BIS, consistent with its faster consumption compared to the monomer VCL, as documented in the literature. This consumption pattern yields a microgel structure characterized by a highly crosslinked core and a less densely crosslinked shell.[64,66] In comparison to literature findings,[72,77] the BIS heat generation rate in this thesis appears slightly slower, yet the associated peak is more pronounced. This discrepancy can be attributed to the considerably slower polymerization of VCL in the presented setup, resulting in a lower heat release over an extended duration.

The heat generation rate and turbidity curves for the p(VCL/NTAMaa) synthesis suggest an even slower polymerization reaction. Polymerization completes after approximately 2600 s for χ_{NTA} = 2.5 mol% and after 4500 s for χ_{NTA} = 5 mol%. Previous studies have demonstrated that the addition of comonomers can influence polymerization rates,[72,79] and in this case, the slower polymerization is attributed to the presence of NTAMaa, which decelerates microgel formation.

Analysis of the turbidity curves reveals a two-step polymerization. For χ_{NTA} = 2.5 mol%, the turbidity reaches an area with a significantly lower incline around 800 s before increasing

again, a phenomenon observed previously in the literature[72] and attributed to varying reactivities of comonomers. Similarly, for χ_{NTA} = 5 mol%, the turbidity plateaus around 1200 s, followed by a decrease and subsequent increase after 1700 s, indicating a change in the microgel's dielectric constant likely due to the altered composition caused by NTAMaa incorporation. The results indicate that NTAMaa exhibits lower reactivity compared to VCL, thus polymerizing mainly after VCL, resulting in the observed two-step process. Since BIS and VCL radicals preferentially react with monomers of the opposite species,[66,79] the batch polymerization likely forms a BIS-rich core followed by a VCL-rich inner shell with few NTAMaa units. The outer shell primarily comprises NTAMaa, which possesses the slowest reaction rate. Transitioning from batch to semi-batch polymerization, where NTAMaa is added after 25-45 s, is expected to accentuate the core-shell morphology, with NTAMaa concentration being highest in the outer shell. Consequently, the presented microgels exhibit a heterogeneous morphology with radially decreasing NTA content, consistent with prior suggestions.

In forthcoming studies, extending the calorimetry data with kinetic modeling, as demonstrated in works by Nevolianis *et al.*[79] could offer deeper insights into the reactivities of various radical species involved in the presented precipitation polymerization process. Additionally, employing molecular simulations akin to those conducted by Grabowski *et al*.[67] might prove beneficial for elucidating the microgel structure and the molecular assembly mechanisms during polymerization. The insights from such simulations could furnish further evidence for the self-assembly of NTAMaa units, thereby elucidating the formation of slightly asymmetric microgels.

3.5.5. Formation Mechanism of the Microgels

This chapter aims to elucidate the anticipated formation mechanism of the microgels based on the findings obtained thus far. Drawing from insights in existing literature regarding pVCL formation,[64,77] these results are consistent with previous observations. The formation process is hypothesized to commence with the formation of a densely crosslinked, BIS-rich core, succeeded by the development of a less densely crosslinked, VCL-rich inner shell. Subsequently, the outer shell of the microgel is expected to exhibit an even lower density, albeit with a similar composition, due to the elongation of polymer chains. **Figure III.12**

provides a schematic representation of this process. It is worth noting that the depicted microgels are presented in their swollen state at 25 °C, facilitating a clearer visualization of the process, whereas the synthesis occurs in the collapsed state at 70 °C.

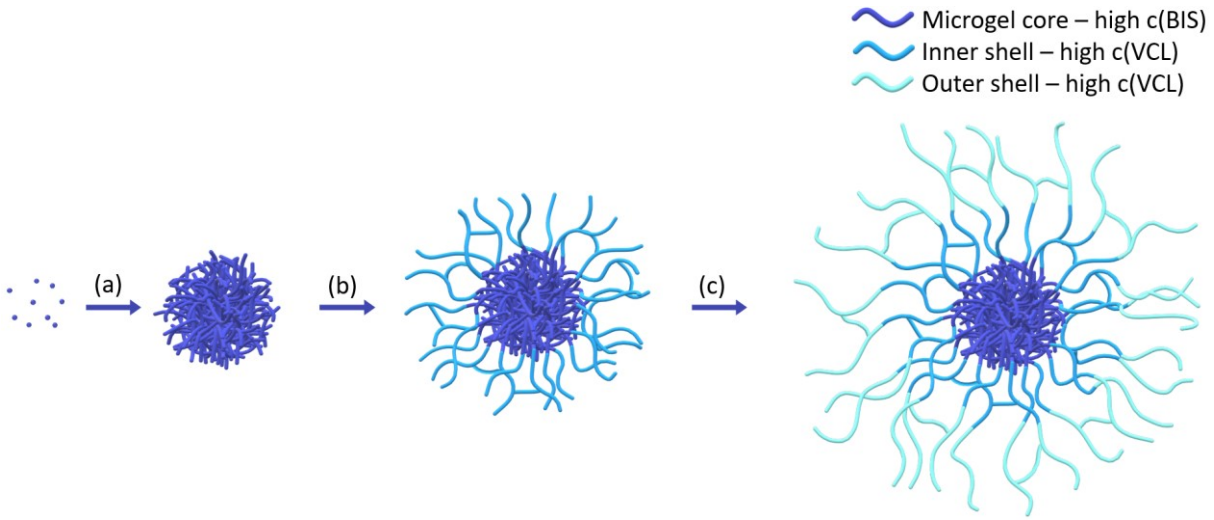

Figure III.12 Formation of a pVCL microgel depicted at different stages of the polymerization. Microgels are shown in their respective swollen states. (a) Initiation and formation of a dense, BIS-rich microgel core. (b) Development of an intermediate-density VCL-rich inner shell. (c) Formation of a low-density VCL-rich outer shell. *Reprinted with permission from the American Chemical Society*[1] *with minor modifications.*

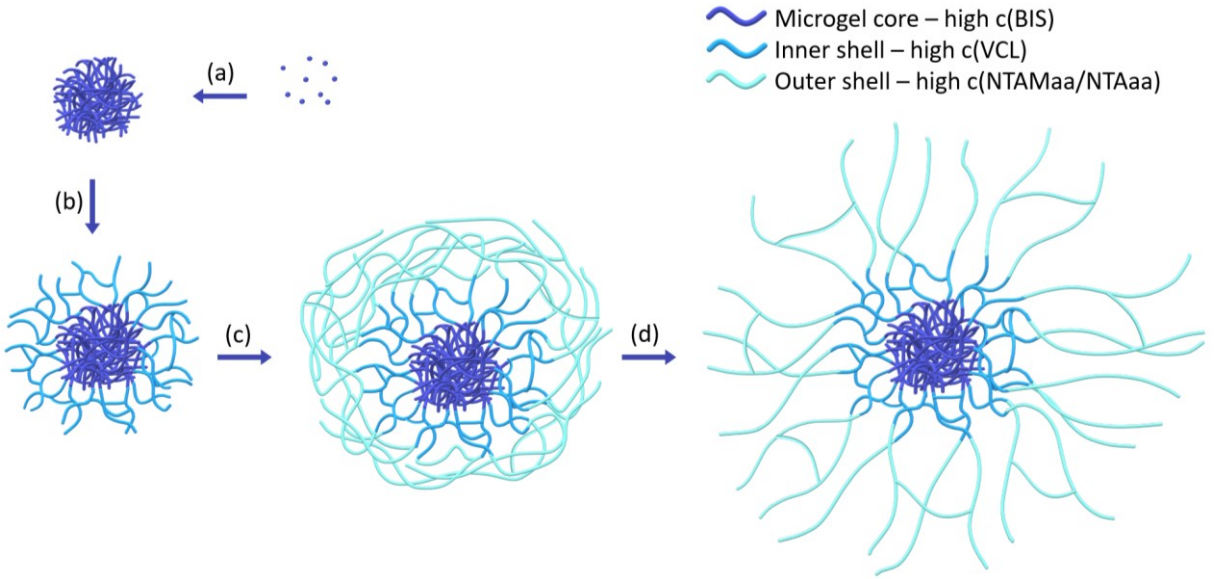

Figure III.13 Formation of a p(VCL/NTAaa) microgel depicted at different stages of the polymerization. Microgels are shown in their respective swollen states. (a) Initiation and formation of a dense, BIS-rich microgel core. (b) Development of an intermediate-density BIS- and VCL-rich inner shell. (c) Formation of an NTAMaa-rich microgel outer shell. The NTAMaa

layer is anticipated to remain in a semi-collapsed state when swollen in aqueous dispersion, owing to the higher hydrophobicity of NTAMaa. (d) Formation of a low-density NTAaa-rich outer shell after hydrolysis of NTAMaa. The prior interaction of the NTAMaa chains during polymerization may contribute to the formation of an asymmetric outer shell. *Reprinted with permission from the American Chemical Society*[1] *with minor modifications.*

The formation mechanism for a p(VCL/NTAaa) microgel is depicted in **Figure III.13**. The presence of DMSO and the delayed addition of NTAMaa impede the formation of the BIS-rich core (**Reaction Calorimetry**). As a result, the dense, BIS-rich core in p(VCL/NTAaa) microgels (**Figure III.13a**) is expected to be less dense compared to pVCL microgels (**Figure III.12a**). Subsequent polymerization leads to the formation of a VCL-rich inner shell, potentially incorporating additional BIS-crosslinks (**Figure III.13b**). As polymerization progresses, NTAMaa is introduced, forming a semi-collapsed layer around the microgel due to its relatively high hydrophobicity (**Figure III.13c**). Eventually, the NTAMaa layer undergoes hydrolysis, resulting in the formation of a low-density NTAaa outer shell (**Figure III.13d**). The hydrophobic interactions among NTAMaa polymer chains before hydrolysis may contribute to slight asymmetry in the resulting microgel shell. With a higher concentration of NTAMaa in the polymerization, microgel shells become more pronounced.

After conducting a comprehensive investigation of microgel stimuli-responsiveness and morphology, the subsequent chapters involve their utilization for biological applications. To this end, cytocompatibility experiments were conducted, alongside the electrostatic immobilization of a model protein.

3.6. Use of Microgels for Biological Applications

3.6.1. Cytotoxicity/Viability Test According to ISO 10993–5

For cytotoxicity assessment following ISO 10993–5 guidelines, p(VCL/NTAaa) microgel samples with varying comonomer contents (χ_{NTA} = 0, 0.5, 2.0, 2.2, and 11.8 mol%) were incubated with cell culture medium for one, three, and seven days. Subsequently, the supernatant was collected and transferred to pre-seeded L929 mouse fibroblasts (5.0 x 10^3 cells cm^{-2}). Cells were then cultured for one day before live/dead stainings were performed. FDA was utilized for staining viable cells. Upon intracellular esterase activity, FDA is converted

into highly fluorescent fluorescein. PI, which can only penetrate cells lacking membrane integrity, was employed for staining dead cells.[80,81] Consequently, viable cells exhibited green fluorescence (FDA), while dead cells exhibited red fluorescence (PI) (**Figure III.14a**). Tissue culture polystyrene (TCPS) served as a viability control, whereas TCPS treated with TritonX-100 served as a dead cell control.

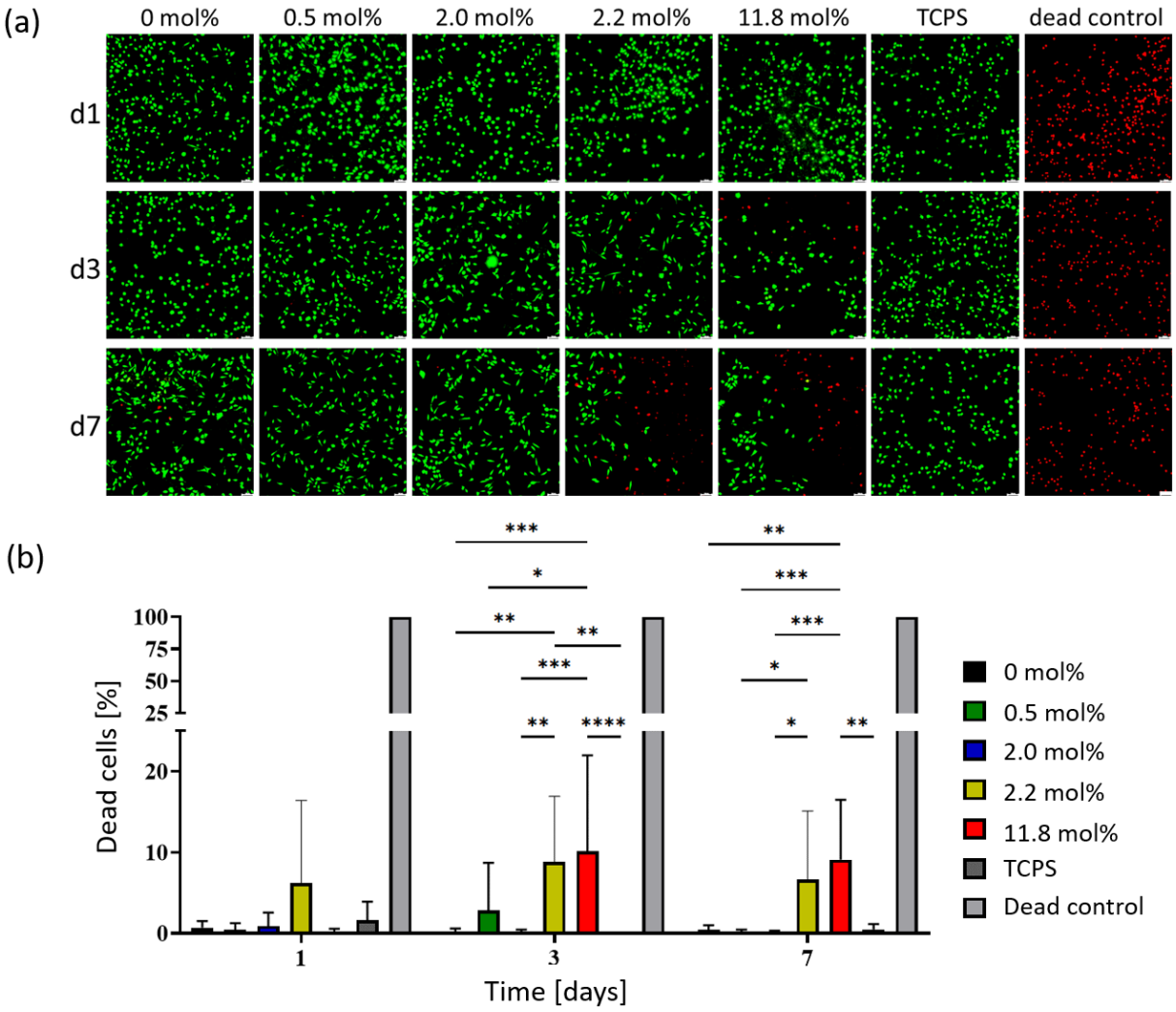

Figure III.14 Cytotoxicity assessment of p(VCL/NTAaa)) microgels with χ_{NTA} = 0, 0.5, 2.0, 2.2, and 11.8 mol%. (a) Live/dead staining of the microgels with tissue culture polystyrene (TCPS) as a viability control and a dead cell control which was treated with 20 µL TritonX-100 (0.1 % dissolved in PBS) to lyze the cells. Fluorescent staining revealed viable cells with green and dead cells with red. Magnitude: 100x, Scale bar 100 µm. (b) After quantification of the images with ImageJ, the percentage of dead cells was calculated. The fraction of dead cells after 1, 3, and 7 days is shown with respective error bars. From left to right, p(VCL/NTAaa)) microgels with χ_{NTA} = 0, 0.5, 2.0, 2.2, and 11.8 mol%, TCPS and a dead cell control are shown. *Reprinted with permission from the American Chemical Society.*[1]

Upon treatment with supernatant, the cellular morphology remained comparable to control conditions on TCPS. Even so, L929 cells exhibited an elevated presence of dead cells when exposed to cell-culture supernatant obtained from the microgels with χ_{NTA} = 2.2 and 11.8 mol% NTA after 3 and 7 days. Image analysis was conducted using ImageJ, whereby cell counts were manually determined and the ratio of dead to viable cells was calculated (**Figure III.14b**). For the supernatant collected on day 1, no significant differences were observed. Contrary, on day 3, an increase in the percentage of dead cells was evident for microgels with 2.2 and 11.8 mol%. (8.84 % and 10.11 %, respectively) and day 7 (6.64 % and 9.11 %, respectively). To summarize, an increase in the number of dead cells was observed in samples containing larger amounts of comonomer (χ_{NTA} = 2.2 and 11.8 mol%), whereas no significant rise in dead cells was noted for microgels with lower comonomer content (χ_{NTA} = 0, 0.5 and 2.0 mol%). Hence, samples with lower χ_{NTA} appear suitable for bio-applications without constraints. The ISO 10993-5:2009 standard defines a non-toxic range where the fraction of dead cells should not exceed 30 %.[82,83] With a maximum of 10.11 % dead cells, even for microgels with higher χ_{NTA}, the results remain well below this threshold, suggesting potential use in biomedical applications. However, the viability of cells relevant to specific clinical treatments must be reassessed depending on the application.

3.6.2. Cell Proliferation Assay

Additionally, a cell proliferation assay was conducted, wherein the microgels (χ_{NTA} = 0, 0.5, 2.0, 2.2, and 11.8 mol%) were cultured with L929 cell culture medium for 7 days. After incubation, the medium was removed, and cells were seeded (5.0×10^4 cells cm^{-2}) in a 24-well plate placed in the CELLCYTE X™. The confluency was quantified using integrated CELLCYTE X™ software and plotted against time in **Figure III.15**, indicating no significant changes in proliferation for the TCPS control and p(VCL/NTAaa) microgels with χ_{NTA} = 0, 0.5, and 2.0 mol%. However, microgels with higher comonomer contents (χ_{NTA} = 2.2 mol% and 11.8 mol%) caused significantly decreased proliferation, with almost no increase in confluency over time.

Although all microgels demonstrated good cytocompatibility according to ISO 10993-5:2009, the results from cell proliferation assays suggest that only microgels with lower comonomer contents (χ_{NTA} = 0, 0.5, 2.0 mol%) are suitable for tissue engineering applications. Significant

disparities were shown between the samples containing χ_{NTA} = 2.0 mol% and χ_{NTA} = 2.2 mol%, for both cytotoxicity and proliferation assays. These differences support the earlier hypothesis regarding the larger anticipated difference in χ_{NTA} between these samples, with the actual concentration of the p(VCL/NTAaa) microgel with a determined χ_{NTA} = 2.0 mol% being closer to its theoretical comonomer content of 1.5 mol%.

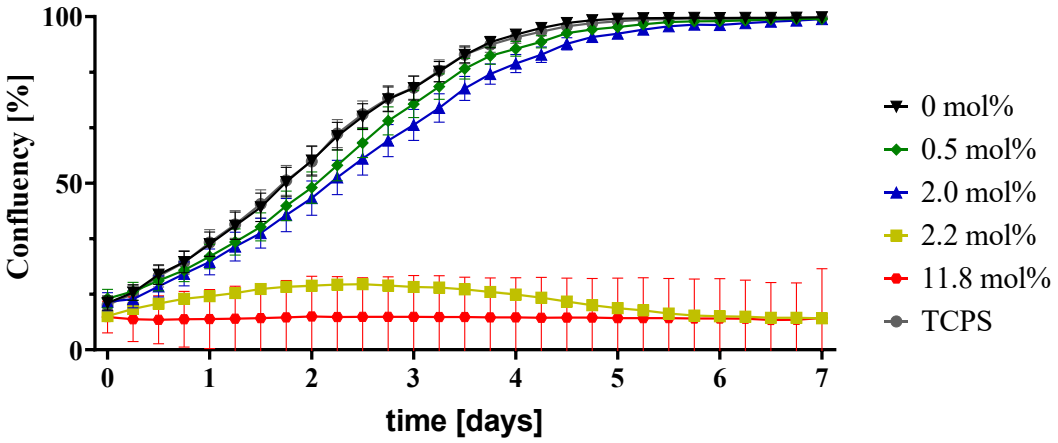

Figure III.15 Proliferation assay of L929 mouse fibroblasts cultured in p(VCL/NTAaa) supernatant of microgels (χ_{NTA} = 0, 0.5, 2.0, 2.2, and 11.8 mol%) over 7 days. A CELLCYTE X™ was used to determine the confluency. *Reprinted with permission from the American Chemical Society.*[1]

In summary, the potential use of microgels in bio-applications appears feasible across all comonomer concentrations, while lower comonomer amounts even enable consideration for tissue engineering applications. Leveraging this data, the next step is to immobilize cyt c into p(VCL/NTAaa) microgels, demonstrating the potential for uptake of positively charged biomolecules *via* electrostatic interactions.

3.6.3. Immobilization of Cytochrome C on Microgels

For the demonstration of biomolecule immobilization in p(VCL/NTAaa) microgels, the model protein cyt c, possessing a low molecular weight of 10 kDa, was employed. With an isoelectric point around 10,[84,85] cyt c maintains a net positive charge across a wide pH range. Immobilization was conducted at a neutral pH of 6.5 to ensure the proteins' positive charge while preserving the negative surface charge of p(VCL/NTAaa) microgels. These are compared to pVCL microgels, where a low uptake of cyt c is expected, as they exhibit a slight positive

charge at neutral pH due to initiator fragment incorporation. After incubation of the microgels with cyt c, the mixture was dialyzed to remove any non-immobilized protein. UV-Vis spectra recorded pre- and post-dialysis are depicted in **Figure III.16ab**, alongside a UV-Vis spectrum of cyt c shown in **Figure III.16c**. Cyt c exhibits characteristic peaks at 408 nm and 530 nm, previously observed for its oxidized form,[86] along with a peak around 360 nm, also consistent with previous UV-Vis spectra.[87,88]

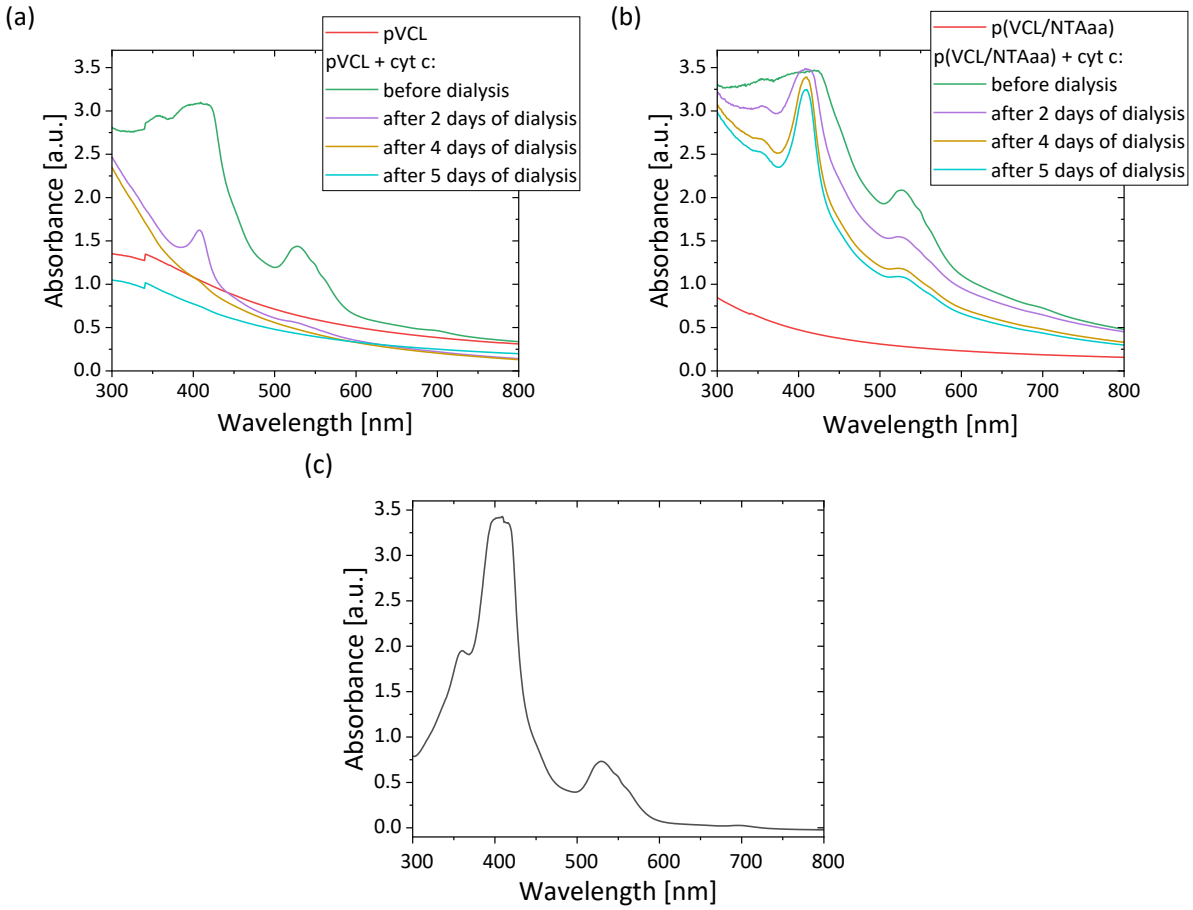

Figure III.16 UV-Vis spectra of microgel-cyt c mixtures before and after dialysis. The samples were prepared in buffer (10 mM MES pH 6.5, ionic strength of 10 mM). Initial concentrations of 2 mg mL^{-1} microgels, and 1 mg mL^{-1} cyt c were used. Samples are compared to pure microgel (2 mg mL^{-1} in buffer). Cyt c was mixed with (a) pVCL and (b) p(VCL/NTAaa) and samples were investigated after 2, 4, and 5 days of dialysis. (c) Data for pure cyt c is shown for comparison. *Reprinted with permission from the American Chemical Society*[1] *with minor modifications.*

The UV-Vis data in **Figure III.16a** illustrates the washout of cyt c from pVCL microgels after 5 days. Notably, the characteristic peaks of cyt c are no longer discernible, indicating its removal, leaving only the absorbance curve of the microgel. This outcome aligns with expectations, as

cyt c can only be immobilized within pVCL microgels through weak forces such as van der Waals interactions or hydrogen bonding. Expectedly, the electrostatic repulsion between pVCL and cyt c exceeds the strength of these weak forces, hindering stable immobilization. A slight decrease in microgel concentration is observed over time, evident from the lower absorbance after 5 days of dialysis compared to the pure microgel sample. This minor reduction in concentration is likely explained due to the semi-permeable membrane used, allowing not only the exchange of small dissolved molecules but also solvent molecules, leading to subtle changes in overall concentration.

Comparing the pVCL and p(VCL/NTAaa) samples, notable differences emerge. While the absorbance of microgel mixed with cyt c before dialysis appears similar, p(VCL/NTAaa) demonstrates effective retention of a large amount of cyt c (**Figure III.16b**). This outcome aligns with expectations, given the electrostatic attraction between cyt c and p(VCL/NTAaa). Over time, a decreasing intensity of the cyt c peak at 530 nm is observed, accompanied by a reduction in peak intensity at 408 nm, albeit less pronounced. The different curve shape may arise from a conformational change in immobilized cyt c compared to its free form. Prior studies have indicated that such conformational changes can alter peak intensities,[87] suggesting adsorption of cyt c to the microgels. Notably, comparing p(VCL/NTAaa) microgels with immobilized cyt c after 4 and 5 days, only minimal changes in absorbance are apparent. The curve shapes remain remarkably similar, unlike the more significant changes observed in previous days. This stability in absorbance is attributed to a similar composition of the samples after 4 and 5 days of dialysis, with the decrease in absorbance likely linked to the overall reduced concentration due to solvent diffusion, as observed in the case of pVCL microgels.

In summary, the experiments conducted illustrate the capacity of p(VCL/NTAaa) microgels to retain a substantial amount of cyt c over multiple days of dialysis, a phenomenon not observed in the case of pVCL microgels. This serves as an initial validation of the biomolecule immobilization potential of p(VCL/NTAaa). Future inquiries should prioritize the quantification of biomolecule incorporation and elucidate their release dynamics from the microgels. Overall, these findings lay the groundwork for future investigations in this domain.

4. Conclusion

The focus of this chapter was laid on synthesizing and characterizing p(VCL/NTAaa) core-shell microgels with stimuli-responsive properties. This is the first instance in which pVCL microgels have been combined with an NTA comonomer. Initially, the NTA content was determined using IR spectroscopy, followed by fundamental characterization of the microgels through DLS and ELS. Subsequently, the stimuli-responsiveness of the microgels was extensively investigated. This involved conducting temperature-dependent DLS and ELS measurements, as well as ionic strength- and pH-dependent DLS measurements.

The findings revealed that the incorporation of NTA resulted in a raised VPTT and thus EPTT of the microgels, attributed to the hydrophilicity and overall charge of NTA. Additionally, a stepwise VPT was identified, likely stemming from the microgels' inhomogeneous core-multi-shell structure with a radial increase in NTA concentration from core to shell. This inhomogeneity leads to an almost linear EPT for p(VCL/NTAaa) microgels with higher NTA concentrations due to the microgel collapse occurring in incremental steps, approximating a continuous collapse. Upon increasing the NTA content in p(VCL/NTAaa) microgels, various changes in stimuli-responsiveness were noted. The higher number of charges leads to enhanced electrostatic stabilization of the microgels, as well as a greater size dependence on ionic strength and pH. Notably, significant alterations in microgel size occurred around the pK_a of the incorporated NTA: The higher number of deprotonated carboxylic groups at the pK_a leads to increased electrostatic repulsion between polymer chains, consequently causing microgel swelling.

NMR relaxometry analysis in water revealed increasing chain mobility with higher NTA content, suggesting greater hydrophilicity. Additionally, an increase in the number of shell protons indicated a thicker shell. Notably, microgel morphology analysis unveiled distinct areas within the microgel structure: a core region followed by inner and outer shells.

AFM and SEM analysis confirmed a visible core-shell structure, which was particularly pronounced at higher NTA concentrations. Additionally, using the STEM detector, a fuzzy shell covering a denser core was observed for all microgels. This observation is attributed to a lower density of polymer chains in the microgel shell, which is connected to a lower amount of crosslinking due to the high reactivity of the crosslinker BIS. Reaction calorimetry revealed

that the comonomer containing NTA exhibited a notably slower reaction rate in comparison to BIS, as well as the primary monomer VCL. The delay in reaction kinetics, attributed to the presence of the NTA-monomer, contributed to a prolonged duration of the microgel synthesis. These findings suggest that the final microgels comprise a core rich in BIS and VCL, followed by an inner shell rich in VCL with minimal NTA content. The outer shell contains a higher proportion of NTA, contributing to the observed core-shell morphology.

The results from cytotoxicity and cell proliferation tests indicate that the p(VCL/NTAaa) microgels hold promise for applications in biomaterials. Specifically, these microgels displayed the ability to take up the positively charged protein cyt c through electrostatic interactions. Notably, this chapter reveals that p(VCL/NTAaa) microgels can retain a substantial amount of cyt c even after several days of dialysis, a behavior not observed in pVCL microgels. This retention capability underscores the potential of p(VCL/NTAaa) microgels for sustained and effective uptake of biomacromolecules such as proteins.

5. References

(1) Sommerfeld, I. K.; Malyaran, H.; Neuss, S.; Demco, D. E.; Pich, A. Multi-Responsive Core-Shell Microgels Functionalized by Nitrilotriacetic Acid. *Biomacromolecules* **2024**, *25*, 903–923.

(2) Bysell, H.; Månsson, R.; Hansson, P.; Malmsten, M. Microgels and Microcapsules in Peptide and Protein Drug Delivery. *Adv. Drug Delivery Rev.* **2011**, *63*, 1172–1185.

(3) Malmsten, M.; Bysell, H.; Hansson, P. Biomacromolecules in Microgels — Opportunities and Challenges for Drug Delivery. *Curr. Opin. Colloid Interface Sci.* **2010**, *15*, 435–444.

(4) Klinger, D.; Landfester, K. Stimuli-Responsive Microgels for the Loading and Release of Functional Compounds: Fundamental Concepts and Applications. *Polymer* **2012**, *53*, 5209–5231.

(5) Echeverria, C.; Fernandes, S. N.; Godinho, M. H.; Borges, J. P.; Soares, P. I. P. Functional Stimuli-Responsive Gels: Hydrogels and Microgels. *Gels* **2018**, *4*, 54.

(6) Schroeder, R.; Richtering, W.; Potemkin, I. I.; Pich, A. Stimuli-Responsive Zwitterionic Microgels with Covalent and Ionic Cross-Links. *Macromolecules* **2018**, *51*, 6707–6716.

(7) Hoare, T.; Pelton, R. Impact of Microgel Morphology on Functionalized Microgel-Drug Interactions. *Langmuir* **2008**, *24*, 1005–1012.

(8) Pérez-Chávez, N. A.; Albesa, A. G.; Longo, G. S. Thermodynamic Theory of Multiresponsive Microgel Swelling. *Macromolecules* **2021**, *54*, 2936–2947.

(9) Hussmann, L.; Belthle, T.; Demco, D. E.; Fechete, R.; Pich, A. Stimuli-Responsive Microgels with Cationic Moieties: Characterization and Interaction with E. Coli Cells. *Soft Matter* **2021**, *17*, 8678–8692.

(10) Nur, H.; Pinkrah, V. T.; Mitchell, J. C.; Benée, L. S.; Snowden, M. J. Synthesis and Properties of Polyelectrolyte Microgel Particles. *Adv. Colloid Interface Sci.* **2010**, *158*, 15–20.

(11) Morris, G. E.; Vincent, B.; Snowden, M. J. Adsorption of Lead Ions onto N-Isopropylacrylamide and Acrylic Acid Copolymer Microgels. *JCIS* **1997**, *190*, 198–205.

(12) Wen, Q.; Vincelli, A. M.; Pelton, R. Cationic Polyvinylamine Binding to Anionic Microgels Yields Kinetically Controlled Structures. *JCIS* **2012**, *369*, 223–230.

(13) Das, M.; Mardyani, S.; Chan, W. C. W.; Kumacheva, E. Biofunctionalized pH-Responsive Microgels for Cancer Cell Targeting: Rational Design. *Adv. Mater.* **2006**, *18*, 80–83.

(14) Kureha, T.; Shibamoto, T.; Matsui, S.; Sato, T.; Suzuki, D. Investigation of Changes in the Microscopic Structure of Anionic Poly(N-isopropylacrylamide-co-Acrylic Acid) Microgels in the

Presence of Cationic Organic Dyes toward Precisely Controlled Uptake/Release of Low-Molecular-Weight Chemical Compound. *Langmuir* **2016**, *32*, 4575–4585.

(15) Smith, M. H.; Lyon, L. A. Tunable Encapsulation of Proteins within Charged Microgels. *Macromolecules* **2011**, *44*, 8154–8160.

(16) Mizrahi, B.; Irusta, S.; McKenna, M.; Stefanescu, C.; Yedidsion, L.; Myint, M.; Langer, R.; Kohane, D. S. Microgels for Efficient Protein Purification. *Adv. Mater.* **2011**, *23*, H258-62.

(17) Heida, T.; Köhler, T.; Kaufmann, A.; Männel, M. J.; Thiele, J. Cell-Free Protein Synthesis in Bifunctional Hyaluronan Microgels: A Strategy for In Situ Immobilization and Purification of His-Tagged Proteins. *ChemSystemsChem* **2020**, *2*, e1900058.

(18) Köhler, T.; Heida, T.; Hoefgen, S.; Weigel, N.; Valiante, V.; Thiele, J. Cell-Free Protein Synthesis and In Situ Immobilization of deGFP-MatB in Polymer Microgels for Malonate-to-Malonyl CoA Conversion. *RSC Adv.* **2020**, *10*, 40588–40596.

(19) Li, C.; Wu, G.; Ma, R.; Liu, Y.; Liu, Y.; Lv, J.; An, Y.; Shi, L. Nitrilotriacetic Acid (NTA) and Phenylboronic Acid (PBA) Functionalized Nanogels for Efficient Encapsulation and Controlled Release of Insulin. *ACS Biomater. Sci. Eng.* **2018**, *4*, 2007–2017.

(20) Vinogradov, S. V. Colloidal Microgels in Drug Delivery Applications. *Curr. Pharm. Des.* **2006**, *12*, 4703–4712.

(21) Smeets, N. M. B.; Hoare, T. Designing Responsive Microgels for Drug Delivery Applications. *J. Polym. Sci. Part A: Polym. Chem.* **2013**, *51*, 3027–3043.

(22) Al Enezy-Ulbrich, M. A.; Malyaran, H.; Lange, R. D.; Labude, N.; Plum, R.; Rütten, S.; Terefenko, N.; Wein, S.; Neuss, S.; Pich, A. Impact of Reactive Amphiphilic Copolymers on Mechanical Properties and Cell Responses of Fibrin-Based Hydrogels. *Adv. Funct. Mater.* **2020**, *30*, 2003528.

(23) Brinkmann, J.; Malyaran, H.; Enezy-Ulbrich, M. A. A.; Jung, S.; Radermacher, C.; Buhl, E. M.; Pich, A.; Neuss, S. Assessment of Fibrin-Based Hydrogels Containing a Fibrin-Binding Peptide to Tune Mechanical Properties and Cell Responses. *Macromol. Mater. Eng.* **2023**, *308*, 2200678.

(24) Jung, S. A.; Malyaran, H.; Demco, D. E.; Manukanc, A.; Häser, L. S.; Kučikas, V.; van Zandvoort, M.; Neuss, S.; Pich, A. Fibrin-Dextran Hydrogels with Tunable Porosity and Mechanical Properties. *Biomacromolecules* **2023**, *24*, 3972–3984.

(25) Beynon, R. J.; Easterby, J. S. *Buffer Solutions*, 1st ed.; Oxford University Press, 1996.

(26) R. R. Ernst, G. Bodenhausen u. A. Wokaun. *Principles of Nuclear Magnetic Resonance in One and Two Dimensions*; Clarendon Press, Oxford, 1987.

(27) Kimmich, R. *NMR: Tomography, Diffusometry, Relaxometry*; Springer International Publishing: Berlin, Heidelberg, 1997.

(28) Belthle, T.; Demco, D. E.; Pich, A. Nanostructuring the Interior of Stimuli-Responsive Microgels by N-Vinylimidazoles Quaternized with Hydrophobic Alkyl Chains. *Macromolecules* **2022**, *55*, 844–861.

(29) Stejskal, E. O.; Tanner, J. E. Spin Diffusion Measurements: Spin Echoes in the Presence of a Time-Dependent Field Gradient. *J. Chem. Phys.* **1965**, *42*, 288–292.

(30) Callaghan, P. T. *Principles of Nuclear Magnetic Resonance Microscopy*, 1st published in paperback, impr. 1; Clarendon Press: Oxford, 1991.

(31) Gau, E.; Mate, D. M.; Zou, Z.; Oppermann, A.; Töpel, A.; Jakob, F.; Wöll, D.; Schwaneberg, U.; Pich, A. Sortase-Mediated Surface Functionalization of Stimuli-Responsive Microgels. *Biomacromolecules* **2017**, *18*, 2789–2798.

(32) Saha, P.; Santi, M.; Frenken, M.; Palanisamy, A. R.; Ganguly, R.; Singha, N. K.; Pich, A. Dual-Temperature-Responsive Microgels from a Zwitterionic Functional Graft Copolymer with Superior Protein Repelling Property. *ACS Macro Lett.* **2020**, *9*, 895–901.

(33) Cortez-Lemus, N. A.; Licea-Claverie, A. Poly(N-Vinylcaprolactam), a Comprehensive Review on a Thermoresponsive Polymer Becoming Popular. *Prog. Polym. Sci.* **2016**, *53*, 1–51.

(34) Hellweg, T.; Dewhurst, C. D.; Eimer, W.; Kratz, K. PNIPAM-co-Polystyrene Core-Shell Microgels: Structure, Swelling Behavior, and Crystallization. *Langmuir* **2004**, *20*, 4330–4335.

(35) Karg, M.; Pastoriza-Santos, I.; Rodriguez-González, B.; Klitzing, R. von; Wellert, S.; Hellweg, T. Temperature, pH, and Ionic Strength Induced Changes of the Swelling Behavior of PNIPAM-Poly(allylacetic Acid) Copolymer Microgels. *Langmuir* **2008**, *24*, 6300–6306.

(36) Kratz, K.; Hellweg, T.; Eimer, W. Influence of Charge Density on the Swelling of Colloidal Poly(N-isopropylacrylamide-co-Acrylic Acid) Microgels. *Colloids Surf., A* **2000**, *170*, 137–149.

(37) Košovan, P.; Richter, T.; Holm, C. Modeling of Polyelectrolyte Gels in Equilibrium with Salt Solutions. *Macromolecules* **2015**, *48*, 7698–7708.

(38) Del Monte, G.; Truzzolillo, D.; Camerin, F.; Ninarello, A.; Chauveau, E.; Tavagnacco, L.; Gnan, N.; Rovigatti, L.; Sennato, S.; Zaccarelli, E. Two-Step Deswelling in the Volume Phase Transition of Thermoresponsive Microgels. *PNAS* **2021**, *118*, e2109560118.

(39) Daly, E.; Saunders, B. R. A Study of the Effect of Electrolyte on the Swelling and Stability of Poly(N-isopropylacrylamide) Microgel Dispersions. *Langmuir* **2000**, *16*, 5546–5552.

(40) Hertle, Y.; Hellweg, T. Thermoresponsive copolymer microgels. *J. Mater. Chem. B* **2013**, *1*, 5874–5885.

(41) Friesen, S.; Hannappel, Y.; Kakorin, S.; Hellweg, T. Accounting for Cooperativity in the Thermotropic Volume Phase Transition of Smart Microgels. *Gels* **2021**, *7*.

(42) Wu, C.; Zhou, S. Volume Phase Transition of Swollen Gels: Discontinuous or Continuous? *Macromolecules* **1997**, *30*, 574–576.

(43) Belthle, T.; Lantzius-Beninga, M.; Pich, A. Pre- and Post-Functionalization of Thermoresponsive Cationic Microgels with Ionic Liquid Moieties Carrying Different Counterions. *Polym. Chem.* **2023**, *14*, 848–861.

(44) Seuss, M.; Schmolke, W.; Drechsler, A.; Fery, A.; Seiffert, S. Core-Shell Microgels with Switchable Elasticity at Constant Interfacial Interaction. *ACS Appl. Mater. Interfaces* **2016**, *8*, 16317–16327.

(45) Gernandt, J.; Frenning, G.; Richtering, W.; Hansson, P. A Model Describing the Internal Structure of Core/Shell Hydrogels. *Soft Matter* **2011**, *7*, 10327.

(46) Richtering, W.; Pich, A. The Special Behaviours of Responsive Core–Shell Nanogels. *Soft Matter* **2012**, *8*, 11423.

(47) Chang, B.; Sha, X.; Guo, J.; Jiao, Y.; Wang, C.; Yang, W. Thermo and pH Dual Responsive, Polymer Shell Coated, Magnetic Mesoporous Silica Nanoparticles for Controlled Drug Release. *J. Mater. Chem.* **2011**, *21*, 9239.

(48) Jones, C. D.; Lyon, L. A. Synthesis and Characterization of Multiresponsive Core−Shell Microgels. *Macromolecules* **2000**, *33*, 8301–8306.

(49) Daly, E.; Saunders, B. R. Temperature–Dependent Electrophoretic Mobility and Hydrodynamic Radius Measurements of Poly(N-Isopropylacrylamide) Microgel Particles: Structural Insights. *Phys. Chem. Chem. Phys.* **2000**, *2*, 3187–3193.

(50) Pelton, R. H.; Pelton, H. M.; Morphesis, A.; Rowell, R. L. Particle Sizes and Electrophoretic Mobilities of Poly(N-isopropylacrylamide) Latex. *Langmuir* **1989**, *5*, 816–818.

(51) López-León, T.; Ortega-Vinuesa, J. L.; Bastos-Gonzalez, D.; Elaïssari, A. Cationic and Anionic Poly(N-isopropylacrylamide) Based Submicron Gel Particles: Electrokinetic Properties and Colloidal Stability. *J. Phys. Chem. B* **2006**, *110*, 4629–4636.

(52) Hoare, T.; Pelton, R. Functional Group Distributions in Carboxylic Acid Containing Poly(N-isopropylacrylamide) Microgels. *Langmuir* **2004**, *20*, 2123–2133.

(53) Rasmusson, M.; Vincent, B.; Marston, N. The Electrophoresis of Poly(N-isopropylacrylamide) Microgel Particles. *Colloid Polym. Sci.* **2000**, *278*, 253–258.

(54) Karg, M.; Pich, A.; Hellweg, T.; Hoare, T.; Lyon, L. A.; Crassous, J. J.; Suzuki, D.; Gumerov, R. A.; Schneider, S.; Potemkin, I. I.; Richtering, W. Nanogels and Microgels: From Model Colloids to Applications, Recent Developments, and Future Trends. *Langmuir* **2019**, *35*, 6231–6255.

(55) Routh, A. F.; Vincent, B. Salt-Induced Homoaggregation of Poly(N-isopropylacrylamide) Microgels. *Langmuir* **2002**, *18*, 5366–5369.

(56) Amalvy, J. I.; Wanless, E. J.; Li, Y.; Michailidou, V.; Armes, S. P.; Duccini, Y. Synthesis and Characterization of Novel pH-Responsive Microgels Based on Tertiary Amine Methacrylates. *Langmuir* **2004**, *20*, 8992–8999.

(57) Irving, H. M.; Miles, M. G.; Pettit, L. D. A Study of Some Problems in Determining the Stoicheiometric Proton Dissociation Constants of Complexes by Potentiometric Titrations Using a Glass Electrode. *Anal. Chim. Acta* **1967**, *38*, 475–488.

(58) Katchalsky, A.; Michaeli, I. Polyelectrolyte Gels in Salt Solutions. *J. Polym. Sci.* **1955**, *15*, 69–86.

(59) Bromberg, L.; Temchenko, M.; Hatton, T. A. Smart Microgel Studies. Polyelectrolyte and Drug-Absorbing Properties of Microgels from Polyether-Modified Poly(acrylic acid). *Langmuir* **2003**, *19*, 8675–8684.

(60) Kodama, H.; Miyajima, T.; Mori, M.; Takahashi, M.; Nishimura, H.; Ishiguro, S. A Unified Analytical Treatment of the Acid-Dissociation Equilibria of Weakly Acidic Linear Polyelectrolytes and the Conjugate Acids of Weakly Basic Linear Polyelectrolytes. *Colloid Polym. Sci.* **1997**, *275*, 938–945.

(61) Wu, B.; Chassé, W.; Peters, R.; Brooijmans, T.; Dias, A. A.; Heise, A.; Duxbury, C. J.; Kentgens, A. P. M.; Brougham, D. F.; Litvinov, V. M. Network Structure in Acrylate Systems: Effect of Junction Topology on Cross-Link Density and Macroscopic Gel Properties. *Macromolecules* **2016**, *49*, 6531–6540.

(62) Guillermo, A.; Cohen Addad, J. P.; Bazile, J. P.; Duracher, D.; Elaissari, A.; Pichot, C. NMR Investigations into Heterogeneous Structures of Thermosensitive Microgel Particles. *J. Polym. Sci., Part B: Polym. Phys.* **2000**, *38*, 889–898.

(63) Lipari, G.; Szabo, A. Model-Free Approach to the Interpretation of Nuclear Magnetic Resonance Relaxation in Macromolecules. 1. Theory and Range of Validity. *JACS* **1982**, *104*, 4546–4559.

(64) Schneider, F.; Balaceanu, A.; Feoktystov, A.; Pipich, V.; Wu, Y.; Allgaier, J.; Pyckhout-Hintzen, W.; Pich, A.; Schneider, G. J. Monitoring the Internal Structure of Poly(N-vinylcaprolactam) Microgels with Variable Cross-Link Concentration. *Langmuir* **2014**, *30*, 15317–15326.

(65) Balaceanu, A.; Demco, D. E.; Möller, M.; Pich, A. Microgel Heterogeneous Morphology Reflected in Temperature-Induced Volume Transition and 1H High-Resolution Transverse Relaxation NMR. The Case of Poly(N-vinylcaprolactam) Microgel. *Macromolecules* **2011**, *44*, 2161–2169.

(66) Kröger, L. C.; Kopp, W. A.; Leonhard, K. Prediction of Chain Propagation Rate Constants of Polymerization Reactions in Aqueous NIPAM/BIS and VCL/BIS Systems. *J. Phys. Chem. B* **2017**, *121*, 2887–2895.

(67) Grabowski, F.; Petrovskii, V. S.; Fink, F.; Demco, D. E.; Herres-Pawlis, S.; Potemkin, I. I.; Pich, A. Anisotropic Microgels by Supramolecular Assembly and Precipitation Polymerization of Pyrazole-Modified Monomers. *Adv. Sci.* **2022**, *9*, e2204853.

(68) Scotti, A.; Bochenek, S.; Brugnoni, M.; Fernandez-Rodriguez, M. A.; Schulte, M. F.; Houston, J. E.; Gelissen, A. P. H.; Potemkin, I. I.; Isa, L.; Richtering, W. Exploring the Colloid-to-Polymer Transition for Ultra-Low Crosslinked Microgels from Three to Two Dimensions. *Nat. Commun.* **2019**, *10*, 1418.

(69) Mourran, A.; Wu, Y.; Gumerov, R. A.; Rudov, A. A.; Potemkin, I. I.; Pich, A.; Möller, M. When Colloidal Particles Become Polymer Coils. *Langmuir* **2016**, *32*, 723–730.

(70) Rey, M.; Fernandez-Rodriguez, M. A.; Karg, M.; Isa, L.; Vogel, N. Poly-N-isopropylacrylamide Nanogels and Microgels at Fluid Interfaces. *Acc. Chem. Res.* **2020**, *53*, 414–424.

(71) Höper, R.; Gesang, T.; Possart, W.; Hennemann, O.-D.; Boseck, S. Imaging Elastic Sample Properties with an Atomic Force Microscope Operating in the Tapping Mode. *Ultramicroscopy* **1995**, *60*, 17–24.

(72) Melle, A.; Balaceanu, A.; Kather, M.; Wu, Y.; Gau, E.; Sun, W.; Huang, X.; Shi, X.; Karperien, M.; Pich, A. Stimuli-Responsive Poly(N-vinylcaprolactam-co-2-Methoxyethyl Acrylate) Core-Shell Microgels: Facile Synthesis, Modulation of Surface Properties and Controlled Internalisation into Cells. *J. Mater. Chem. B* **2016**, *4*, 5127–5137.

(73) Woodward, N. C.; Chowdhry, B. Z.; Snowden, M. J.; Leharne, S. A.; Griffiths, P. C.; Winnington, A. L. Calorimetric Investigation of the Influence of Cross-Linker Concentration on the Volume Phase Transition of Poly(N-isopropylacrylamide) Colloidal Microgels. *Langmuir* **2003**, *19*, 3202–3211.

(74) Fernández-Barbero, A.; Suárez, I. J.; Sierra-Martín, B.; Fernández-Nieves, A.; las Nieves, F. J. de; Marquez, M.; Rubio-Retama, J.; López-Cabarcos, E. Gels and Microgels for Nanotechnological Applications. *Adv. Colloid Interface Sci.* **2009**, *147-148*, 88–108.

(75) Xia, X.; Hu, Z. Synthesis and Light Scattering Study of Microgels with Interpenetrating Polymer Networks. *Langmuir* **2004**, *20*, 2094–2098.

(76) Samuels, R. J. Application of Refractive Index Measurements to Polymer Analysis. *J. Appl. Polym. Sci.* **1981**, *26*, 1383–1412.

(77) Janssen, F. A. L.; Kather, M.; Kröger, L. C.; Mhamdi, A.; Leonhard, K.; Pich, A.; Mitsos, A. Synthesis of Poly(N-vinylcaprolactam)-Based Microgels by Precipitation Polymerization: Process Modeling and Experimental Validation. *Ind. Eng. Chem. Res.* **2017**, *56*, 14545–14556.

(78) Janssen, F. A.; Ksiazkiewicz, A.; Kather, M.; Kröger, L. C.; Mhamdi, A.; Leonhard, K.; Pich, A.; Mitsos, A. Kinetic Modeling of Precipitation Terpolymerization for Functional Microgels. *28th European Symposium on Computer Aided Process Engineering*; Computer Aided Chemical Engineering; Elsevier, 2018; pp 109–114.

(79) Nevolianis, T.; Wolter, N.; Kaven, L. F.; Krep, L.; Huang, C.; Mhamdi, A.; Mitsos, A.; Pich, A.; Leonhard, K. Kinetic Modeling of a Poly(N-vinylcaprolactam-co-Glycidyl Methacrylate) Microgel Synthesis: A Hybrid In Silico and Experimental Approach. *Ind. Eng. Chem. Res.* **2023**, *62*, 893–902.

(80) Ross, D. D.; Joneckis, C. C.; Ordóñez, J. V.; Sisk, A. M.; Wu, R. K.; Hamburger, A. W.; Nora, R. E. Estimation of Cell Survival by Flow Cytometric Quantification of Fluorescein Diacetate/Propidium Iodide Viable Cell Number. *Cancer Res.* **1989**, *49*, 3776–3782.

(81) Jones, K. H.; Senft, J. A. An Improved Method to Determine Cell Viability by Simultaneous Staining with Fluorescein Diacetate-Propidium Iodide. *J. Histochem. Cytochem.* **1985**, *33*, 77–79.

(82) Jung, O.; Smeets, R.; Hartjen, P.; Schnettler, R.; Feyerabend, F.; Klein, M.; Wegner, N.; Walther, F.; Stangier, D.; Henningsen, A.; Rendenbach, C.; Heiland, M.; Barbeck, M.; Kopp, A. Improved In Vitro Test Procedure for Full Assessment of the Cytocompatibility of Degradable Magnesium Based on ISO 10993-5/-12. *Int. J. Mol. Sci.* **2019**, *20*, 255.

(83) Romano, M. R.; Ferrara, M.; Gatto, C.; Ferrari, B.; Giurgola, L.; D'Amato Tóthová, J. Evaluation of Cytotoxicity of Perfluorocarbons for Intraocular Use by Cytotoxicity Test In Vitro in Cell Lines and Human Donor Retina Ex Vivo. *Transl. Vis. Sci. Technol.* **2019**, *8*, 24.

(84) Baglioni, P.; Fratini, E.; Lonetti, B.; Chen, S. H. Gelation in Cytochrome C Concentrated Solutions Near the Isoelectric Point: The Anion Role. *Curr. Opin. Colloid Interface Sci.* **2004**, *9*, 38–42.

(85) Hristova, S. H.; Zhivkov, A. M. Isoelectric Point of Free and Adsorbed Cytochrome C Determined by Various Methods. *Colloids Surf. B* **2019**, *174*, 87–94.

(86) Hulko, M.; Hospach, I.; Krasteva, N.; Nelles, G. Cytochrome C Biosensor—A Model for Gas Sensing. *Sensors* **2011**, *11*, 5968–5980.

(87) Jiang, X.; Jiang, J.; Jin, Y.; Wang, E.; Dong, S. Effect of Colloidal Gold Size on the Conformational Changes of Adsorbed Cytochrome C: Probing by Circular Dichroism, UV-Visible, and Infrared Spectroscopy. *Biomacromolecules* **2005**, *6*, 46–53.

(88) Xu, W.; Rudov, A. A.; Schroeder, R.; Portnov, I. V.; Richtering, W.; Potemkin, I. I.; Pich, A. Distribution of Ionizable Groups in Polyampholyte Microgels Controls Interactions with Captured Proteins: From Blockade and "Levitation" to Accelerated Release. *Biomacromolecules* **2019**, *20*, 1578–1591.

6. Supplementary Data

Monomer Synthesis and Characterization

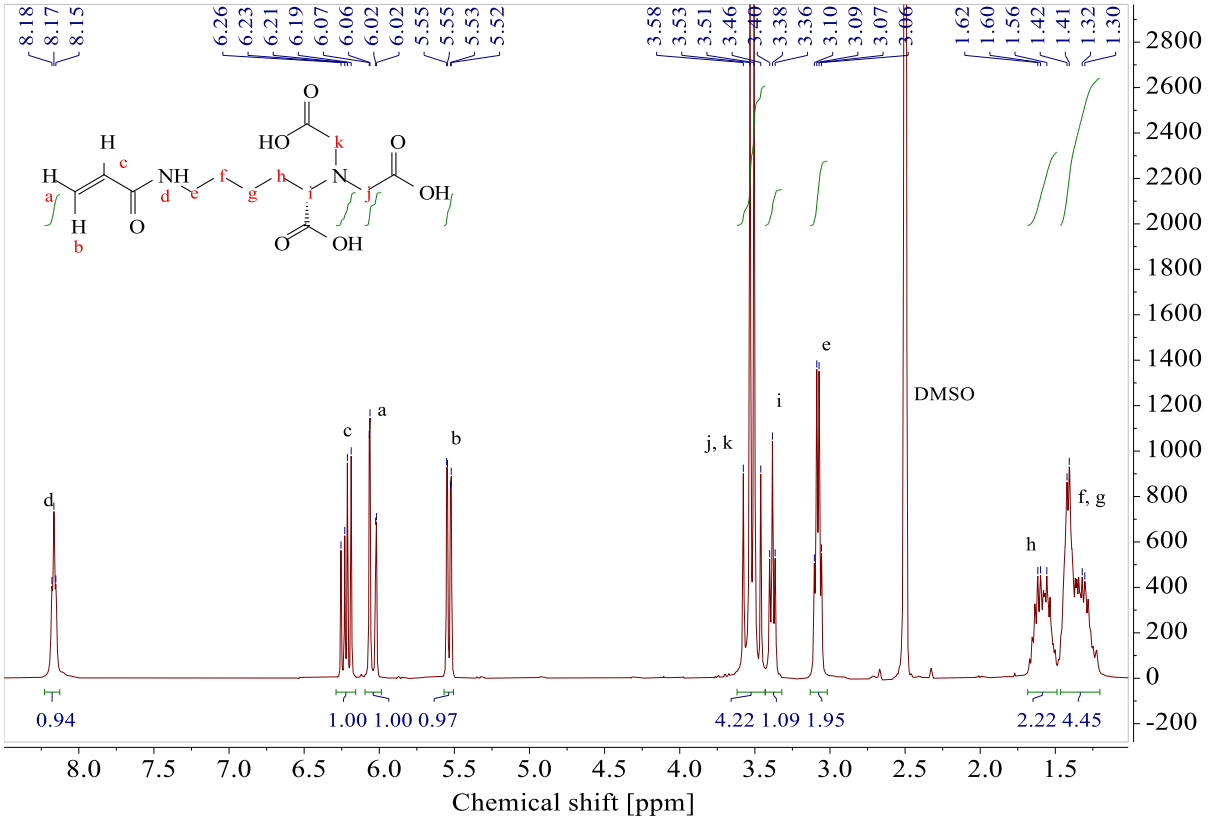

Figure SIII.1 NMR spectrum of NTAaa. ^{1}H-NMR (400 MHz, DMSO-d_6, δ = 2.50): δ = 8.16 (t, 1H, NH), 6.21 (dd, 1H, CH), 6.03 (dd, 1H, CH), 5.53 (dd, 1H, CH), 3.46 (q, 4H, CH_2), 3.32 (t, 1H, CH), 3.07 (q, 2H, CH_2), 1.56 (m, 2H, CH_2), 1.40 (m, 2H, CH_2), 1.28 (m, 2H, CH_2) ppm. *Reprinted with permission from the American Chemical Society.*[1]

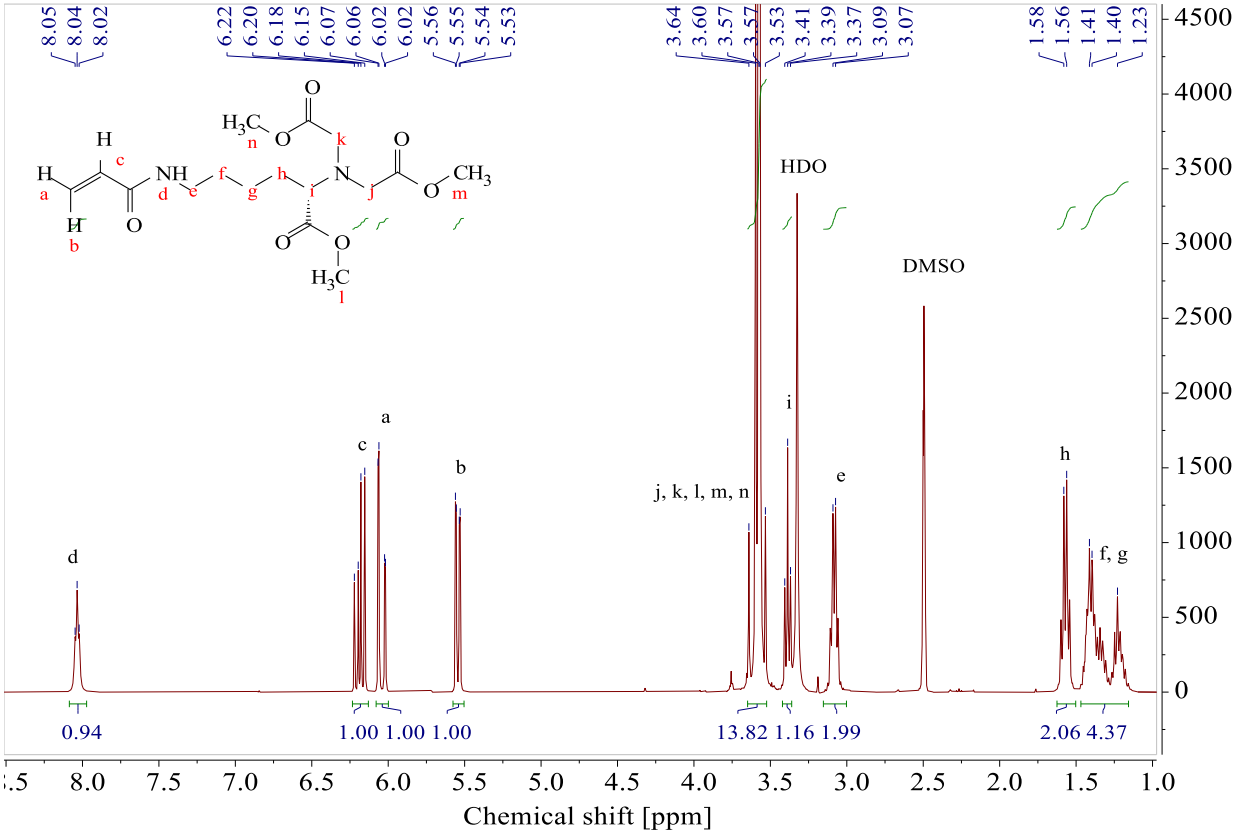

Figure SIII.2 NMR spectrum of dimethyl NTAMaa. ^{1}H-NMR (400 MHz, DMSO-d_6, δ = 2.50): δ = 8.04 (t, 1H, NH), 6.19 (dd, 1H, CH), 6.04 (dd, 1H, CH_2), 5.54 (dd, 1H, CH_2), 3.58 (m, 13H, CH_2, CH_3), 3.39 (t, 1H, CH), 3.08 (m, 2H, CH_2), 1.57 (m, 2H, CH_2), 1.40 (m, 2H, CH_2), 1.22 (m, 2H, CH_2) ppm. *Reprinted with permission from the American Chemical Society.*[1]

Temperature-Responsiveness of the Microgels

Table SIII.1 VPTT of aqueous p(VCL/NTAaa) microgels (0.5 mg mL^{-1}) with varying NTA contents (χ_{NTA}). Temperature-dependent DLS measurements of the hydrodynamic radius D_h were performed for data acquisition (5 °C to 65 °C in 2.5 °C steps). A scattering angle of θ = 90° was employed and the VPTT was determined by a sigmoidal Boltzmann fit.

χ_{NTA} [mol%]	VPTT [°C]	VPTT 1 [°C]	VPTT 2 [°C]	EPTT [°C]
0[a)]	28.2 ± 0.8[d)]	n.d.	n.d.	37.9 ± 0.6
0.5[a)]	37.2 ± 0.3[d)]	n.d.	n.d.	41.1 ± 1.0
2.0[b)]	43.4 ± 1.6[d)]	33.1 ± 0.7[e)]	53.1 ± 0.7[f)]	n.d.
2.2[c)]	50.8 ± 3.5[d)]	33.1 ± 0.6[e)]	n.d.	n.d.
11.8[c)]	40.6 ± 0.3[d)]	n.d.	n.d.	n.d.

The pH values of the 0.5 mg mL^{-1} p(VCL/NTAaa) dispersions were determined at 25 °C [a)] pH 6; [b)] pH 5; [c)] pH 4. [d)] Fit function between 5 °C and 65 °C; [e)] 5 °C and 47.5 °C; [f)] 40 °C and 65 °C; n.d. = not determined.

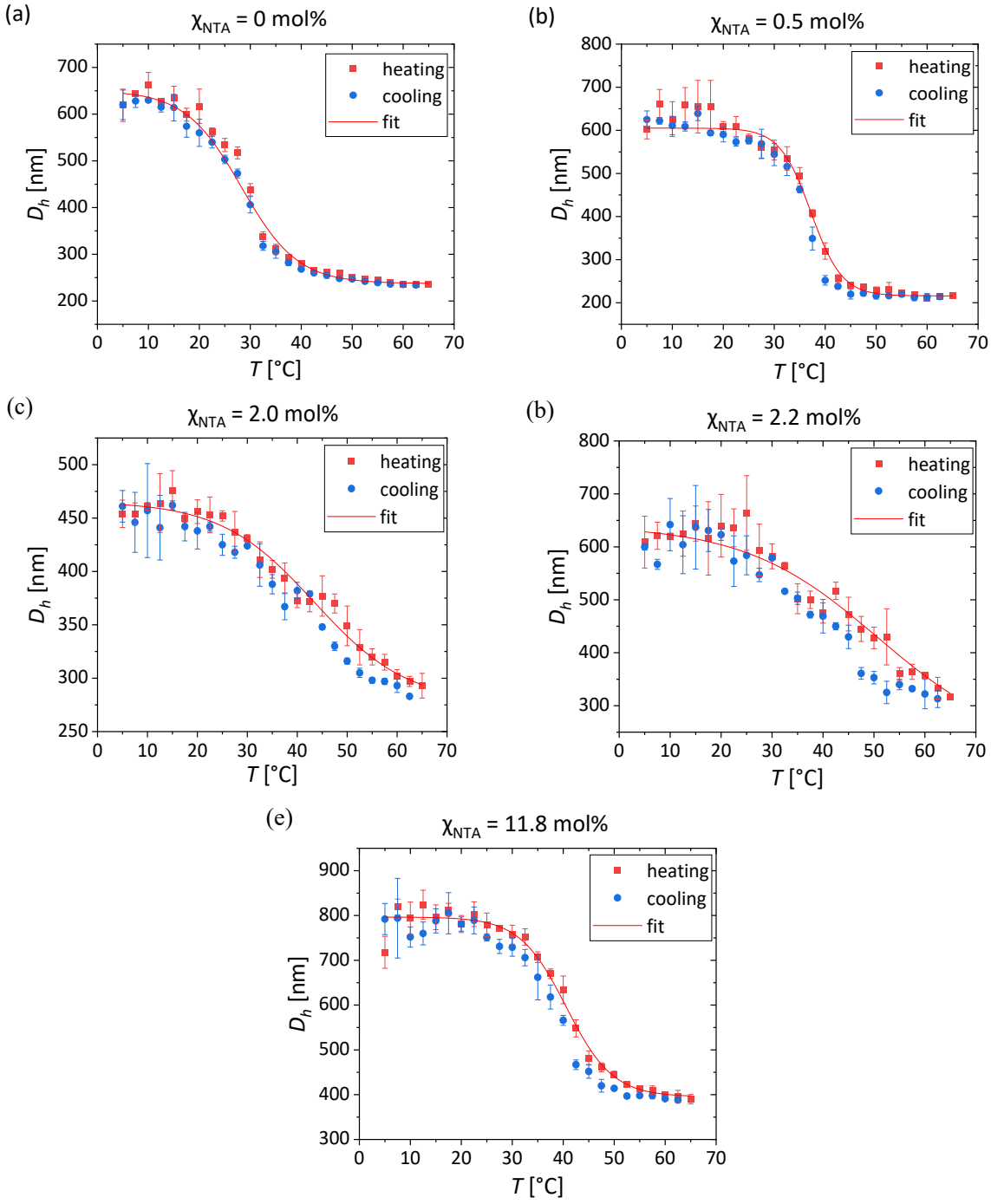

Figure SIII.3 The D_h of microgels was examined regarding its temperature-dependence, through DLS measurements conducted with a scattering angle of θ = 90° in H_2O. Results for p(VCL/NTAaa) microgels with varying comonomer content are presented: χ_{NTA} = (a) 0 mol%, (b) 0.5 mol%, (c) 2.0 mol%, (d) 2.2 mol%, (e) 11.8 mol%. A sigmoidal Boltzmann function was used for fitting the data of each heating cycle. Resultant VPTTs are (a) 28.2 ± 0.8 °C, (b) 37.2 ± 0.3 °C, (c) 43.4 ± 1.6 °C, (d) 50.8 ± 3.5 °C, and (e) 40.6 ± 0.3 °C with degrees of determination of R^2 = (a) 0.999(7), (b) 0.994, (c) 0.989, (d) 0.992, and (e) 0.998. *Reprinted with permission from the American Chemical Society*[1] *with minor modifications.*

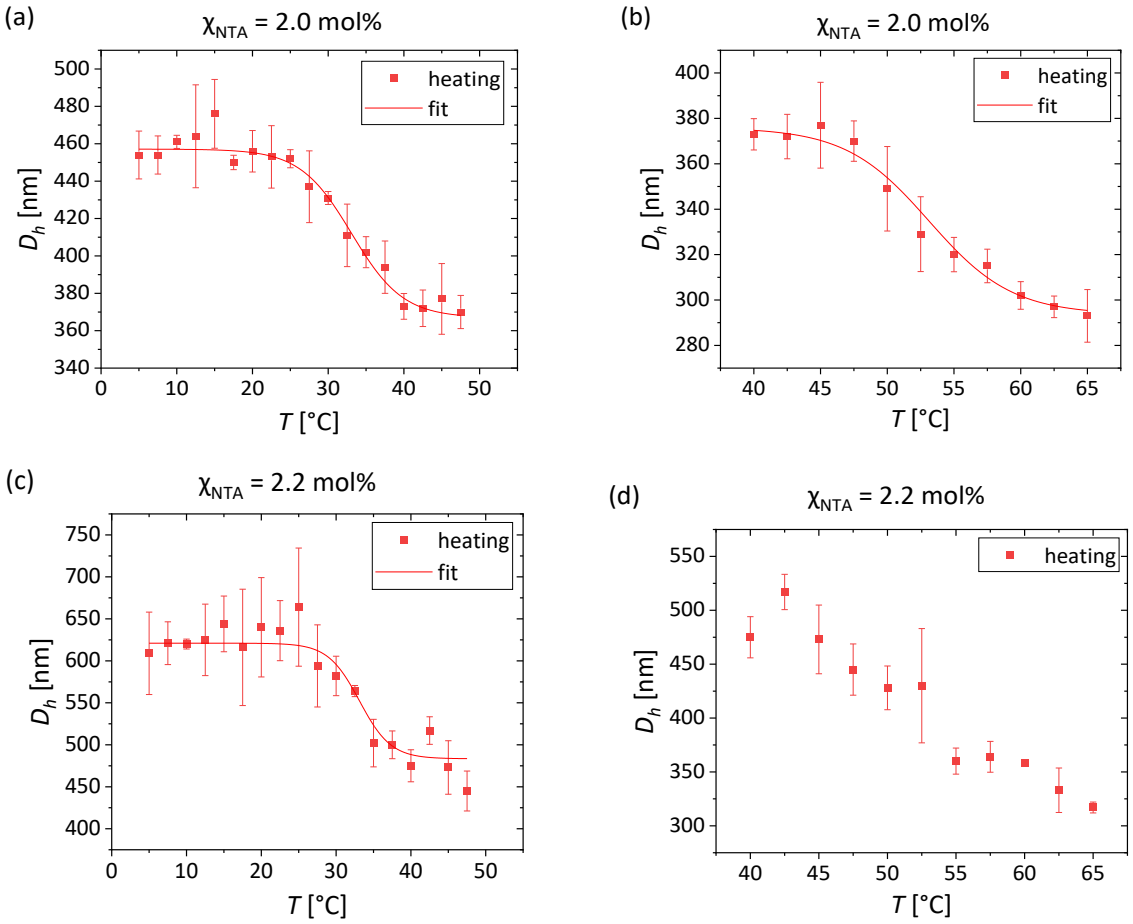

Figure SIII.4 The D_h of microgels was examined regarding its temperature-dependence, through DLS measurements conducted with a scattering angle of θ = 90° in H_2O. Results for p(VCL/NTAaa) microgels with varying comonomer content are presented: χ_{NTA} = (a,b) 2.0 mol% and (c,d) 2.2 mol%. If possible, a sigmoidal Boltzmann function was used for fitting the data of each heating cycle. Resultant VPTTs are (a) 33.1 ± 0.7, (b) 53.1 ± 0.7, and (c) 33.1 ± 0.6 with degrees of determination of R^2 = (a) 0.979, (b) 0.990, and (c) 0.948. *Reprinted with permission from the American Chemical Society*[1] *with minor modifications.*

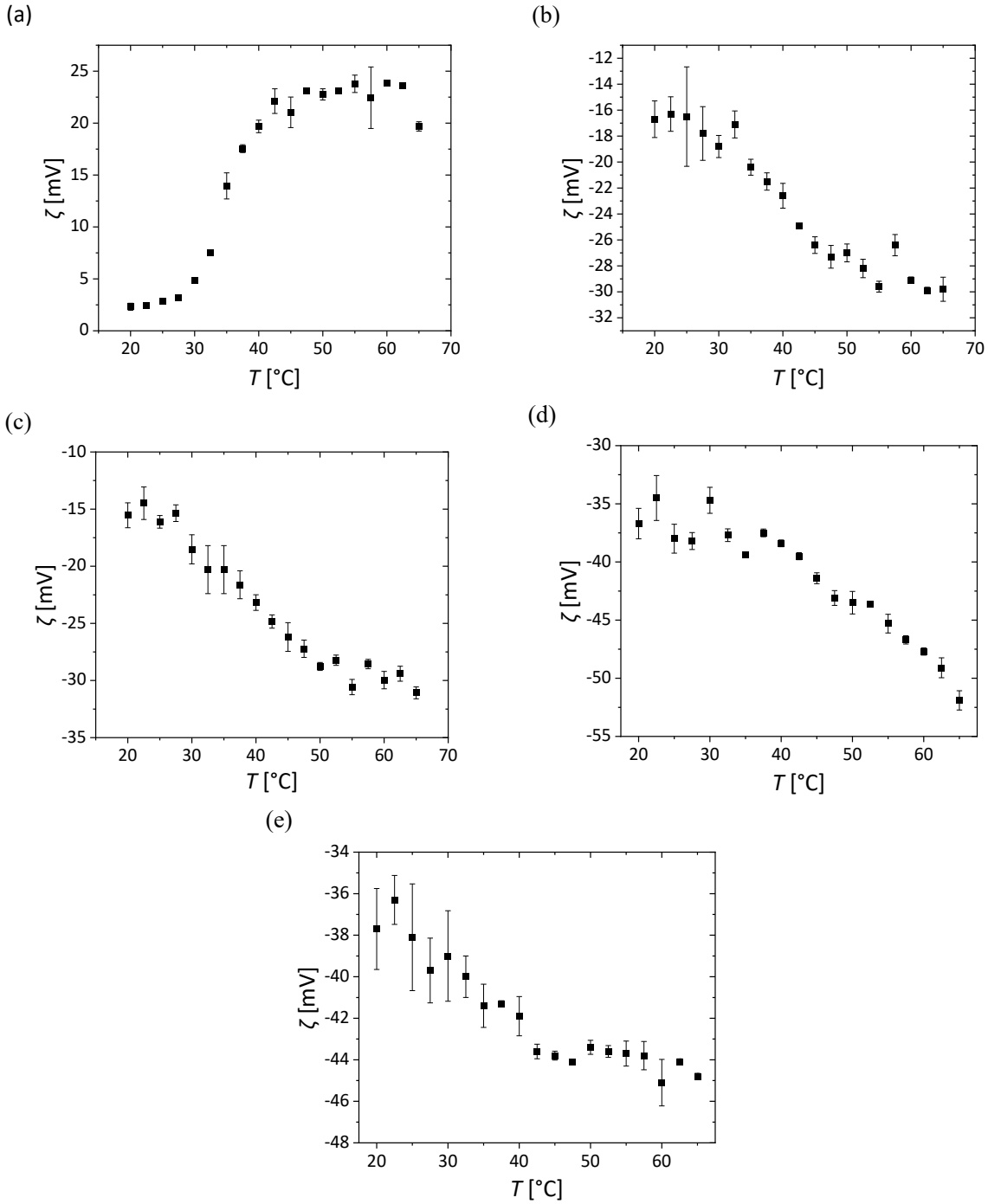

Figure SIII.5 The zeta potential (ζ) of microgels was examined regarding its temperature dependence, obtained through ELS measurements, carried out with a scattering angle of θ = 12.8° in H_2O. p(VCL/NTAaa) microgels containing different χ_{NTA} = (a) 0 mol% (b) 0.5 mol%, (c) 2.0 mol%, (d) 2.2 mol%, and (e) 11.8 mol%. *Reprinted with permission from the American Chemical Society*[1] *with minor modifications.*

^{1}H Transverse Relaxation Measurements for Analysis of the Microgel Morphology

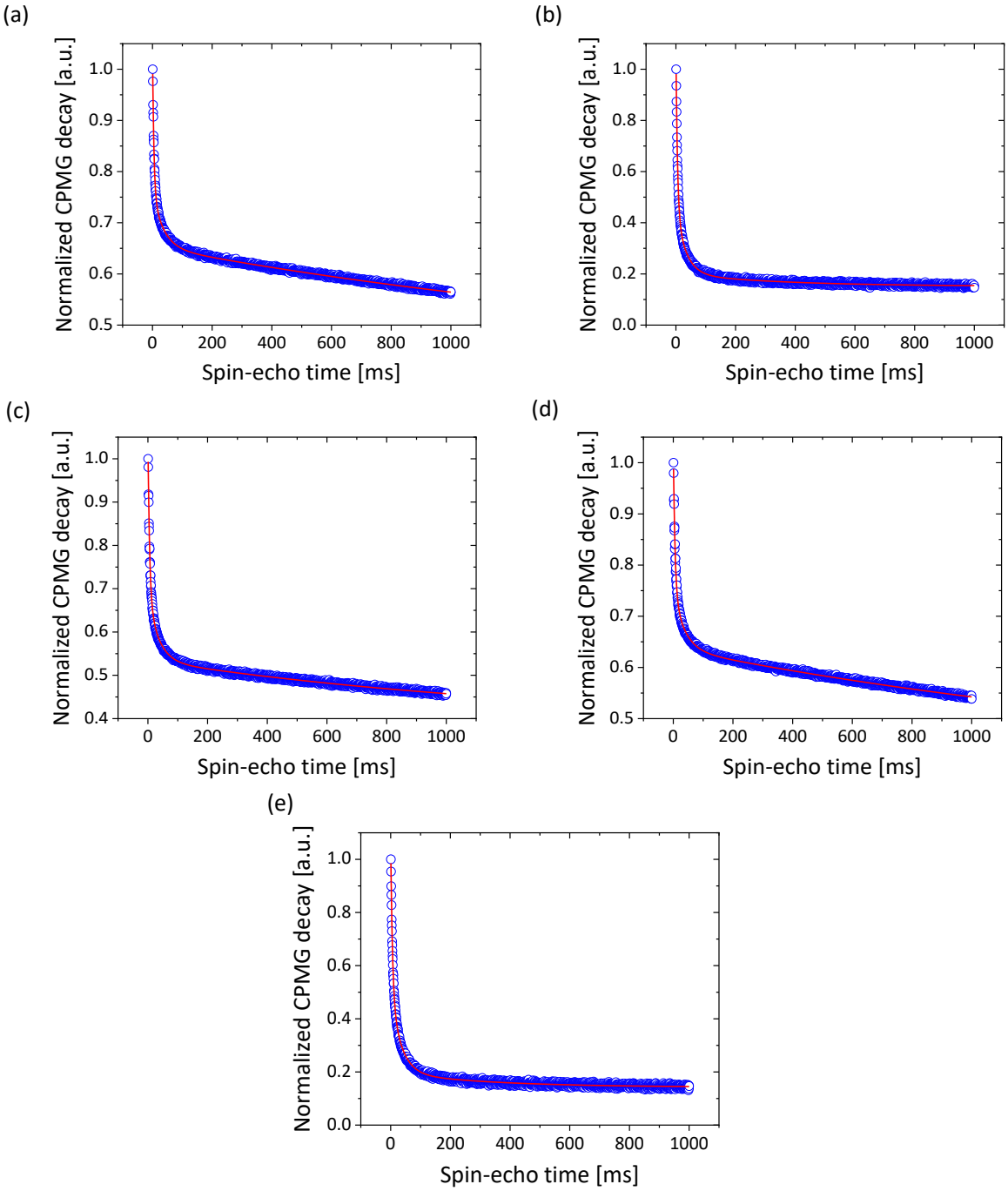

Figure SIII.6 Normalized ^{1}H NMR spin-echo decays of p(VCL/NTAaa) with χ_{NTA} = (a) 0 mol%, (b) 0.5 mol%, (c) 2.0 mol%, (d) 2.2 mol% and (e) 11.8 mol%. Samples were measured with a CPMG pulse sequence at 24 °C in D_2O with a microgel concentration of 5 mg mL^{-1}. All data were fitted using a three-phase exponential fit with degrees of determination of R^2 = (a) 0.998, (b) 0.995, (c) 0.997, (d) 0.997, and (e) 0.998. *Reprinted with permission from the American Chemical Society*[1] *with minor modifications.*

Atomic Force Microscopy of the Microgels

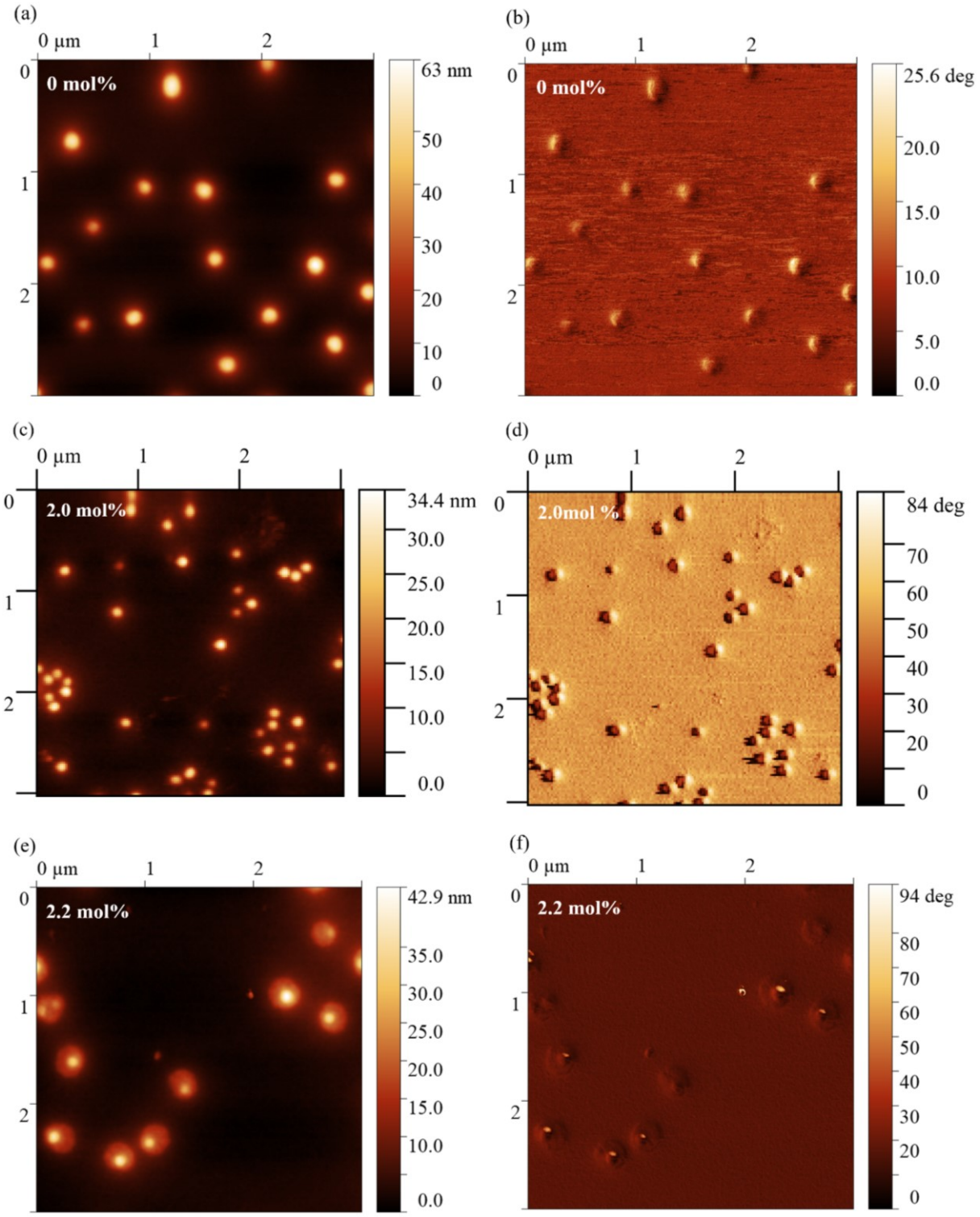

Figure SIII.7 AFM images of p(VCL/NTAaa) microgels containing comonomer contents χ_{NTA} of (a, b) 0 mol%, (c, d) 2.0 mol% and (e, f) 2.2 mol% %: (a, c, d) height profiles, (b, d, f) phase images. The samples were spin-coated onto plasma-activated Si wafers. *Reprinted with permission from the American Chemical Society*[1] *with minor modifications.*

Scanning Electron Microscopy of the Microgels

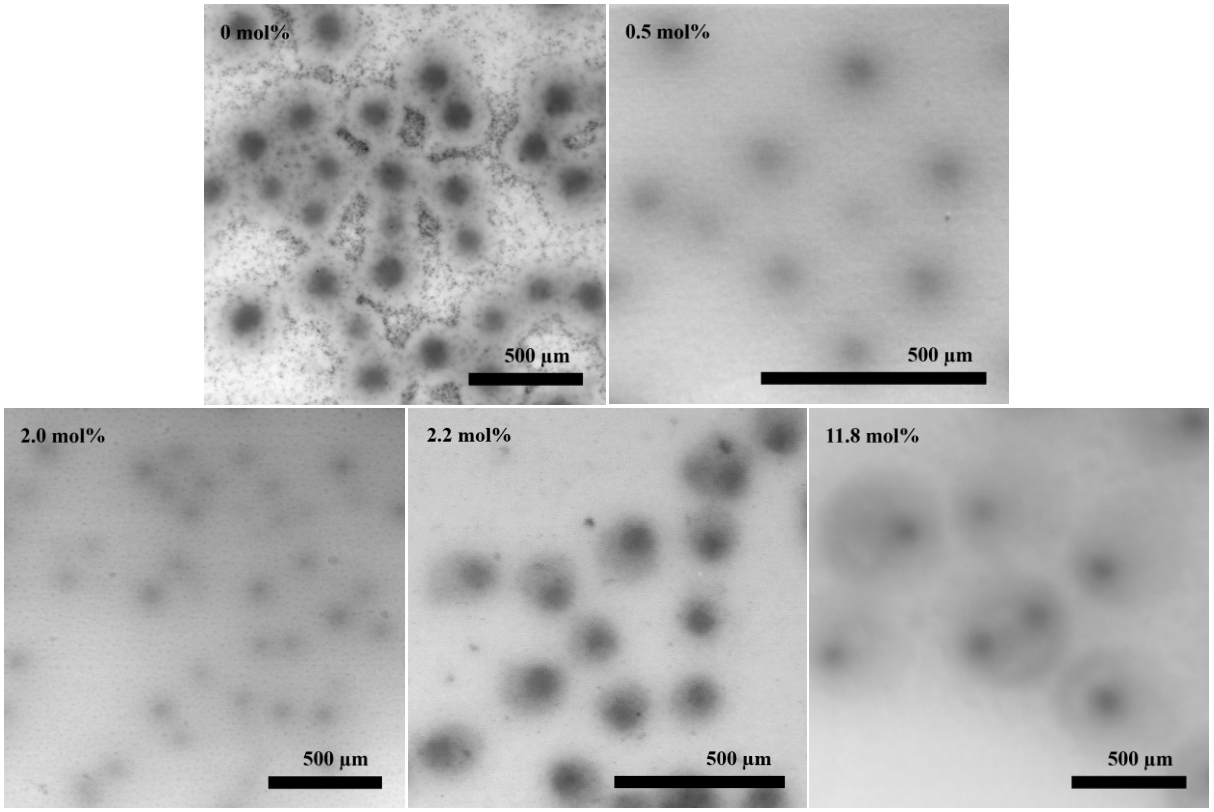

Figure SIII.8 BFSTEM images of p(VCL/NTAaa) microgels with χ_{NTA} = 0 mol%, 2.0 mol% and 2.2 mol%. *Reprinted with permission from the American Chemical Society*[1] *with minor modifications.*

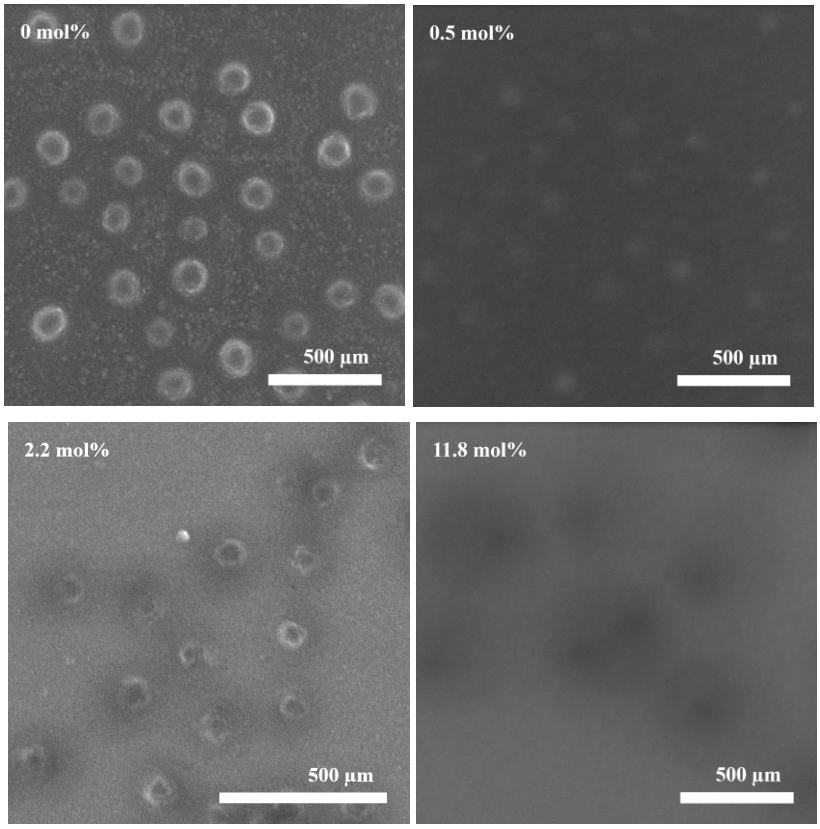

Figure SIII.9 SEM images of p(VCL/NTAaa) microgels with χ_{NTA} = 0 mol%, 0.5 mol%, 2.2 mol% and 11.8 mol%. The 2.0 mol% sample is not shown due to low contrast. *Reprinted with permission from the American Chemical Society*[1] *with minor modifications.*

Reaction Calorimetry

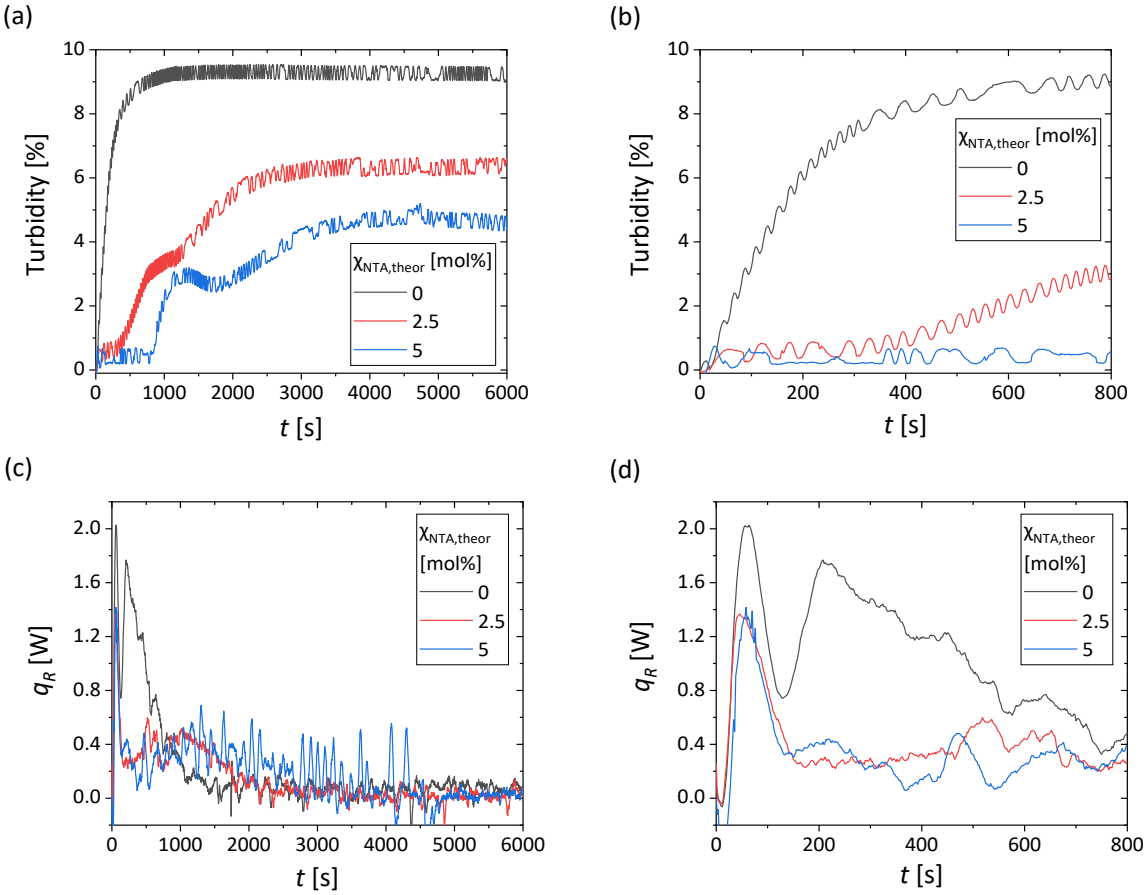

Figure SIII.10 Real-time measurements of (a), (b) turbidity, (c), and (d) heat generation rate, recorded during batch polymerization of p(VCL/NTAaa) microgels with 2.6 mol% BIS. Different time slots are shown. *Reprinted with permission from the American Chemical Society*[1] *with minor modifications.*

IV. Nitrilotriacetic Acid Functionalized Microgels as Carriers for Hyaluronan Synthase: Enzymatic Hyaluronic Acid Synthesis

Large parts of this chapter are reprinted from Sommerfeld, Isabel K.; Dälken, Esther; Elling, Lothar; Pich, Andrij. Nitrilotriacetic Acid Functionalized Microgels for Efficient Immobilization of Hyaluronan Synthase. *Macromol. Biosci.* **2024**, 2400075. *Specifically, most Figures are adapted from this publication, with minor modifications. This material is reused under the terms of the Creative Commons Attribution-NonCommercial 4.0 International (CC BY-NC 4.0) license.*

Contributions to this Chapter

The synthesis of the reported compounds was conducted either by myself or by Esther Dälken under my supervision during her employment as a research assistant and during her research internship at DWI – Leibniz-Institute for Interactive Materials in 2022. Dan E. Demco performed ^{1}H transverse relaxation measurements. Renate Jansen conducted ICP-OES measurements, and Dr. Michael Pohl and Rainer Haas acquired SEC data. Truc Pham performed enzyme production and Bradford measurements. Further Bradford measurements were conducted by Kai P. Hussnaetter. All data were processed and evaluated by me. Johannes Gottschalk assisted with preliminary enzyme activity tests. Although these results are not included in this thesis, the insights gained from these preliminary experiments were invaluable and played a significant role in guiding me toward achieving more successful outcomes in my research.

1. Introduction

The use of immobilized enzymes for the synthesis of complex biological materials, such as oligo- or polysaccharides, can be highly advantageous. Enzymes offer a straightforward approach to synthesizing complex materials, eliminating the need for multi-step chemical

syntheses involving selective protection and deprotection, often accompanied by low yields.[1,2] Moreover, enzyme immobilization facilitates the straightforward recovery of products and enzymes, repeated enzyme reuse, and enables continuous enzymatic production towards more sustainable chemistry.[3]

Recapping **Chapter III**, ionic binding was utilized for the incorporation of the biomacromolecule. While this method often enables strong binding, the presence of a charged carrier can present challenges during biocatalysis. When enzyme substrates or products are charged, it can lead to disturbed kinetics and general difficulties with substrate and product diffusion. Additionally, changes in pH stability and the pH optimum of the enzyme may occur.[4] Given the transition from simple protein immobilization to the incorporation of enzymes for biocatalysis, alternative methods may prove more advantageous. Therefore, in this chapter, an advancement of the previously used method is sought by employing affinity binding, where the microgel support interacts with a specific group in the enzyme without affecting its enzymatic activity.[5]

The NTA functional group incorporated into pVCL-based microgels can serve not only for electrostatic immobilization but also as a chelating ligand for metals. These chelated metal ions then interact with a polyhistidine tag (His-Tag) in the enzyme,[4,6] enabling enzyme immobilization. This method is adapted from Immobilized Metal Affinity Chromatography (IMAC), a widely used technique for protein purification.[6–8] Metal affinity binding not only enables highly specific binding but also facilitates the reuse of the support through reversible attachment of the enzyme.[5,9] With the possibility of reversibility, this mechanism, much like stimuli-responsiveness, is useful for the uptake and release of biomacromolecules.

NTA-microgels have previously been employed for immobilizing enzymes and proteins using metal affinity binding.[9–12] For instance, Mizrahi *et al.* utilized NTA-microgels to attach His-tagged green fluorescent protein (GFP-His).[9] Similarly, Heida, Köhler, *et al.* immobilized the same protein, albeit in a different manner, with GFP-His being formed *in situ* by DNA linked to the microgel network.[10] In another study, they incorporated active malonyl-CoA synthetase into NTA microgels.[11] Xu *et al.* successfully immobilized sucrose phosphorylase while retaining the majority of its enzymatic activity.[12]

Gottschalk *et al.* successfully immobilized His_6-tagged Hyaluronan Synthase from *Pasteurella multocida* (*Pm*HAS), onto NTA-functionalized magnetic particles, showcasing the feasibility of using affinity binding for enzyme attachment while preserving the enzymatic functionality of *Pm*HAS.[13] Building upon this foundation, this chapter shifts its focus towards developing a soft microgel platform with reversibly immobilized *Pm*HAS, departing from the use of hard magnetic particles.

To go further into detail, in this thesis, the objective is to immobilize *Pm*HAS, followed by the enzymatic production of hyaluronic acid (HA). For this purpose, p(VCL/NTAaa) microgels were synthesized. Instead of relying on electrostatic interactions for immobilization (**Chapter III**), metal ions were introduced into the microgels, with NTA serving as a ligand for complexation. The metal content in the microgels was determined *via* Inductively Coupled Plasma Optical Emission Spectroscopy (ICP-OES). The resulting microgels were then employed for the immobilization of His_6-tagged *Pm*HAS, using the Bradford assay[14] to determine the immobilization efficiency. As a Leloir glycosyltransferase (GT), *Pm*HAS catalyzes the assembly of nucleotide sugars, here for the formation of the polysaccharide HA.[15,16] Additionally, *Pm*HAS can elongate supplied HA oligosaccharides.[16] The formation of the glycosaminoglycan HA thereby involves the sequential arrangement of uridine diphosphate glucuronic acid (UDP-GlcA) and UDP *N*-acetylglucosamine (UDP-GlcNAc) units, connected by alternating β-(1,3) and β-(1,4) glycosidic linkages.[17] The process of HA formation was carefully observed, utilizing Multiplexed Capillary Electrophoresis (MP-CE). The formed HA was characterized by Fourier Transform Infrared (FT-IR) spectroscopy and Size Exclusion Chromatography (SEC).

In **Figure IV.1**, a schematic representation of the objective of this chapter is presented. The enzyme *Pm*HAS is immobilized on a microgel *via* metal affinity binding, leveraging its biocatalytic activity to repetitively synthesize HA.

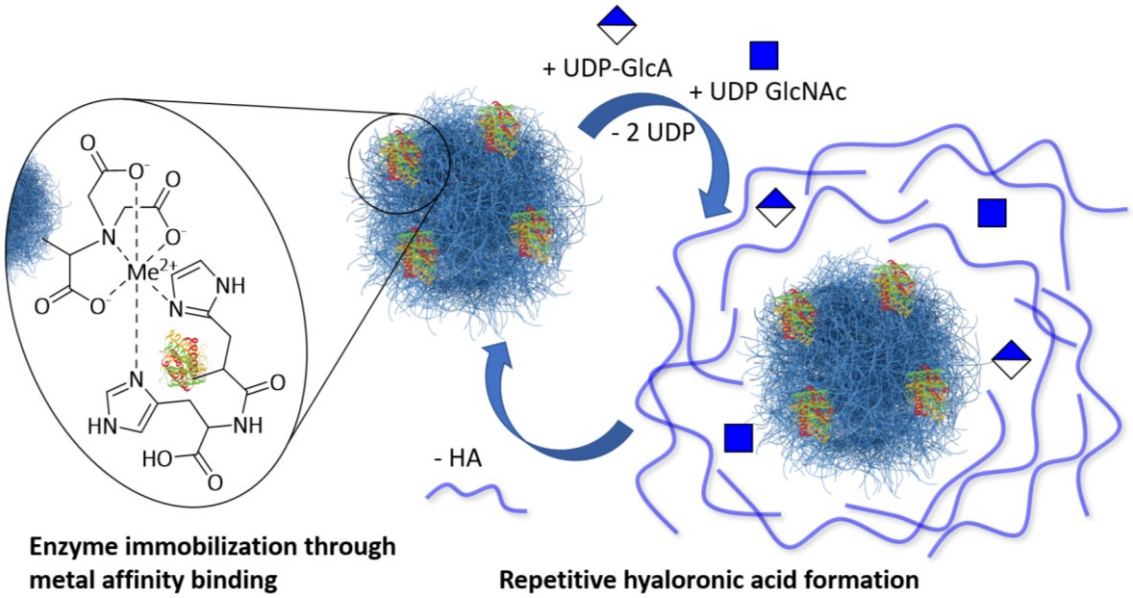

Figure IV.1 Schematic depiction of the scope of the current chapter: The enzyme *Pm*HAS is immobilized onto p(VCL/NTAaa) microgels through metal affinity binding, facilitated by NTA serving as a ligand for metal ions capable of binding to the His_6-tag of *Pm*HAS. This setup harnesses the biocatalytic activity of *Pm*HAS to repeatedly synthesize HA.

2. Materials and Methods

2.1. Materials

Ultra-pure water (Merck, HPLC grade) was utilized for all aqueous reactions. Analytical grade organic solvents were sourced from Omnisolv. For preparation of buffers, the following substances were acquired: ammonium acetate (Carl Roth, 97 %), ethylenediaminetetraacetic acid (EDTA, Sigma-Aldrich, 99 %), *N*-(2-hydroxyethyl)piperazine-N'-(2-ethanesulfonic acid) (HEPES, Sigma-Aldrich, 99 %) and sodium hydroxide (NaOH, Merck, 99.5 %). The enzyme production involved isopropyl β-D-1-thiogalactopyranoside (IPTG, AppliChem GmbH, 99 %), yeast extract (Serva), tryptone (Carl Roth), ampicillin sodium salt (Carl Roth, 97 %), agar-agar (Carl Roth), potassium hydrogen phosphate (Carl Roth, 98 %), potassium dihydrogen phosphate (Carl Roth, 98 %), NaCl (Carl Roth, 99,5 %), and imidazole (PanReac AppliChem). Metal salts were acquired from Sigma Aldrich: $CoCl_2 \cdot 6\ H_2O$ (98 %), $FeSO_4 \cdot 7\ H_2O$ (99 %), $FeCl_2 \cdot 4\ H_2O$ (99 %), KCl (85 %), $MnCl_2 \cdot 4\ H_2O$ (98 %), $MgSO_4$ (99.5 %), $NiSO_4 \cdot 6\ H_2O$ (98 %). Additionally, *para*-aminobenzoic acid (PABA, 99 %) and *para*-aminophtalic acid (PAPA, 97 %) were purchased from Sigma Aldrich, and sodium dodecyl sulfate (SDS ≥99.8) was purchased from Carl Roth. Nucleotide sugars were acquired from Carbosynth or Sigma Aldrich: uridine diphosphate glucuronic acid (UDP-GlcA, 98 %) and uridine 5'-diphospho-*N*-acetylglucosamine sodium salt (UDP-GlcNAc, 98 %). For SEC, water (HiPerSolv CHROMANORM® HPLC grade, VWR), Na_2HPO_4 (Carl Roth, 99 %), 0.069 NaCl (Bernd Kraft, 99 %), dextran standards (Polymer Standards Service), and ethylene glycol (Fluka analytical, 99.5 %) were employed. HNO_3 (Carl Roth, 95 %) was employed for additional measurements.

2.2. Enzyme Production

His_6-tagged *Pm*HAS was synthesized following the methods described by Gottschalk et al.[18,19] Specifically, the enzyme is *Pm*HAS 1-703, a soluble class 2 hyaluronan synthase[13] with the following amino acid sequence, supplied by the group of Professor L. Elling. Here, the His_6-tag and other His residues are highlighted in red and blue, respectively:

MNTLSQAIKA	YNSNDYQLAL	KLFEKSAEIY	GRKIVEFQIL	KCKEKLSAHP	SVNSAHLSMN
KEEKVNVCDS	PLDIATQLLL	SNVKKLVLSD	SEKNTLKNKW	KLLAEKKSEN	AEVRAVALVP
KDFPKDLVLA	PLPDHVNDFT	WYKKRKKRLG	IKPEHQHVGL	SIIVTTFNRP	AILSITLACL
VNQKTHYPFE	VIVTDDGSQE	DLSPIIRQYE	NKLDIRYVRQ	KDNGFQASAA	RNMGLRLAKY
DFIGLLDCDM	APNPLWVHSY	VAELLEDDDL	TIIGPRKYID	TQHIDPKDFL	NNASLLESLP
EVKTNNSVAA	KGEGTVSLDW	RLEQFEKTEN	LRLSDSPFRF	FAAGNVAFAK	KWLNKSGFFD
EEFNHWGGED	VEFGYRLFRY	GSFFKTIDGI	MAYHQEPPGK	ENETDREAGK	NITLDIMREK
VPYIYRKLLP	IEDSHINRVP	LVSIYIPAYN	CANYIQRCVD	SALNQTVVDL	EVCICNDGST
DNTLEVINKL	YGNNPRVRIM	SKPNGGIASA	SNAAVSFAKG	YYIGQLDSDD	YLEPDAVELC
LKEFLKDKTL	ACVYTTNRNV	NPDGSLIANG	YNWPEFSREK	LTTAMIAHHF	RMFTIRAWHL
TDGFNEKIEN	AVDYDMFLKL	SEVGKFKHLN	KICYNRVLHG	DNTSIKKLGI	QKKNHFVVVN
QSLNRQGITY	YNYDEFDDLD	ESRKYIFNKT	AEYQEEIDIL	KDINKNAAAL	EHHHHHH

Plasmids were introduced into *Escherichia coli* (*E. coli*) BL21 (DE3) through heat shock, and positive clones were identified on agar plates containing Lysogeny Broth (LB) and ampicillin (100 µg mL^{-1}). A 20 mL LB medium supplemented with ampicillin was inoculated with positive clones and incubated in a 100 mL baffled flask for 18 hours at 37 °C and 120 rpm for preculture. Subsequently, 20 mL of the preculture medium were transferred to inoculate 1 L of terrific broth medium in a 5 L baffled flask, and cells were grown at 37 °C and 80 rpm until reaching an optical density of 0.6-0.8 at 600 nm. Expression was induced by adding 0.1 mM IPTG, and the temperature was lowered to 25 °C. After 20 hours of cultivation, cells were harvested by centrifugation at 7000 rpm for 30 minutes at 4 °C, and the cell pellets were stored at -20 °C.

For protein extraction, 4 g of frozen cells were resuspended in 10 mL of binding buffer (20 mM sodium phosphate, 500 mM sodium chloride, 30 mM imidazole, pH 7.4), disrupted by ultrasound (6 cycles of 15 seconds on, 60 seconds off, 52 % amplitude), and centrifuged at 15000 rpm for 30 minutes at 4 °C. The crude extract containing *Pm*HAS was filtered through a 0.8 µm filter and subjected to Immobilized Metal Ion Affinity Chromatography (IMAC) using 5 mL HisTrap HP columns (GE Healthcare) on an ÄKTApurifier 100 (GE Healthcare) controlled by the Unicorn program. Side products were eliminated by washing with 20 mM Na_2HPO_4, 500 mM NaCl, and 30 mM imidazole at pH 7.4. The purified *Pm*HAS was eluted with an elution

buffer consisting of 20 mM Na_2HPO_4, 500 mM NaCl, and 500 mM imidazole at pH 7.4. Following purification, buffer exchange was performed by dialysis against 100 mM HEPES at pH 8, and the resulting product was stored at 4 °C. The protein concentration was determined using a Bradford protein assay.[14]

2.3. Synthesis of Monomers and Microgels

The polymerization reactions in this chapter were based on the use of two compounds: 2,2'-((5-acrylamido-1-carboxypentyl)azanediyl)diacetic acid (NTAaa) and dimethyl 2,2'-((6-acrylamido-1-methoxy-1-oxohexan-2-yl)azanediyl) diacetate (NTAMaa). Detailed synthesis instructions and characterization results for these compounds can be found in **Chapter III**. Additionally, **Chapter III** provided instructions for the synthesis and FT-IR characterization of poly(*N*-vinylcaprolactam (pVCL) and poly(*N*-vinylcaprolactam-2,2'-((5-acrylamido-1-carboxypentyl)azanediyl)diacetic acid) (p(VCL/NTAaa)) microgels. The microgels were synthesized, utilizing a fixed amount of BIS (2.6 mol%) and varying NTAaa contents ($\chi_{NTA,theor.}$ = 0, 0.1, 0.25, 0.5, 1, 2, and 2.5 mol%).

2.4. Incorporation of Metal(II) Ions into Microgels

The p(VCL/NTAaa) samples (5 mg) were treated with a metal (Me) salt solution (0.75 M, 1mL) utilizing the salts $CoCl_2 \cdot 6\ H_2O$, $FeCl_2 \cdot 4\ H_2O$, $MnCl_2 \cdot 4\ H_2O$, $MgSO_4$, and $NiSO_4 \cdot 6\ H_2O$ and subsequently subjected to mixing on a head-over-head shaker for a minimum of 12 hours. Co^{2+}, Fe^{2+}, Mn^{2+}, and Mg^{2+} were exclusively incorporated into p(VCL/NTAaa) microgels containing χ_{NTA} = 1 mol%, whereas Ni^{2+} was incorporated into microgels across all NTAaa concentrations. Purification was conducted through dialysis against water employing a regenerated cellulose membrane (MWCO = 12 - 14 kDa) for 5 days. Following lyophilization, p(VCL/NTAaa@Me) microgels were obtained as white to slightly colored powders.

2.5. Immobilization of Hyaluronan Synthase into Microgels

To immobilize His_6-tagged *Pm*HAS on p(VCL/NTAaa@Me) microgels, enzyme stock solution and microgels were mixed in HEPES (100 mM, pH 8) at concentrations of 3.0 mg mL^{-1} microgel and 1.5 mg mL^{-1} purified *Pm*HAS. Following incubation at 4 °C for a minimum of 2 days, the sample was centrifuged (3 x 10000 rpm, 4 °C, 30 min) to remove any residual enzyme. After each centrifugation step, the precipitated p(VCL/NTAaa@Me@*Pm*HAS) microgels were resuspended in HEPES (100 mM, pH 8), maintaining the previous microgel concentration.

2.6. Production of Hyaluronic Acid and Enzyme Activity Assay

The nucleotide sugars UDP-GlcA trisodium salt (58.1 mg, 0.09 mmol) and UDP-GlcNAc disodium salt (58.6 mg, 0.09 mmol) were mixed with enzyme cofactors $MgCl_2 \cdot 6\ H_2O$ (27.4 mg, 0.135 mmol), KCl (6.8 mg, 0.09 mmol) and $MnCl_2 \cdot 4H_2O$ (2.7 mg, 0.0135 mmol) in HEPES (100 mM, pH 8, 1.8 mL). This substrate solution was used to activate the production of HA *via* the enzymatic action of *Pm*HAS. Additionally, a stop solution was prepared, consisting of SDS (201.9 mg, 14 mM), PABA (137 mg, 2 mM), and PAPA (18.1 mg, 2 mM) in 50 mL of water.

Subsequently, the substrate solution (200 µL) was mixed with the test solution (800 µL), comprising the previously obtained p(VCL/NTAaa@Me@*Pm*HAS) solution or a control sample (*Pm*HAS solution without microgels). This mixture was formulated to contain final concentrations of 15 mM Mg^{2+}, 10 mM K^{+}, and 1.5 mM Mn^{2+}, known to provide optimal conditions for high conversion rates.[18,19] In accordance with previous publications, a concentration of 10 mM was used for both nucleotide sugars, UDP-GlcA and UDP-GlcNAc.[13,18]

Samples were collected at various time points (0, 2, 4, 6, 25, and 54 h) to monitor HA formation. The reaction was stopped using the previously prepared stop solution. Specifically, 45 µL of the stop solution were added to 45 µL of the sample taken at each time point. The samples were subsequently stored at -20 °C until analyzed by MP-CE.

Recovery and reuse tests were conducted by reusing p(VCL/NTAaa@Me@*Pm*HAS) for two additional cycles of HA formation. After HA formation in the first cycle, following the aforementioned instructions, collecting samples at 0, 2, 4, 6, and 24 h, the mixture underwent

centrifugation (3 x 10000 rpm, 4 °C, 30 min). Subsequently, the supernatant was removed, and the remaining solution was brought up to a total volume of 800 µL using 100 mM HEPES at pH 8. Fresh substrate solution (200 µL) was added to initiate another cycle of HA formation. This procedure was repeated twice for a total of three cycles.

2.7. Analytical Methods

2.7.1. Fourier-Transform Infrared Spectroscopy

Fourier-Transform Infrared (FT-IR) spectroscopy was conducted following the procedures outlined in **Chapter III**. The NTA contents were calculated using **Equation III.2**.

2.7.2. Dynamic Light Scattering

Dynamic Light Scattering (DLS) measurements were conducted on a Malvern Instruments Zetasizer Ultra Pro. Microgel samples (0.5 mg mL^{-1}, in ultrapure water) were measured threefold at a scattering angle θ = 90°, in square 12 mm polystyrene DTS0012 cuvettes, each with 5 runs at 25 °C. ZS Xplorer software was utilized for result analysis.

2.7.3. Electrophoretic Light Scattering

Additionally, Electrophoretic Light Scattering (ELS) measurements were conducted on the Zetasizer Ultra Pro from Malvern Instruments. Samples (0.5 mg mL^{-1} in ultrapure water) were placed into disposable folded capillary cells (DTS1070) and measured threefold at 25 °C with up to 100 runs each at a scattering angle of θ = 12.8° and an applied voltage of 150 V. Data were analyzed using ZS Xplorer software.

2.7.4. Multiplexed Capillary Electrophoresis

MP-CE measurements were performed utilizing a multiplexed cePRO 9600TM operated by pK_a-analyzer software (Advanced Analytical Technologies, Ames, IA, USA). This device allows

for the simultaneous analysis of multiple samples. The enzymatic reaction of *Pm*HAS was assessed by separating nucleotide sugars (UDP-GlcA and UDP-GlcNAc) and nucleotides (UDP and uridine monophosphate (UMP)). The experimental setup and method were adapted from previous work by Gottschalk *et al*.[13]

A 96-capillary array was utilized for the analysis, with each capillary having an inner diameter of 50 µm and effective and total lengths of 55 cm and 80 cm, respectively. Before separation, the system was washed with 0.1 M NaOH and water. Vacuum (−0.7 psi, 10 s) was used for sample injection, and the separation of substances was realized by applying a voltage of 10 kV. The electrophoresis buffer consisted of 70 mM ammonium acetate containing 1 mM EDTA at pH 9.2. Internal standards PABA and PAPA (1 mM each) were employed for calibration. Analytes were detected by UV light (254 nm), and data were processed using the pK_a-analyzer software, calculating quantities of the analytes based on their respective peak areas.

2.7.5. Inductively Coupled Plasma Optical Emission Spectroscopy

The metal content in the microgels was determined *via* ICP-OES on a PlasmaQuant PQ9000 Elite. Measurements were conducted after sample solubilization in 3 mL HNO_3 in the microwave. Data were analyzed using the program Jena.

2.7.6. Bradford Protein Assay

To prepare the Bradford reagent, 10 mL of Roti®-Quant were diluted with 27.5 mL of purified water. A test solution of 6 µL was then appropriately diluted in HPLC-grade water. Subsequently, 25 µL of each sample was dispensed into a well plate, followed by the addition of 100 µL of the Bradford reagent to each well, with each sample measured in triplicate. After an incubation period of 11.5 minutes, the absorbance was measured at a wavelength of 595 nm on a Multi-Mode Microplate Reader SynergyTM 2 from BioTek® (Vermont, USA). Calibration was conducted using a bovine serum albumin standard, following the same experimental procedure.

2.7.7. Atomic Force Microscopy

Atomic Force Microscopy (AFM) images were acquired in tapping mode utilizing a NanoScope V system manufactured by Veeco Instruments. The cantilever employed was an NCH-50 POINTPROBE® silicone SPM sensor sourced from Nanoworld, featuring a resonant frequency of 320 kHz and a force constant of 42 Nm^{-1}. Analysis was conducted using Gwyddion software.

2.7.8. Size Exclusion Chromatography

For the determination of molecular weights (M_w and M_n) and molecular weight distributions (M_w/M_n), a neutral to anionic SEC setup was employed. The eluent consisted of water containing 5 mM Na_2HPO_4 and 69 mM NaCl at pH 3.9. Samples were prepared with 0.7 µL mL^{-1} ethylene glycol as an internal standard. The SEC system utilized an HPLC pump (1200, Agilent) and was equipped with two detectors: a refractive index (RI) (1200, Agilent) and a UV (VWD, 1200, Agilent). Separation was implemented using a pre-column (8x50 mm) and three Suprema-Lux gel columns (8x300 mm, Polymer Standards Service) at a flow rate of 1.0 mL min^{-1} at 40 °C. The columns had nominal pore widths of 30, 1000, and 1000 Å with 5 µm gel particles. Calibration was performed with narrowly distributed Dextran standards (Polymer Standards Service), and data analysis was conducted using PSS WinGPC UniChrom software (Version 8.3.2).

3. Results and Discussion

3.1. Synthesis and Fundamental Characterization of Microgels

The p(VCL/NTAaa) microgels were prepared using the semi-batch synthesis procedure described in **Chapter III**.[20] **Figure SIV.1** and **Figure SIV.2** present the obtained FT-IR spectra. Due to the limited intensity of the peak associated with the C=O vibration of the carboxylic acid groups of NTA, only NTA contents exceeding 1 mol% were determined. In addition to other measurement data, **Table IV.1** presents both theoretical ($\chi_{NTA,theor}$) and measured ($\chi_{NTA,actual}$) NTA contents. A close correspondence between $\chi_{NTA,theor}$ and $\chi_{NTA,actual}$ was demonstrated. Subsequent references to p(VCL/NTAaa) microgels will use the denotation χ_{NTA}, utilizing their theoretical NTA amounts for concentrations up to 1 mol% and their actual NTA amounts for concentrations exceeding 1 mol%.

Table IV.1. Zeta potential (ζ), hydrodynamic diameter (D_h), and polydispersity index (PDI) of p(VCL/NTAaa) microgels synthesized with different amounts of NTA ($\chi_{NTA,theor}$). The actual NTA content ($\chi_{NTA,actual}$) was determined using FT-IR spectroscopy while ζ, D_h, and PDI were determined using ELS (ζ) and DLS (D_h, PDI) measurements at T = 25 °C with scattering angles of θ = 90° (DLS) and θ = 12.8° (ELS) in H_2O. Yields of the microgel synthesis were determined gravimetrically.

$\chi_{NTA,theor.}$ [mol %]	$\chi_{NTA,actual}$ [mol %]	Z [mV][a)]	D_h [nm][a)]	PDI [a.u.][a)]	Yield [%]
0 [d)]	0	3.2 ± 0.2[b)]	576 ± 15[b)]	0.086 ± 0.051[b)]	83.1
0.1	-	-6.0 ± 0.7[b)]	349 ± 10[b)]	0.080 ± 0.027[b)]	72.1
0.25	-	-10.2 ± 1.1[b)]	451± 23[b)]	0.119 ± 0.043[b)]	68.7
0.5 [d)]	-	-18.0 ± 1.3[b)]	584 ± 20[b)]	0.132 ± 0.035[b)]	68.4
1	-	-21.3± 1.2[c)]	644± 24[c)]	0.143 ± 0.019[c)]	58.0
2	1.9	-25.7 ± 0.4[c)]	759 ± 55[c)]	0.283 ± 0.013[c)]	74.1
2.5 [d)]	2.2	-38.4 ± 0.2[c)]	640 ± 11[c)]	0.147 ± 0.018[c)]	85.4

[a)] The dilute p(VCL/NTAaa) dispersion (0.5 mg mL^{-1}) prepared for ELS and DLS measurements resulted in a neutral pH at low NTA contents ($\chi_{NTA,actual}$ = 0.1 to 0.5 mol%) and in a slightly acidic pH of 5 at higher NTA contents ($\chi_{NTA,actual}$ = 1 to 2.2 mol%); [b)] pH 6, the pH corresponds to the pH of the used HPLC water; [c)] pH 5. [d)] characterization results of marked microgels have been previously reported[20] but are listed here for comprehensiveness.

Furthermore, p(VCL/NTAaa) microgels were analyzed using ELS and DLS measurements. This resulted in the determination of parameters such as ζ, the hydrodynamic diameter (D_h), and the polydispersity index (PDI), as summarized in **Table IV.1**. Due to the pronounced acidity of NTA, the dilute p(VCL/NTAaa) dispersions, utilized for ELS and DLS measurements, possess pH levels below that of the employed H_2O (pH 6) at higher χ_{NTA}. D_h of the microgels at 25 °C

exhibited varying sizes ranging from 349 to 759 nm with a monomodal, reasonably narrow size distribution, as indicated by the PDI. Notably, an increase in size was evident from microgels containing χ_{NTA} = 0.1 mol% (349 nm) to those with χ_{NTA} = 1 mol% (644 nm), attributed to the higher swelling degree caused by the mutual repulsion of negatively charged polymer chains. However, no clear trend emerged at higher χ_{NTA}, consistent with previous findings (**Chapter III**) where no distinct correlation between size and comonomer amount was observed.[20] This lack of correlation could be attributed to variations in microgel morphology, as evidenced by previous studies demonstrating the influence of comonomer concentration on microgel shape:[21] As explored in **Chapter III**, the morphology of the presented p(VCL/NTAaa) is indeed dependent on its comonomer content which can in turn affect microgel size.[20] Therefore, the dependency of D_h obtained from DLS measurements on both the microgel shape and its actual size is likely the cause of the undetectable trend.

At low χ_{NTA}, ζ can serve as a qualitative indicator of the comonomer content, as COOH groups of NTA are anticipated to reside in the microgel shell (**Chapter III**). Their pronounced acidity results in a negative surface potential, increasing in magnitude with increasing χ_{NTA}. This was proven in the range of χ_{NTA} values utilized (**Table IV.1**).

3.2. Incorporation of Metal Ions into p(VCL/NTAaa) Microgels

3.2.1. Inductively Coupled Plasma Optical Emission Spectroscopy

Following their synthesis and characterization, p(VCL/NTAaa) microgels were further modified to enable enzyme immobilization by metal affinity binding. For this, metal ions were incorporated into the microgels *via* complexation. Concentrated metal salt solutions were added to the microgel dispersions, followed by dialysis for the removal of residual, non-complexed metal ions. An NTA-metal ion complex is formed in this process, primarily driven by electrostatic interactions,[22] with NTA serving as a tetradentate ligand through the binding of three COOH groups and one amine group.[22,23] However, this is not the case for all metal ions. For alkaline earth metals such as Mg^{2+}, NTA serves solely as a tridentate ligand.[24] This results in a lower chelate effect and thus lower binding strength. After incorporation of Ni^{2+}, Co^{2+}, Mn^{2+}, Mg^{2+}, and Fe^{2+} into p(VCL/NTAaa) microgels (χ_{NTA} = 1 mol%), the metal content was

determined through ICP-OES. From this, the amount of occupied NTA groups was calculated, assuming the binding of exactly one metal (Me) ion per NTA unit. Additionally, p(VCL/NTAaa@Me) yields were determined gravimetrically. In **Table IV.2**, the metal content and yield of p(VCL/NTAaa@Me) are listed, along with the amount of occupied NTA groups and the metal concentration in a 3 mg mL^{-1} p(VCL/NTAaa@Me) dispersion.

Table IV.2. Metal (Me) ions were incorporated into p(VCL/NTAaa) (χ_{NTA} = 1 mol%) microgels leading to the formation of p(VCL/NTAaa@Me) hybrids. ICP-OES was employed to determine metal contents and the amount of occupied NTA coordination sites. The yields of p(VCL/NTAaa@Me) were determined gravimetrically. From the attained results, the metal concentrations in 3 mg mL^{-1} p(VCL/NTAaa@Me) dispersions were calculated.

Metal ion	Metal content [mg g^{-1}]	Metal content [µmol $mmol^{-1}$]	Occupied NTA sites [%]	Yield [%]	Metal concentration [mM]
Ni^{2+}	3.90	9.31	95.5	74	0.199
Co^{2+}	3.62	7.98	81.8	99	0.171
Mn^{2+}	1.59	4.07	41.8	93	0.087
Mg^{2+}	0.48	2.77	28.4	87	0.059
Fe^{2+}	(59.74)[a)]	(131.31)[a)]	(1346.8)[a)]	(111)[a)]	3.209

[a)] Fe^{2+} ions strongly interact with NTA but also with VCL, leading to an exceeded Fe incorporation in p(VCL/NTAaa).

ICP-OES reveals a varying loading efficiency of metal ions into p(VCL/NTAaa) microgels (**Table IV.2**). For Ni^{2+} and Co^{2+} high loading of 81.8 % (Co^{2+}) to 95.5 % (Ni^{2+}) was obtained. For Mn^{2+} (41.8 %) and Mg^{2+} (28.4 %), the loading efficiency was lower. Therefore, Ni^{2+} and Co^{2+} seem to be more suitable for this application. These findings are consistent with the reported formation constants of NTA complexes in the literature. The highest affinity for NTA@Me complexes is observed with Ni^{2+}, followed by Co^{2+}, whereas the complexes formed with Mn^{2+} and Mg^{2+} exhibit lower binding affinities.[25,26]

Obtained yields range between 74 % and 99 %, where lower yields are explained by material loss during transfer into dialysis tubes. Particularly the introduction of Ni^{2+} caused microgel aggregation through the lowered electrostatic stabilization in the highly concentrated metal salt solution. All materials lead to the formation of homogeneous p(VCL/NTAaa@Me) dispersions after the removal of residual metal ions. Dried samples appear similar to p(VCL/NTAaa) microgels as homogeneous white powders, slightly blueish because of immobilized Ni^{2+}.

Notably, the detected amount of Fe exceeds the maximum number of available NTA binding sites by tenfold. Additionally, the gravimetric yield was determined to exceed 100 %, indicating the incorporation of more metal than expected. This was further evident in the inhomogeneous appearance of dry p(VCL/NTAaa@Fe) microgels. The powders exhibit non-uniform coloring, displaying a gradient ranging from brown and orange to pale yellowish hues, suggesting an uneven distribution of metal salts and microgel within the sample. These findings indicate that Fe^{2+} ions interact not only with NTA but also with other parts of the microgel, such as the VCL units. Consequently, complete removal of dissolved metal ions may not be achievable. Furthermore, the color change (green to yellow) during metal ion incorporation indicates that Fe^{2+} is partially oxidized to Fe^{3+}. Overall, the obtained results suggest that Fe^{2+} may not be a suitable choice for the complexation with NTA.

To ensure the absence of unintended interactions with VCL, metal ions (Ni^{2+}, Co^{2+}, Mn^{2+}, Mg^{2+}, Fe^{2+}) were further incorporated into pVCL microgels without added NTA comonomer. Obtained ICP-OES results for p(VCL@Me) are compared to p(VCL/NTAaa@Me) (**Figure IV.2a**).

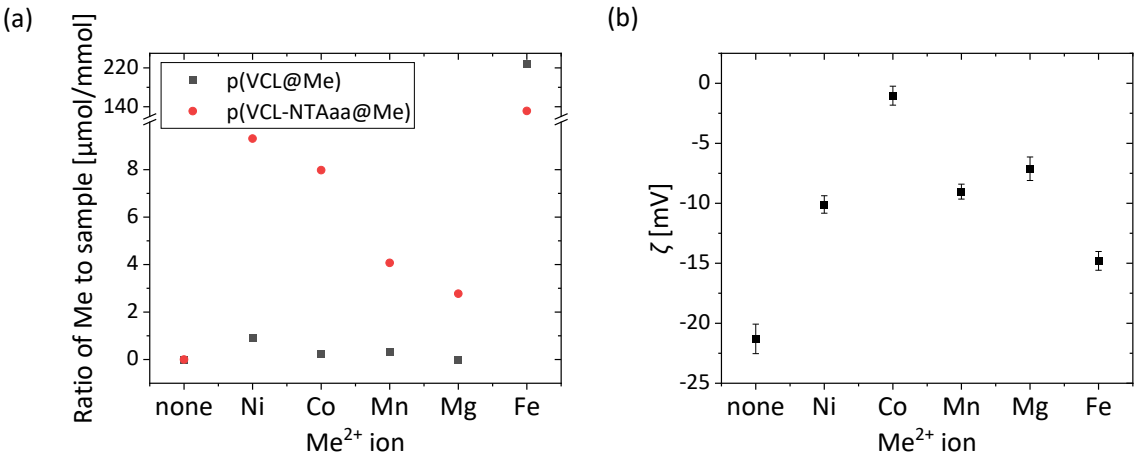

Figure IV.2 (a) Comparison of the amount of metal per total sample amount in µmol/mmol after metal incorporation into pVCL and p(VCL/NTAaa) (χ_{NTA} = 1 mol%) microgels. The metal content was obtained *via* ICP-OES measurements. (b) The ζ of p(VCL/NTAaa) (χ_{NTA} = 1 mol%) and p(VCL/NTAaa@Me) microgels.

The results confirm that in both pVCL and p(VCL/NTA) a large amount of Fe was detected, attributed to unspecific interactions between the microgel network and Fe^{2+}/Fe^{3+}. Hence, the complexation Fe^{2+}/Fe^{3+} cannot be confirmed, rendering this metal ion unsuitable for this application. For all other metal ions negligible metal content in p(VCL@Me) was detected, whereas much higher contents were observed in p(VCL/NTAaa@Me). This suggests that these

metal ions are mostly complexed by the NTA groups, with minimal interactions with other parts of the microgel, and are thus suitable for this application.

3.2.2. Dynamic and Electrophoretic Light Scattering

Comparing p(VCL/NTAaa@Me) to the initial p(VCL/NTAaa) microgels, the incorporation of metal ions leads to an increasing ζ due to their positive charge (**Figure IV.2b**). The negatively charged carboxylic groups of the microgel, primarily situated in its shell, interact with positively charged metal ions through complexation, resulting in partial electrostatic neutralization of the charges. Initially, one might anticipate a proportional increase in ζ with the incorporation of metal ions. Surprisingly, despite the decreasing metal content observed from Fe^{2+}, Ni^{2+}, Co^{2+}, Mn^{2+} to Mg^{2+}, the lowest ζ was measured for Fe^{2+} and Ni^{2+}, rather than Mg^{2+}. The unexpectedly low ζ of p(VCL/NTAaa@Fe) microgels may be attributed to the localization of Fe^{2+}/Fe^{3+} within the VCL-rich microgel core. While Fe^{2+}/Fe^{3+} complexation by NTA units cannot be confirmed, the interaction between Fe and VCL units is plausible, given the high Fe content observed in p(VCL@Fe) microgels. The deviations of ζ from expectations for p(VCL/NTAaa@Me) with Ni^{2+}, Co^{2+}, Mn^{2+}, or Mg^{2+} have other underlying reasons: Deviations are most likely attributed to alterations in microgel morphology, as suggested by the findings presented in **Figure IV.3**, where no clear trend can be observed between the metal content and D_h and PDI of the microgels. P(VCL/NTAaa@Me) containing Fe^{2+} and Ni^{2+}, exhibit smaller D_h compared to the respective p(VCL/NTAaa) microgel, along with a small PDI, likely caused by a size decrease due to a lower electrostatic repulsion of polymer chains. For all other metal ions, an increase in D_h and PDI was observed, indicating the presence of agglomerations. Enhanced swelling of the microgels may result in fewer exposed NTA groups on their surface, potentially explaining the elevated ζ observed for Mn^{2+} and Mg^{2+}.

In summary, changes in D_h and PDI were observed for the p(VCL/NTAaa@Me) compared to the initial p(VCL/NTAaa) microgels. While these changes are noteworthy, they fall beyond the scope of the present thesis and will not be further explored herein.

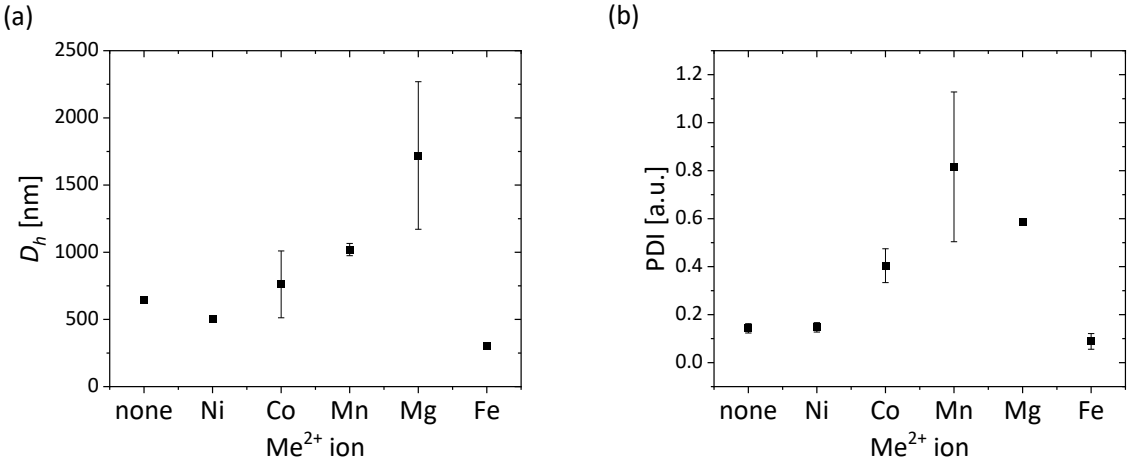

Figure IV.3 (a) D_h and (b) PDI of p(VCL/NTAaa) (χ_{NTA} = 1 mol%) and p(VCL/NTAaa@Me) microgels obtained by DLS.

3.2.3. Atomic Force Microscopy

Through AFM imaging p(VCL/NTAaa) microgels were compared to p(VCL/NTAaa@Ni) regarding their morphology (**Figure IV.4**, **Figure SIV.3**), both with varying χ_{NTA}.

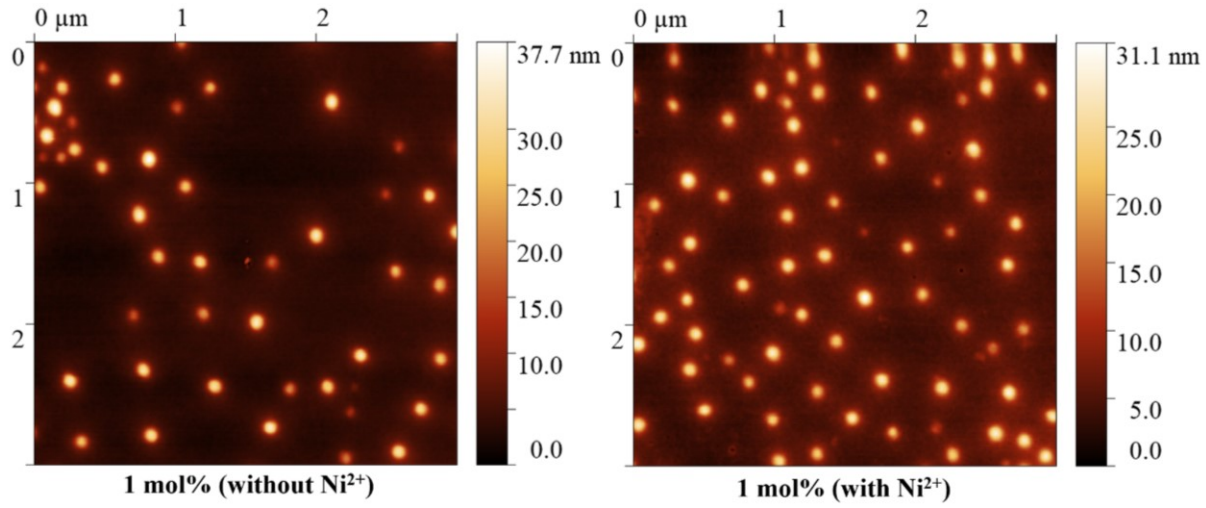

Figure IV.4 AFM images (height profiles) of p(VCL/NTAaa) and corresponding p(VCL/NTAaa@Ni) microgels with χ_{NTA} = 1 mol%.

For the comparison to p(VCL/NTAaa), p(VCL/NTAaa@Ni) were chosen as they appear to be the most promising microgels for this application due to their high metal content. The p(VCL/NTAaa) microgels with varying χ_{NTA} are relatively monodisperse, with a slightly higher polydispersity for χ_{NTA} = 1.9 mol%, confirming the higher PDI in DLS. Microgels without a

strongly visible shell are observed for χ_{NTA} ranging from 0.1 mol% to 1 mol%, while those containing 1.9 mol% exhibit a fuzzy morphology. A distinct core-shell behavior is observed in microgels containing 2.2 mol% NTA. The influence of the comonomer NTAMaa during copolymerization explains these morphological differences, as discussed in detail in **Chapter III**. These variations in morphology may also account for the differences in sizes observed for microgels with higher χ_{NTA} content. When contrasting p(VCL/NTAaa) with the corresponding p(VCL/NTAaa@Ni) microgels, negligible alterations in size and morphology are observed in samples containing 0.1 mol% to 1 mol% NTA. However, for microgels containing 2.2 mol% NTA, a reduction in shell height is noticeable, likely attributed to diminished electrostatic repulsion among the carboxylic acid groups. These findings corroborate the earlier results obtained (**Chapter III.3.2.2**).

3.3. Fabrication and Characterization of Enzyme-Microgel Hybrids

The objective of this chapter is to develop an active p(VCL/NTAaa@Me@PmHAS) enzyme-microgel hybrid, inspired by the methodology outlined by Gottschalk *et al.*[13] who utilized His Mag Sepharose™ Ni beads for immobilizing His_6-tagged *Pm*HAS. The adoption of pVCL-based microgels as a carrier presents an alternative to magnetic beads, offering scalability in synthesis and suitability for biomedical applications.[20] Therefore, the goal is to incorporate the His_6-tagged *Pm*HAS into p(VCL/NTAaa@Me) microgels through metal affinity binding.

To accommodate two free coordination sites for the enzyme, the metal-NTA complex ideally adopts an octahedral geometry with a coordination number of six. The ideal immobilization process is illustrated in **Scheme IV.1**. However, the specific complex geometry is contingent upon the metal ion and its electron shell, resulting in different orbital hybridization,[23] which in turn influences the immobilization of the enzyme on p(VCL/NTAaa@Me) microgels. If the coordination number is lower than six, there may be less free coordination sites for the enzyme.Literature suggests that NTA@Ni^{2+} and NTA@Co^{2+} complexes exhibit an octahedral structure,[27–29] represented by [Me-(NTA)$(H_2O)_2$] (**Scheme IV.1**). In the case of Mn^{2+}, Zetter et al.[30] propose a non-octahedral structure with a coordination number greater than six. While the exact structure remains undetermined, the coordination number suggests the presence

of available coordination sites for enzyme binding. Fe^{2+} likely oxidizes, forming six-coordinate Fe^{3+} complexes with NTA, typically distorted octahedral structures.[31,32] Conversely, Mg^{2+} is not anticipated to form stable complexes with NTA due to its small size[33] and the fact that NTA coordinates as a tridentate ligand only.[24] Minimal binding to *Pm*HAS is expected for Mg^{2+}, irrespective of the complex geometry, due to its low binding strength. However, it was included in this comparison due to the positive impact of Mg^{2+} on *Pm*HAS activity.[19]

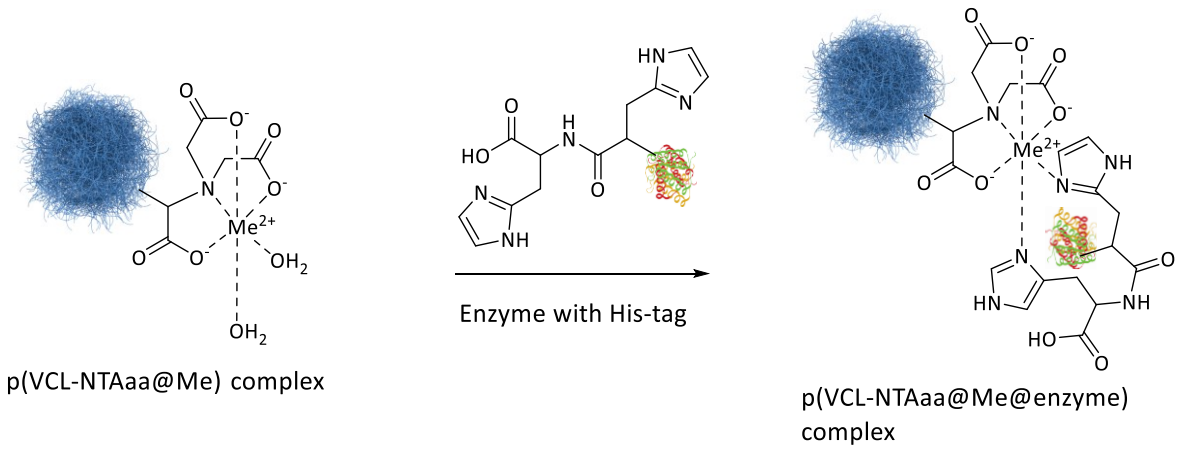

p(VCL-NTAaa@Me) complex

p(VCL-NTAaa@Me@enzyme) complex

Scheme IV.1. Immobilization of a His-tagged enzyme through metal affinity binding on p(VCL/NTAaa@Me). For immobilization, the depicted octahedral geometry of NTA@Me is favorable, leaving two available coordination sites for the enzyme.

After the successful fabrication of p(VCL/NTAaa@Me@PmHAS), the enzyme content in each hybrid microgel was determined. This was indirectly implemented by determining the amount of non-incorporated enzymes through a Bradford assay. The *Pm*HAS-microgels were further assessed regarding their ability of enzymatic HA formation by determining the UDP content at defined time points. UDP can be used as a measure for HA formation, because *Pm*HAS forms HA from UDP-GlcNAc and UDP-GlcA and is, therefore, accompanied by the release of UDP (**Scheme IV.2**). MP-CE was employed for the measurement of the UDP concentration.

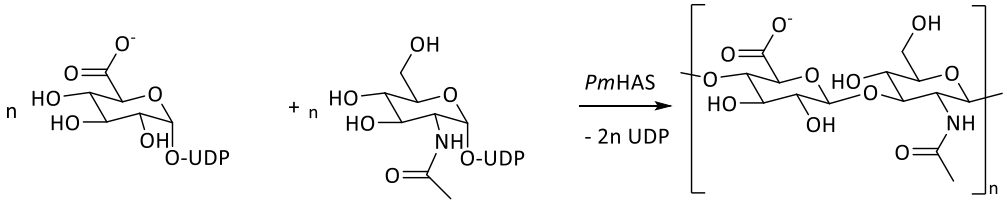

Scheme IV.2 The enzymatic formation of HA through *Pm*HAS involves the polymerization of deprotonated UDP-GlcA and UDP-GlcNAc and is accompanied by UDP formation.

In the subsequent steps, the performance of p(VCL/NTAaa@Me@*Pm*HAS) was enhanced by varying parameters. The effect of incorporating different metal ions (Ni^{2+}, Co^{2+}, Mn^{2+}, Mg^{2+}, and Fe^{2+}/Fe^{3+}) in p(VCL/NTAaa@Me@*Pm*HAS) was investigated to compare their influence on the microgel's capacity to generate UDP. Choosing Ni^{2+} as the most suitable option, χ_{NTA} in p(VCL/NTAaa@Ni@*Pm*HAS) was varied, resulting in a simultaneous variation of the Ni^{2+} content. In the subsequent step, the quantity of *Pm*HAS in the immobilization step was varied, enabling the occupation of all available coordination sites. After improving the overall performance of p(VCL/NTAaa@Ni@*Pm*HAS), its reusability was controlled by performing three cycles of HA formation, removing the formed products after each cycle.

3.3.1. Variation of the Used Cation

The incorporation of Ni^{2+}, Co^{2+}, Mn^{2+}, Mg^{2+}, and Fe^{2+}/Fe^{3+} into p(VCL/NTAaa) resulted in the formation of p(VCL/NTAaa@Me), followed by the immobilization of *Pm*HAS to form p(VCL/NTAaa@Ni@*Pm*HAS). Considering the determined metal loading efficiency, immobilization may exhibit optimal conditions in microgels containing Ni^{2+} and Co^{2+}. However, it is essential to account for various factors influencing the binding efficiency, including complex stability and the enzyme's affinity to the metal complex. While the His_6Tag mediates the enzyme's affinity for Ni^{2+} and Co^{2+},[6,34] its role in binding to Mn^{2+}, Mg^{2+}, and Fe^{2+}/Fe^{3+}, remains uncertain, as other amino acid residues may also contribute to binding. Moreover, the presence of Mn^{2+} and Mg^{2+} as *Pm*HAS cofactors, complexed by UDP-sugars for active substrate formation, might affect the enzyme's affinity binding. The behavior of p(VCL/NTAaa@Fe) is particularly challenging to predict due to the strong unspecific interactions of Fe^{2+}/Fe^{3+} with the microgel.

The progression of HA synthesis over time was tracked by monitoring UDP formed by various p(VCL/NTAaa@Me@PmHAS) hybrids (**Figure IV.5a**).

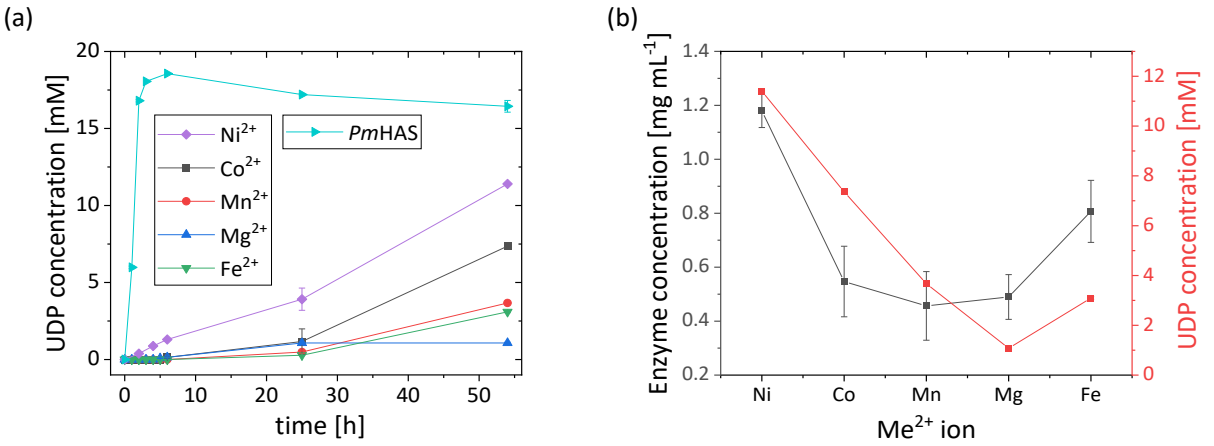

Figure IV.5 p(VCL/NTAaa@Me@*Pm*HAS) (χ_{NTA} = 1 mol%) containing different metal ions (Ni^{2+}, Co^{2+}, Mn^{2+}, Mg^{2+}, and Fe^{2+}/Fe^{3+}) were prepared by employing 1.5 mg mL^{-1} purified *Pm*HAS during enzyme immobilization. Using these concentrations, 3.78 NTA coordination sites are available for each His in the His_6-Tag of *Pm*HAS. (a) The investigation of microgels included the monitoring of UDP formation over time, comparing the microgel samples to purified His_6-tagged *Pm*HAS (1.5 mg mL^{-1}). (b) The UDP formed after 54 hours of reaction time (right Y axis) is compared to the number of immobilized enzymes determined through a Bradford assay (left Y axis).

Figure IV.5a indicates a decreased rate of HA synthesis in all p(VCL/NTAaa@Me@*Pm*HAS) compared to the pure enzyme, likely due to different factors: Steric hindrance by the microgel may impede HA formation, and incomplete immobilization results in a slightly lowered enzyme concentration (as discussed below). The analysis of UDP concentration in the purified *Pm*HAS sample reveals a rapid increase to 18.6 mM (92.8 % of the maximum possible UDP concentration of 20 mM). This is followed by a gradual decrease to 16.4 mM (82.2 %), which is caused by the hydrolysis of UDP in an alkaline environment, accompanied by the formation of UMP and phosphate (**Scheme IV.3**). This UMP formation has been previously demonstrated during the synthesis of HA from *Pm*HAS.[18,19]

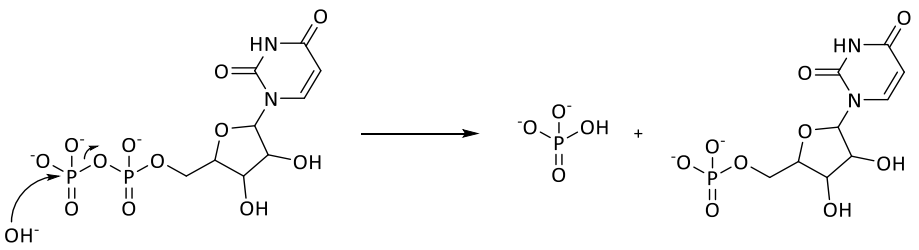

Scheme IV.3 Alkaline hydrolysis of UDP leads to the generation of UMP and phosphate.

Upon comparison of the p(VCL/NTAaa@Me@*Pm*HAS) hybrids based on their ability for UDP formation (**Figure IV.5b**), a clear trend can be identified. Microgels containing Ni^{2+} attain the highest UDP concentration after 54 hours, accounting for 57.0 % of the maximum yield, followed by those containing Co^{2+} at 36.8 %. Conversely, p(VCL/NTAaa@Me@*Pm*HAS) containing Mn^{2+} (18.3 %), Fe^{2+}/Fe^{3+} (15.5 %), and Mg^{2+} (5.4 %) attained lower yields. Using p(VCL/NTAaa@Fe) has led to partial *Pm*HAS immobilization but it remains uncertain whether this is explained by the complexation of Fe^{2+}/Fe^{3+} through NTA.

In addition to the UDP concentration after 54 hours (**Figure IV.5b**, right y-axis), connecting the obtained data for UDP formation with the amount of immobilized *Pm*HAS delivers further valuable information (**Figure IV.5b**, left y-axis), not only assessing the overall activity of p(VCL/NTAaa@Me@*Pm*HAS) but taking into account the amount of immobilized *Pm*HAS. This enables drawing conclusions about the activity of individual *Pm*HAS enzymes within the microgels. Additionally, the relationship between the concentration of *Pm*HAS in the samples and the metal ion concentration is illustrated in the **Supplementary Data** (**Figure SIV.4**) to discern any potential correlations. However, since the choice of metal is a crucial factor, this relationship is of secondary importance and will not be extensively discussed: The binding affinity to *Pm*HAS may play a more significant role than the metal content.

Ni^{2+} facilitated the incorporation of the highest amount of enzymes, while other metal ions led to lower enzyme content. Interestingly, despite Fe^{2+}/Fe^{3+} exhibiting the second-highest enzyme binding, the resulting UDP formation was not correspondingly high. This discrepancy suggests that the excessive presence of Fe^{2+}/Fe^{3+} in the microgels may disrupt enzyme activity despite facilitating *Pm*HAS immobilization. Given the nonspecific interactions of Fe^{2+}/Fe^{3+} with the microgels, its usage is not recommended. Surprisingly, Co^{2+} displayed slightly lower immobilization despite its high content and enzyme activity. This observation suggests that while the immobilized *Pm*HAS might be more active, it is present in a lower concentration. Conversely, p(VCL/NTAaa@Me@*Pm*HAS) with Mn^{2+} and Mg^{2+} exhibited the lowest enzyme content, consistent with their low metal contents. Most Bradford measurements exhibited relatively large standard deviations, potentially attributed to single microgels present in the supernatant. These microgels could interfere with UV-Vis measurements as they are UV-Vis

active,[20] and interactions between the Bradford reagent and the microgels may marginally distort the results.

It is important to note that dissolved metal ions have the potential to influence the *Pm*HAS activity, as demonstrated in prior studies by Eisele *et al.*[19] Their research indicates that Ni^{2+} can lead to nearly complete *Pm*HAS deactivation, at concentrations of 1 mM and higher. In this system, the Ni^{2+} concentration is 0.2 mM, as indicated in **Table IV.2**. Nevertheless, even at lower concentrations, a deactivating effect cannot be ruled out. However, the behavior of Ni^{2+} complexed by NTA in this system may differ from that of free metal ions and thus a deactivating effect cannot be predicted.

In summary, p(VCL/NTAaa@Ni) stands out as the most favorable hybrid microgel for *Pm*HAS immobilization and HA production. Consequently, additional investigations utilizing p(VCL/NTAaa@Ni) are performed to refine enzymatic activity. This entails varying the NTAaa content within the microgel, thereby adjusting the Ni^{2+} concentration to facilitate the immobilization of the optimal enzyme quantity.

3.3.2. Variation of the Ni-NTA Content

Microgels with different χ_{NTA} were synthesized and employed for Ni^{2+} incorporation and subsequent *Pm*HAS immobilization. The enzymatic activity of p(VCL/NTAaa@Me@*Pm*HAS) microgels was assessed by comparing the amount of UDP formed after specific time intervals (0, 2, 4, 6, 25, and 54 h). The complete dataset, including measurements at various time points, is detailed in **Figure IV.6a**. For enhanced comparability, the UDP concentration after 54 hours of enzymatic reaction is depicted in **Figure IV.6b**, contrasted with the enzyme concentration in p(VCL/NTAaa@Ni@*Pm*HAS).

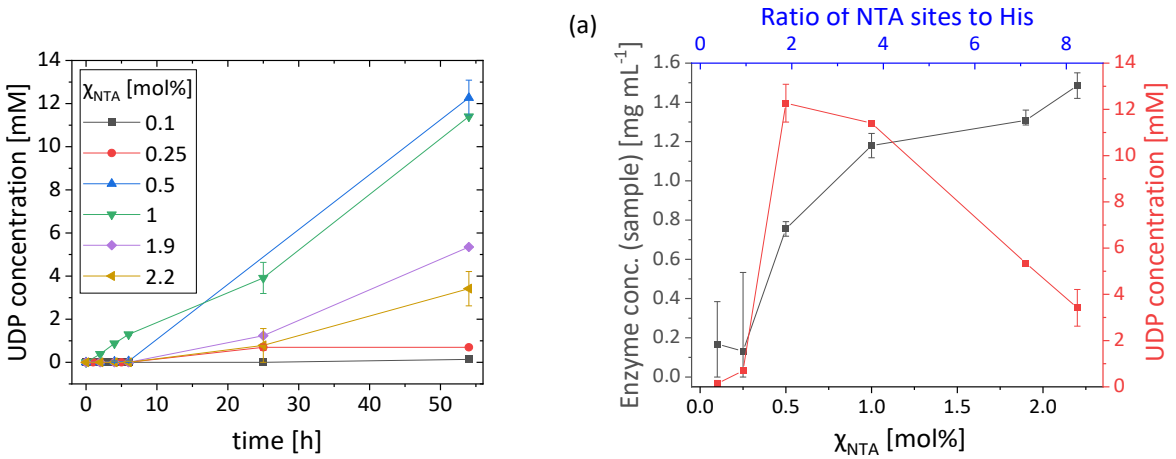

Figure IV.6 p(VCL/NTAaa@Ni@*Pm*HAS) containing different NTA contents (χ_{NTA} = 0.1, 0.25, 0.5, 1.0, 1.9, and 2.2 mol%) were prepared by employing 1.5 mg mL^{-1} purified *Pm*HAS during enzyme immobilization. Using these concentrations, the number of available NTA coordination sites for each His in the His_6-Tag of *Pm*HAS is varied (0.38, 0.95, 1.90, 3.78, 7.10, and 8.19) according to **Table IV.3**. (a) The investigation of microgels included the monitoring of UDP formation over time. (b) The UDP formed after 54 hours of reaction time (right y-axis) is compared to the amount of immobilized enzymes determined through a Bradford assay (left y-axis). The x-axis indicates χ_{NTA}, while a second x-axis shows the ratio of available coordination sites to His groups in the His_6-Tag of *Pm*HAS.

A rise in *Pm*HAS concentration in p(VCL/NTAaa@Me@*Pm*HAS) samples with higher χ_{NTA} values was revealed (**Figure IV.6b**, left y-axis) while holding a constant concentration of 1.5 mg mL^{-1} purified *Pm*HAS during enzyme loading. This observation stems from the fact that χ_{NTA} dictates the number of available binding sites for *Pm*HAS. This trend is further reflected in the amount of UDP formed at lower χ_{NTA} up to 0.5 mol%, displaying an increase with increasing χ_{NTA} (**Figure IV.6b**, right y-axis). However, at higher χ_{NTA} values, a decrease in the UDP concentration is observed instead of a further increase. To scrutinize this unexpected trend, the ratio of available coordination sites to each of the six His units in the His_6-Tag of *Pm*HAS is shown as an additional x-axis in **Figure IV.6b**. Exact ratios are listed in **Table IV.3**.

Theoretically, the number of coordination sites for all microgels with comonomer contents above χ_{NTA} = 0.25 mol%, is sufficiently high to enable the attachment of all His units in the His_6-Tag. However, the number of immobilized enzymes indicates otherwise, and not all His units can attach to p(VCL/NTAaa@Ni) at the same time: The binding of all six His units would mean that three NTA units would have to be close to each other and in the vicinity of the enzyme, resulting in high steric repulsion. A slight surplus of available coordination sites prevents this problem. Thus, p(VCL/NTAaa@Ni) with such a surplus of coordination sites, containing χ_{NTA} =

0.5 to 1 mol%, enable the immobilization of a much higher number of enzymes, resulting in a further increase of UDP formation. At higher χ_{NTA} values of 1.9 to 2.2 mol% the amount of immobilized *Pm*HAS increases further, but is not accompanied by a higher enzymatic activity, but by a decrease. This phenomenon can be further elucidated by reconsidering the proportion of NTA coordination sites relative to the number of His groups in the His_6-Tag of *Pm*HAS (**Table IV.3**). *Pm*HAS enzyme, comprises a total of 23 His residues, and not only the His_6-Tag, as delineated in its amino acid sequence (**Materials and Methods**). The relatively large number of available coordination sites (approximately seven to eight), results in undesirable interactions of NTA with His residues apart from those in the His_6-Tag, which can cause deactivation especially if these are located in the active center. These findings suggest that maintaining an appropriate ratio between NTA coordination sites and His units in the His_6-Tag may be crucial. Apart from altering the NTA concentration, this ratio could also be influenced by changes in the *Pm*HAS concentration. As a result, the next phase of the investigation involved varying the enzyme concentration during immobilization.

Table IV.3. The ratio of available coordination sites in p(VCL/NTAaa@Ni) (two per NTA unit) to His units in the His_6-Tag of *Pm*HAS, when employing 1.5 mg mL^{-1} purified *Pm*HAS during enzyme immobilization for p(VCL/NTAaa@Ni@*Pm*HAS) fabrication. χ_{NTA} thereby dictates the number of available coordination sites.

NTA content χ_{NTA} [mol %]	Ratio NTA sites to His
0.1	0.38
0.25	0.95
0.5	1.90
1	3.78
1.9	7.10
2.2	8.19

3.3.3. Variation of the Enzyme Amount During Immobilization

This chapter aims towards the increase of immobilized *Pm*HAS in p(VCL/NTAaa@Ni@*Pm*HAS) by increasing the employed concentration during immobilization. Microgels with χ_{NTA} = 1 mol% and 2.2 mol% were used. Both microgels possess available NTA sites for sufficient *Pm*HAS immobilization. The amount of immobilized *Pm*HAS (**Figure IV.7c**, left y-axis) and the amount of UDP formed during the enzymatic synthesis were determined (**Figure IV.7a-b**; **Figure IV.7c**, left y-axis). The complete datasets for UDP formation are shown in

Figure IV.7a-b, indicating the typical increase of UDP concentration over time. **Figure IV.7c** then depicts the UDP concentration after 54 hours of enzymatic reaction, compared to the concentration of immobilized enzymes in p(VCL/NTAaa@Ni@*Pm*HAS). The only exception here is the data point for p(VCL/NTAaa@Ni@*Pm*HAS) with χ_{NTA} = 1 mol% and an enzyme concentration of 2.1 mg mL^{-1} which was taken at 24 h. Even though a shorter reaction time was used, the expected activity increase can already be seen for this data point.

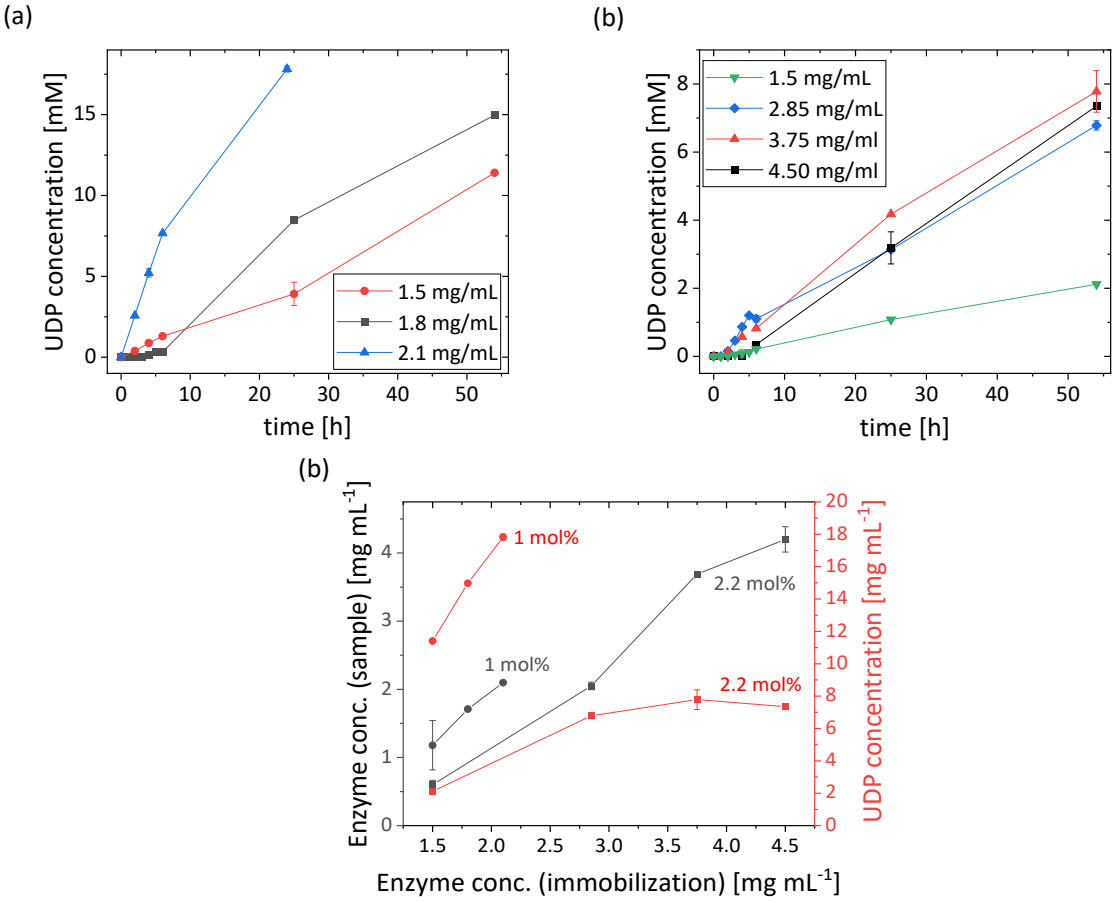

Figure IV.7 p(VCL/NTAaa@Ni@*Pm*HAS) containing different NTA contents (χ_{NTA} = 1.0, and 2.2 mol%) were prepared by employing varying concentrations of purified *Pm*HAS during enzyme immobilization (1.5, 1.8, 2.1, 2.85, 3.76, and 4.50 mg mL^{-1}). Using these concentrations, the number of available NTA coordination sites for each His in the His_6-Tag of *Pm*HAS is varied (0.38, 0.95, 1.90, 3.78, 7.10, and 8.19) according to **Table IV.4**. (a), (b) The investigation of microgels included the monitoring of UDP formation over time. (c) The UDP formed after 54 hours of reaction time (right y-axis) is compared to the amount of immobilized enzymes determined through a Bradford assay (left y-axis). The x-axis indicates the employed *Pm*HAS concentration during immobilization.

Comparing the amount of immobilized *Pm*HAS (**Figure IV.7c**, left y-axis), p(VCL/NTAaa@Ni@*Pm*HAS) microgels display the expected behavior: With increasing *Pm*HAS

concentration during immobilization, its concentration in the microgels also increases. For all employed enzyme concentrations an excess of available coordination sites ensures near-complete immobilization (**Table IV.4**). Notably, at an employed *Pm*HAS concentration of 1.5 mg mL^{-1}, the microgels with χ_{NTA} = 1 mol% can immobilize a larger enzyme amount, possibly due to the variations in morphology between both microgels and an associated variation in NTA distribution throughout the microgel.

Table IV.4. The ratio of available coordination sites in p(VCL/NTAaa@Ni) (two per NTA unit) to His units in the His_6-Tag of *Pm*HAS, when employing different concentrations of purified *Pm*HAS during enzyme immobilization for p(VCL/NTAaa@Ni@*Pm*HAS) fabrication. χ_{NTA} (1 or 2.2 mol%) and *Pm*HAS concentration thereby dictate the number of available coordination sites.

NTA content χ_{NTA} [mol%]	Enzyme concentration [mg mL^{-1}]	Ratio NTA sites to His
1	1.5	3.78
1	1.8	3.15
1	2.1	2.70
2.2	1.5	8.19
2.2	2.85	4.31
2.2	3.75	3.28
2.2	4.5	2.73

The increase of *Pm*HAS concentration in p(VCL/NTAaa@Ni@*Pm*HAS) microgels does not necessarily result in higher enzymatic activity. While microgels containing χ_{NTA} = 1 mol% exhibit a significant increase in UDP concentration, those with 2.2 mol% do not display this behavior. Despite containing a higher amount of *Pm*HAS than microgels with lower χ_{NTA}, the higher NTA content does not correlate with a greater amount of UDP formed; instead, its activity is markedly lower. The observed trend may be attributed to the increased concentration of Ni^{2+} in the system. It has been noted earlier that the presence of Ni^{2+} ions, can significantly deactivate *Pm*HAS,[19] possibly even when complexed. Comparing the concentrations of Ni^{2+} in the microgel dispersions employed, the sample with 1 mol% contains 0.199 µmol mL^{-1}, while the 2.2 mol% sample contains approximately 2.2 times this amount (0.438 µmol mL^{-1}). Consequently, the likelihood of *Pm*HAS deactivation increases: The findings by Eisele et al.[19] indicate that *Pm*HAS deactivation can occur even at low Ni^{2+} concentrations, with complete deactivation observed at concentrations as low as 1 mM. Therefore, it is expected that deactivation would occur at the lower concentration of 0.4 mM for non-

complexed Ni^{2+}. While this effect might be less pronounced for complexed metal ions, due to their reduced ability to diffuse freely within the enzyme structure, the presented results suggest that even complexed Ni^{2+} results in partial deactivation of *Pm*HAS.

In conclusion, based on these findings, p(VCL/NTAaa@Ni@PmHAS) with χ_{NTA} = 1 mol% emerges as the most promising microgel for HA synthesis.

3.3.4. Enzyme Recovery and Reuse

The possibility of reusing the p(VCL/NTAaa@Ni@*Pm*HAS) microgel with χ_{NTA} = 1 mol% for several cycles of enzymatic HA formation was assessed. A concentration of 2.1 mg mL^{-1} purified *Pm*HAS was employed for enzyme immobilization. The enzymatic HA formation was allowed to proceed for 24 hours, after which the microgel hybrid was separated from the reaction solution. Subsequently, the HA formation process was repeated with a fresh substrate solution. This recovery and reuse process was carried out twice, and the resulting data are depicted in **Figure IV.8a** in comparison to the UDP formation curve of purified *Pm*HAS.

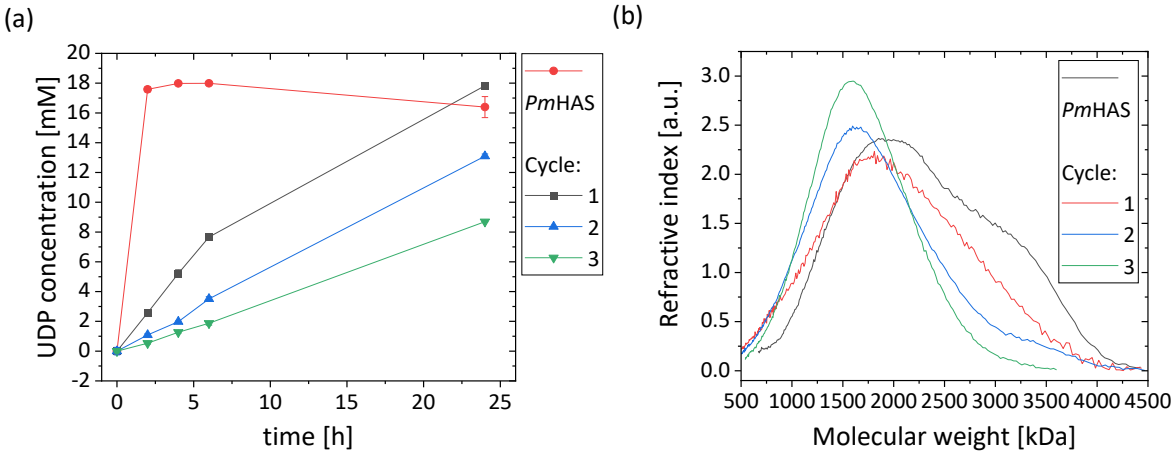

Figure IV.8 p(VCL/NTAaa@Ni@*Pm*HAS) (χ_{NTA} = 1 mol%) was prepared by employing 2.1 mg mL^{-1} purified His_6-tagged *Pm*HAS during enzyme immobilization. (a) The investigation of microgels was performed by monitoring UDP formation over time, comparing the *Pm*HAS-microgel samples to purified, non-immobilized *Pm*HAS (2.1 mg mL^{-1}). Three cycles of recovery and reuse were performed, by reusing p(VCL/NTAaa@Me@*Pm*HAS) for three cycles of HA formation. (b) The resulting HA was investigated with SEC regarding its molecular weight distribution, compared to HA formed by purified *Pm*HAS.

The UDP formation rate of the optimized p(VCL/NTAaa@Ni@*Pm*HAS) hybrid microgels is still lower than the one of the purified, non-immobilized *Pm*HAS. This observed phenomenon has also been demonstrated using immobilization in microbeads, as evidenced in the study of Gottschalk *et al*.[13] The deceleration is most likely mainly attributed to hindered substrate diffusion within the microgel matrix. However, while the formation rate is slower, p(VCL/NTAaa@Ni@*Pm*HAS) attains similar UDP concentrations in the first cycle (17.8 mM after 24 h) as purified *Pm*HAS (18.0 mM after 6 h).

Comparing the first cycle, reaching 89.1 % of the maximum UDP concentration, to the other cycles, the yield after 24 hours is slightly decreased to 65.5 % (13.1 mM), and then 43.5 % (8.7 mM). However, these yields are still superior compared to yields from UDP formation in magnetic beads containing immobilized *Pm*HAS, which are 61 % (12.2 mM), 55 % (11.1 mM), and 39 % (7.8 mM).[13]

In both systems, the decline in UDP production observed in each recovery and reuse cycle is likely attributed to partial enzyme deactivation or loss, possibly stemming from non-permanent affinity binding. Upon centrifugation at high speeds during the work-up, the formation of a strongly pelleted enzyme-microgel hybrid was realized, minimizing potential losses of p(VCL/NTAaa@Ni@*Pm*HAS). Next to enzyme loss or deactivation, residual HA in the reaction solution from the preceding cycles might impede substrate and product transfer, hindered by electrostatic repulsion and steric interactions. The direct repetition of HA formation without intervening washing steps suggests that remaining HA could impact reaction kinetics.

To conclude, high enzymatic activity combined with PmHAS immobilized in soft microgels enables a large number of applications. Unlike the His Mag Sepharose™ Ni beads employed previously,[13] p(VCL/NTAaa) microgels are evidently biocompatible.[20] Metal ion leaching from the microgels can generally cause a decrease in biocompatibility,[35] but the employed concentrations of metal ions are far below the previously reported limits.[36,37]

Therefore, the potential application of these microgels in biological contexts appears promising. Inspired by natural mucin's capacity to produce polysaccharides, these microgels could serve as a basis for developing adaptive hydrogel materials. Scaling up the synthesis of these microgels in the future could enable the production of larger quantities of HA,

addressing the considerable demand for this compound in medical,[38,39] cosmetic,[40] and other applications.

3.4. Characterization of the Formed Hyaluronic Acid

Subsequently, characterization of the synthesized HA concerning its molecular weight and composition was undertaken, employing SEC and FT-IR spectroscopy. Therefore, the HA from recovery and reuse tests was characterized, isolating HA from the microgels by centrifugation. The SEC data, depicted in **Figure IV.8b**, illustrates comparable molecular weights (M_w) for all cycles, albeit slightly diminishing with each successive cycle (**Table IV.5**).

Additionally, the polymer dispersities exhibit relatively low values (< 1.24), displaying a tendency to decrease with each cycle of HA formation (**Table IV.5**). Jing et al.[16] demonstrated that *Pm*HAS undergoes an initial phase wherein it forms HA oligosaccharides at a slow rate, which are subsequently elongated to produce HA polysaccharides. When numerous HA oligosaccharides are already present in the solution, the formed HA polysaccharides may exhibit more uniform chain lengths and lower molecular weight.[16,18] Hence, the hypothesis is that with each recovery and reuse step, an increased quantity of HA oligosaccharides is initially generated, leading to an overall reduction in molecular weight as well as lower dispersities.

Table IV.5. Molecular weights and dispersities of p(VCL/NTAaa@Me@*Pm*HAS) after different recovery and reuse steps (three cycles) regarding the formed HA. The samples were analyzed using SEC and compared to pure *Pm*HAS.

Sample	Molar mass (M_n) [MDa]	Molar mass (M_w) [MDa]	Dispersity (D) [a.u.]
Enzyme	1.77	2.03	1.15
Cycle 1	1.40	1.74	1.24
Cycle 2	1.35	1.61	1.19
Cycle 3	1.39	1.55	1.12

The resulting dispersity values are comparable to those observed with the purified enzyme (**Table IV.5**). However, a notable difference is observed in the molecular weight distribution of HA formed from p(VCL/NTAaa@Ni@*Pm*HAS) hybrid microgels compared to that formed with the purified enzyme (**Figure IV.8b**). Specifically, the shoulder present in the molecular weight distribution of HA from the purified enzyme is barely discernible for the HA formed

with the hybrid microgels. While the first cycle still exhibits indications of a shoulder, it disappears for the second and third cycles. In summary, although the dispersities are similar, a more uniform molecular weight distribution is observed for HA formed by p(VCL/NTAaa@Ni@*Pm*HAS). It is noteworthy that the higher molecular weight obtained with the purified enzyme may be attributed to longer contact time, as the enzyme was exposed to the substrate for an extended duration compared to the p(VCL/NTAaa@Ni@*Pm*HAS) samples, where the HA/substrate solution was separated from the microgel hybrid directly after each 24-hour cycle.

Notably, a direct comparison between the presented M_w values and those reported by Gottschalk *et al*.[13] is challenging due to differences in the methodologies employed for determination. Nevertheless, the differences will be mentioned shortly: In comparison to their study (1st cycle: 1.2 MDa, 2nd cycle: 2.3 MDa, 3rd cycle: 2.8 MDa), the observed molecular weights (M_w) in this thesis are lower. Additionally, the strongly increasing M_w with each cycle observed in their study was not confirmed in the presented work. Here, an opposite trend was observed, albeit much less pronounced: a decreasing M_w with each cycle was demonstrated (**Table IV.5**). Gottschalk *et al*.[13] elucidate that the increasing molecular weight with each cycle results from the elongation of existing HA chains rather than the formation of new chains, as polymerization is favored over *de novo* HA synthesis. In this study, the near-complete removal of HA was achievable after each recovery and reuse step, whereas in their work, larger amounts of HA were left in the reaction vial, available for further elongation by *Pm*HAS in the subsequent cycle. The uniformity in M_w achieved in this thesis may prove beneficial for applications that demand consistent HA properties across multiple batches.

HA was additionally analyzed using FT-IR spectroscopy, employing a commercial HA sodium salt as a reference. The spectra, exhibit overlapping signals for all major functional groups (**Figure IV.9**). While there are some differences between the recorded spectra, these can be attributed to the protonated carboxylic groups in the synthesized HA, resulting in additional peaks at 1730 cm^{-1} and 1255 cm^{-1}. Contrary, the commercial HA exists solely as its sodium salt. Peak assignments were confirmed by previous studies.[41,42]

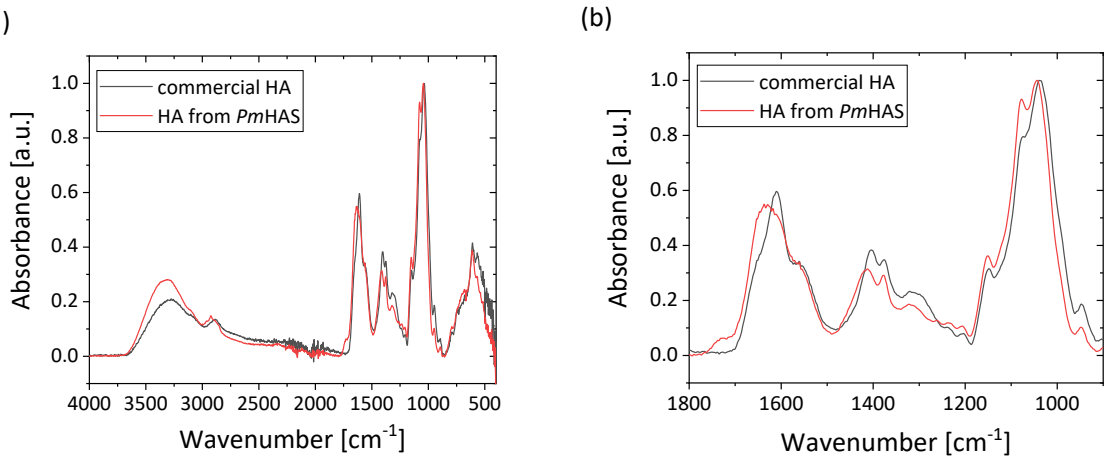

Figure IV.9 (a) Comparison of the FT-IR spectra of HA, enzymatically synthesized by *Pm*HAS and commercial HA sodium salt. Peaks overlap and display similar intensities. Differences in spectra are explained by the presence of the acidic form of HA in the sample: Commercial HA was purchased as its sodium salt, whereas enzymatically synthesized HA is a mixture of HA salt and acid and possesses additional peaks at 1730 cm^{-1} and 1255 cm^{-1}. (b) Magnified section of the FT-IR spectra displaying important peaks.

The O-H stretching vibration of residual water is reflected in a broad band observed at 3500-3000 cm^{-1}. Furthermore, the abundance of HA-inherent hydroxyl groups, contributions from the N-H stretching vibration of the amide group of GlcNAc, and the O-H stretching vibration of the carboxylic group of the GlcA moiety, are present in this peak. Within the range of 3000-2800 cm^{-1}, C-H stretching vibrations are predominant. The band spanning from 1680-1500 cm^{-1} arises from the asymmetric C=O stretching vibrations of the carboxylate group, along with the characteristic amide I and II bands of HA.[42] Another peak observed at 1730 cm^{-1} in the FT-IR spectrum of the HA from *Pm*HAS is attributed to the C=O stretching vibration of protonated carboxylic groups, absent in the commercial HA sodium salt spectrum. This shift indicates the presence of partially protonated HA carboxylic groups,[41,42] likely resulting from purification *via* dialysis. Furthermore, the peak at 1430-1390 cm^{-1} corresponds to the symmetric C-O stretching of the carboxylate group, with an anticipated shift to 1255 cm^{-1} for the C-O stretching of the protonated carboxylate group,[42] a detail emphasized in the magnified FT-IR spectrum in **Figure IV.9b** to differentiate the synthesized HA from the commercial HA sodium salt. The band at 1380-1370 cm^{-1} arises from C-H and O-H bending vibrations, while the one at 1320 cm^{-1} corresponds to the characteristic amide III band of HA.[41,42] Additionally, the peak at 1150 cm^{-1} can be associated with C-O stretching vibrations and asymmetric stretching vibrations, along with the bending of C-O-C.[42] Other notable

regions relate to characteristic HA bands: The band at 1077 cm^{-1} corresponds to C-C and C-O stretching, and C-OH bending. The peak at 1040 cm^{-1} is attributed to C-OH stretching, and the band at 950 cm^{-1} indicates asymmetrical ring out-of-phase vibrations.[42] Moreover, the bands in the fingerprint region overall align with existing literature.[41,42] All peaks are additionally listed in **Table IV.6**.

Table IV.6 FT-IR peaks of hyaluronic acid spectra (shown in **Figure IV.9**) in accordance with the literature.[41,42]

Peak [cm^{-1}]	Peak assignment
3500-3000	O-H stretching vibration of residual water and HA-inherent hydroxyl groups; N-H stretching vibration of the amide group of GlcNAc; O-H stretching vibration of the carboxylic group of the GlcA moiety
3000-2800	C-H stretching vibration
1680-1500	Asymmetric C=O stretching vibration of the carboxylate group; Amide I and II bands of HA
1730	C=O stretching vibration of the protonated carboxylic groups
1430-1390	Symmetric C-O stretching of the carboxylate group
1255	C-O stretching of protonated the carboxylate group
1380-1370	C-H and O-H bending vibrations
1320	Amide III band of HA
1150	C-O stretching vibrations and asymmetric stretching vibrations; Bending vibration of C-O-C
1077	C-C and C-O stretching; C-OH bending
1040	C-OH stretching
950	asymmetrical ring out-of-phase vibrations

In summary, SEC and FT-IR spectroscopy were successfully employed to investigate the HA formed during the enzymatic action of *Pm*HAS, either immobilized in microgels or dissolved in solution. In this thesis, the highest UDP and, thus HA yield was achieved by repetitive enzymatic synthesis through *Pm*HAS. Additionally, the developed p(VCL/NTAaa) microgels exhibit the potential for immobilizing various other enzymes containing a His-Tag.

4. Conclusion

Having established the utility of nitrilotriacetic acid (NTA) microgels for electrostatic immobilization, this chapter focused on the expansion of their application areas by immobilizing enzymes. The synthesis of p(VCL/NTAaa) microgels served as the foundation. Characterization methods such as FT-IR spectroscopy, ELS, and DLS were employed. The p(VCL/NTAaa) microgels containing varying amounts of NTA were used for the complexation of Ni^{2+}, Co^{2+}, Mn^{2+}, Mg^{2+}, and Fe^{2+}/Fe^{3+} which was confirmed by ICP-OES and ζ measurements. Using metal affinity, the enzyme Hyaluronan Synthase from *Pasteurella multocida* (*Pm*HAS) was attached to the microgels. A polyhistidine tag (His_6-Tag) in the enzyme amino acid sequence enabled enzyme immobilization by mutual complexation of a metal ion by enzyme and microgel. Examination of uridine diphosphate (UDP) formation during HA synthesis *via* capillary electrophoresis demonstrated that p(VCL/NTAaa@Ni) microgels exhibited the most favorable characteristics for *Pm*HAS immobilization and HA production: By employing p(VCL/NTAaa@Ni) microgels, not only was the highest amount of *Pm*HAS immobilized, but the resulting p(VCL/NTAaa@Ni@*Pm*HAS) microgels also exhibited the highest activity, confirming successful immobilization of active *Pm*HAS.

Detailed investigation of HA formation using a range of p(VCL/NTAaa@Ni) microgels revealed specific biocatalytic behavior as the NTA content increased. Initially, there was a rise in *Pm*HAS activity, but this was followed by a decline, attributed to interactions between Ni^{2+} and the His units in the enzyme. Through optimization efforts, a hybrid microgel with maximal productivity was developed, resulting in the highest yield of UDP and consequently, HA polysaccharides *via* the biocatalysis of immobilized *Pm*HAS reported so far. This achievement in HA production was further validated by demonstrating the system's reusability over three 24-hour cycles, emphasizing reusability and simple recovery of the enzyme-microgel hybrid.

In summary, the prepared microgels with immobilized *Pm*HAS serve as continuous producers of HA when providing the necessary enzyme substrates. Furthermore, they hold the potential for designing adaptive hydrogel materials, drawing inspiration from natural mucin, which also continuously produces lubricant polysaccharides.

5. References

(1) Wang, C.-C.; Lee, J.-C.; Luo, S.-Y.; Kulkarni, S. S.; Huang, Y.-W.; Lee, C.-C.; Chang, K.-L.; Hung, S.-C. Regioselective One-Pot Protection of Carbohydrates. *Nature* **2007**, *446*, 896–899.

(2) Weijers, C. A. G. M.; Franssen, M. C. R.; Visser, G. M. Glycosyltransferase-Catalyzed Synthesis of Bioactive Oligosaccharides. *Biotechnol. Adv.* **2008**, *26*, 436–456.

(3) Torres-Salas, P.; Del Monte-Martinez, A.; Cutiño-Avila, B.; Rodriguez-Colinas, B.; Alcalde, M.; Ballesteros, A. O.; Plou, F. J. Immobilized Biocatalysts: Novel Approaches and Tools for Binding Enzymes to Supports. *Adv. Mater.* **2011**, *23*, 5275–5282.

(4) Guisan, J. M., Ed. *Immobilization of Enzymes*; Immobilization of Enzymes and Cells. Methods in Biotechnology 22; Humana Press, 2006.

(5) Guisan, J. M., Ed. *Affinity Immobilization of Tagged Enzymes*; Immobilization of Enzymes and Cells. Methods in Biotechnology 22; Humana Press, 2006.

(6) Block, H.; Maertens, B.; Spriestersbach, A.; Brinker, N.; Kubicek, J.; Fabis, R.; Labahn, J.; Schäfer, F. Immobilized-Metal Affinity Chromatography (IMAC): A Review. *Methods Enzymol.* **2009**, *463*, 439–473.

(7) Porath, J.; Olin, B. Immobilized Metal Affinity Adsorption and Immobilized Metal Affinity Chromatography of Biomaterials. Serum Protein Affinities for Gel-Immobilized Iron and Nickel Ions. *Biochem.* **1983**, 1621–1630.

(8) Gaberc-Porekar, V.; Menart, V. Perspectives of immobilized-metal affinity chromatography. *J. Biochem. Biophys. Methods* **2001**, *49*, 335–360.

(9) Mizrahi, B.; Irusta, S.; McKenna, M.; Stefanescu, C.; Yedidsion, L.; Myint, M.; Langer, R.; Kohane, D. S. Microgels for Efficient Protein Purification. *Adv. Mater.* **2011**, *23*, H258-62.

(10) Heida, T.; Köhler, T.; Kaufmann, A.; Männel, M. J.; Thiele, J. Cell-Free Protein Synthesis in Bifunctional Hyaluronan Microgels: A Strategy for In Situ Immobilization and Purification of His-Tagged Proteins. *ChemSystemsChem* **2020**, *2*, e1900058.

(11) Köhler, T.; Heida, T.; Hoefgen, S.; Weigel, N.; Valiante, V.; Thiele, J. Cell-Free Protein Synthesis and In Situ Immobilization of deGFP-MatB in Polymer Microgels for Malonate-to-Malonyl CoA Conversion. *RSC Adv.* **2020**, *10*, 40588–40596.

(12) Xu, H.; Wei, B.; Liu, X.; Huang, Y.; Zhou, W.; Liang, H. Robust Enhancing Stability and Fructose Tolerance of Sucrose Phosphorylase by Immobilization on Ni-NTA Functionalized

Agarose Microspheres for the Biosynthesis of 2-α-Glucosylglycerol. *Biochem. Eng. J.* **2022**, 108362.

(13) Gottschalk, J.; Aßmann, M.; Kuballa, J.; Elling, L. Repetitive Synthesis of High-Molecular-Weight Hyaluronic Acid with Immobilized Enzyme Cascades. *ChemSusChem* **2022**, *15*, e202101071.

(14) Bradford, M. M. A Rapid and Sensitive Method for the Quantitation of Microgram Quantities of Protein Utilizing the Principle of Protein-Dye Binding. *Anal. Biochem.* **1976**, *72*, 248–254.

(15) Gottschalk, J.; Elling, L. Current State on the Enzymatic Synthesis of Glycosaminoglycans. *Curr. Opin. Chem. Biol.* **2021**, *61*, 71–80.

(16) Jing, W.; DeAngelis, P. L. Synchronized Chemoenzymatic Synthesis of Monodisperse Hyaluronan Polymers. *J. Biol. Chem.* **2004**, *279*, 42345–42349.

(17) DeAngelis, P. L. Hyaluronan Synthases: Fascinating Glycosyltransferases from Vertebrates, Bacterial Pathogens, and Algal Viruses. *Cell. Mol. Life Sci.* **1999**, *56*, 670–682.

(18) Gottschalk, J.; Zaun, H.; Eisele, A.; Kuballa, J.; Elling, L. Key Factors for A One-Pot Enzyme Cascade Synthesis of High Molecular Weight Hyaluronic Acid. *Int. J. Mol. Sci.* **2019**, *20*, 5664.

(19) Eisele, A.; Zaun, H.; Kuballa, J.; Elling, L. In Vitro One-Pot Enzymatic Synthesis of Hyaluronic Acid from Sucrose and N-Acetylglucosamine: Optimization of the Enzyme Module System and Nucleotide Sugar Regeneration. *ChemCatChem* **2018**, *10*, 2969–2981.

(20) Sommerfeld, I. K.; Malyaran, H.; Neuss, S.; Demco, D. E.; Pich, A. Multi-Responsive Core-Shell Microgels Functionalized by Nitrilotriacetic Acid. *Biomacromolecules* **2024**, *25*, 903–923.

(21) Grabowski, F.; Petrovskii, V. S.; Fink, F.; Demco, D. E.; Herres-Pawlis, S.; Potemkin, I. I.; Pich, A. Anisotropic Microgels by Supramolecular Assembly and Precipitation Polymerization of Pyrazole-Modified Monomers. *Adv. Sci.* **2022**, *9*, e2204853.

(22) Irving, H. M.; Miles, M. G.; Pettit, L. D. A Study of Some Problems in Determining the Stoicheiometric Proton Dissociation Constants of Complexes by Potentiometric Titrations Using a Glass Electrode. *Anal. Chim. Acta* **1967**, *38*, 475–488.

(23) Das, A. K. Astatistical Aspects of the Stabilities of Ternary Complexes of Cobalt(II), Nickel(II), Copper(II) and Zinc(II) Involving Aminopolycarboxylic Acids as Primary Ligands and Salicylaldoxime as a Secondary Ligand. *Transition Met. Chem.* **1990**, *15*, 75–77.

(24) Tomita, Y.; Ueno, K. The Properties and Infrared Absorption Spectra of Nitrilotriacetate Chelates. *BCSJ* **1963**, *36*, 1069–1073.

(25) Anderson, R. L.; Bishop, W. E.; Campbell, R. L. A Review of the Environmental and Mammalian Toxicology of Nitrilotriacetic Acid. *Crit. Rev. Toxicol.* **1985**, *15*, 1–102.

(26) Martell, A. E.; Smith, R. M. *Critical Stability Constants: Inorganic Complexes*; Springer: New York, NY, 1976.

(27) Salam, M. A.; Aoki, K. Interligand Interactions Affecting Specific Metal Bonding to Nucleic Acid Bases: The Tripodal Nitrilotriacetato (NNTA) Ligand-System. Crystal Structures of [(NTA)(Adeninium)(Aqua)Nickel(II)] Hydrate, [(NTA)(Diaqua)Nickel(II)]·(Cytosinium) Hydrate, and [(NTA)(Diaqua)Nickel(II)]·(Cytosinium)·(Cytosine) Hydrate. *Inorg. Chim. Acta* **2000**, *311*, 15–24.

(28) Dung, N.-H.; Viossat, B.; Busnot, A.; González Pérez, J. M.; González García, S. Copper(II) and Nickel(II) Chelates of the Dihydrogen Nitrilotriacetate(1-) Ion: Crystal and Molecular Structure of Bis(N,N-Bis(Carboxymethyl) Glycinato) Copper(II) Dihydrate. *Inorg. Chem.* **1988**, 1227–1231.

(29) Souaya, E.; Hanna, W.; Ismail, E.; Milad, N. Studies On Some Acid Divalent-Metal Nitrilotriacetate Complexes. *Molecules* **2000**, *5*, 1121–1129.

(30) Zetter, M. S.; Grant, M. W.; Wood, E. J.; Dodgen, H. W.; Hunt, J. P. Water-Exchange Studies on Manganese(II) Nitrilotriacetate and Ethylenediaminetetraacetate Complexes by Oxygen-17 Nuclear Magnetic Resonance. *Inorg. Chem.* **1972**, *11*, 2701–2706.

(31) Motekaitis, R. J.; Martell, A. E. The Iron(III) and Iron(II) Complexes of Nitrilotriacetic Acid. *J. Coord. Chem.* **1994**, *31*, 67–78.

(32) Walters, M. A.; Vapnyar, V.; Bolour, A.; Incarvito, C.; Rheingold, A. L. Iron(III) Nitrilotriacetate and Iron(III) Iminodiacetate, their X-ray Crystallographic Structures and Chemical Properties. *Polyhedron* **2003**, *22*, 941–946.

(33) Sawada, K.; Duan, W.; Ono, M.; Satoh, K. Stability and Structure of Nitrilo(acetate–Methylphosphonate) Complexes of the Alkaline-Earth and Divalent Transition Metal Ions in Aqueous Solution. *J. Chem. Soc., Dalton Trans.* **2000**, 919–924.

(34) Chaga, G.; Bochkariov, D. E.; Jokhadze, G. G.; Hopp, J.; Nelson, P. Natural Poly-Histidine Affinity Tag for Purification of Recombinant Proteins on Cobalt(II)-carboxymethylaspartate Crosslinked Agarose. *J. Chromatogr. A* **1999**, *864*, 247–256.

(35) Büdinger, L.; Hertl, M. Immunologic Mechanisms in Hypersensitivity Reactions to Metal Ions: An Overview. *Allergy* **2000**, *55*, 108–115.

(36) Horie, M.; Nishio, K.; Fujita, K.; Kato, H.; Nakamura, A.; Kinugasa, S.; Endoh, S.; Miyauchi, A.; Yamamoto, K.; Murayama, H.; Niki, E.; Iwahashi, H.; Yoshida, Y.; Nakanishi, J. Ultrafine NiO Particles Induce Cytotoxicity in Vitro by Cellular Uptake and Subsequent Ni(II) Release. *Chem. Res. Toxicol.* **2009**, *22*, 1415–1426.

(37) Jia, W.; Beatty, M. W.; Reinhardt, R. A.; Petro, T. M.; Cohen, D. M.; Maze, C. R.; Strom, E. A.; Hoffman, M. Nickel Release from Orthodontic Arch Wires and Cellular Immune Response to Various Nickel Concentrations. *J. Biomed. Mater. Res.* **1999**, *48*, 488–495.

(38) Hansen, I. M.; Ebbesen, M. F.; Kaspersen, L.; Thomsen, T.; Bienk, K.; Cai, Y.; Malle, B. M.; Howard, K. A. Hyaluronic Acid Molecular Weight-Dependent Modulation of Mucin Nanostructure for Potential Mucosal Therapeutic Applications. *Mol. Pharmaceutics* **2017**, *14*, 2359–2367.

(39) Salwowska, N. M.; Bebenek, K. A.; Żądło, D. A.; Wcisło-Dziadecka, D. L. Physiochemical Properties and Application of Hyaluronic Acid: A Systematic Review. *J. Cosmet. Dermatol.* **2016**, *15*, 520–526.

(40) Juncan, A. M.; Moisă, D. G.; Santini, A.; Morgovan, C.; Rus, L.-L.; Vonica-Țincu, A. L.; Loghin, F. Advantages of Hyaluronic Acid and Its Combination with Other Bioactive Ingredients in Cosmeceuticals. *Molecules* **2021**, *26*.

(41) Pan, N. C.; Pereira, H. C. B.; Da Silva, M. d. L. C.; Vasconcelos, A. F. D.; Celligoi, Maria Antonia Pedrine Colabone. Improvement Production of Hyaluronic Acid by Streptococcus zooepidemicus in Sugarcane Molasses. *Appl. Biochem. Biotechnol.* **2017**, *182*, 276–293.

(42) Gilli, R.; Kacuráková, M.; Mathlouthi, M.; Navarini, L.; Paoletti, S. FTIR Studies of Sodium Hyaluronate and its Oligomers in the Amorphous Solid Phase and in Aqueous Solution. *Carbohydr. Res.* **1994**, *263*, 315–326.

6. Supplementary Data

Investigation of the Microgel Composition via FT-IR Spectroscopy

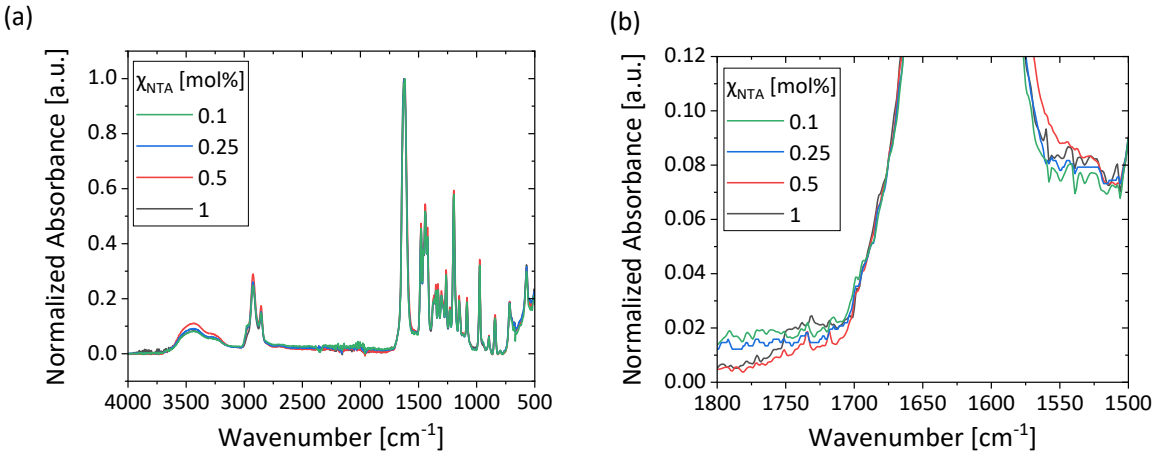

Figure SIV.1 (a) FT-IR spectra of p(VCL/NTAaa) microgels (χ_{NTA} = 0.1, 0.25, 0.5, and 1.0 mol%), along with (b) enlarged FT-IR spectra (1800 to 1500 cm^{-1}) of the microgels.

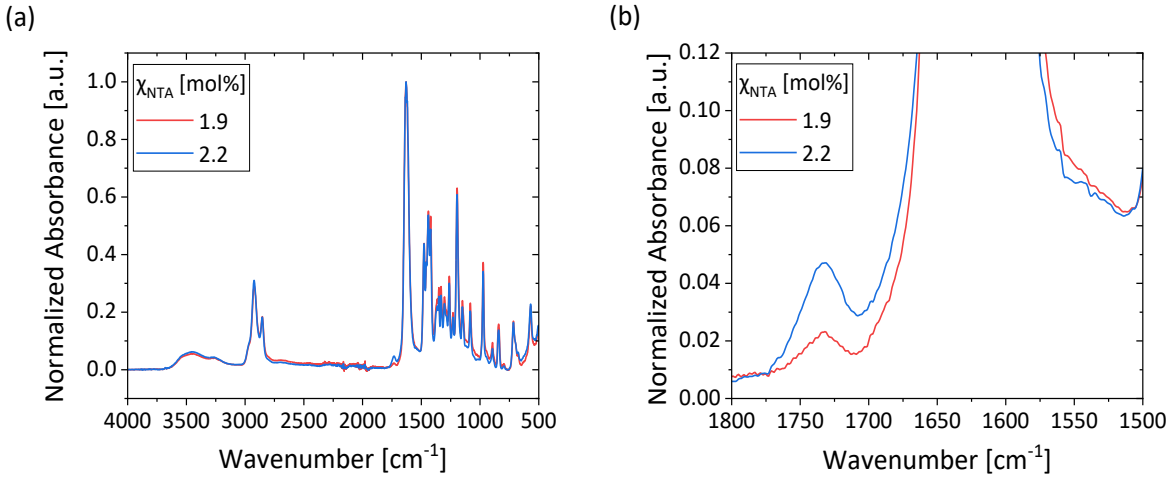

Figure SIV.2 (a) FT-IR spectra of p(VCL/NTAaa) microgels (χ_{NTA} = 1.9 and 2.2 mol%), along with (b) enlarged FT-IR spectra (1800 to 1500 cm^{-1}) of the microgels.

Incorporation of Metal Ions into p(VCL/NTAaa) Microgels

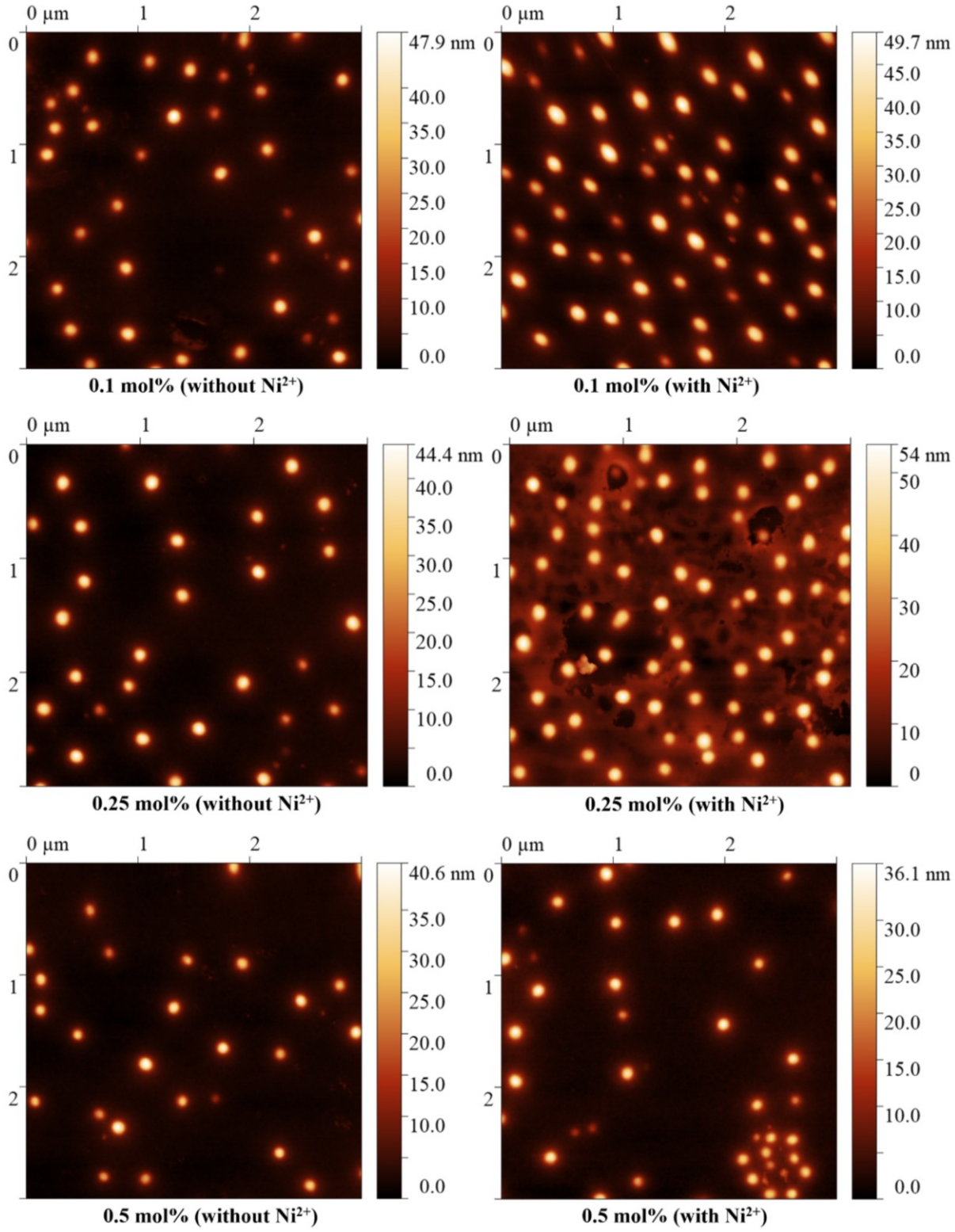

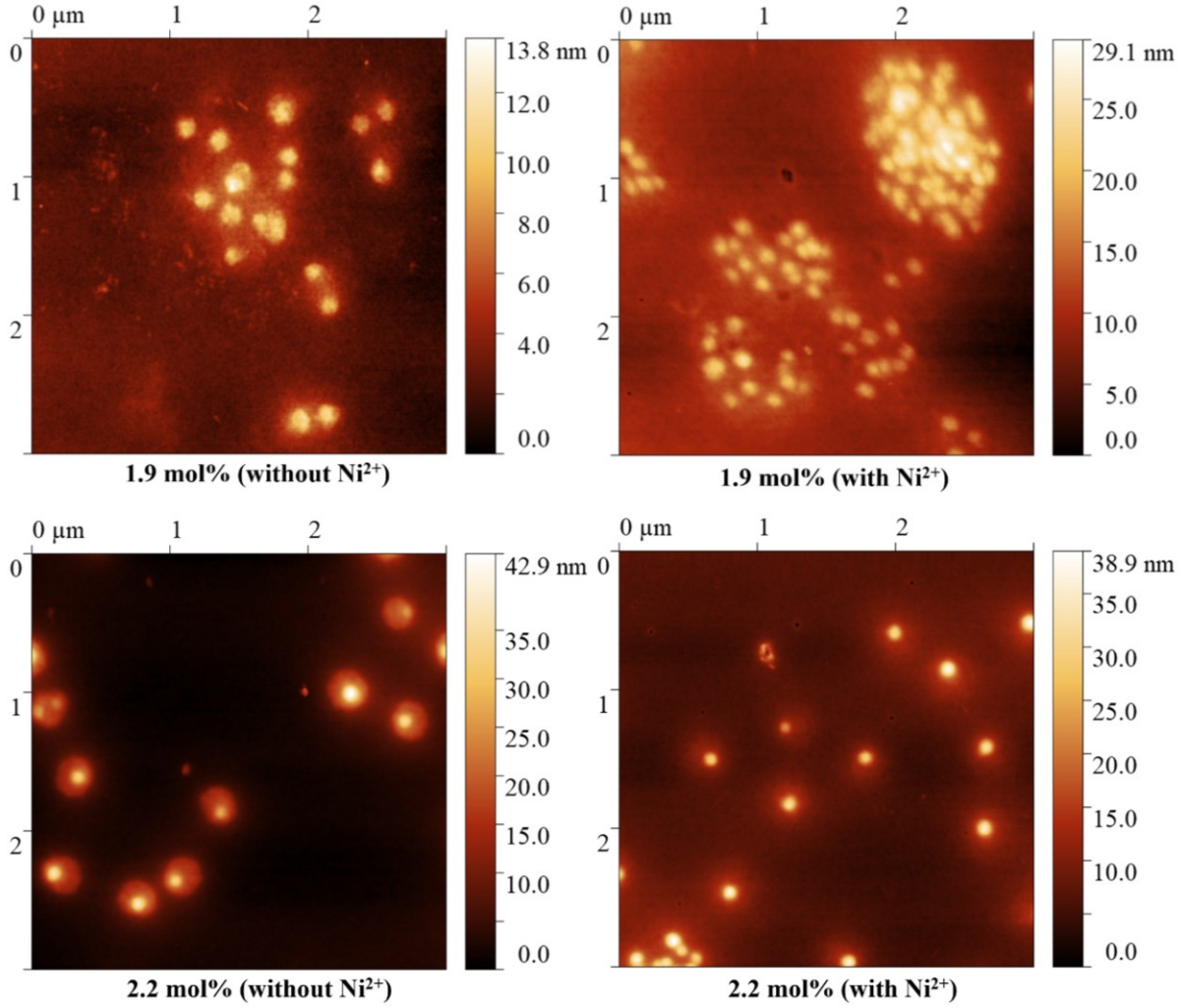

Figure SIV.3 Height profiles obtained from AFM imaging of p(VCL/NTAaa) (χ_{NTA} = 0.1, 0.25, 0.5, and 1.9 mol%) and their corresponding p(VCL/NTAaa@Ni) microgels. *In part reprinted with permission from the American Chemical Society.*[1]

Variation of the Used Cation

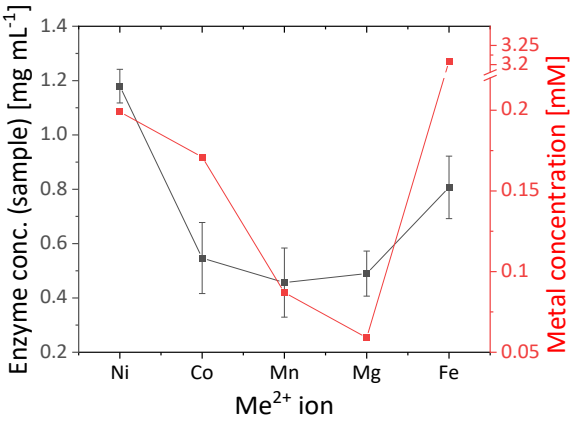

Figure SIV.4 p(VCL/NTAaa@Me) and p(VCL/NTAaa@Me@*Pm*HAS) samples (χ_{NTA} = 1 mol%) containing different metal ions (Ni^{2+}, Co^{2+}, Mn^{2+}, Mg^{2+}, and Fe^{2+}) are assessed regarding their metal content and amount of immobilized *Pm*HAS with 1.5 mg mL^{-1} purified *Pm*HAS being employed for enzyme immobilization.

V. PEG-Based Microgels as Carriers for Glycosyltransferase: Enzymatic Cascading for Glycan Synthesis

Large parts of this chapter are reprinted with permission from Sommerfeld, Isabel K.; Palm, Philip; Hussnaetter, Kai P.; Pieper, Maria I.; Bulut, Selin; Lile, Tudor; Wagner, Rebekka; Walkowiak, Jacek; Elling, Lothar, Pich; Andrij. Microgels with Immobilized Glycosyltransferases for Enzymatic Glycan Synthesis. *Biomacromolecules* **2024**, 25, 6, 3807–3822.[1] *Copyright 2024 American Chemical Society (ACS). Specifically, most Figures are adapted from this publication, with minor modifications.*

Contributions to this Chapter

The synthesis of the reported compounds was conducted either by myself or by my research assistant Tudor Lile under my supervision. Maria I. Pieper repeated one of the syntheses using my synthesis conditions. Microscopy and size determination were partially performed by my research assistant Tudor Lile under my supervision. Fluorescamine assays were partially conducted by Maria I. Pieper with a method previously developed by me. Permeability assays were performed by Selin Bulut, along with processing the obtained data, which was evaluated by me. Kai P. Hussnaetter and Philip Palm produced and purified the enzymes, conducted glycosyltransferase reactions, and provided me with the results in the form of enzyme activities or molar fractions of educts and products as well as HPLC chromatograms. All remaining data were processed and evaluated by me. Truc Pham assisted with enzyme production and purification.

1. Introduction

Glycans are fundamental to life and play pivotal roles in numerous biological processes[2,3] underscoring their significance in diverse applications such as drug development,[2,4] vaccine formulation,[5,6] nutrition,[7–10] and cosmetics.[11,12] Therefore, after successfully synthesizing the

glycosaminoglycan HA using immobilized *Pm*HAS (**Chapter IV**), the objective of this chapter is to utilize additional glycosyltransferases (GTs) for the synthesis of various other glycans using microgels as enzyme-carriers. This approach seeks to expand the range of applications and products not only through individual enzymatic synthesis but also through cascade reactions involving different enzymes. By employing one-pot-multienzyme reactions, the synthesis of a broader spectrum of products can be implemented without the need to isolate intermediate compounds.[13] Consequently, this chapter will explore both monoenzymatic GT reactions and cascade reactions involving different GTs.

There are various methods for the immobilization of enzymes (**Theoretical Background**). To employ microgels as carriers, entrapment and post-attachment can be used.[14,15] The distinction between entrapment and post-attachment relies on the selected synthesis approach. If microgels are synthesized in the presence of the enzyme, entrapment within the polymer matrix occurs during fabrication. Conversely, if microgels are prepared before enzyme immobilization, this process can be referred to as post-attachment.[15]

For both methods, different interactions can be utilized to immobilize enzymes. For example, weak or ionic interactions, covalent binding, or complexation, can be employed,[15] each possessing different advantages and disadvantages.[16,17] Among these, binding techniques that rely on the selective interaction of a reactive group with a specific part of the enzyme may be particularly favorable.[18,19] Metal affinity binding relies on the selective interaction of a His-tag in the enzyme with a metal ion incorporated into the microgel network (**Chapter IV**).[20] In addition to this concept, a range of other methods has been developed for the implementation of specific binding. Zou *et al.* introduced an enzyme immobilization technique employing sortase-mediated covalent ligation.[18] Moreover, protein fusions such as Halo-Tag[21] or SNAP-Tag[22] have been employed for interaction with chlorine-functionalized ligands or benzyl guanine.[13] Another approach involves the SpyTag (SpyT) and SpyCatcher (SpyC) technology, which enables linking of the two components through an isopeptide bond.[1,23]

Establishing a fully automated and scalable synthesis of customized glycans is of particular interest.[13,24] However, while this thesis lays important groundwork, the total realization is beyond the scope. With this superordinate goal in mind, instead of using previously designed pVCL-based microgels (**Chapter III**, **Chapter IV**), this chapter aims towards the synthesis of

larger microgels using microfluidics. Due to their larger size, the embedment and implementation in a reactor might be simpler when approaching automated enzymatic glycan synthesis (AEGS). Furthermore, it allows for an expansion of usable immobilization techniques due to the mild conditions used during microgel fabrication (**Theoretical Background**).

The presented microgels are synthesized using droplet-based microfluidics. Two complementary poly(ethylene glycol) (PEG) pre-polymers, one terminated with vinyl sulfone (VS) end groups and the other terminated with thiol (SH) end groups, are introduced separately into the aqueous phase through different channels. Upon mixing the aqueous phases, rapid crosslinking occurs, resulting in the formation of spherical microgels in the size of the droplets. Using this microgel synthesis as a basis, different recombinantly expressed SpyC GT fusion proteins[25] are immobilized on microgels employing various techniques falling either in the category of enzyme encapsulation or post-attachment. For enzyme encapsulation, GTs are introduced through the aqueous phase on-chip, with the extent of covalent binding adjusted by the number of VS groups present in the droplet. In post-attachment methods, microgels are also synthesized on-chip, but with enzymes immobilized after synthesis. For attachment, either VS groups are utilized, binding to thiol or amine groups in the GTs, or a more selective binding technique is employed. To achieve selective binding, microgels are modified with SpyT to leverage SpyT-SpyC interactions, enabling the attachment of SpyC GT fusion proteins[25] to the microgels *via* isopeptide bonds.[23]

All produced microgels were analyzed by optical microscopy, while a subset of microgels underwent FT-IR spectroscopy to identify any remaining unreacted VS groups. The binding of SpyT to microgels and the immobilization of enzymes were verified using a fluorescamine assay. This assay detects primary amines, which are essential components of both, SpyT and enzymes, confirming their presence in the microgels.

The microgel-bound GTs were subsequently employed in the enzymatic synthesis of specific glycan structures. Sugar acceptors and donors were combined with the GT-microgels to synthesize precisely defined glycans. The enzymatic activities of the GT-microgels were assessed using High-Performance Liquid Chromatography (HPLC). This way, the most effective immobilization method for each GT was identified. Finally, multiple enzymatic reactions were

integrated into a single cascade synthesis. In this process, microgels containing different GTs were mixed to facilitate a multi-step, one-pot synthesis.

Figure V.1 shows the objective of this chapter: the synthesis of multiple glycan products utilizing three distinct GTs, either in monoenzymatic or cascade reactions. The future objective is to integrate the biocatalytically active microgels into a modular membrane bioreactor, thereby enabling AEGS and facilitating the fully automatic production of specific glycans. This chapter will establish the foundation for implementing a cascade reaction within such a bioreactor, progressing from the initial substrate to the refined product.

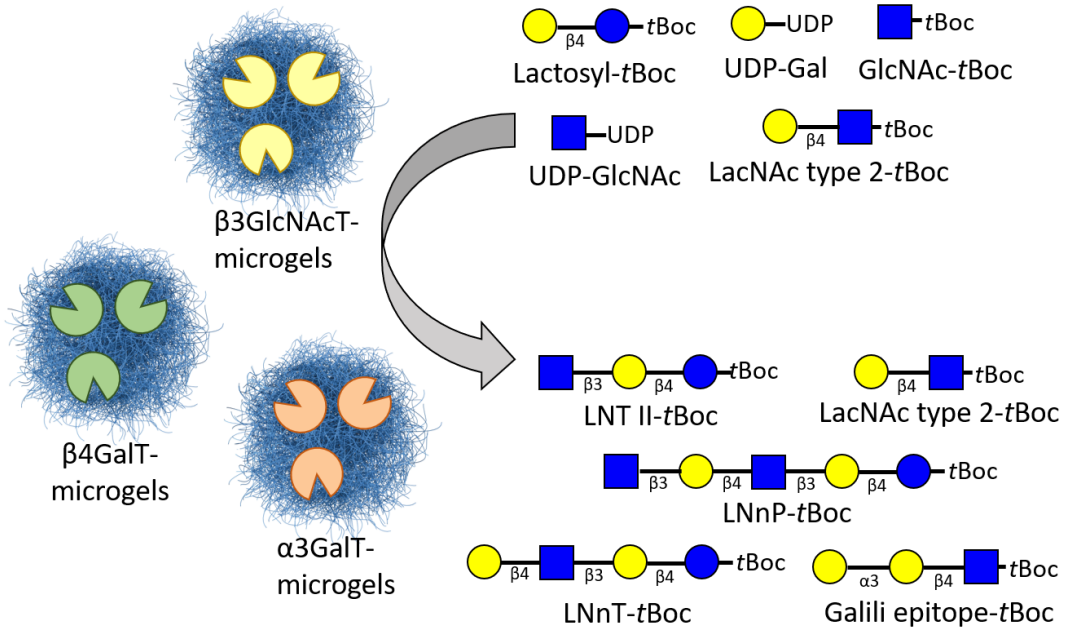

Figure V.1 Schematic depiction of the scope of the current chapter: The goal is to synthesize multiple glycan products utilizing three distinct GTs, employed either in monoenzymatic or multienzymatic cascade reactions. Among others, Lacto-*N*-triose II-*t*Boc (LNT II-*t*Boc), Type 2 *N*-Acetyl-D-Lactosamine (LacNAc type 2-*t*Boc), Lacto-*N*-neopentaose-*t*Boc (LNnP-*t*Boc), Lacto-*N*-neotetraose-*t*Boc (LNnT-*t*Boc), and the Galili epitope-*t*Boc were produced from educts such as Lactosyl-*t*Boc, UDP-Gal, GlcNAc-*t*Boc, UDP-GlcNAc, and LacNAc type 2-*t*Boc. For the depiction of the saccharides, the Symbol Nomenclature for Glycans (SNFG) was used. For the synthesis of each specific product, selected GT-microgels are mixed with the specific acceptor and donor substrates of the employed GT.

2. Materials and Methods

2.1. Materials

For aqueous reactions and buffer preparation, ultra-pure water (Merck, HPLC grade) was utilized. Buffer components included *N*-(2-hydroxyethyl)piperazine-*N*'-(2-ethanesulfonic acid) (HEPES, Sigma-Aldrich, 99 %), sodium hydroxide (NaOH, Merck, 99.5 %), and KCl (Sigma Aldrich, 85 %). The microfluidic chip fabrication involved the Sylgard® 184 Elastomer Kit (Mavom) and Aquapel® (PWG Auto Glass, LLC). The microfluidic synthesis utilized FluoSurf ™ (Emulseo) mixed with 2 % (w/w) of the hydrofluoroether (HFE) oil Novec™ (Emulseo), along with methacryloxyethyl thiocarbamoyl rhodamine B (RhB-MA, Polysciences Inc, 98 %). Poly(ethylene glycol) (PEG) derivatives, including 8-arm PEG- vinyl sulfone (VS) (20 kDa, 10 kDa), 4-arm PEG-VS (10 kDa, 5 kDa), and 4-arm PEG-thiol (SH) (10 kDa, 5 kDa), were purchased from Creative PEGWorks and Biopharma PEG Scientific Inc. Additionally, *n*-heptane (VWR, 99.9 %) was employed for microgel purification. SpyT peptide (amino acid sequence: CRGVPHIVMVDAYKRYK, 98 %, 2034.06 g mol^{-1}) was custom-synthesized by BioCat GmbH along with an N-terminal cysteine. Furthermore, GT production employed *Escherichia coli* (*E. coli*) SHuffle T7 Express, *E. coli* BL 21 (DE3) (New England Biolabs, Ipswich, MA, USA), and *E. coli* Rosetta 2 (DE3) plysS (Sigma Aldrich, Taufkirchen, Germany), along with plasmids pETDuet1_SpyC-MBP-α3GalT (α3GalT), pETDuet1_SpyC-pp-catβ4GalT (β4GalT), pETDuet1-SpyC-MBP-LgtA (β3GlcNacT), which were obtained from BioCat GmbH. Fluorescein isothiocyanate (FITC)-dextrans were purchased from Sigma Aldrich.

2.2. Production and Purification of Recombinant Glycosyltransferases

In this chapter, three plasmids were employed, each containing the genetic sequence for one GT fused with various tags to aid in purification, immobilization, and solubility. All constructs featured a His-tag for IMAC purification and detection, alongside a SpyCatcher (SpyC) derived from *Streptococcus pyogenes* for immobilization in the microgel.[26] The plasmid pETDuet1_SpyC-MBP-α3GalT encoded *Mus musculus* (mouse) α3GalT, coupled with a Maltose Binding Protein (MBP) from *E. coli* K-12, improving enzyme solubility.[27] Another plasmid,

pETDuet1_SpyC-pp-catβ4GalT, encoded human β4GalT fused with the lipase propeptide (pp) from *Staphylococcus hyicus* to enhance solubility.[28] Additionally, the plasmid pETDuet1-SpyC-MBP-LgtA carried the gene for β3GlcNacT from *Neisseria meningitidis*, coupled with an N-terminal MBP tag. These plasmids were transformed into *E. coli* expression strains to enable the production of distinct GTs: *E. coli* BL21 (DE3) was utilized for SpyC-MBP-α3GalT (α3GalT), *E. coli* SHuffle T7 Express strain for SpyC-pp-β4GalT (β4GalT), and *E. coli* Rosetta 2 (DE3) plysS for SpyC-MBP-LgtA (β3GlcNacT), with their expression described in previous works.[29,30] To summarize, inoculation of the expression strains was performed at 37 °C, transferring from a Lysogeny Broth (LB) preculture to a Terrific Broth (TB) main culture. Protein production was started upon reaching an optical density at 600 nm (OD_{600}) between 0.5 and 0.8. For this, 0.1 mM isopropyl 1-thio-β-D-galactopyranoside (IPTG) was added, followed by cell incubation at 25 °C for 20 hours. Cells were harvested through centrifugation.

Enzymes were purified by employing Immobilized Metal Ion Affinity Chromatography (IMAC) on a HisTrap column with an Äkta system (Cytiva, Marlborough, MA, USA). After cell disruption in specific lysis buffers (**Table V.1**) through sonication (6.5 min, 15 s pulse, 60 s pause, 52 % amplitude), cell debris was separated from the protein extract by centrifugation, followed by filtration of the supernatant. After attachment of the enzymes to the column by metal ion affinity, the column was washed with the binding buffer, and subsequently eluted with the elution buffer (**Table V.1**). The eluted protein was dialyzed in 100 mM HEPES pH 8 buffer. The protein concentration was determined using a Bradford assay,[31] while protein identity was confirmed through SDS-PAGE and Western Blot analysis (data not shown).

Table V.1 Composition of buffers for cell lysis, washing, and enzyme elution during purification through IMAC, respectively. The pH of all buffers was adjusted to 7.5.

Enzyme	Lysis buffer	Binding buffer	Elution buffer
α3GalT	50 mM HEPES; 500 mM NaCl; 250 U Pierce Nuclease; 20 mM Imidazole	50 mM HEPES; 500 mM NaCl; 20 mM Imidazole	50 mM HEPES; 500 mM NaCl; 500 mM Imidazole
β4GalT	20 mM NaH_2PO_4; 500 mM NaCl; 250 U Pierce Nuclease; 10 mM Imidazole	20 mM NaH_2PO_4; 500 mM NaCl; 10 mM Imidazole	20 mM NaH_2PO_4; 500 mM NaCl; 500 mM Imidazole
β3GlcNAcT	50 mM Tris-HCl; 500 mM NaCl; 250 U Pierce Nuclease; 30 mM Imidazole	50 mM Tris-HCl; 500 mM NaCl; 30 mM Imidazole	50 mM Tris-HCl; 500 mM NaCl; 300 mM Imidazole

2.3. Fabrication of the Microfluidic Device

The master molds for the microfluidic devices were fabricated using photolithography.[32] The microfluidic channels were designed in a two-dimensional layout using AutoCAD® software from Autodesk, USA. This layout was then printed onto a high-resolution (25000 dpi) dark-field photomask. Photolithography techniques were applied to transfer this pattern onto a silicon wafer coated with an epoxy-based photoresist (SU-8), utilizing the printed photomask as a template. Soft lithography was employed to replicate the patterned silicon wafer onto PDMS-based microfluidic devices. The Sylgard 184 Elastomer Kit, consisting of a two-component system comprising 10 parts siloxane and 1 part curing agent (crosslinker), was used for this purpose. The mixture was poured into the master molds, subjected to vacuum for removal of air bubbles, and cured overnight at 60 °C. Once cured, the solidified, completely crosslinked PDMS device was carefully peeled off from the master mold, and inlet and outlet ports for tube connections were created utilizing a biopsy puncher (0.75 mm). Subsequently, the PDMS device and a glass slide were cleaned by washing three times with isopropyl alcohol and three times with water. The cleaned components were then dried at 60 °C overnight.

To enhance hydrophilicity and prepare the surfaces for bonding, the glass slide and the PDMS device were treated with oxygen plasma in a TePla 100 plasma oven from PVA MPS GmbH. This treatment altered the surface functionalities through the introduction of polar silanol groups. Bonding of the PDMS and glass slide was realized by pressing both parts together, forming irreversible covalent Si-O-Si bonds between the glass and PDMS. Wetting of the aqueous phases within the microfluidic channels was minimized by channel functionalization with Aquapel®. The channels were flooded with Aquapel®, followed by its removal after 2 minutes of exposure. With this process, hydrophobic fluoroalkyl chains were covalently bound to the hydroxyl groups present on the channel surfaces.

2.4. Droplet-Based Microfluidics for Microgel Synthesis

The microfluidic experiments were conducted using specialized equipment, including an inverted microscope (Motic AE2000, TED PELLA, INC., Redding, CA) fitted with a camera (Flea3, Point Grey, Richmond, CA) for real-time monitoring of flow dynamics and droplet formation.

This setup contained three syringe pumps (PHD Ultra, Harvard Apparatus, Holiston, USA) equipped with GASTIGHT® Syringes (Hamilton, USA) to precisely control flow rates within the microfluidic channels. To connect the syringes to the microfluidic device, fine-bore PE tubing (inner diameter: 0.38 mm) was employed. Two different aqueous phases were introduced into the microfluidic system at a flow rate of 150 µL h^{-1} through separate inlets. These phases merged into a single channel at a Y-junction, maintaining laminar flow conditions throughout the process, followed by water-in-oil (W/O) droplet formation in a flow-focusing microfluidic cross-junction. For this, an immiscible oil phase (comprising HFE-7500 with 2 w/w % of the surfactant FluoSurf-C) was utilized to tear off the aqueous stream at a flow rate of 600 µL h^{-1}. After thorough mixing of the reactants in a serpent-shaped mixing section, the pre-polymers contained within the droplets were allowed to undergo Michael-type addition overnight. This resulted in the formation of monodisperse, spherical microgels that were purified by three rinses with HFE-7500, one rinse with *n*-heptane, and five rinses with a buffer solution (100 mM HEPES pH 7 with 150 mM KCl).

The aqueous phases in the microfluidic system comprised an SH-phase containing PEG thiol (PEG-SH) and a VS-phase containing PEG vinyl sulfone (PEG-VS). To prepare the VS-phase, PEG-VS of various molecular weights and architectures were utilized. This involved employing either a 5 w/v % solution of 4-arm PEG-VS (10 kDa or 5 kDa) or a 10 w/v % solution of 8-arm PEG-VS (20 kDa or 10 kDa) in 100 mM HEPES pH 8. The composition of the SH-phase depends on the intended method of enzyme incorporation which can be either post-attachment or encapsulation of the enzyme. For enzyme encapsulation, the SH-phase comprised contained 5 w/v % 4 arm PEG-SH (10 kDa or 5 kDa) in 100 mM HEPES at pH 8, along with 0.01 w/v % RhB-MA (0.2 v/v % in H_2O). Additionally, the enzyme (49.8 v/v % in 100 mM HEPES pH 7 with 150 mM KCl) was introduced into the SH-phase. The enzyme concentration in the SH-phase varied: 0.9 mg mL^{-1} for α3GalT, 0.3 mg mL^{-1} for β4GalT, and 0.5 mg mL^{-1} for β3GlcNAcT.

Post-attachment of enzymes was enabled by the synthesis of microgels with reactive groups. For the synthesis of VS-functionalized microgels, the SH-phase contained 5 w/v % 4 arm PEG-SH (10 kDa or 5 kDa) and 0.01 w/v % RhB-MA in 100 mM HEPES at pH 8. For the fabrication of SpyT-functionalized microgels, the SH-phase components were dissolved in water, owing to

the limited solubility of the SpyT in the utilized buffer. An additional 2 w/v % SpyT was added to the SH-phase. The parameters and abbreviations used are listed in **Table V.6**.

2.5. Post-Attachment of Enzymes to Microgels

VS- or SpyT-functionalized microgels were then used for post-attachment of microgels. 1000 µL 100 mM HEPES pH 7 with 150 mM KCl were added to 200 µL of a highly concentrated microgel dispersion. After the addition of 200 µL of GT solution (1.9 mg mL^{-1} α3GalT, 0.6 mg mL^{-1} β4GalT, or 1.0 mg mL^{-1} β3GlcNAcT), the mixture was placed on a vortex shaker at 500 rpm. Following incubation for 24 hours at room temperature and supernatant removal, the GT-microgels were rinsed with buffer (100 mM HEPES pH 7 with 150 mM KCl) thrice. For determination of the enzyme content, the first supernatant was assessed with a Bradford assay[31] to calculate the amount of immobilized enzymes.

2.6. Glycosyltransferase Reactions

5 mM acceptor (*t*Boc-linker sugar)[33,34] and 6.5 mM nucleotide sugar donor were employed to perform GT-catalyzed reactions. The GT-microgels were mixed with the respective reaction buffer (**Table V.2**), followed by incubation at 30 °C for 24 hours. The *t*Boc-linker (*tert*-butyl (2-thioureidoethyl)carbamate, abbreviated with *t*Boc) comprises an *N*-(2-aminoethyl)thiourea linker, protected by a *tert*-butyloxycarbonyl protecting group, as depicted in **Scheme V.1**

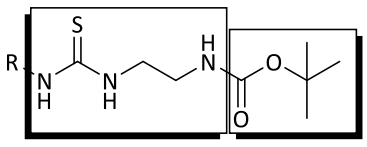

Scheme V.1 Structural formula of the *t*Boc-linker (*t*Boc) comprising a 1-(2-aminoethyl)thiourea linker, protected by a *tert*-butyloxycarbonyl group. R = sugar residue.

Table V.2 Buffers employed for the GT-catalysed reactions along with the utilized donor and acceptor substrates. 28.5 µL GT-microgel dispersion were employed.

Enzyme	Donor substrate / Acceptor substrate	Residual compounds
α3GalT	6.5 mM UDP-Gal[a] / 5 mM LacNAc (type 2)-*t*Boc[b]	100 mM HEPES pH 7; 150 mM KCl; 2 mM $MnCl_2$; 1 % glycerol; 1 mg mL^{-1} BSA[c]; 20 U mL^{-1} FastAP[d]
β4GalT	6.5 mM UDP-Gal[a] / 5 mM GlcNAc-*t*Boc[e]	100 mM glycine pH 10; 5 mM $MnCl_2$; 30 U mL^{-1} FastAP[d]
β3GlcNAcT	6.5 mM UDP-GlcNAc[f] / 5 mM Lactosyl-*t*Boc	100 mM glycine pH 10; 5 mM $MnCl_2$; 20 U mL^{-1} FastAP[d]

[a] Uridine-5'-diphospho-D-galactose, [b] *N*-acetyllactosamine type 2-*t*Boc, [c] Bovine serum albumin fraction V, [d] Alkaline phosphatase (ThermoFischer, Schwerte, Germany), [e] *N*-acetyl-D-glucosamine-*t*Boc, [f] Uridine-5'-diphospho-*N*-acetyl-D-glucosamine

To perform cascade reactions, different GT-microgels were combined in a one-pot synthesis. Within the first cascade reaction, the GT-microgels α3GalT-cov-L (18.0 mU mL^{-1}) and β4GalT-cov-L (25.2 mU mL^{-1}) were used, mixed in specific ratios according to **Table V.3**. Within the second cascade reaction, the GT-microgels β4GalT-cov-L (25.2 mU mL^{-1}) and β3GlcNAcT-noncov-S (6.3 mU mL^{-1}) were employed, according to **Table V.3**.

Table V.3. For cascade reactions, several GT-microgels were combined in a one-pot synthesis, employing either α3GalT and β4GalT or β4GalT and β3GlcNAcT. The employed GT-microgels were α3GalT-cov-L (18.0 mU mL^{-1}), β4GalT-cov-L (25.2 mU mL^{-1}), β4GalT-cov-L (25.2 mU mL^{-1}) and β3GlcNAcT-noncov-S (6.3 mU mL^{-1}). GT-microgels were mixed to reach specific activity ratios according to their known volumetric activities, mixing β4GalT and α3GalT in 2:1, 1:1, and 1:2 activity ratios (β4GalT to α3GalT), and mixing β4GalT to β3GlcNAcT in a 2:1 ratio.

Cascade	Ratio of enzyme activities	Microgel mixture	Total activity
β4GalT, α3GalT	2:1	28.5 µL β4GalT-cov-L, 20.4 µL α3GalT-cov-L	1.1 mU
β4GalT, α3GalT	1:1	20.4 µL β4GalT-cov-L 28.5 µL α3GalT-cov-L	1.0 mU
β4GalT, α3GalT	1:2	39.8 µL α3GalT-cov-L, 14.6 µL β4GalT-cov-L	1.1 mU
β4GalT, β3GlcNAcT	2:1	57.0 µL β3GlcNAcT-noncov-S, 39.7 µL β4GalT-cov-L	1.1 mU

The enzymatic cascade reaction was initiated by the addition of the reaction buffer, which was premixed according to **Table V.4**, to GT-microgels.

Table V.4 Buffers employed for the GT-catalysed cascade reactions along with the utilized donor and acceptor substrates. For each cascade, two different GT-microgel dispersions were used.

Cascade	Donor substrate / Acceptor substrate	Residual compounds
Galili	13 mM UDP-Gal[a] / 5 mM LacNAc (type 2)-*t*Boc[b]	100 mM HEPES pH 7; 150 mM KCl; 6 mM $MgCl_2$ 5 mm $MnCl_2$; 1 % glycerol; 1 mg mL^{-1} BSA[c]; 20 U mL^{-1} FastAP[d]
Lacto-*N*-neo glycans-*t*Boc	6.5 mM UDP-GlcNAc[e] 6.5 mM UDP-Gal[a] / 5 mM Lactosyl-*t*Boc	100 mM glycine pH 10; 5 mM $MnCl_2$; 30 U mL^{-1} FastAP[d]

[a] Uridine-5'-diphospho-D-galactose, [b] *N*-acetyllactosamine type 2, [c] Bovine serum albumin fraction V, [d] Alkaline phosphatase (ThermoFischer, Schwerte, Germany), [e] Uridine-5'-diphospho-*N*-acetyl-D-glucosamine

The reactions were performed at 30 °C with samples collected at specified intervals. Sampling involved withdrawing 5 µL of the reaction mixture, which was then diluted 1:5 with water and subjected to boiling at 95 °C for 5 minutes to halt the enzymatic reaction. Following this, centrifugation at 13000 rpm for 5 minutes was conducted to eliminate denatured protein impurities. The resulting supernatant was transferred to HPLC vials for subsequent analysis.

2.7. Assessment of Enzymatic Activities

Samples from reaction mixtures were collected at specified intervals and subjected to analysis using HPLC employing an UltiMate 3000 system (Thermo Fisher Scientific, Waltham, MA, USA) equipped with a Silica-C18 column (MultoKrom 100-5 C18, 250 × 4 mm, CS Chromatographie, Langerwehe, Germany). Chromatograms were generated with Chromatography Data System Chromeleon 7.2.6 software (Thermo Fisher Scientific, Waltham, MA, USA). After sample injection, they were migrated for 30 minutes at a flow rate of 1 mL min^{-1} utilizing a polar mobile phase comprising 15 % acetonitrile (Roth, Karlsruhe, Germany). After the detection of *t*Boc-linked saccharides at 254 nm, the ratios of the acceptor peak area to the product peak area were used to compute the conversion and enzymatic activity. An illustrative calculation of volumetric activity is presented below (**Equation V.1** to **Equation V.3**). Here, relative peak areas of Galili-*t*Boc and LacNAc-*t*Boc were measured, resulting in the calculation of the synthesized molar amount of Galili-*t*Boc according to **Table V.5**.

Table V.5 Exemplary calculation of the amount of substance of both, product (Galili-*t*Boc) and acceptor (LacNAc-*t*Boc) at specified intervals. The relative peak areas of both substances at specific time intervals were measured through HPLC. The relative peak areas were then used to calculate the amount of substance in µmol, starting from 0.3 µmol (5 mM in 60 µL) for the initial acceptor (LacNAc-*t*Boc).

Time [min]	Galili-*t*Boc Rel. Area [%]	LacNAc-*t*Boc Rel. Area [%]	Galili-*t*Boc [µmol]	LacNAc-*t*Boc [µmol]
3	0.44	99.56	0.0013	0.2987
6	1.03	98.97	0.0031	0.2969
10	3.93	96.07	0.0118	0.2882
15	7.54	92.46	0.0226	0.2774
30	17.5	82.5	0.0525	0.2475
60	35	65	0.1050	0.1950
120	64.32	35.68	0.1930	0.1070
240	90.82	9.18	0.2725	0.0275
480	93.56	6.44	0.2807	0.0193
1440	95.18	4.82	0.2855	0.0145

From the initial 60 minutes, the linear regression of the conversion rate was calculated (**Equation V.1**).

$$b = \frac{\sum(x - \bar{x}) \cdot (y - \bar{y})}{\sum(x - \bar{x})^2}$$

Equation V.1 Calculation of the linear regression (Microsoft Excel Version 1808).

The slope thereby equals the enzymatic activity in µmol min^{-1} or Units (U). The volumetric activity (U mL^{-1}) was then calculated by inserting the known volume of GT-microgels (**Equation V.2**).

$$A_{vol}\left[\frac{U}{mL}\right] = \frac{b}{V}$$

Equation V.2 Calculation of the volumetric enzyme activity (A_{vol}). b: the slope of the obtained regression line in µmol min^{-1} (**Equation V.1**); V: the volume of GT-microgel dispersion (28.5 µL).

According to **Equation V.1**, a slope of 0.0017 µmol min^{-1} was calculated, resulting in a volumetric activity of 60.2 mU mL^{-1} according to **Equation V.2**. The specific activities can be calculated by dividing the volumetric enzymatic activity by the mass concentration of enzymes in the utilized volume, as indicated by **Equation V.3**.

$$A_{specific}\ \left[\frac{U}{mg}\right] = \frac{A_{vol}\ V}{m_E}$$

Equation V.3 Calculation of the specific enzyme activity ($A_{specific}$) from the volumetric activity (A_{vol}). V: the volume of GT-microgel dispersion (28.5 µL); m_E: the mass of employed enzymes.

To ascertain the mass of enzymes in GT-microgels synthesized through enzyme encapsulation, the GT-microgels were freeze-dried at a fixed volume, and the total mass of microgels per mL was measured. For the mass of enzymes per mL, the maximum loading was determined based on the quantities utilized in the microfluidic synthesis, assuming full loading. The precise amount of enzymes in the microgels could not be accurately determined, resulting in an underestimation of the specific activity.

For GT-microgels obtained through post-attachment, the precise amount of immobilized enzyme and thus the specific activity was calculated by determining the amount of unbound enzymes through a Bradford assay.

2.8. Analytical methods

2.8.1. Optical Microscopy

Optical microscopy images were recorded on an Olympus CKX53 equipped with a camera (Olympus DP23) and Olympus cellSens Standard 3.2 software. Microgel sizes and size distributions were manually determined from obtained images with Fiji (ImageJ) for a minimum of 20 particles.

2.8.2. Fourier-Transform Infrared Spectroscopy

Fourier-Transform Infrared (FT-IR) spectroscopy was conducted over the range of 4000 to 400 cm^{-1} with 4 scans per measurement and a resolution of 4 cm^{-1}. Before analysis, microgel samples underwent a washing step with water to eliminate buffer molecules, as well as drying by lyophilization. The samples were then positioned on a diamond crystal plate of an FT-IR Spectrum 3 instrument by PerkinElmer, employing a GladiATR Single reflection by PIKE

Technologies. Spectrum v10.7.2. software was utilized for data acquisition, with a background measurement performed before sample measurement. All spectra underwent baseline correction and normalization.

2.8.3. Confocal Microscopy

Proteins and enzymes were localized in microgels utilizing the fluorescamine assay.[35] Employing concentrations according to the publication of Watkin *et al.*,[36] 10 µl of a 3 mg mL^{-1} 4'-phenylspiro[2-benzofuran-3,2'-furan]-1,3'-dione (fluorescamine) solution in acetone were rigorously mixed with 40 µL of (GT-)microgels in buffer (100 mM HEPES pH 7, 150 mM KCl). The fluorescent products were examined with confocal microscopy, according to their excitation wavelength λ_{ex} of 390 nm and emission wavelength λ_{em} of 475 nm.[35]

Furthermore, permeability studies were conducted according to Bulut *et al*.[37] For this, 1 mg mL^{-1} FITC-dextran solutions of varying molecular weights (4, 40, 150, and 500 kDa) were added to microgels, and investigated regarding their fluorescence intensity profile: The fluorescence intensity along the diameter of the microgel is assessed within the range of 0 to 200 µm. For comparative analysis of various microgels, the average fluorescence intensity within the core of the microgel was calculated by averaging fluorescence intensity profile measurements taken between distances of 88 and 100 µm.

Confocal laser scanning microscopy (SP8 Tandem Confocal, Leica Microsystems Inc.) was employed for the visualization of fluorescent microgel samples. The microscope was outfitted with different light sources: a photodiode at 405 nm (fluorescamine derivates, 455-500 nm emission, HyD detector), an Argon laser at 488 nm (FITC-dextran, 500-550 nm emission, PMT detector), and a diode-pumped solid-state laser at 561 nm (RhB-MA, 575-610 nm emission, HyD detector). Images were processed by LAS X software.

2.8.4. Scanning Electron Microscopy

Scanning Electron Microscopy (SEM) analyses were conducted using a Hitachi SU9000 equipped with a secondary electron (SE) detector for surface imaging. Microgel samples

dispersed in H_2O were dried on a 300 mesh copper electron microscopy grid with a carbon coating. Before measurement, the samples were coated with approximately 3 nm of carbon using the Leica ACE EM 600. The measurements were carried out at an acceleration voltage of 30 kV and currents ranging between 10.5 and 10.9 µA.

3. Results and Discussion

3.1. Microgel Synthesis and Characterization

3.1.1. Size Determination

Microgel synthesis was performed by droplet-based microfluidics, employing the parameters according to **Table V.6**. Here, abbreviations for the microgels are defined. All microgels were produced through the reaction of the reactive pre-polymers PEG thiol (PEG-SH) and PEG vinyl sulfone (PEG-VS) *via* a Michael-type addition reaction within aqueous droplets. Enzymes were introduced into the microgels either through encapsulation within the droplets or through post-attachment methods.

Table V.6. Parameters employed for (GT-)microgel synthesis through droplet-based microfluidics. Enzymes were immobilized either by on-chip enzyme encapsulation or off-chip post-attachment. The molecular weight of PEG-SH and PEG-VS was varied: large (L): 20 kDa 8-arm-PEG or 10 kDa 4-arm PEG; small (S): 10 kDa 8-arm-PEG or 5 kDa 4-arm PEG). The chosen binding type was either covalent (cov) or non-covalent (noncov) during encapsulation, for post-attachment SpyT- or VS-attachment was employed. The abbreviation for each microgel indicates the chosen immobilization type and pre-polymer size. The enzyme denotations (α3GalT, β4GalT, and β3GlcNAcT) can be inserted for the denotation of GT-microgels.

Method, MW	PEG-VS	PEG-SH	Binding type	Functional group	Abbreviation
Enzyme encapsulation, L MW PEG	8-arm 20 kDa	4-arm 10 kDa	covalent	VS	cov-L = VS-L[a)]
	4-arm 10 kDa	4-arm 10 kDa	non-covalent	-	noncov-L
Enzyme encapsulation, S MW PEG	8-arm 10 kDa	4-arm 5 kDa	covalent	VS	cov-S = VS-S[a)]
	4-arm 5 kDa	4-arm 5 kDa	non-covalent	-	noncov-S
Post attachment through SpyT, L MW PEG	8-arm 20 kDa	4-arm 10 kDa	covalent (SpyT)	2 w/v % SpyT[a)]	SpyT-L
Post attachment through SpyT, S MW PEG	8-arm 10 kDa	4-arm 5 kDa	covalent (SpyT)	2 w/v % SpyT[b)]	SpyT-S
Post attachment through VS, L MW PEG	8-arm 20 kDa	4-arm 10 kDa	covalent (VS)	VS[b)]	VS-L = cov-L[a)]
Post attachment through VS, S MW PEG	8-arm 10 kDa	4-arm 5 kDa	covalent (VS)	VS[b)]	VS-S = cov-S[a)]

[a)] Due to the synthesis type chosen, cov-L microgels without immobilized GTs equal VS-L microgels. The same is the case for cov-S and VS-S microgels.

For the encapsulation of enzymes, they were introduced directly onto the microfluidic chip, with the primary binding mechanism (covalent or non-covalent) controlled by adjusting the incorporation of additional VS groups within the microgel. This adjustment was realized by adding either 8-arm PEG-VS (for covalent binding) or 4-arm PEG-VS (for primarily non-covalent

binding) to 4-arm PEG-SH according to **Scheme V.2**. VS groups can react with amine or thiol residues present in the enzyme network.

The attachment of enzymes off-chip after microgel synthesis is referred to as post-attachment. Enzymes can be attached either to SpyT or to VS (**Scheme V.2**). For the synthesis of SpyT-functionalized microgels, SpyT is added on-chip, enabling the reaction between VS and an N-terminal cysteine in SpyT through thiol-Michael-addition. Enzyme attachment is carried out by covalent SpyT-SpyC interaction, with the SpyC counterpart being linked to the enzymes. To use VS for post-attachment, an excess of VS groups was employed without further modification of the microgels.

Besides the enzyme attachment techniques, the PEG molecular weights were varied (large (L): 20 kDa 8-arm-PEG or 10 kDa 4-arm PEG; small (S): 10 kDa 8-arm-PEG or 5 kDa 4-arm PEG). With a variation in building block size, different mesh sizes were obtained.

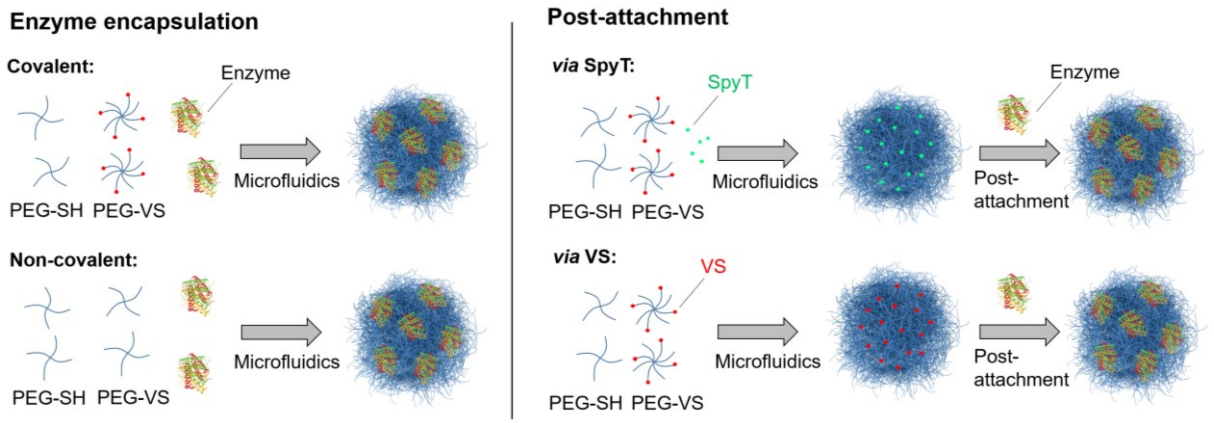

Scheme V.2. GT-microgels were prepared by encapsulation (left) or post-attachment (right) of enzymes. For enzyme encapsulation, enzymes were added on-chip, either forming covalent bonds to present VS-groups or only being encapsulated non-covalently. This was enabled by the VS-content in the added polymers. Excess VS groups that are not expected to react during crosslinking of the polymer network, are marked in red and can react with the enzymes (top). For non-covalent enzyme encapsulation, a 1:1 ratio of VS and SH groups was utilized (bottom). Post-attachment was enabled by off-chip enzyme immobilization *via* reactive functional groups. For SpyT-SpyC interaction, SpyT, here in green, was attached to the polymer network through excess VS groups, here in red (top). For attachment through VS groups, the excess of VS groups was not further functionalized but instead left for enzyme attachment (bottom). Additionally, different molecular weight PEGs were employed (large/L: 20 kDa 8-arm-PEG or 10 kDa 4-arm PEG; small/S: 10 kDa 8-arm-PEG or 5 kDa 4-arm PEG).

Using these methods, several different (GT-)microgels were synthesized, employing the GTs α3GalT, β4GalT, and β3GlcNAcT. These (GT-)microgels were subjected to optical microscopy

imaging (**Figure V.2**, **Figure SV.1**, **Figure SV.2**) with diameters measured between 140 and 170 µm (**Table SV.1**, **Table SV.2**). Notably, SpyT-functionalized microgels and cov-type microgels are slightly larger compared to noncov-type microgels, which may be explained by the larger polymer weight in their pre-microgel droplets compared to noncov-droplets. After redispersing the microgels in water, the larger weight concentration can cause a higher degree of swelling for cov-type microgels.

While GT-microgels fabricated by enzyme encapsulation already contain enzymes, obtained SpyT and VS-functionalized microgels were subsequently employed for post-attachment of GTs. SpyT- and GT-microgels were then subjected to a fluorescamine assay.

3.1.2. Fluorescamine Assay

Fluorescamine can be employed for primary amine detection. The non-fluorescent reagent reacts with primary amines to generate a fluorophore (**Scheme V.3**). Notably, any unbound reagent reacts with water to produce non-fluorescent products within seconds.[35]

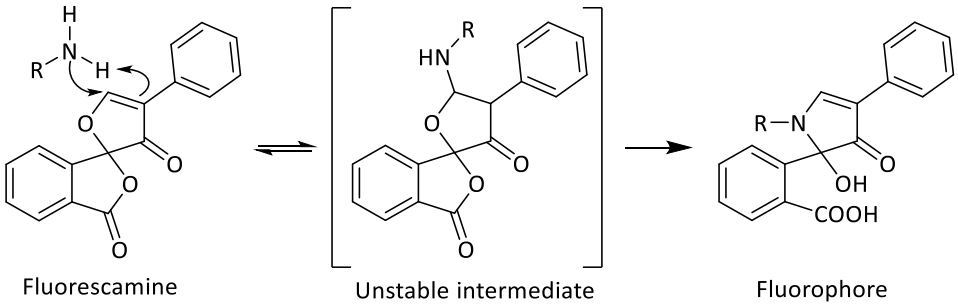

Scheme V.3 Fluorescamine reacts with a primary amine to form a fluorophore with a typical excitation wavelength of 390 nm and an emission wavelength of 475 nm.

This assay enables the detection of both the SpyT peptide and the enzymes α3GalT, β4GalT, and β3GlcNAcT. The stained GT- and SpyT-functionalized microgels confirm successful enzyme and peptide incorporation in all cases (**Figure SV.3**, **Figure SV.4**). Expectedly, non-functionalized microgels do not generate fluorophores when treated with fluorescamine (**Figure SV.3**). This proves the absence of peptides or enzymes. A selection of stained microgels are depicted in **Figure V.2**, alongside their optical microscopy brightfield images.

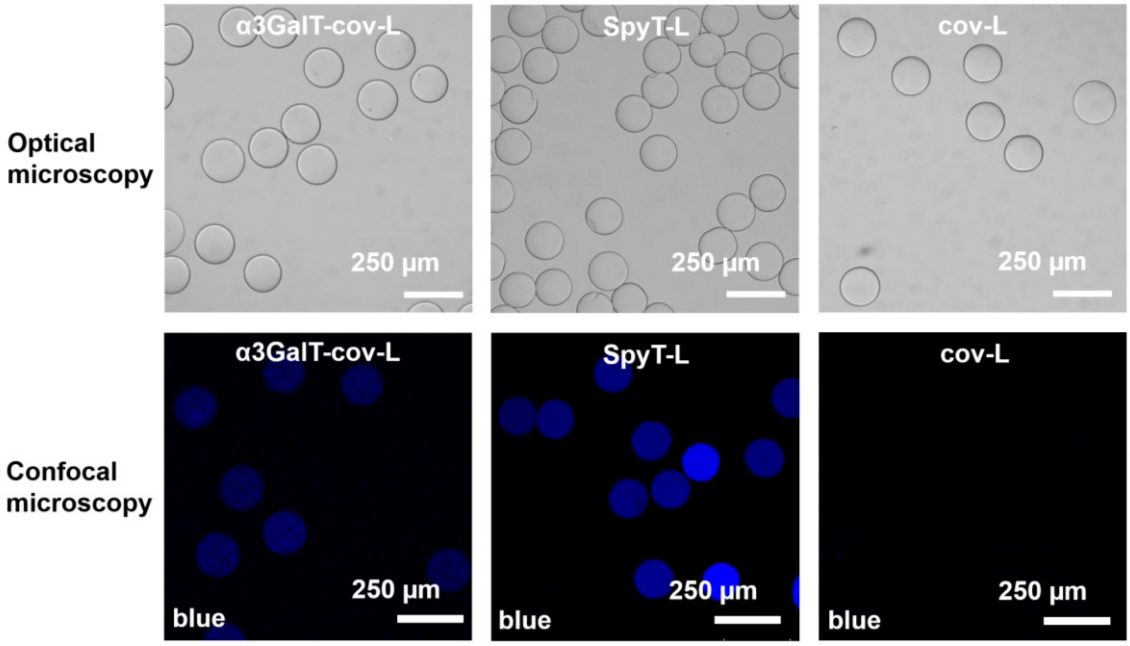

Figure V.2 Microscopy (optical and confocal) images of different microgels, including α3GalT-cov-L, SpyT-L, and cov-L microgels. Before confocal microscopy (blue channel, fluorescamine derivates: λ_{ex} = 405 nm, λ_{em} = 455-500 nm), microgels were stained with fluorescamine. The images delivered qualitative indications only. The presence of enzymes and peptides is indicated by blue fluorescence, confirming the incorporation of α3GalT and SpyT, whereas non-functionalized microgels do not contain primary amines.

While the presence of primary amines is evident from confocal microscopy images, accurately quantifying the number of incorporated enzymes or SpyT is challenging. This difficulty arises from various factors affecting fluorescence, which extend beyond the enzyme or SpyT quantity alone. These factors encompass the penetration of fluorescamine into the microgels, impacted by varying porosity; the accessibility of primary amines within the structure, influenced by peptide or enzyme folding; and the overall count of primary amines in each enzyme or SpyT. Therefore, the fluorescamine assay conducted in this study only serves as a qualitative indicator.

3.1.3. Fourier-Transform Infrared Spectroscopy

To examine the presence of unreacted VS groups in the microgel, FT-IR spectroscopy was conducted. **Figure V.3a** displays the spectra of the microgels cov-L and noncov-L, along with the pre-polymers PEG-VS and PEG-SH. A magnified section is shown in **Figure V.3c**, highlighting the C=C bending vibration around 760 cm^{-1} that indicates unreacted VS groups. Notably, PEG-

SH lacks a characteristic absorption in this range. The C=C vibration is prominent for PEG-VS and cov-L, whereas nearly all C=C bonds have reacted in noncov-L, as evidenced by the absence of a distinct band. Therefore, the suitability of cov-L microgels for the covalent attachment of enzymes through unreacted VS units has been validated.

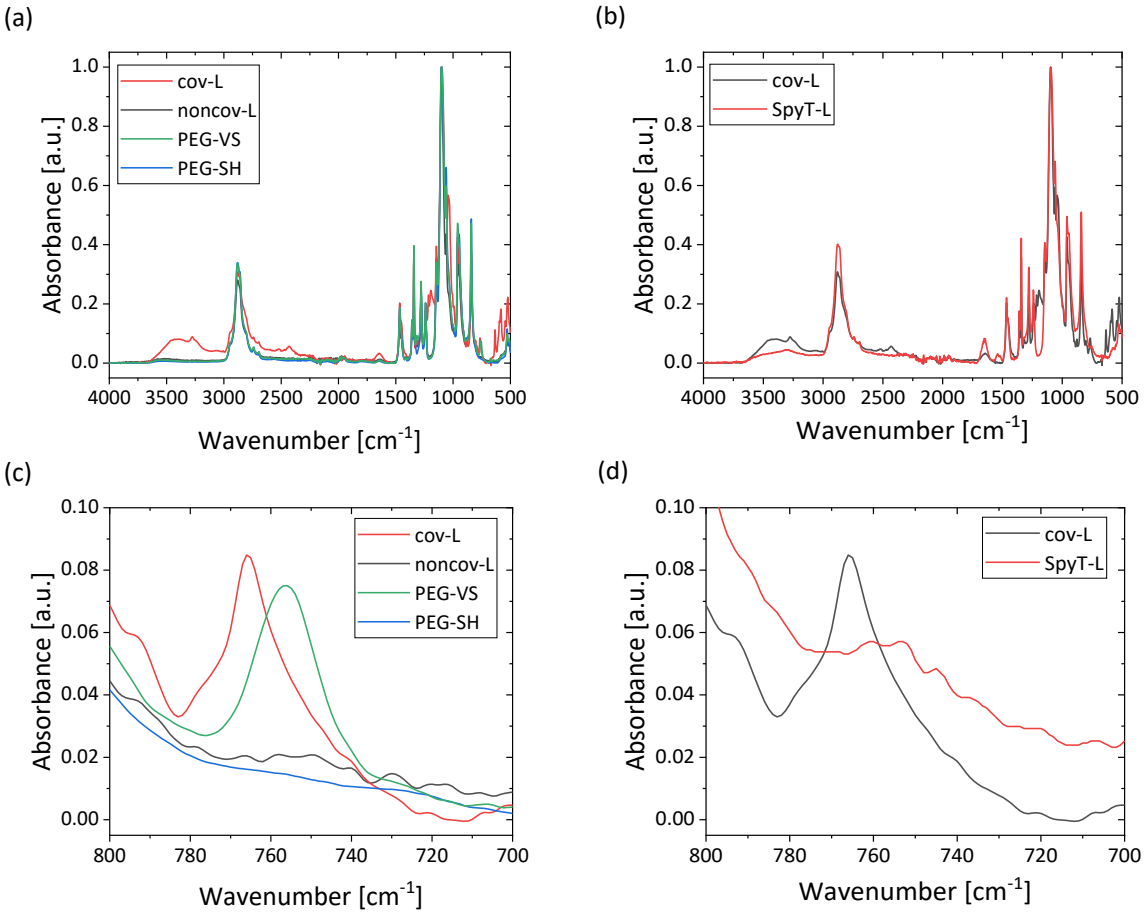

Figure V.3 (a) FT-IR spectra of the microgels cov-L and noncov-L, and the pre-polymers PEG-VS and PEG-SH, along with (c) a magnified section. (b) FT-IR spectra of the microgels cov-L and SpyT-L, along with (d) a magnified section. The C=C bending vibration around 760 cm^{-1} can be used as an indication of the presence of reactive VS groups.

The functionalization of microgels with SpyT can also be monitored with the characteristic C=C band. Comparing the spectrum of SpyT-L to the one of cov-L, the C=C vibration has disappeared almost completely for SpyT-L (**Figure V.3b** and **Figure V.3d**). This indicates a successful reaction of SpyT with VS and thus the formation of a SpyT-functionalized microgel.

3.1.4. Permeability Studies

To evaluate variations in microgel permeability arising from compositional differences, a methodology outlined by Bulut *et al*.[37] was adopted. After dispersing microgels in solutions of FITC-dextran with varying molecular weights (4, 40, 150, and 500 kDa), fluorescence intensity profiles were obtained using confocal microscopy. This allowed for an assessment of microgel permeability, which is mainly determined by the mesh size of the polymer network. Permeability is crucial for facilitating enzyme uptake in post-attachment or preventing enzyme release in non-covalent encapsulation, as well as for enabling the diffusion of substrates and products during enzyme catalysis. In general, fluorescence intensities within the microgels decrease with increasing FITC-dextran size, as lower molecular weight molecules can penetrate the polymer network more easily. Within the present permeability assay, cov-L, cov-S, noncov-L, and noncov-S microgels were investigated (**Figure V.4**).

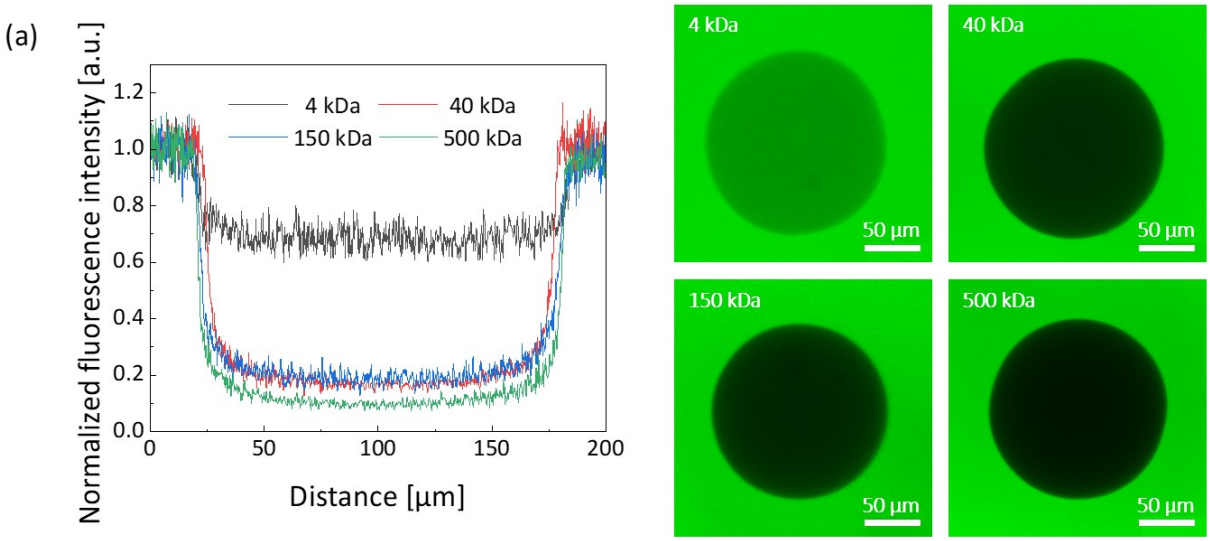

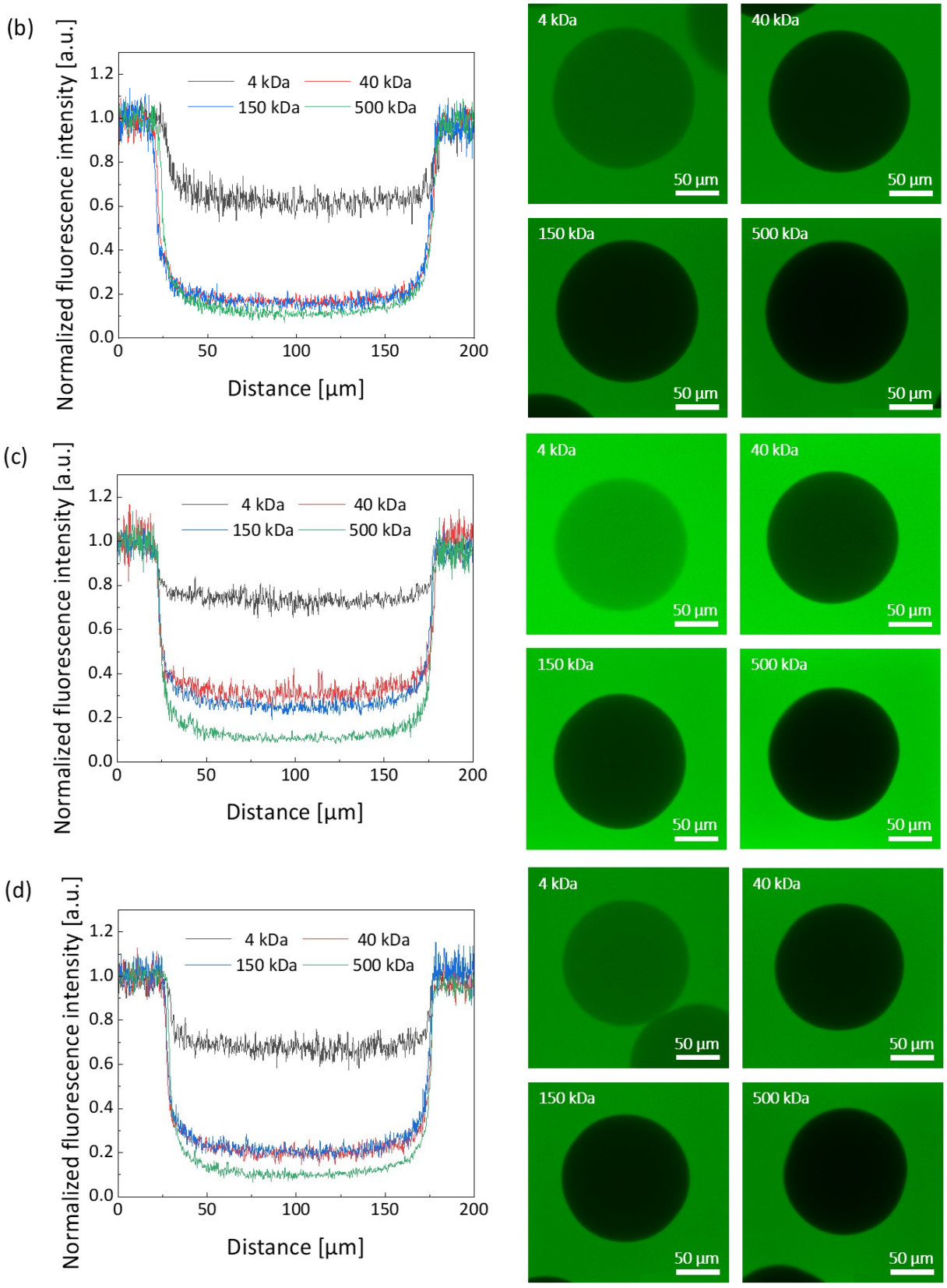

Figure V.4 Microgel permeability was investigated through fluorescence intensity profiles (left) of microgel cross-sections. These cross-sections were obtained from confocal imaging (right). All images were measured in the green channel (FITC-dextran: λ_{ex} = 488 nm, λ_{em} = 500-

550 nm) after microgels immersion in 1 mg mL^{-1} FITC-dextran solutions (4 to 500 kDa). The following microgels were investigated: (a) cov-L, (b) cov-S, (c) noncov-L, and (d) noncov-S.

The hydrodynamic radii (R_h) of FITC-dextrans (as outlined in **Table V.7**) have been previously established,[38,39] offering insight into the microgels' porosity: When considering an FITC-dextran of a particular molecular weight, such as the 4 kDa FITC-dextran, its ability to penetrate the microgel implies the existence of pores with radii larger than 1.3 nm due to its hydrodynamic radius of 1.3 nm. Therefore, it is expected that the pore size enables the diffusion of molecules smaller than this threshold, while acknowledging that interactions with the polymer chains also influence whether molecules can permeate the microgel.

Table V.7 Molecular weight and hydrodynamic radii (Rh) for specific FITC-dextrans were measured in PBS. The shown data were obtained from the literature.[38,39]

Molecular weight [kDa]	R_h [nm]
4	1.3
40	4.5
150	8.3
500	15.9

Analysis of normalized fluorescence intensities reveals that the diffusion of 4 kDa FITC-dextran is notably superior to that of higher molecular weight FITC-dextrans, as expected: 60-80% of the fluorescence intensity of 4 kDa FITC-dextran can be detected within these microgels, indicated by the intensities ranging between 0.6 to 0.8. This implies that a significant proportion of pores possesses radii larger than 1.3 nm, enabling the penetration of smaller molecules into the microgel. Conversely, a smaller subset of pore apertures are larger, as evidenced by the notably lower fluorescence intensity of FITC-dextrans with higher molecular weights within the microgels. When assessing the permeability, background fluorescence, which can contribute to the observed fluorescence in the microgels, must be taken into account: The consistent fluorescence intensity observed across all microgels for 500 kDa FITC-dextrans suggests that background fluorescence is the probable cause. The fluorescence intensity of 500 kDa FITC-dextran is likely overestimated. It is anticipated that pores do not exceed a radius of 15.7 nm, or that only a negligible fraction of pores fall within this size range.

Comparing different microgels amongst each other reveals distinct differences in permeability. For enhanced comparability, **Figure V.5** illustrates the intermediate

fluorescence intensity around the center of the microgel, showcasing variations with different molecular weights of FITC-dextran.

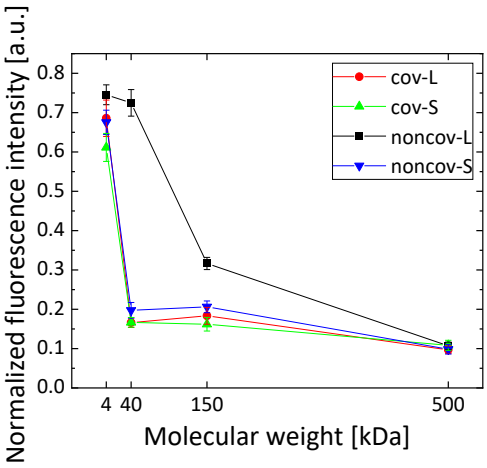

Figure V.5 Summary of the outcomes of the permeability assays (as depicted in **Figure V.4**). Different samples are compared: cov-L, cov-S, noncov-L, and noncov-S. The normalized fluorescence intensities within the microgel cores are plotted versus the molecular weight of the utilized FITC-dextrans.

A lower permeability can be observed for cov-S as opposed to cov-L, with the fluorescence intensity for 4 kDa FITC-dextran decreasing from around 0.7 to 0.6. Furthermore, all higher molecular weight dextrans also exhibit lower diffusion into cov-S microgels. Comparable outcomes arise when contrasting noncov-S with noncov-L. Both results are explained by the smaller molecular weight of the PEG building blocks causing a smaller mesh size. Additionally, the microgels cov-L and noncov-L were compared, indicating that the additional PEG arms in cov-L reduce microgel permeability through steric hindrance. This effect was also observed for the comparison of cov-S to noncov-S. Due to its low crosslinking degree and low PEG concentration, noncov-L demonstrates the highest permeability. Conversely, cov-S, characterized by a high degree of crosslinking and a high PEG concentration, exhibits the lowest permeability among all microgels.

The overall molecular weight of enzymes ranges from 73.1 kDa to 94.7 kDa (**Table SV.3**), which is most likely in the range of partial penetration. However, while the impact of PEG selection on the overall permeability of microgels has been established, it should be noted that the results obtained with FITC-dextrans may not directly correlate with enzyme permeability. Variations in permeability between dextrans and enzymes of the same molecular weights may

arise due to differences in molecular structure and their interactions with the polymer network. Permeability is not exclusively determined by molecular weight and interactions with the polymer network; the unique architecture of molecules also significantly influences their ability to penetrate the microgel network. Especially for proteins this architecture can be very complex, and the position of each amino acid plays an important role in determining their three-dimensional shape.[40]

Due to their different molecular structure, it is also not feasible to predict which enzymes will exhibit high penetration, particularly during post-attachment. However, indications may be provided by their tendency to form multimers, which are associated with a significant increase in size. Among the enzymes utilized, α3GalT is not known to form multimers,[41] whereas β4GalT exhibits a dynamic equilibrium between monomers and dimers.[42] The multimer formation of β3GlcNAcT has not been previously studied. At this stage, it is important to note that the success of post-attachment to microgels is not solely dependent on enzyme penetration. The accessibility of reactive functional groups in enzymes also plays a crucial role.

Next to enzyme immobilization through post-attachment, non-covalent encapsulation may be strongly dependent on the enzyme size, albeit in an opposite manner. Particularly, larger enzymes may be successfully immobilized, as their diffusion out of the microgel network is reduced after encapsulation. Partial retention of enzymes within the microgel network is expected, with a fraction of pores sufficiently small to trap enzymes effectively.

In covalent enzyme encapsulation, permeability plays a less significant role. Due to covalent attachment, the diffusion of enzymes out of the microgels is effectively impeded. In this context, factors such as reactive group accessibility or enzyme deactivation due to changes in the molecular structure may play a more significant role during immobilization.

While definite assumptions about enzyme uptake may not be feasible, it is reasonable to suggest that diffusion of enzyme substrates should not pose a challenge, as they should be able to permeate freely through the microgel network. To assess the performance of GT-microgels across various immobilization techniques, factors such as alterations to the enzyme structure, modifications to the electrostatic environment, and diffusion constraints imposed by the polymer network can be considered along with the permeability.[14] To identify the most

effective approach, the performance of all enzymes immobilized using different techniques is compared in **Chapter 3.2**.

3.1.5. Scanning Electron microscopy

In addition to permeability assays, electron microscopy techniques can provide further structural elucidation. For the visualization of the microgel surface, SEM was performed, with the aid of an SE detector. The resulting images of the microgels cov-L, noncov-L, cov-S, and noncov-S are shown in **Figure V.6**. All microgels display a spherical shape with relatively smooth surfaces. Only a low amount of dangling chains, defects, or drying artifacts, and no pores were detected. Fine pores can not be visualized using the employed method because imaging at higher magnification requires a high energy input. This resulted in sample instability under the electron beam. The absence of larger pores aligns with previous results indicating predominantly small pores with a radius of above 1.3 nm, whereas, based on our findings, pores exceeding a radius of 15.9 nm are not present.

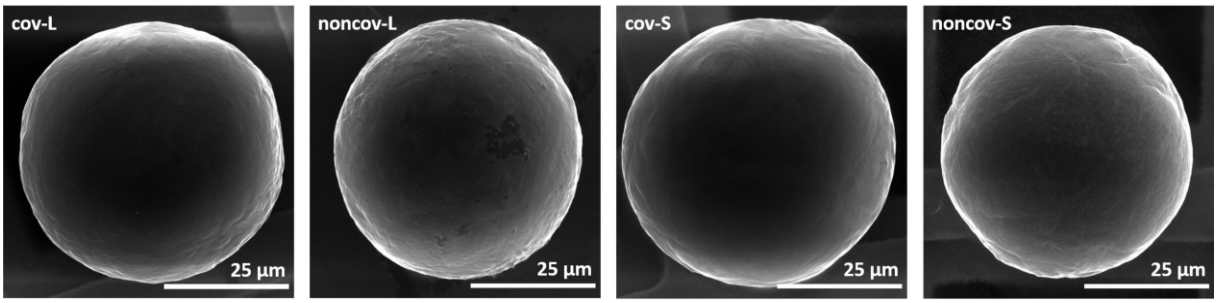

Figure V.6 SEM images of different microgels, including cov-L, noncov-L, cov-S, and noncov-S microgels. The microgel samples were measured in the dried state.

The dried microgels observed *via* SEM are approximately 50 to 54 µm in diameter. Among the microgels, cov-L (about 52 µm) and cov-S (about 54 µm) display slightly larger sizes compared to noncov-L (about 51 µm) and noncov-S (about 50 µm). Upon comparing the diameters of dried state to the hydrodynamic diameters of swollen microgels (as outlined in **Table SV.1**), a swelling ratio of approximately 300% is evident. This confirms the high water content of the microgels. After investigating the microgels regarding their chemical structure and morphology, the subsequent part is dedicated to evaluating the effectiveness of the microgels as immobilized enzyme reactors by evaluation of the enzymatic activity of GT-microgels.

3.2. Enzymatic Activity of Glycosyltransferase-Microgels

After a thorough investigation of the properties of (GT-)microgels, the subsequent section delves into the enzymatic activity observed for GT-microgels. The enzyme immobilization methods according to **Table V.6** are employed: covalent (cov-L, cov-S) and non-covalent (noncov-L, noncov-S) encapsulation techniques, or post-attachment *via* SpyT (SpyT-L, SpyT-S) or VS (VS-L, VS-S).

The enzymatic activities were calculated from the conversion of the initial substrate to the product as described in **Materials and Methods**. For this, a defined volume of swollen GT-microgels was employed and their volumetric enzymatic activities (in mU mL^{-1}) were obtained.

The volumetric activity provides a useful metric for evaluating the overall efficiency of GT-microgels and allows for comparisons between the chosen immobilization methods. Achieving a high volumetric activity is advantageous as it indicates efficient enzyme utilization and can lead to lower material consumption. However, it is important to note that volumetric activity does not take into account the specific activity of each enzyme, focusing instead on the collective performance of the GT-microgels. Therefore, the specific activities (in mU mg^{-1}) were determined according to **Equation V.3**, dividing the volumetric activity by the mass concentration of enzymes in the utilized volume.

Since it was not feasible to precisely determine the enzyme content in the GT-microgels obtained from enzyme encapsulation, the expected enzyme mass was calculated under the assumption of retaining 100% of all enzymes in the microgels during the process. While this approach may result in underestimating the specific activities, it is considered acceptable to present results that are at least as high as shown. The calculated activity can still be used for comparison with specific activities of the unbound enzyme, although it should be noted that the underestimation is particularly significant for non-covalent immobilization due to the absence of permanent bonds.[14]

GT-microgels obtained *via* post-attachment provide more accurate results for the enzyme mass uptake and therefore for the specific activity. With fewer washing steps involved, the enzyme content in the microgels could be more precisely determined using a Bradford assay.

Comparing both volumetric and specific activities should enable the selection of the most suitable immobilization method for each enzyme. Specific and volumetric activities are depicted in **Figure V.7**, **Figure V.8**, and **Figure V.9**. Furthermore, the calculation of the maximum amount of enzymes immobilized through enzyme encapsulation (**Figure SV.5a**) and the number of enzymes attached by post-attachment, as determined by the Bradford assay (**Figure SV.5b**) are depicted in the **Supplementary Data**.

3.2.1. Enzymatic Activity of α3GalT-Microgels

The GT α3GalT has been immobilized in microgels through all presented immobilization methods, albeit with strong differences in their efficiency. Covalent encapsulation (cov-L and cov-S) results in comparable enzyme activities for both pre-polymers employed. Contrarily, the enzyme activity in non-covalent encapsulation (noncov-L and noncov-S) is strongly dependent on the size of pre-polymers: The smaller mesh size in noncov-S microgels results in improved retainment of the enzyme. Much more notable is, however, the contrast to α3GalT-microgels acquired *via* SpyT-SpyC interaction, apparent in both specific (**Figure V.7a**) and volumetric activities (**Figure V.7b**).

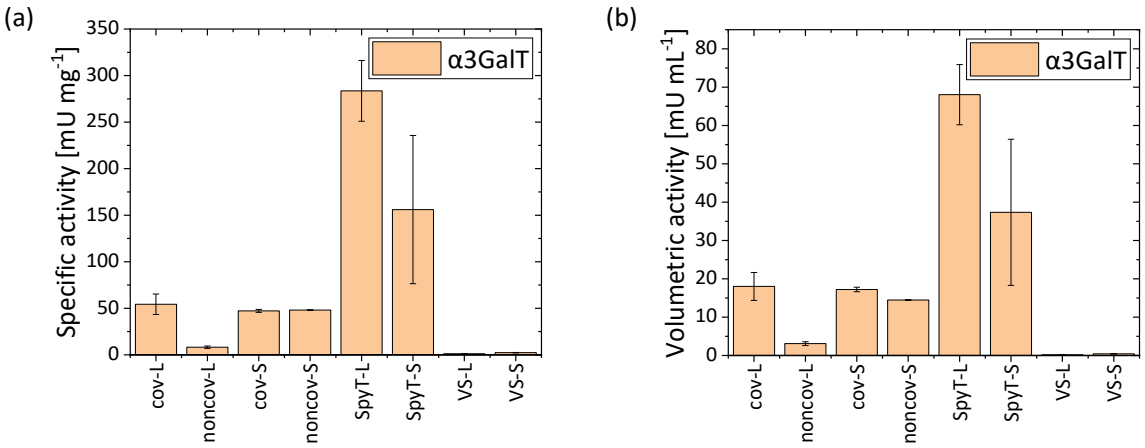

Figure V.7 (a) Specific and (b) volumetric activities of GT-microgels synthesized through various immobilization techniques, including covalent (cov) or non-covalent (noncov) enzyme encapsulation and post-attachment through SpyT or VS groups. Additionally, the molecular weight of the pre-polymers was varied (large: L, small: S). GT-microgels contain α3GalT.

α3GalT encapsulation resulted in the volumetric activities of up to 18 mU mL^{-1}, while the activities of α3GalT-SpyT microgels are considerably higher, reaching up to 68 mU mL^{-1}

(284 mU mg^{-1}). Compared to the specific activity of the non-immobilized enzyme (200 mU mg^{-1}), a 142 % increase was observed. Such an increase in activity is typically associated with the creation of ideal conditions for the enzymatic reaction within the microenvironment of the microgel.[14] In contrast, low enzymatic activity is observed for α3GalT immobilized through post-attachment *via* VS groups, despite the concentration of α3GalT in microgels being relatively similar (**Figure SV.5b**). Hence, the elevated activity of SpyT-immobilized α3GalT stems not from the sheer enzyme quantity, but primarily from the more conducive conditions the immobilized enzyme, with SpyT-SpyC interaction playing a pivotal role in the effective immobilization of active α3GalT.

3.2.2. Enzymatic Activity of β4GalT-Microgels

In contrast to the previously assessed α3GalT, β4GalT displays less favorable outcomes for GT-SpyT microgels, evident in the diminished activities observed in both β4GalT-SpyT-L and β4GalT-SpyT-S formulations. Likewise, a comparison with VS-L and VS-S configurations reveals similarly modest activities (**Figure V.8**).

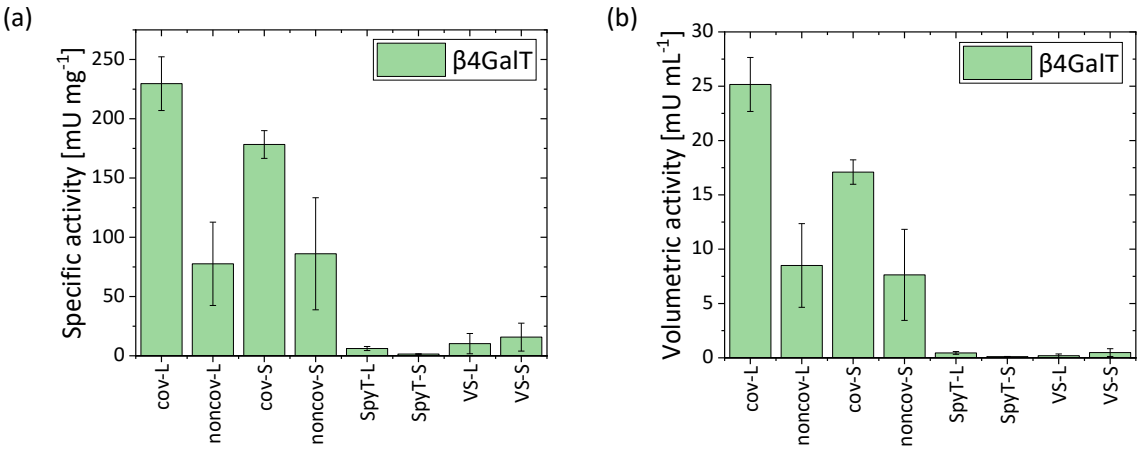

Figure V.8 (a) Specific and (b) volumetric activities of GT-microgels synthesized through various immobilization techniques, including covalent (cov) or non-covalent (noncov) enzyme encapsulation and post-attachment through SpyT or VS groups. Additionally, the molecular weight of the pre-polymers was varied (large: L, small: S). GT-microgels contain β4GalT.

In the case of post-attachment facilitated by SpyT, the underwhelming activities observed seem to stem from other factors than low enzyme uptake. Despite the enhanced enzyme immobilization realized with SpyT compared to VS groups (**Figure SV.5b**), the resultant

β4GalT-microgels exhibit similarly low activity levels. This discrepancy suggests that while the microenvironment within the microgel may enhance enzyme uptake, it appears to lead to a loss in activity. Contrarily, the enzyme immobilization by post-attachment through VS groups resulted in only low enzyme uptake (**Figure SV.5b**), suggesting diffusional limitations of β4GalT into the microgel, potentially linked to its partial presence as a dimer with a significantly larger size.[42] The variations in enzyme uptake by SpyT- versus VS-modified microgels can be caused by differences in the hydrophilicity and chemical microenvironment.

In this instance, higher activities were enabled through enzyme encapsulation compared to post-attachment. Thereby, microgels obtained by covalent binding possess a higher resulting activity up to 230 mU mg^{-1}. Microgels produced through non-covalent immobilization exhibit smaller activities (up to 86 mU mg^{-1}) along with larger standard deviations. This may be attributed to partial leaching of enzymes from the microgels, due to the absence of covalent binding sites.

VS-attachment seems to facilitate enzyme encapsulation: While cov-S microgels have a higher quantity of available VS groups, the smaller pore size may reduce enzymatic activity by limiting access to the enzyme's active sites. Hence, future research could investigate increasing the VS content to enhance enzyme uptake further while preserving a larger mesh size.

To ensure the proper folding and activity of the enzyme, preserving specific disulfide bridges is imperative for β4GalT functionality, as highlighted in previous research.[28,43] During the immobilization process, the integrity of disulfide bonds could potentially be compromised through thiol-disulfide exchange reactions with the employed PEG-SH. Additionally, reactions involving cysteine groups within the catalytic domain of β4GalT may contribute to a decrease in its overall activity, as these groups are crucial for substrate binding.[28,43] This probably explains, at least in part, the reduction in activity following the covalent attachment of PEG-VS to amino- or thiol-groups in the enzyme. Moreover, the immobilization of enzymes in microgels often results in hindered substrate diffusion,[14] which may further contribute to the overall reduction in activity. While a decline in activity is undesirable, the simplified reusability of immobilized β4GalT still advocates for the utilization of the synthesized β4GalT-microgels.

In summary, 38 % of the activity of non-immobilized β4GalT (598 mU mg^{-1}) was reached, employing cov-L microgels (230 mU mg^{-1}). Despite not achieving an increase of enzymatic

activity as observed in α3GalT, the decrease in activity remains within acceptable limits, considering the initially high activity. It is noteworthy that previous studies have reported significantly higher activity losses in numerous enzyme-microgel systems, with many realized activities well below 10 % of the initial level.[14]

3.2.3. Enzymatic Activity of β3GlcNAcT-Microgels

Like α3GalT and β4GalT, the GT β3GlcNAcT displays enzymatic activity with strong variations between the different immobilization techniques (**Figure V.9**). Post-attachment of enzymes resulted in overall low enzymatic activities, with smaller pre-polymers (SpyT-S, VS-S) resulting in further reduction, despite comparable amounts of enzymes being immobilized (**Figure SV.5b**). Hence, the likely explanation is partial deactivation of β3GlcNAcT due to interactions with SpyT and VS. These expectations are also mirrored in the notably higher activities realized through non-covalent enzyme encapsulation compared to covalent enzyme encapsulation, attributed to the interaction of β3GlcNAcT with reactive VS groups.

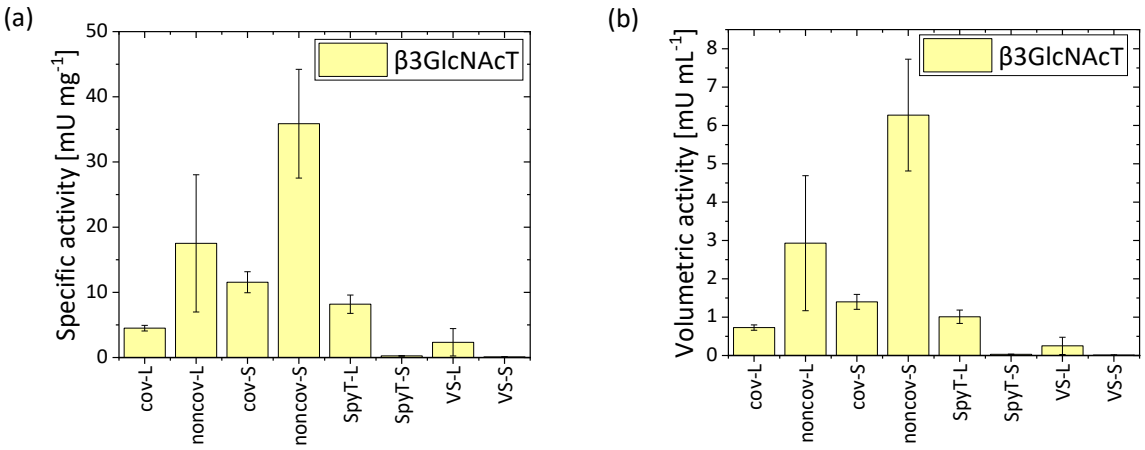

Figure V.9 (a) Specific and (b) volumetric activities of GT-microgels synthesized through various immobilization techniques, including covalent (cov) or non-covalent (noncov) enzyme encapsulation and post-attachment through SpyT or VS groups. Additionally, the molecular weight of the pre-polymers was varied (large: L, small: S). GT-microgels contain β3GlcNAcT.

In short, enzyme encapsulation demonstrates better performance when employing smaller pre-polymers (cov-S compared to cov-L; noncov-S compared to noncov-L). This phenomenon is attributed to the enhanced non-covalent immobilization within smaller pores, which leads to reduced enzyme leaching. It is anticipated that, in the case of cov-S microgels, there is at

least partial non-covalent immobilization occurring as well, contributing to an overall larger enzyme activity. In contrast, post-attachment is unlikely to involve non-covalent immobilization, mainly because enzymes are unlikely to be encapsulated within sufficiently small pores. This limitation stems from the need for enzymes to diffuse into the pores, which prevents enzyme confinement.

To summarize, 12 % of the specific activity of non-immobilized β3GlcNAcT (303 mU mg^{-1}) has been reached utilizing β3GlcNAcT-microgels with the smallest mesh size for non-covalent immobilization (noncov-S). As previously emphasized, it is worth noting that the specific activity may be underestimated. However, the similarly low volumetric activity also suggests the need for further optimization. Enhancing the successful immobilization of active β3GlcNAcT could involve a strategic reduction in mesh size. This adjustment aims to capture a greater number of enzymes within the microgel network, while simultaneously minimizing leaching effects. Subsequent strategies may involve utilizing an even smaller molecular weight pre-polymer or employing a combination of 8-arm PEG-VS with 8-arm PEG-SH. These approaches aim to realize a further reduction in mesh size, emphasizing non-covalent binding by maintaining a 1:1 ratio of VS and SH groups.

In addition to enzyme loss, the process of immobilization can potentially affect catalytic activity, even in cases of non-covalent immobilization. Changes to enzyme structure, alterations in the electrostatic environment, and limitations in diffusion imposed by the polymer network may all influence enzymatic activity.[14]

In summary, active GT-microgels were successfully synthesized for three different enzymes. Specific activity for α3GalT increased to 142 % of the initial level, while β4GalT exhibited a slight decrease to approximately 38 % of its initial activity. β3GlcNAcT showed a reduction to around 12 % of its initial activity, although this activity may be underestimated due to the potential leaching of β3GlcNAcT, primarily incorporated through non-covalent interactions. Future research could concentrate on enhancing volumetric activity by incorporating more enzymes into the polymer network through further mesh size reduction.

Following this stage, different GT-microgels were combined in a one-pot cascade reaction.

3.2.4. Cascade Reaction of β4GalT- and α3GalT-Microgels

After identifying β4GalT and α3GalT as enzymes that yield GT-microgels with optimal specific and volumetric activities through the methods outlined earlier, the intention is to utilize them in a one-pot cascade reaction. In this setup, β4GalT and α3GalT were incorporated into a reaction sequence, each catalyzing a partial reaction with UDP-Gal serving as the donor substrate for both GTs. Initially, starting from the acceptor GlcNAc-*t*Boc, β4GalT facilitates the formation of LacNAc type 2-*t*Boc. Subsequently, this product acts as a substrate for α3GalT, which proceeds to generate the Galili epitope-*t*Boc. In **Figure V.10a** the SNFG is employed for the depiction of this reaction sequence, while **Figure SV.6** shows the respective structural formulas.

For the cascade reaction, GT-microgels possessing similar volumetric activities were utilized, namely β4GalT-cov-L (25.2 mU mL^{-1}) and α3GalT-cov-L (18.0 mU mL^{-1}). This was done to ensure similar numbers of GT-microgels were present in the mixture when employing a 1:1 ratio of total activities. GT-microgels were mixed not only in a 1:1 activity ratio but also in ratios of 2:1 and 1:2 according to **Table V.3** (**Materials and Methods**), reaching total activities of 1.0 mU to 1.1 mU. The activity ratio is varied due to its possible influence on the overall reaction speed: Besides the individual activities of β4GalT and α3GalT, the reaction speed is dependent on the chemical equilibrium of each reaction. The β4GalT to α3GalT activity ratio causes changes in the turnover rate of each enzyme, causing changes in the substrate-to-product ratios of each enzyme. This in turn results in changes in the chemical equilibrium.

The molar fractions of the initial substrate GlcNAc-*t*Boc, the intermediate LacNAc, and the product Galili epitope-*t*Boc were monitored over time (**Figure V.10b-d**). The molar fractions (**Table SV.4**) were obtained from HPLC with exemplary chromatograms shown in **Figure SV.7**. The formation of the Galili epitope-*t*Boc by β4GalT and α3GalT was further catalyzed with non-immobilized enzymes, employing a total of 2.6 mU (**Figure SV.8**). Initial considerations may suggest only small differences between the reaction speeds of non-immobilized enzymes (2.6 mU) and the GT-microgels (1.0 to 1.1 mU) within the cascade. The presence of two different GT-microgel species, however, decelerates the biocatalytic reaction. This is caused by the significantly higher diffusional limitations: initial donor and acceptor substrates need to diffuse into the β4GalT-microgel to enable the first enzymatic reaction, followed by the

intermediate product needing to diffuse out of the microgel into an α3GalT-microgel, along with the donor substrate. Only then, the second enzymatic reaction can be enabled. The diffusion process is unspecific and product formation is only possible when the appropriate substrates diffuse into the appropriate type of GT-microgel.

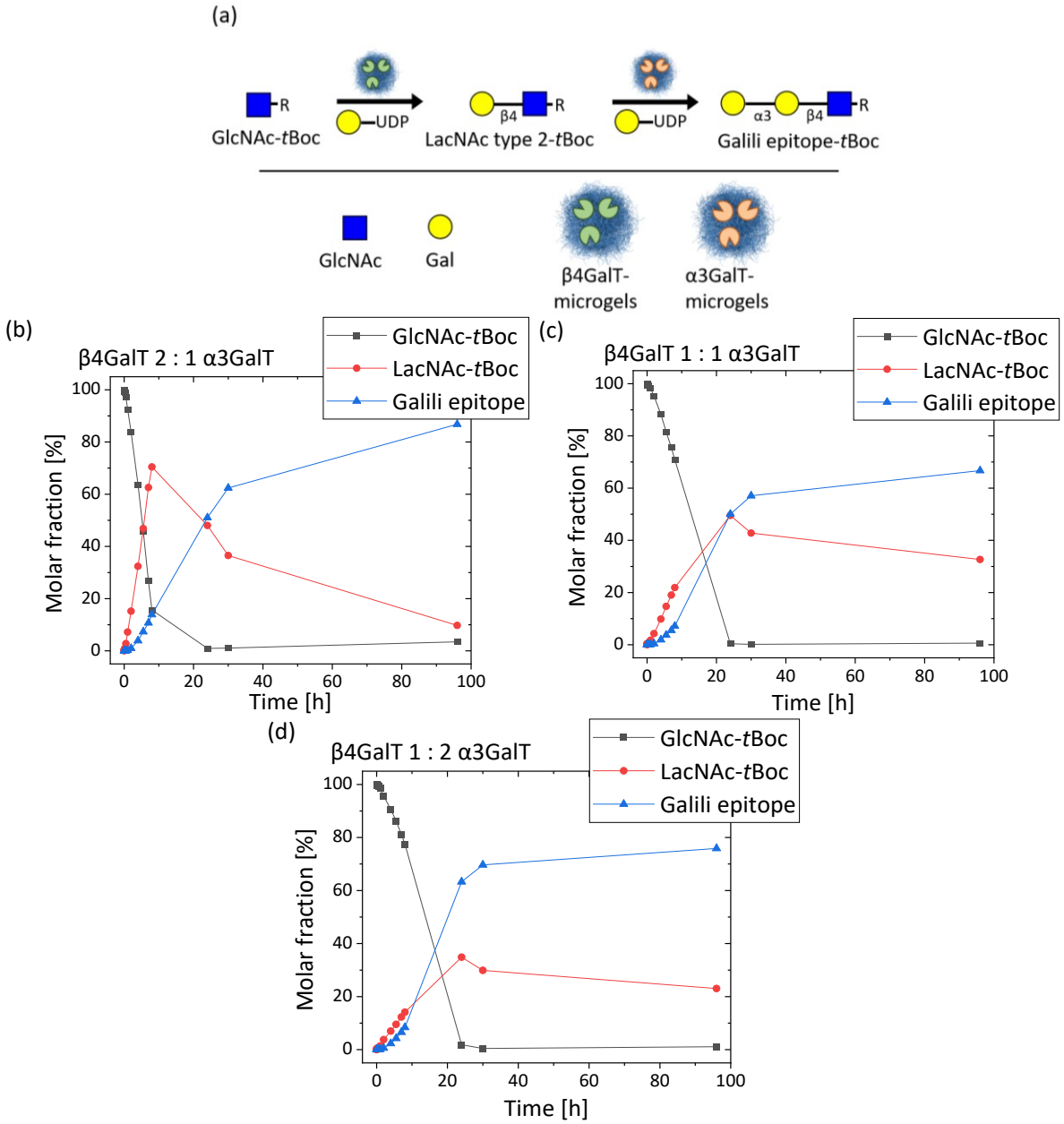

Figure V.10 One-pot cascade reaction of GT-microgels. The successive reaction is enabled by mixing β4GalT-microgels and α3GalT-microgels with the initial acceptor substrate GlcNAc-*t*Boc and the donor substrate UDP-Gal, which serves as the donor substrate for both enzymes. (a) GlcNAc-*t*Boc is transformed to LacNAc type 2 (t2)-*t*Boc by β4GalT. Subsequently, LacNAc t2-*t*Boc is transformed to the Galili epitope-*t*Boc by α3GalT. The *t*Boc residue is labeled with R. (b)-(d) The molar fractions of the different molecules were observed over time. The β4GalT to α3GalT activity ratio was varied: (b) 2:1 to (c) 1:1 and (d) 1:2 with total activities of (b), (d)

1.1 mU and (c) 1.0 mU in 120 µL reaction volume. GT-microgels were mixed according to **Table V.3**.

With the presented cascade, 66.7-86.8 % yield was realized after 96 h. 9.8-32.7 % of unreacted LacNAc and 0.6-3.5 % of unreacted GlcNAc were left in the reaction mixture (**Figure V.10b-d**). For non-immobilized enzymes, a yield of 79.2-90.3 % was realized after 24 h, along with residual amounts of 9.7-16.6 % LacNAc. GlcNAc was not detected after 24 h (**Figure SV.8**).

Subsequently, the different activity ratios are compared. At a β4GalT to α3GalT activity ratio of 2:1, GT-microgels demonstrate the highest performance (86.8 % yield). The 1:2 ratio demonstrates inferior performance (75.9 % yield). Comparing these results to activities of non-immobilized enzymes, it is striking that here, obtained yields are almost identical (90.1 % at 2:1; 90.3 % at 1:2). The larger differences in performance for GT-microgels are caused by the GT-microgel quantities employed: For the 2:1 ratio, 48.9 µL of GT-microgels are employed, whereas a larger amount of 54.4 µL is needed for the 1:2 ratio. The higher microgel volume decelerates the reaction due to the longer time needed for substrate diffusion into the specific GT-microgel. An even lower yield was obtained for the 1:1 ratio (66.7 %), consistent with the lowest performance in non-immobilized enzymes (79.2 %). The low yield is encouraged by the slightly lower activity in the reaction (1.0 mU).

In summary, the highest attained yield (86.8 %) is satisfactory, reaching 96.1 % of the yield realized by the non-immobilized enzyme, albeit attained through a slower reaction. The results underscore the feasibility of enzymatic cascade synthesis within multiple GT-microgels. Forthcoming studies will focus on augmenting the overall reaction rate through further optimization of GT-microgels. Furthermore, the cascade could be enhanced by evolving the one-pot cascade synthesis into a modular membrane reactor configuration. The adoption of distinct compartments for individual enzymatic reactions within the modular membrane reactor may result in a significant enhancement in reaction velocity by impeding the diffusion of multiple substrates into inappropriate microgels. Additionally, the implementation of a current within such a reactor could boost substrate and product movement within the GT-microgels, thus further amplifying reaction velocity.

3.2.5. Cascade Reaction of β3GlcNAcT- and β4GalT-Microgels

A second one-pot cascade was performed in this thesis employing β3GlcNAcT-microgels and β4GalT-microgels. In this cascade, several alternating reactions are catalyzed by the GTs. A total activity of 1.1 mU, along with a ratio of β4GalT to β3GlcNAcT activity of 2:1 was employed.

β3GlcNAcT catalyzes the formation of a β-1,3-glycosidic bond between GlcNAc and a galactose residue in lactosyl-*t*Boc, employing UDP-GlcNAc as donor substrate. After cascade initiation, β4GalT enables the formation of a β-1,4-glycosidic bond between Gal and terminally attached GlcNAc residues, utilizing UDP-Gal as the donor substrate. Further reactions alternatively elongate the glycan with Gal or GlcNAc moieties (**Figure V.11a**, **Figure SV.6**). The predominant product is lacto-*N*-neotetraose-*t*Boc (LNnT-*t*Boc), but under the employed reaction conditions, glycans as long as hexasaccharides are formed. The molar fractions of the substrates lactosyl-*t*Boc, lacto-*N*-triose II-*t*Boc (LNT II-*t*Boc), LNnT-*t*Boc, lacto-*N*-neopentaose-*t*Boc (LNnP-*t*Boc), lacto-*N*-neohexaose-*t*Boc (LNnH-*t*Boc) are observed over time (**Figure V.11b**). Exemplary HPLC chromatograms are provided in the **Supplementary Data** (**Figure SV.9**), along with the corresponding molar fractions (**Table SV.5**). The analogous cascade reaction of non-immobilized GTs was performed with 20 mU (**Figure SV.10**). When employing non-immobilized enzymes, a LNnT-*t*Boc yield of 93 % was realized with a total enzyme activity of 20.0 mU over a 24-hour period. However, upon immobilization within the microgel, the yield decreases to just below 4.5 % during the same duration, with enzyme activity measuring at 1.1 mU. After 96 hours, a LNnT-*t*Boc yield of 5.1 % and a lacto-*N*-neohexaose yield of 0.9 % are obtained, with 94.0 % of the starting material remaining in the reaction mixture. Notably, the majority of biocatalysis occurs within the initial 24-hour timeframe.

On the one hand, the differences in yield are explained by activity differences (1.1 mU versus 20.0 mU). On the other hand, the immobilization of GTs results in further reduction of the performance, caused by the diffusion-limited transportation of educts and products into the suitable GT-microgel. Contrarily, the biocatalysis by non-immobilized enzymes is less diffusion-hindered.

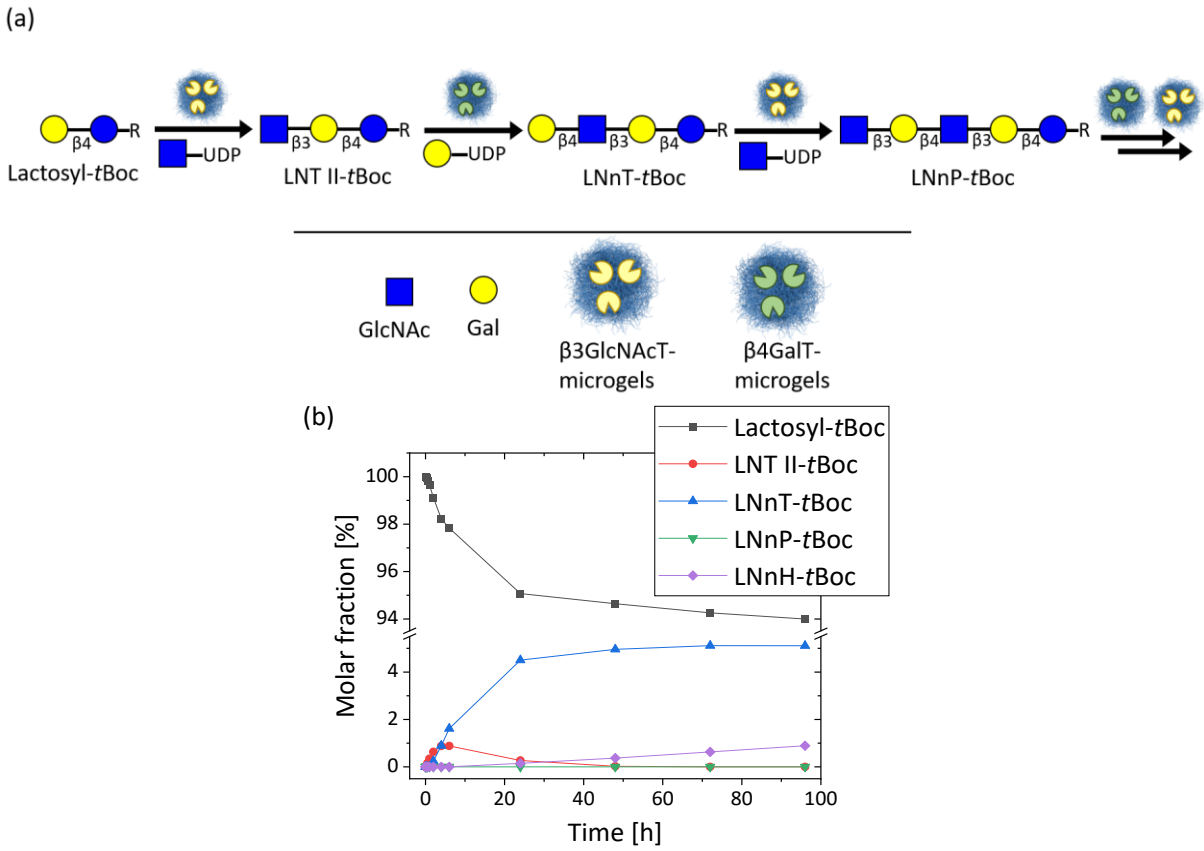

Figure V.11 One-pot cascade reaction of GT-microgels. The successive reaction is enabled by mixing β3GlcNAcT-microgels and β4GalT-microgels with the initial acceptor substrate lactosyl-*t*Boc and the donor substrates UDP-GlcNAc and UDP-Gal. UDP-GlcNAc serves as a donor substrate for β3GlcNAcT while UDP-Gal serves as the donor substrate of β4GalT. (a) lactosyl-*t*Boc is transformed to Lacto-*N*-triose II-*t*Boc (LNT II-*t*Boc) by β3GlcNAcT. Subsequently, the formation of Lacto-*N*-neotetraose-*t*Boc (LNnT-*t*Boc) is catalyzed by β4GalT. Both enzymes catalyze reactions in an alternating manner for the formation of Lacto-*N*-neopentaose-*t*Boc (LNnP-*t*Boc) and Lacto-*N*-neohexaose-*t*Boc (LNnH-*t*Boc). The *t*Boc residue is labeled with R. (b) The molar fractions of the different molecules were observed over time. The β4GalT-to-β3GlcNAc activity ratio was set to 2:1 with a total activity of 1.1 mU and in 150 µL reaction volume. GT-microgels were mixed according to **Table V.3**.

For this cascade, a larger volume of GT-microgels (96.7 µL) was needed, caused by the low volumetric activity of β3GlcNAcT-microgels (6.3 mU mL^{-1}). This results in even more deceleration of the reaction because of the associated higher diffusional barriers. This increase in volume explains the significantly lower yield for this cascade, despite the same total activity compared to the previous one.

The acceleration of the reaction speed can be facilitated upon integration of the GT-microgels into modular reactors. However, before proceeding, the activities of the GT-microgels in this

cascade need to be further enhanced, particularly focusing on the β3GlcNAcT-microgels. This could be realized by further reducing the mesh size and encapsulating a larger amount of β3GlcNAcT non-covalently.

In summary, the cascade reaction by β3GlcNAcT-microgels and β4GalT-microgels presented here serves only as an initial proof-of-concept. Subsequent efforts will focus on enhancing enzymatic activity further and integrating GT-microgels into a reactor for automated enzymatic glycan synthesis.

4. Conclusion

In this chapter, the synthesis of poly(ethylene glycol) (PEG)-based microgels was conducted through the generation of W/O droplets on a microfluidic chip. Reactive pre-polymers with vinyl sulfone (VS) and thiol (SH) end groups were utilized for this purpose. The primary objective was to immobilize different active GTs for enzymatic glycan synthesis. Therefore, various methods for enzyme immobilization were developed and evaluated, including both covalent and non-covalent encapsulation techniques, as well as different post-attachment strategies. For the latter, a comparison was made between selective binding *via* SpyTag-SpyCatcher interactions and non-selective binding to VS groups.

The microgels underwent characterization using optical microscopy, revealing sizes ranging from 140 to 170 µm and narrow size distributions. FT-IR spectroscopy was utilized to verify the presence of VS groups in cov-type microgels and their consumption upon functionalization with SpyTag. The presence of enzymes and SpyT was confirmed through a fluorescamine assay. Additionally, a permeability assay was conducted to assess variations in mesh size attributable to different PEG molecular weights. Adjustments in the mesh size offer the potential for tailoring enzyme capture.

Using HPLC analysis, the enzymatic activities of the synthesized GT-microgels were assessed, uncovering that each GT necessitates a distinct immobilization technique. Specifically, GT-microgel specific activities of 284 mU mg^{-1}, 230 mU mg^{-1}, and 36 mU mg^{-1} were realized for the SpyCatcher fusion GTs α3GalT, β4GalT, and β3GlcNAcT, respectively. These values represent 142 %, 38 %, and 12 % of the specific activity of the unbound GTs in solution.

Choosing the most suitable GT-microgels, cascade reactions were performed. α3GalT and β4GalT catalyzed a two-step reaction to form the Galili epitope, achieving an 86.8 % yield utilizing the enzymatic cascade reaction within the GT-microgels. Despite the increased time required for substrates to diffuse into the appropriate type of GT-microgels, resulting in some differences in performance compared to free enzymes, the results were overall promising. In the second cascade, β3GlcNAcT and β4GalT alternated in extending lactosyl-*t*Boc to produce longer glycans, predominantly yielding lacto-*N*-neotetraose, consistent with the synthesis catalyzed by free enzymes. However, compared to the previous cascade, a much lower yield

was realized. This was attributed to the overall lower volumetric activity of GT-microgels and thus a larger number of employed GT-microgels, which increased diffusional limitations. The multi-step nature of the process further aggravated this issue. Future efforts should prioritize enhancing the activity of each GT-microgel before considering potential improvements to the cascade reaction itself.

This study represents the first instance where a cascade of distinct GT-microgels has been utilized for glycan synthesis, addressing a gap in prior research on automated enzymatic glycan synthesis within GT-microgels. These findings mark the initial steps toward the development of a GT-microgel reactor, with further investigations and optimizations necessary for future research.

The presented biocatalytic GT-microgels pave the way for establishing a fully automated and scalable synthesis of tailored glycans with wide-ranging applications in drug development, vaccines, nutrition, and cosmetics. The potential advantages of incorporating these microgels into a modular membrane reactor extend beyond enabling continuous glycan production. Reaction kinetics could potentially be enhanced through the spatial separation of different GT-microgels. This avenue merits further exploration in future studies.

5. References

(1) Sommerfeld, I. K.; Palm, P.; Hussnaetter, K. P.; Pieper, M. I.; Bulut, S.; Lile, T.; Wagner, R.; Walkowiak, J.; Elling, Lothar, Pich; Andrij. Microgels with Immobilized Glycosyltransferases for Enzymatic Glycan Synthesis. *Biomacromolecules* **2024**, *25*, 3807–3822.

(2) Valverde, P.; Ardá, A.; Reichardt, N.-C.; Jiménez-Barbero, J.; Gimeno, A. Glycans in Drug Discovery. *MedChemComm* **2019**, *10*, 1678–1691.

(3) Varki, A. Biological Roles of Glycans. *Glycobiology* **2017**, *27*, 3–49.

(4) Moghaddam, F. D.; Heidari, G.; Zare, E. N.; Djatoubai, E.; Paiva-Santos, A. C.; Bertani, F. R.; Wu, A. Carbohydrate Polymer-Based Nanocomposites for Breast Cancer Treatment. *Carbohydr. Polym.* **2023**, *304*, 120510.

(5) Seabright, G. E.; Doores, K. J.; Burton, D. R.; Crispin, M. Protein and Glycan Mimicry in HIV Vaccine Design. *J. Mol. Biol.* **2019**, *431*, 2223–2247.

(6) Terra, V. S.; Mills, D. C.; Yates, L. E.; Abouelhadid, S.; Cuccui, J.; Wren, B. W. Recent Developments in Bacterial Protein Glycan Coupling Technology and Glycoconjugate Vaccine Design. *J. Med. Microbiol.* **2012**, *61*, 919–926.

(7) Bode, L. Human Milk Oligosaccharides: Every Baby Needs a Sugar Mama. *Glycobiol.* **2012**, *22*, 1147–1162.

(8) Bode, L. The Functional Biology of Human Milk Oligosaccharides. *Early Hum. Dev.* **2015**, *91*, 619–622.

(9) González-Morelo, K. J.; Vega-Sagardía, M.; Garrido, D. Molecular Insights Into O-Linked Glycan Utilization by Gut Microbes. *Front. Microbiol.* **2020**, *11*, 591568.

(10) Gibson, G. R.; Probert, H. M.; van Loo, J.; Rastall, R. A.; Roberfroid, M. B. Dietary Modulation of the Human Colonic Microbiota: Updating the Concept of Prebiotics. *Nutr. Res. Rev.* **2004**, *17*, 259–275.

(11) Ullah, H.; Santos, H. A.; Khan, T. Applications of bacterial cellulose in food, cosmetics and drug delivery. *Cellulose* **2016**, *23*, 2291–2314.

(12) Bukhari, S. N. A.; Roswandi, N. L.; Waqas, M.; Habib, H.; Hussain, F.; Khan, S.; Sohail, M.; Ramli, N. A.; Thu, H. E.; Hussain, Z. Hyaluronic Acid, a Promising Skin Rejuvenating Biomedicine: A Review of Recent Updates and Pre-Clinical and Clinical Investigations on Cosmetic and Nutricosmetic Effects. *Int. J. Biol. Macromol.* **2018**, *120*, 1682–1695.

(13) Hussnaetter, K. P.; Palm, P.; Pich, A.; Franzreb, M.; Rapp, E.; Elling, L. Strategies for Automated Enzymatic Glycan Synthesis (AEGS). *Biotechnol. Adv.* **2023**, *67*, 108208.

(14) Nöth, M.; Gau, E.; Jung, F.; Davari, M. D.; El-Awaad, I.; Pich, A.; Schwaneberg, U. Biocatalytic microgels (μ-Gel zymes): synthesis, concepts, and emerging applications. *Green Chem.* **2020**, *22*, 8183–8209.

(15) Sheldon, R. A.; Basso, A.; Brady, D. New Frontiers in Enzyme Immobilisation: Robust Biocatalysts for a Circular Bio-Based Economy. *Chem. Soc. Rev.* **2021**, *50*, 5850–5862.

(16) Miletić, N.; Nastasović, A.; Loos, K. Immobilization of Biocatalysts for Enzymatic Polymerizations: Possibilities, Advantages, Applications. *Bioresour. Technol.* **2012**, *115*, 126–135.

(17) Brena, B. M.; Batista-Viera, F. Immobilization of Enzymes. *Immobilization of Enzymes and Cells*; Humana Press, 2006; pp 15–30.

(18) Zou, Z.; Gau, E.; El-Awaad, I.; Jakob, F.; Pich, A.; Schwaneberg, U. Selective Functionalization of Microgels with Enzymes by Sortagging. *Bioconjugate Chem.* **2019**, *30*, 2859–2869.

(19) Wong, L. S.; Khan, F.; Micklefield, J. Selective Covalent Protein Immobilization: Strategies and Applications. *Chem. Rev.* **2009**, *109*, 4025–4053.

(20) Sommerfeld, I. K.; Malyaran, H.; Neuss, S.; Demco, D. E.; Pich, A. Multi-Responsive Core-Shell Microgels Functionalized by Nitrilotriacetic Acid. *Biomacromolecules* **2024**, *25*, 903–923.

(21) England, C. G.; Luo, H.; Cai, W. HaloTag Technology: A Versatile Platform for Biomedical Applications. *Bioconjug. Chem.* **2015**, *26*, 975–986.

(22) Juillerat, A.; Heinis, C.; Sielaff, I.; Barnikow, J.; Jaccard, H.; Kunz, B.; Terskikh, A.; Johnsson, K. Engineering Substrate Specificity of O6-Alkylguanine-DNA Alkyltransferase for Specific Protein Labeling in Living Cells. *ChemBioChem* **2005**, *6*, 1263–1269.

(23) Reddington, S. C.; Howarth, M. Secrets of a Covalent Interaction for Biomaterials and Biotechnology: SpyTag and SpyCatcher. *Curr. Opin. Chem. Biol.* **2015**, *29*, 94–99.

(24) Petschacher, B.; Nidetzky, B. Biotechnological Production of Fucosylated Human Milk Oligosaccharides: Prokaryotic Fucosyltransferases and Their Use in Biocatalytic Cascades or Whole Cell Conversion Systems. *J. Biotech.* **2016**, *235*, 61–83.

(25) Palm, P.; Hußnätter, K.; Elling, L. Development and Characterization of SpyCatcher-Glycosyltransferase-Fusion Proteins for Highly Specific Automated Glycan Synthesis. *Chem. Ing. Tech.* **2022**, *94*, 1303.

(26) Keeble, A. H.; Turkki, P.; Stokes, S.; Khairil Anuar, I. N. A.; Rahikainen, R.; Hytönen, V. P.; Howarth, M. Approaching Infinite Affinity Through Engineering of Peptide-Protein Interaction. *PNAS* **2019**, *116*, 26523–26533.

(27) Logan, S. M.; Altman, E.; Mykytczuk, O.; Brisson, J.-R.; Chandan, V.; Schur, M. J.; St Michael, F.; Masson, A.; Leclerc, S.; Hiratsuka, K.; Smirnova, N.; Li, J.; Wu, Y.; Wakarchuk, W. W. Novel Biosynthetic Functions of Lipopolysaccharide rfaJ Homologs from Helicobacter Pylori. *Glycobiology* **2005**, *15*, 721–733.

(28) Sauerzapfe, B.; Namdjou, D.-J.; Schumacher, T.; Linden, N.; Křenek, K.; Křen, V.; Elling, L. Characterization of Recombinant Fusion Constructs of Human β1,4-Galactosyltransferase 1 and the Lipase Pre-Propeptide from Staphylococcus hyicus. *J. Mol. Catal. B: Enzym.* **2008**, *50*, 128–140.

(29) Fischöder, T.; Cajic, S.; Reichl, U.; Rapp, E.; Elling, L. Enzymatic Cascade Synthesis Provides Novel Linear Human Milk Oligosaccharides as Reference Standards for xCGE-LIF Based High-Throughput Analysis. *Biotechnol. J.* **2019**, *14*, e1800305.

(30) Heinzler, R.; Hübner, J.; Fischöder, T.; Elling, L.; Franzreb, M. A Compartmented Flow Microreactor System for Automated Optimization of Bioprocesses Applying Immobilized Enzymes. *Front. Bioeng. Biotechnol.* **2018**, *6*, 189.

(31) Bradford, M. M. A Rapid and Sensitive Method for the Quantitation of Microgram Quantities of Protein Utilizing the Principle of Protein-Dye Binding. *Anal. Biochem.* **1976**, *72*, 248–254.

(32) Jung, S.-H.; Bulut, S.; Busca Guerzoni, L. P. B.; Günther, D.; Braun, S.; Laporte, L. de; Pich, A. Fabrication of pH-Degradable Supramacromolecular Microgels with Tunable Size and Shape via Droplet-Based Microfluidics. *JCIS* **2022**, *617*, 409–421.

(33) Slámová, K.; Červený, J.; Mészáros, Z.; Friede, T.; Vrbata, D.; Křen, V.; Bojarová, P. Oligosaccharide Ligands of Galectin-4 and Its Subunits: Multivalency Scores Highly. *Molecules* **2023**, *28*, 4039.

(34) Sauerzapfe, B.; Krenek, K.; Schmiedel, J.; Wakarchuk, W. W.; Pelantová, H.; Kren, V.; Elling, L. Chemo-Enzymatic Synthesis of Poly-N-Acetyllactosamine (Poly-LacNAc) Structures

and Their Characterization for CGL2-Galectin-Mediated Binding of ECM Glycoproteins to Biomaterial Surfaces. *Glycoconjugate J.* **2009**, *26*, 141–159.

(35) Udenfriend, S.; Stein, S.; Böhlen, P.; Dairman, W.; Leimgruber, W.; Weigele, M. Fluorescamine: A Reagent for Assay of Amino Acids, Peptides, Proteins, and Primary Amines in the Picomole Range. *Science* **1972**, *178*, 871–872.

(36) Watkin, S. A. J.; Hashemi, A.; Thomson, D. R.; Pearce, F. G.; Dobson, R. C. J.; Nock, V. M. Laminar Flow-Based Microfluidic Systems for Molecular Interaction Analysis-Part 1: Chip Development, System Operation and Measurement Setup. *Methods Enzymol.* **2023**, *682*, 53–100.

(37) Bulut, S.; Jung, S.-H.; Bissing, T.; Schmitt, F.; Bund, M.; Braun, S.; Pich, A. Tuning the Porosity of Dextran Microgels with Supramacromolecular Nanogels as Soft Sacrificial Templates. *Small* **2023**, *19*, e2303783.

(38) Ambati, J.; Canakis, C. S.; Miller, J. W.; Gragoudas, E. S.; Edwards, A.; Weissgold, D. J.; Kim, I.; Delori, F. C.; Adamis, A. P. Diffusion of High Molecular Weight Compounds through Sclera. *Invest. Ophthalmol. Vis. Sci.* **2000**, *41*, 1181–1185.

(39) Heida, T.; Otto, O.; Biedenweg, D.; Hauck, N.; Thiele, J. Microfluidic Fabrication of Click Chemistry-Mediated Hyaluronic Acid Microgels: A Bottom-Up Material Guide to Tailor a Microgel's Physicochemical and Mechanical Properties. *Polymers* **2020**, *12*.

(40) Alberts, B.; Johnson, A.; Lewis, J.; Raff, M.; Roberts, K.; Walter, P., Eds. *Molecular Biology of the Cell. 4th edition*; Garland Science, 2002.

(41) Chen, X.; Liu, Z.; Wang, J.; Fang, J.; Fan, H.; Wang, P. G. Changing the Donor Cofactor of Bovine Alpha 1,3-Galactosyltransferase by Fusion with UDP-Galactose 4-epimerase. More Efficient Biocatalysis for Synthesis of Alpha-Gal Epitopes. *JBC* **2000**, *275*, 31594–31600.

(42) Harrus, D.; Khoder-Agha, F.; Peltoniemi, M.; Hassinen, A.; Ruddock, L.; Kellokumpu, S.; Glumoff, T. The Dimeric Structure of Wild-Type Human Glycosyltransferase B4GalT1. *PloS one* **2018**, *13*, e0205571.

(43) Wang, Y.; Wong, S. S.; Fukuda, M. N.; Zu, H.; Liu, Z.; Tang, Q.; Appert, H. E. Identification of Functional Cysteine Residues in Human Galactosyltransferase. *Biochem. Biophys. Res. Commun.* **1994**, *204*, 701–709.

6. Supplementary Data

Size determination

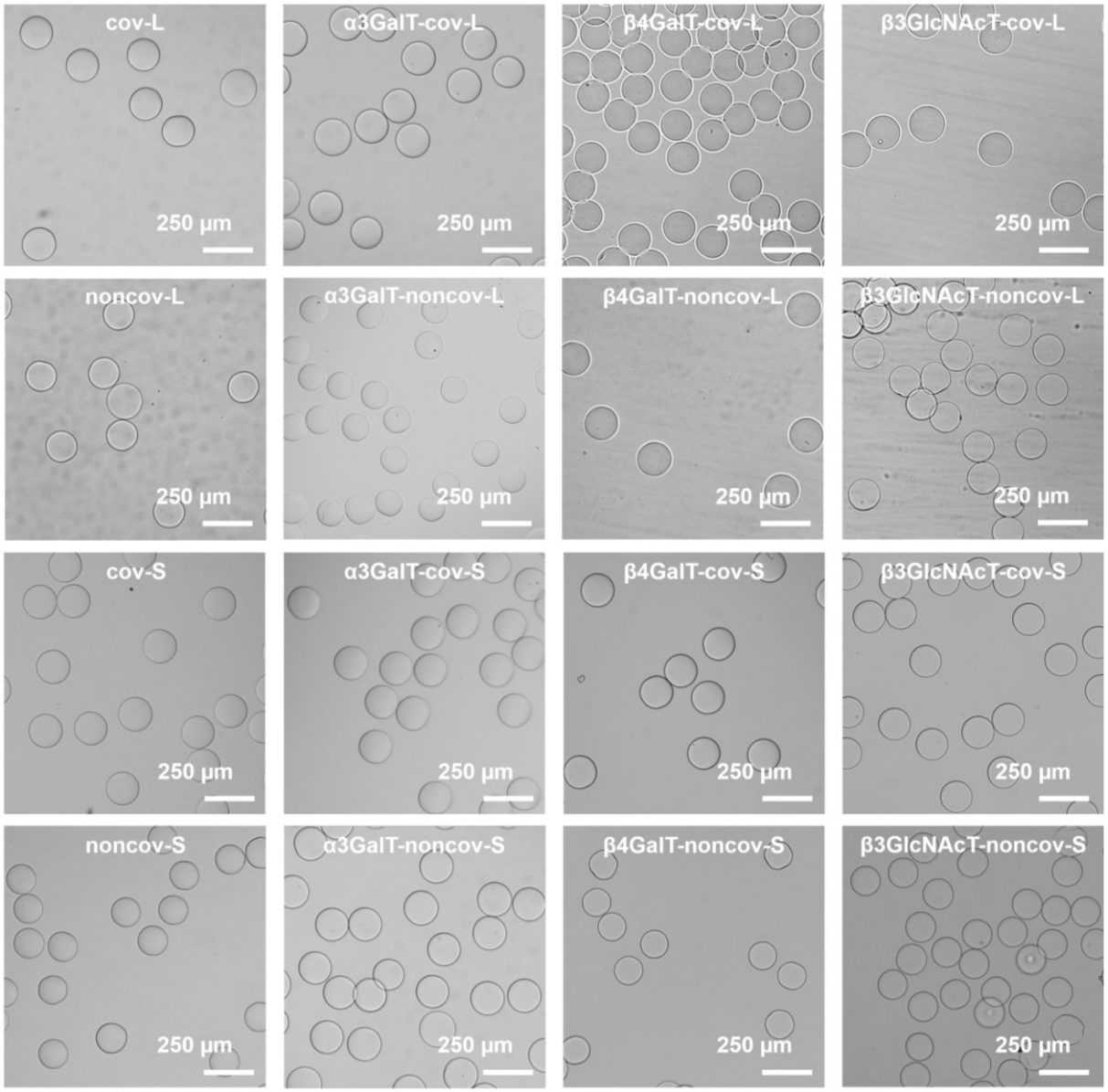

Figure SV.1 The left column displays optical microscopy images of microgels synthesized without immobilized enzymes. The subsequent columns depict GT-microgels containing the enzymes α3GalT, β4GalT, and β3GlcNAcT, respectively, arranged from left to right. Microgels labeled with the abbreviation cov-L comprise 20 kDa 8-arm PEG-VS and 10 kDa 4-arm PEG-SH, while those labeled noncov-L contain 10 kDa 8-arm PEG-VS and 10 kDa 4-arm PEG-SH. Conversely, microgels denoted as cov-S consist of 10 kDa 8-arm PEG-VS and 5 kDa 4-arm PEG-SH, whereas those labeled noncov-S incorporate 5 kDa 8-arm PEG-VS and 5 kDa 4-arm PEG-SH.

Table SV.1 (GT-)microgels fabricated by enzyme encapsulation were characterized by their respective diameters obtained from optical microscopy. The microgels, distinguished by their abbreviation indicating the method of enzyme attachment (covalent/cov or non-covalent/noncov) and the molecular weights of the PEG used in synthesis (large/L: 20 kDa 8-arm-PEG or 10 kDa 4-arm PEG; small/S: 10 kDa 8-arm-PEG or 5 kDa 4-arm PEG), incorporated the enzymes α3GalT, β4GalT, and β3GlcNAcT.

without enzyme	α3GalT	β4GalT	β3GlcNAcT
cov-L	α3GalT-cov-L	β4GalT-cov-L	β3GlcNAcT-cov-L
160 ± 7 µm	164 ± 9 µm	152 ± 4 µm	168 ± 9 µm
noncov-L	α3GalT-noncov-L	β4GalT-noncov-L	β3GlcNAcT-noncov-L
153 ± 10 µm	138 ± 5 µm	165 ± 3 µm	153 ± 5 µm
cov-S	α3GalT-cov-S	β4GalT-cov-S	β3GlcNAcT-cov-S
168 ± 4 µm	166 ± 3 µm	160 ± 4 µm	159 ± 3 µm
noncov-S	α3GalT-noncov-S	β4GalT-noncov-S	β3GlcNAcT-noncov-S
147 ± 3 µm	147 ± 4 µm	140 ± 3 µm	149 ± 4 µm

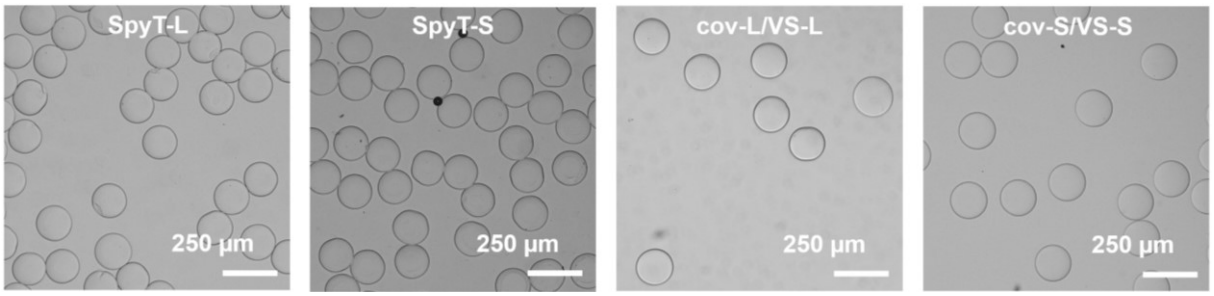

Figure SV.2 Optical microscopy images depict microgels containing SpyT, intended for post-attachment of enzymes. These microgels were synthesized from PEG of varying molecular weights: large microgels utilized 20 kDa 8-arm PEG-VS and 10 kDa 4-arm PEG-SH, while small microgels employed 10 kDa 8-arm PEG-VS and 5 kDa 4-arm PEG-SH. SpyT was incorporated into these microgels at a concentration of 2 w/v%. Additionally, images of microgels synthesized without SpyT but using the same molecular weights are included for comparison. These microgels were initially synthesized for direct comparison with cov-L and cov-S microgels containing encapsulated enzymes, and their inclusion here enhances comprehensiveness. The abbreviations VS-large-PEG and VS-small-PEG are utilized for clarity.

Table SV.2 The sizes (diameters in µm) of microgels containing SpyT obtained from optical microscopy are presented below. These microgels, intended for post-attachment of enzymes, were synthesized using PEG of different molecular weights: large/L microgels utilized 20 kDa 8-arm-PEG or 10 kDa 4-arm PEG, while small/S microgels employed 10 kDa 8-arm-PEG or 5 kDa 4-arm PEG. SpyT was incorporated into these microgels at a concentration of 2 w/v%. Additionally, sizes for microgels synthesized without SpyT but using the same molecular weights are included for comparison. These microgels were initially synthesized for direct comparison with cov-L and cov-S microgels containing encapsulated enzymes, and their inclusion here enhances comprehensiveness. The abbreviations VS-large-PEG and VS-small-PEG are utilized for clarity.

VS-L = cov-L	SpyT-L	VS-S = cov-S	SpyT-S
160 ± 7 µm	156 ± 4 µm	168 ± 4 µm	159 ± 4 µm

Fluorescamine assay

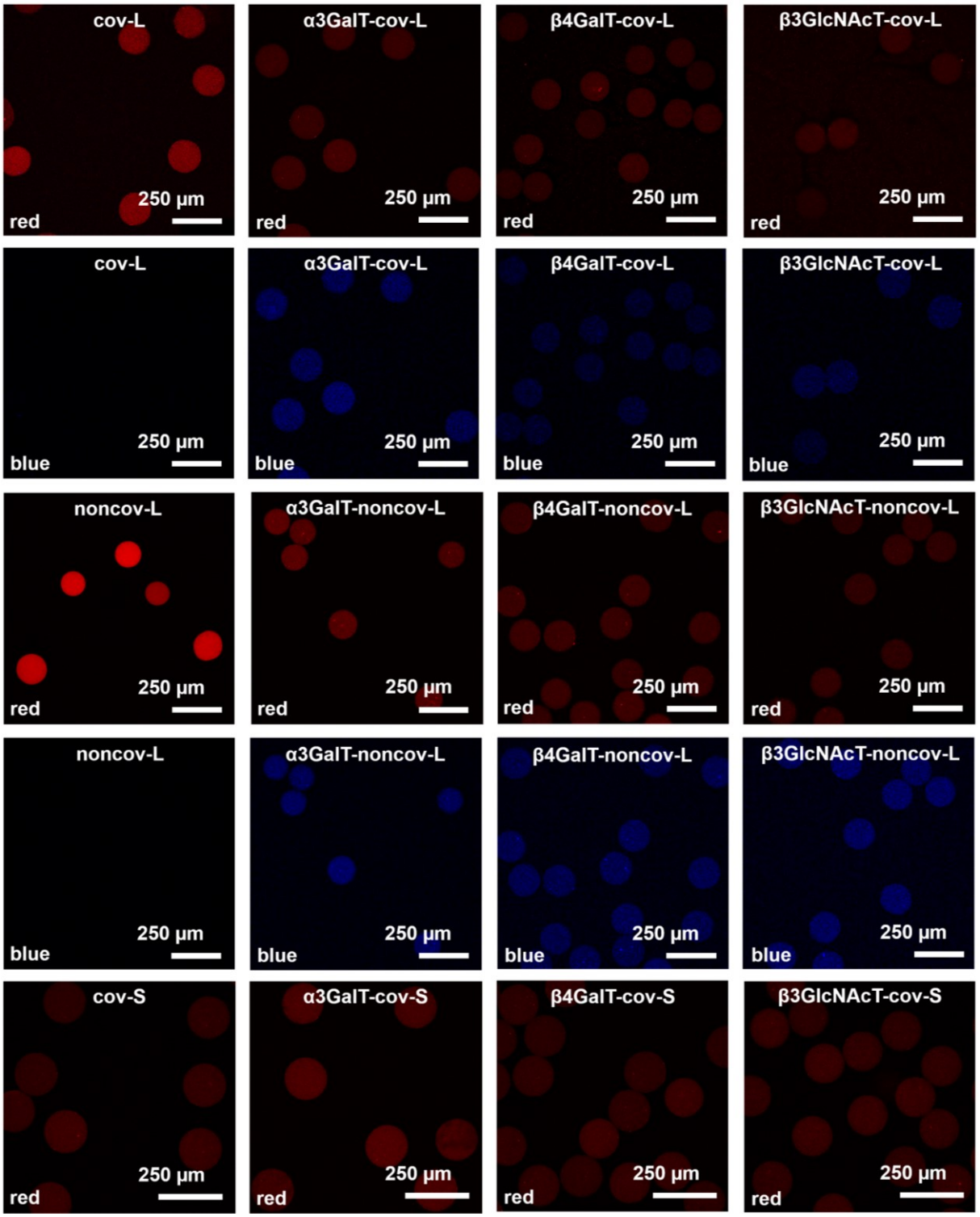

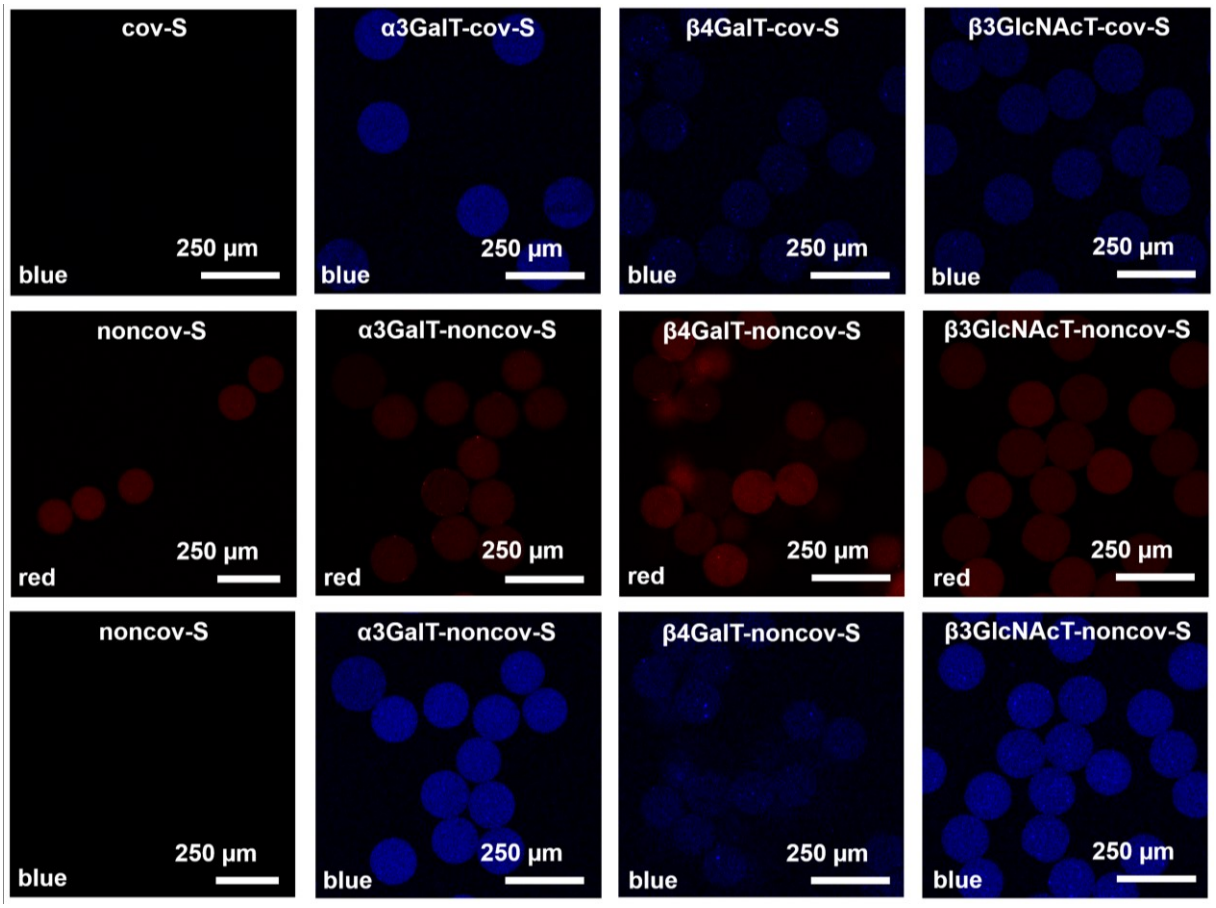

Figure SV.3 The confocal microscopy images display microgels after conducting the fluorescamine assay, showcasing both the red channel (RhB-MA: λ_{ex} = 475 nm, λ_{em} = 575-610 nm) and the blue channel (fluorescamine derivates: λ_{ex} = 405 nm, λ_{em} = 455-500 nm). The GT-microgels, synthesized *via* enzyme encapsulation, exhibit blue fluorescence attributed to the reaction of fluorescamine with primary amines present in the encapsulated enzymes (α3GalT, β4GalT, and β3GlcNAcT). On the left side, images of their respective counterparts without enzymes are shown, which do not demonstrate blue fluorescence. Microgels labeled with the abbreviation cov-L comprise 20 kDa 8-arm PEG-VS and 10 kDa 4-arm PEG-SH, while those labeled noncov-L contain 10 kDa 8-arm PEG-VS and 10 kDa 4-arm PEG-SH. Conversely, microgels denoted as cov-S consist of 10 kDa 8-arm PEG-VS and 5 kDa 4-arm PEG-SH, whereas those labeled noncov-S incorporate 5 kDa 8-arm PEG-VS and 5 kDa 4-arm PEG-SH.

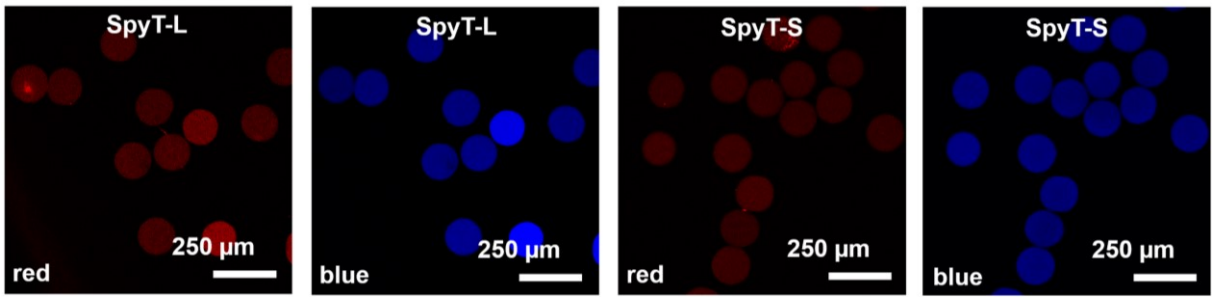

Figure SV.4 The confocal microscopy images depict microgels after conducting the fluorescamine assay, showcasing both the red channel (RhB-MA: λ_{ex} = 475 nm, λ_{em} = 575-610 nm) and the blue channel (fluorescamine derivates: λ_{ex} = 405 nm, λ_{em} = 455-500 nm). These images reveal the blue fluorescence exhibited by the microgels, attributed to the reaction of fluorescamine with primary amines present in the peptide SpyT. These microgels are intended for post-attachment of enzymes. They were synthesized using PEG of varying molecular weights: large microgels employed 20 kDa 8-arm-PEG-VS and 10 kDa 4-arm PEG-SH, while small microgels utilized 10 kDa 8-arm-PEG-VS and 5 kDa 4-arm PEG-SH. The synthesis incorporated 2 w/v% SpyT.

Enzymatic activity of glycosyltransferase-microgels

Table SV.3 Employed GTs along with the utilized abbreviation, full name, molecular weight (M_w), and enzyme substrates/products.

Enzyme	Full name	M_W [kDa]	Acceptor substrate	Donor substrate	Product
α3GalT	SpyC-MBP-α3GalT	94.7	LacNAc t2-*t*Boc[a)]	UDP-Galactose	Galili epitope-*t*Boc[b)]
β4GalT	SpyC-pp-*β*4GalT	73.1	GlcNAc-*t*Boc[c)]	UDP-Galactose	LacNAc t2-*t*Boc[a)]
β3GlcNAcT	SpyC-MBP-LgtA	94.3	Lactosyl-*t*Boc	UDP-GlcNAc	LNT II-*t*Boc[d)]

[a)] Type 2 *N*-Acetyl-D-Lactosamine [b)] Galactose-α-1,3-galactose-β-1,4- N-Acetyl-D-glucosamine epitope [c)] *N*-Acetyl-D-glucosamine [d)] Lacto-*N*-triose II

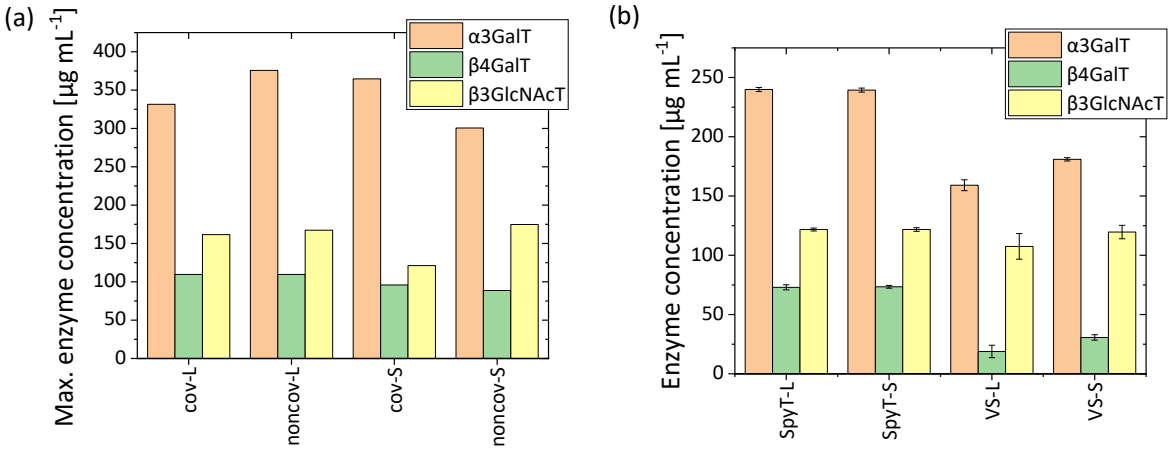

Figure SV.5 (a) The maximum achievable enzyme concentration in microgels was determined through enzyme encapsulation. The depicted concentration assumes a 100 % enzyme loading, thus potentially overestimating the actual amount of incorporated enzyme. (b) The enzyme concentration in GT-microgels synthesized *via* post-attachment of enzymes was assessed using a Bradford assay.

Cascade Reactions

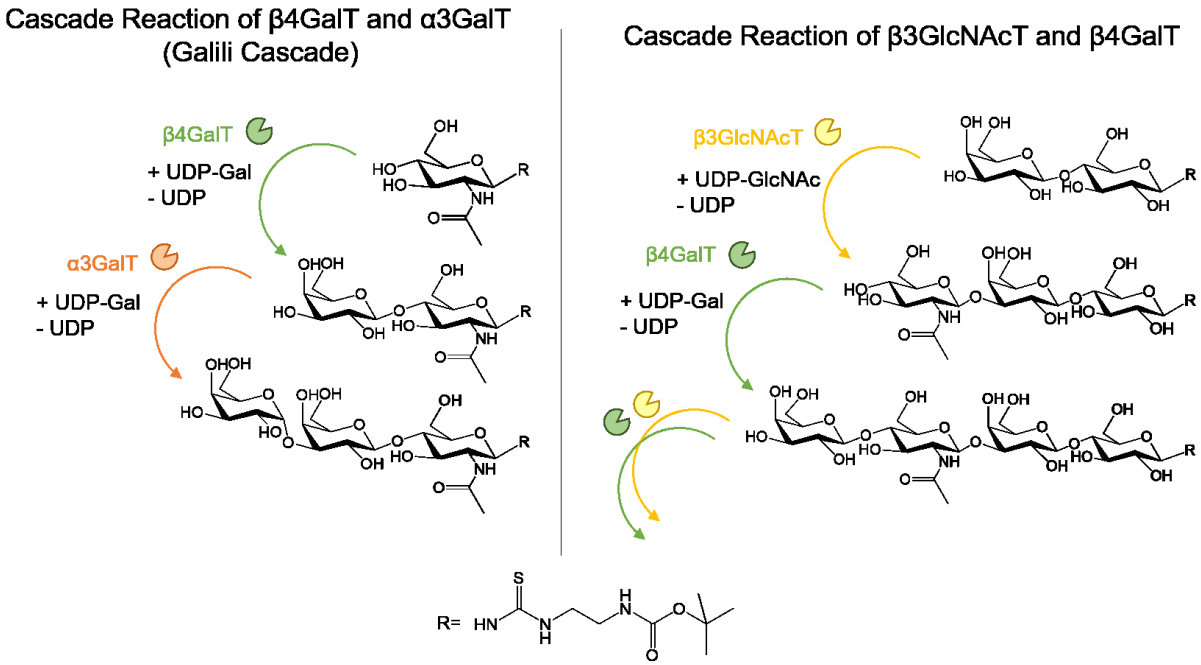

Figure SV.6 The left side illustrates the synthesis of the Galili epitope through a cascade reaction involving β4GalT and α3GalT. Initially, GlcNAc-*t*Boc serves as an acceptor for UDP-Gal, catalyzed by β4GalT, resulting in the formation of LacNAc type 2-*t*Boc. Subsequently, α3GalT catalyzes the attachment of another UDP-Gal, leading to the formation of the Galili epitope-*t*Boc. On the right side, the cascade reaction of β3GlcNAcT and β4GalT is depicted. β3GlcNAcT catalyzes the conversion of Lactosyl-*t*Boc to Lacto-*N*-triose II-*t*Boc (LNT II-*t*Boc).

Then, β4GalT catalyzes the further reaction to Lacto-*N*-neotetraose-tBoc (LNnT-*t*Boc). This process continues with alternating catalysis by both enzymes, resulting in the formation of longer glycan chains such as Lacto-*N*-neopentaose-*t*Boc (LNnP-*t*Boc) and Lacto-*N*-neohexaose-*t*Boc (LNnH-*t*Boc). In these reactions, UDP-GlcNAc serves as the donor substrate for β3GlcNAcT, while UDP-Gal acts as the donor substrate for β4GalT. The *t*Boc residue is indicated with the label R.

Cascade Reaction of β4GalT and α3GalT

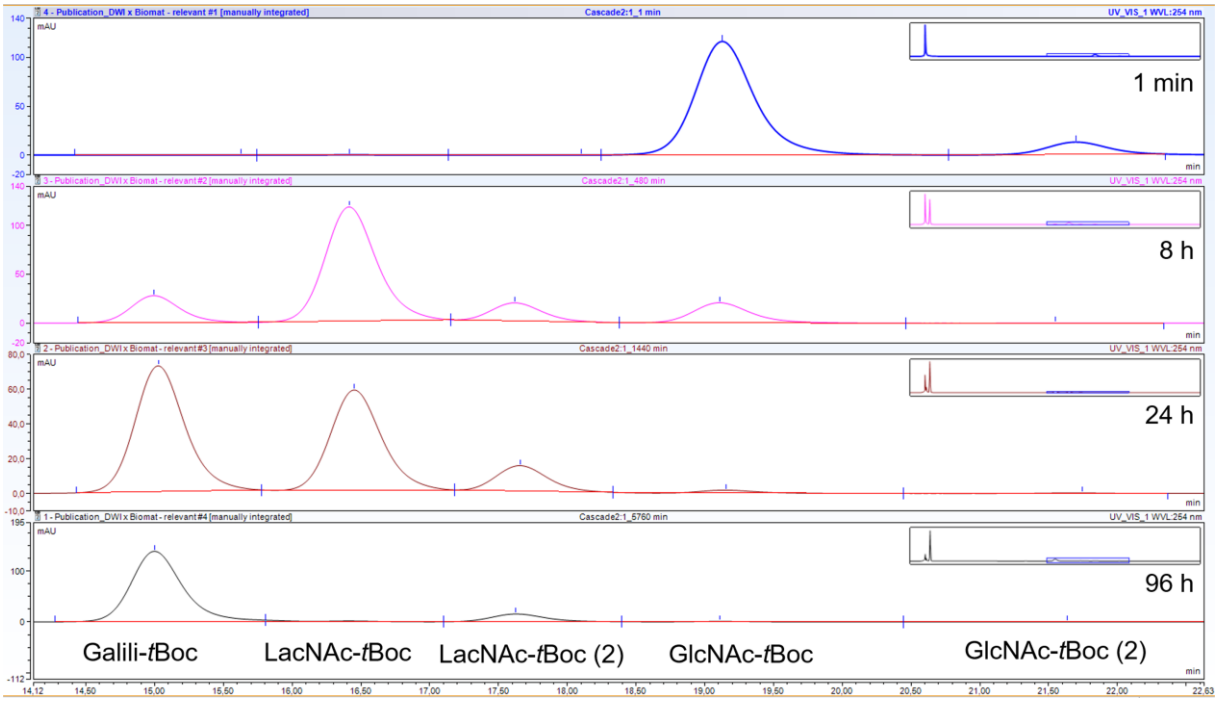

Figure SV.7 The HPLC chromatogram illustrates selected time points (from top to bottom: 1 min, 8 h, 24 h, 96 h) of the cascade reaction involving β4GalT and α3GalT (in a 2:1 ratio) for the synthesis of the Galili epitope-*t*Boc. The *t*Boc-linker was detected at a wavelength of 254 nm, with the y-axis representing arbitrary units (mAU) and the x-axis indicating retention time in minutes. A zoomed detailed section is provided in the upper right corner of each chromatogram. Peaks corresponding to expected retention times were manually integrated, and the relative area of these peaks was compared. GlcNAc-*t*Boc and LacNAc-*t*Boc exhibited two peaks each, and the peak areas were combined for calculation purposes. The molecular fractions obtained from this analysis are presented in **Table SV.4**. The chromatographic analysis was performed using Chromatography Data System Chromeleon 7.2.6 software.

Table SV.4 Molecular fractions (in %) of the substrates, obtained from the manual integration and comparison of the relative peak areas from HPLC chromatography of selected time points (1 min, 8 h, 24 h, 96 h) (**Figure SV.7**).

Molecular fraction [%]	1 min	8 h	24 h	96 h
GlcNAc-*t*Boc	90,02	12,42	0,62	0,33
GlcNAc-*t*Boc (2)	9,69	0,01	0,19	0,19
LacNAc-*t*Boc	0,15	63,59	39,79	0,9
LacNAc-*t*Boc (2)	0,11	9,69	10,05	10,22
Galili-*t*Boc	0,03	14,29	49,35	88,36

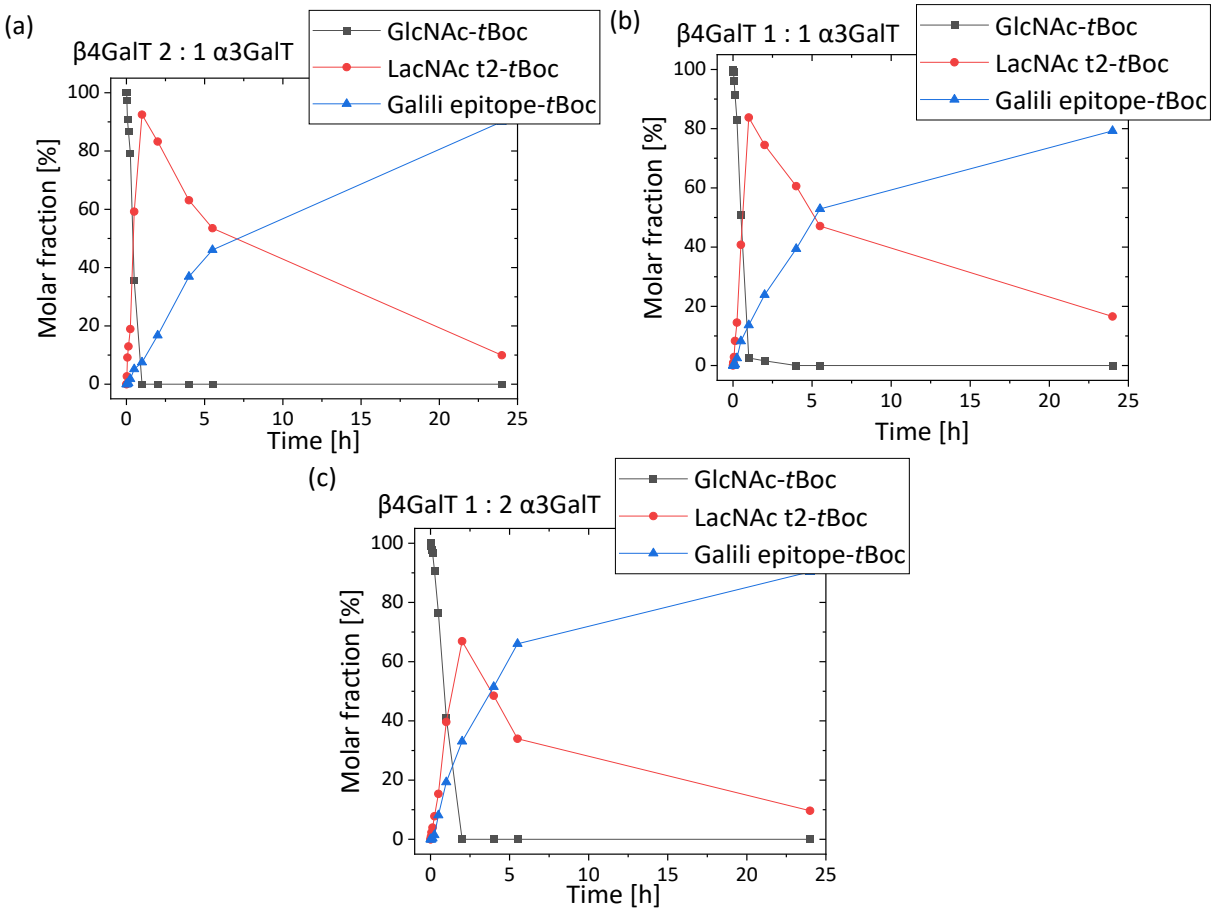

Figure SV.8 One-pot cascade reaction of non-immobilized GTs in solution. The successive reaction is enabled by mixing β4GalT and α3GalT with the initial acceptor substrate GlcNAc-*t*Boc and the donor substrate UDP-Gal, which serves as the donor substrate for both enzymes. GlcNAc-*t*Boc is transformed to LacNAc type 2 (t2)-*t*Boc by β4GalT. Subsequently, LacNAc t2-*t*Boc is transformed to the Galili epitope-*t*Boc by α3GalT. The molar fractions of the different molecules were observed over time. The β4GalT to α3GalT activity ratio was varied: (a) 2:1 to (b) 1:1 and (c) 1:2 with a total activity of 2.6 mU in 70 µL reaction volume.

Cascade Reaction of β4GalT and β3GlcNAcT

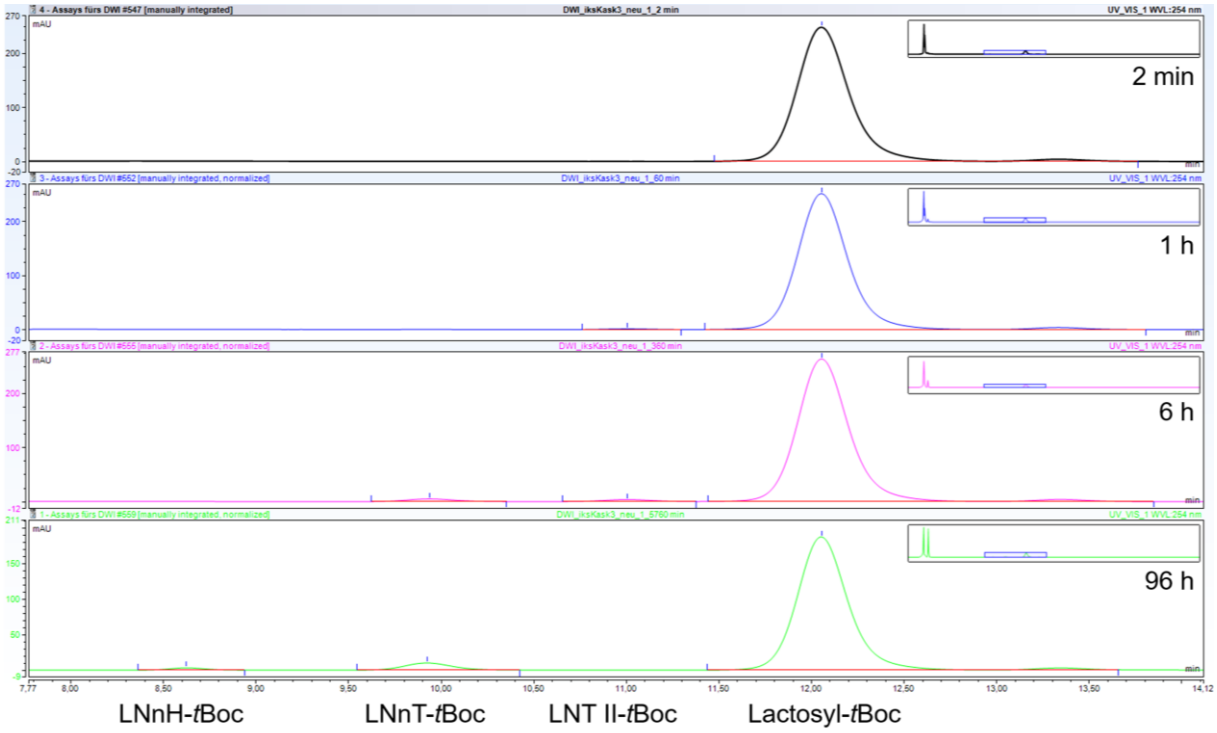

Figure SV.9 HPLC chromatogram for selected time points (from the top to the bottom: 1 min, 8 h, 24 h, 96 h) of the cascade of β3GlcNAcT and β4GalT. The *t*Boc-linker was detected at a wavelength of 254 nm, shown in arbitrary units (mAU) on the y-axis, and retention time in minutes is shown on the x-axis. A zoomed detailed section is shown in the upper right section of each chromatogram. Peaks at expected retention time were manually integrated and the relative area of the peaks were compared. Obtained molecular fractions are shown in **Table SV.5**. Analysis was conducted with Chromatography Data System Chromeleon 7.2.6 software.

Table SV.5 Fractions are obtained from the manual integration and comparison of the relative peak area. Molecular fractions (in %) of the substrates, obtained from the manual integration and comparison of the relative peak areas from HPLC chromatography of selected time points (2 min, 1 h, 6 h, 96 h) (**Figure SV.9**).

Molecular fraction [%]	2 min	1 h	6 h	96 h
Lactosyl-*t*Boc	100	99.7	97.78	93.74
LNT II-*t*Boc	0	0.3	0.58	0
LNnT-*t*Boc	0	0	1.64	5.56
LNnP-*t*Boc	0	0	0	0
LNnH-*t*Boc	0	0	0	0.69

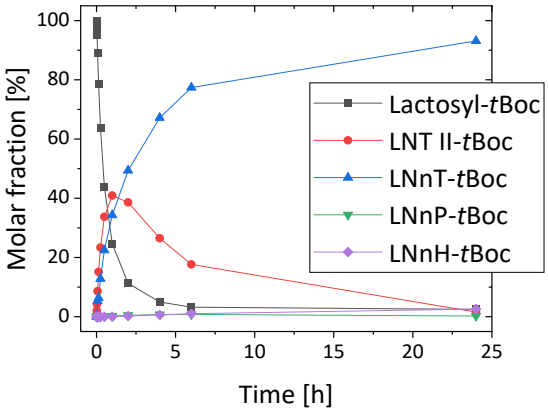

Figure SV.10 One-pot cascade reaction of non-immobilized GTs in solution. The successive reaction is enabled by mixing β3GlcNAcT and β4GalT with the initial acceptor substrate Lactosyl-*t*Boc and the donor substrates UDP-GlcNAc and UDP-Gal. UDP-GlcNAc serves as a donor substrate for β3GlcNAcT while UDP-Gal serves as the donor substrate of β4GalT. (a) Lactosyl-*t*Boc is transformed to Lacto-*N*-triose II-*t*Boc (LNT II-*t*Boc) by β3GlcNAcT. Subsequently, the formation of Lacto-*N*-neotetraose-*t*Boc (LNnT-*t*Boc) is catalyzed by β4GalT. Both enzymes catalyze reactions in an alternating manner for the formation of Lacto-*N*-neopentaose-*t*Boc (LNnP-*t*Boc) and Lacto-*N*-neohexaose-*t*Boc (LNnH-*t*Boc). The *t*Boc residue is labeled with R. (b) The molar fractions of the different molecules were observed over time. The β4GalT-to-β3GlcNAc activity ratio was set to 2:1 with a total activity of 20.0 mU and in 70 µL reaction volume.

VI. Summary and Outlook

This thesis focuses on the use of microgels as multifunctional carriers for proteins and enzymes. This combination presents versatile applications in biomedical and biotechnological fields.

In the initial section of this thesis (**Chapter III**), multi-responsive (p(VCL/NTAaa) core-shell microgels were synthesized and characterized regarding their biocompatibility. These microgels demonstrated the ability to take up the positively charged model protein cytochrome c (cyt c). Following the validation of nitrilotriacetic acid (NTA) functionalized microgels for electrostatic immobilization, the subsequent chapter (**Chapter IV**) aimed to expand their utility through enzyme immobilization. Hyaluronan Synthase from *Pasteurella multocida* (*Pm*HAS) was immobilized on the microgels *via* a polyhistidine tag within the enzyme's amino acid sequence. NTA enabled enzyme immobilization through the mutual complexation of a metal ion by the enzyme and microgel. This setup enabled repeated enzymatic production of hyaluronic acid (HA). Finally, the last chapter (**Chapter V**) demonstrated the immobilization of additional glycosyltransferases (GTs) using poly(ethylene glycol) (PEG)-based microgels synthesized *via* droplet-based microfluidics. Three distinct GTs were immobilized, with optimization realized through specific immobilization techniques. The resulting GT-microgels were employed for single-reaction catalysis and one-pot cascade reactions involving multiple enzymatic steps.

In **Chapter III**, the primary objective was to establish the suitability of p(VCL/NTAaa) microgels for bio-applications. Having demonstrated the uptake of cyt c in this chapter, these biocompatible microgels may in the future be considered as effective platforms for stimuli-dependent uptake and release of other biomacromolecules, with potential applications in drug delivery.

Subsequently, the focus moved forward to biomimetic enzymatic production of HA in the following chapter (**Chapter IV**). This endeavor resulted in achieving the highest yield of HA *via* the biocatalysis of immobilized *Pm*HAS reported to date, demonstrating the reusability of the system over three 24-hour cycles. With their demonstrated biocompatibility, this unique enzyme-microgel system presents promising prospects for various biological applications.

Drawing inspiration from the natural polysaccharide production of mucin, such microgels can serve as a basis for the development of adaptive hydrogel materials. Additionally, with the increasing demand for HA in fields such as medicine and cosmetics, this microgel system presents a unique opportunity to efficiently meet this demand. Therefore, addressing the scaling up of microgel synthesis in future endeavors is imperative.

In **Chapter V**, a substantial milestone was achieved by employing a cascade of GT-microgels for glycan synthesis, marking the first utilization of such a strategy and addressing a gap in prior research on automated enzymatic glycan synthesis within GT-microgels. These findings represent the initial strides toward developing a GT-microgel reactor, with further investigations set for the future. The biocatalytic GT-microgels showcased in this study demonstrate the potential for establishing a fully automated and scalable synthesis of tailored glycans, with diverse applications spanning drug development, vaccines, nutrition, and cosmetics. Furthermore, integrating these microgels into a modular membrane reactor holds potential advantages beyond facilitating continuous glycan production. The spatial segregation of different GT-microgels within the reactor could potentially enhance reaction kinetics, presenting a promising avenue for further exploration in future small-scale production and research endeavors, marking a transition from fundamental research to application.